La méthode de substitution appliquée au 240Pu

Ricardo Pérez Sánchez

Ricardo Pérez Sánchez. La méthode de substitution appliquée au 240Pu. Astrophysique [astro-ph]. Université de Bordeaux, 2019. Français. NNT : 2019BORD0136 . tel-02426248

HAL Id: tel-02426248
https://theses.hal.science/tel-02426248
Submitted on 2 Jan 2020

THÈSE

Présentée à

L'UNIVERSITÉ DE BORDEAUX

ÉCOLE DOCTORALE DES
SCIENCES PHYSIQUES ET DE L'INGÉNIEUR

Par **Ricardo PÉREZ SÁNCHEZ**

pour obtenir le grade de
Docteur
Spécialité : Astrophysique, Plasmas et Nucléaire

"La méthode de substitution apliquée au ^{240}Pu"

"The surrogate reaction method applied to ^{240}Pu"

Thèse dirigée par Mme. Beatriz JURADO et M. Vincent MÉOT
et encadrée par M. Olivier ROIG

préparée au
Centre d'Études Nucléaires de Bordeaux Gradignan
et au
Commissariat à l'Énergie Atomique de la DAM - Ile de France

Soutenue le 17 septembre 2019

Devant la commission d'examen formée de :

Rapporteurs :	M Frank GUNSING	Directeur de Recherche - CEA/DRF - Saclay
	M Jonathan WILSON	Directeur de Recherche - IPN - Orsay
Examinateurs :	M Bertram BLANK	Directeur de Recherche - CENBG - Bordeaux
	M Marc DUPUIS	Ingenieur Chercheur - CEA/DAM - Ile de France
Directeurs :	Mme Beatriz JURADO	Directrice de Recherche - CENBG - Bordeaux
	M Vincent MÉOT	Directeur de Recherche - CEA/DAM - Ile de France
Encadrant :	M Olivier ROIG	Ingenieur Chercheur - CEA/DAM - Ile de France

Synthèse

Cette thèse porte principalement sur l'étude des probabilités d'émission gamma et de fission du noyau composé $^{240}Pu^*$ obtenues en utilisant la méthode de substitution. Cette méthode expérimentale vise, par le choix approprié de réactions nucléaires, à former un noyau composé identique en masse et en énergie d'excitation à celui formé dans une réaction de capture neutronique. Le but est de combler le manque de données nucléaires, entre autres des sections efficaces de capture neutronique intéressantes pour la physique des réacteurs et l'astrophysique. En effet, dès lors que les expériences de réactions en neutron induit sur ces noyaux ne sont pas réalisables, par exemple si le noyau cible est trop eloigné de la vallée de stabilité, les capacités prédictives des modèles de réactions sont faibles, elles sont difficilement ajustables avec trop peu de données. Du point de vue théorique, l'amélioration de la prédictibilité des réactions porte sur une description plus microscopique des processus en jeu amenant à être moins empirique. Les probabilités d'émission gamma ou de fission du noyau composé formé dans ces réactions de substitution peuvent servir à améliorer significativement les prédictions. Pour cela, l'élément crucial est de comprendre les différences entre les processus de formation et de désexcitation des noyaux formés dans ces réactions et dans celles induites par neutron. Depuis plusieurs années, une collaboration entre les laboratoires de physique nucléaire CENBG et CEA/DAM/DIF fournit des éléments pour la compréhension de ces processus. Notamment en s'intéressant à la distribution en spin et parité du noyau composé dans les réactions de substitution, elle a pu montrer qu'elle était très différente de celle induite par neutron et jouait un rôle important dans la compétition entre l'émission gamma et neutron. Cependant, son rôle dans la fission était plus ambigu, pour laquelle les données de substitution reproduisent bien les données neutroniques. De tout ce travail en commun ont resulté divers articles [1], [2], [3], [4], [5], [6], et diverses thèses [7], [8], [9], [10].

Les réactions de substitution sont des réactions de "pick-up", transfert ou de diffusion inélastique qui amènent à un noyau composé de mêmes masse et énergie d'excitation que dans la réaction induite par neutron. Différentes réactions de substitution sont étudiées depuis leur introduction par Cramer et Britt dans les années 70. La figure 1 montre schématiquement le concept de la méthode de substitution.

La méthode s'appuie sur l'hypothèse du noyau composé de Bohr [11], qui dit que la voie de sortie est indépendante de la voie d'entrée. Dans cette hypothèse, on peut écrire, en fonction de l'énergie d'excitation E^* du noyau $A+1$, la section efficace induite par neutron $\sigma_\chi^n(E^*)$, de chaque voie de désexcitation χ, comme un produit de la section efficace de formation du noyau composé $\sigma_{CN}^{A+1}(E^*)$ et la probabilité de désexcitation par une certaine voie de ce noyau $P_\chi^{mes.}$, eq. (1).

$$\sigma_\chi^n(E^*) = \sigma_{CN}^{A+1}(E^*) \cdot P_\chi^{mes.}(E^*) \tag{1}$$

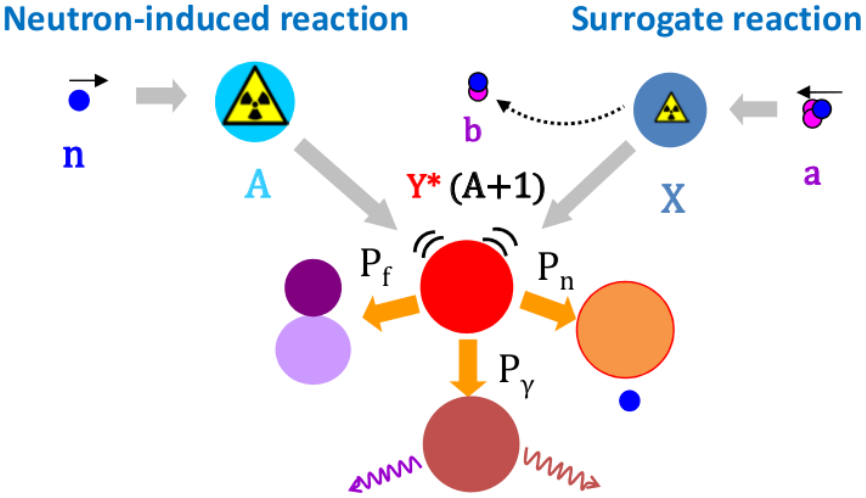

Figure 1: Représentation schématique d'une réaction de capture neutronique, $n+A \rightarrow Y^*$, et d'une des réactions de substitution possibles, $X(a,b)Y^*$. Lorsque le noyau composé Y^* est formé il va se désexciter avec une certaine probabilité d'émettre des gammas (P_γ), ou bien des neutrons (P_n), ou de fissionner (P_f). La figure montre que la cible associée à la réaction de substitution est moins radioactive que celle asscociée à la réaction neutronique.

L'équation 1 est valable pour une réaction de substitution sous certaines conditions: d'abord que les probabilités de désexcitation mesurées par réaction de substitution et induites par neutron soient égales à $P_\chi^{mes.}(E^*) = P_\chi^n(E^*)$, ce qui a lieu dans la limite de Weisskopf-Ewing [12] (W.E.) ou si les noyaux composés sont formés dans des états d'excitation et de spin et parité identiques. En effet, les probabilités $P_\chi(E^*)$, équations (2), dépendent aussi de la distribution de spin et parité $S(E^*, J^\pi)$ dans le cas des réactions de capture neutronique, $F(E^*, J^\pi)$ dans le cas des réactions de substitution, et des rapports d'embranchement $G_\chi(E^*, J^\pi)$, qui sont simplement la probabilité de désexcitation par la voie χ du noyau formé excité dans un état d'énergie E^*, de spin J et de parité π.

$$\begin{aligned} P_\chi^n(E^*) &= \sum_{J^\pi} S(E^*, J^\pi) G_\chi(E^*, J^\pi) \\ P_\chi^{mes.}(E^*) &= \sum_{J^\pi} F(E^*, J^\pi) G_\chi(E^*, J^\pi) \end{aligned} \tag{2}$$

Dans la limite W.E., l'approximation donne que les rapports d'embranchement G_χ deviennent indépendants de J^π. L'équation (2) montre alors directement l'égalité entre les probabilités mesurées en réaction de capture et de substitution, car la somme sur la distribution en spin vaut 1. Cependant, ceci reste une approximation valable uniquement pour des énergies d'excitation très élevées.

Dans le cadre de cette thèse, nous avons proposé de mesurer les probabilités d'émission gamma et de fission dans la réaction de diffusion inélastique (α, α') sur une cible de ^{240}Pu. Les deux probabilités seront pour la première fois mesurées simultanéement dans le même domaine en énergie d'excitation, entre 4 et 8 MeV, en sachant que le $S_n = 6.5$ MeV. Ceci va permettre d'extraire les distributions en spin et parité $F(E^*, J^\pi)$ à partir des deux voies, émission de gamma et fission, pour la réaction de substitution (α, α'), comme cela a été réalisé avec la même méthode que les études précédentes sur la capture neutronique radiative et la réaction ($^3He,p$) [8] [9] et indépendamment sur la fission et les réactions de transfert [10], [5]. Ces distributions de spin seront comparées à un calcul microscopique. Celui-ci, combiné aux rapports d'embranchement $G_\chi(E^*, J^\pi)$ caractéristiques du noyau composé $^{240}\mathrm{Pu}^*$, permettra de calculer les probabilités et les comparer à celles mesurées dans la réaction $^{240}\mathrm{Pu}(\alpha, \alpha')$.

De nombreux travaux ont mesuré des probabilités de fission des actinides et en ont déduit des sections efficaces en utilisant l'hypothèse de W.E. Ils ont trouvé généralement un bon accord entre les sections efficaces déduites avec des réactions de substitution et celles induites par neutron. Les articles de Cramer et Britt [13], Back *et al.* [14], Petit *et al.* [15] ou Kessedjian *et al.* [16] le montrent bien. Il y a eu aussi des études de la fission effectuées avec la méthode SRM ("surrogate ratio method"), qui utilisent le rapport entre la section efficace à mesurer et une autre bien connue, comme celles de Ressler *et al.* en 2011 [17] et de Hughes *et al.* [18] en 2014. Ils donnent les sections efficaces de fission $^{236,237,238}\mathrm{Pu}(n,f)$ en bon accord avec les données neutroniques existantes. En revanche, peu de mesures existent pour la capture radiative car l'hypothèse de W.E. ne peut s'appliquer. La première mesure de l'émission gamma date de 2006, où Boyer *et al.* [19] ont déduit la section efficace $^{234}\mathrm{Pa(n,\gamma)}$ en utilisant la réaction de substitution $^{232}\mathrm{Th}(^3\mathrm{He,p})^{234}\mathrm{Pa}$. Ce travail a été suivi de plusieurs travaux comme ceux de Bernstein *et al.* [20], Scielzo *et al.* [21] ou de Boutoux *et al.* [4]. À différence de la fission, les sections efficaces obtenues pour la capture radiative en appliquant la méthode de substitution sont en désaccord avec les sections efficaces neutroniques de capture. Ceci a été attribué à une plus grande sensibilité de la probabilité P_γ à la distribution de spin et parité du noyau composé pour $E_n < 3$ MeV où l'hypothèse de W.E. ne peut pas être appliquée. Pour cette raison, des travaux plus récents se sont focalisés sur les prédictions des distributions de spin des noyaux formés lors d'une réaction de substitution, notamment les nôtres, et aussi ceux décrits dans les articles très récents de Escher *et al.* [22] en 2018 et de Ratkiewicz *et al.* [23] en 2019. Dans ce dernier article, ils étudent la réaction $^{95}Mo(d,p)$ avec une approche similaire à ce que nous décrivons dans cette thèse. Limité à la capture radiative, ils obtiennent un résultat prometteur qui est en accord avec les sections efficaces de capture neutronique.

Néanmoins, la question qui demeure, et que nous traitons ici, est qu'en-t-il de la fission quand elle apparaît dans un domaine en énergie où l'hypothèse de W.E. ne s'applique pas. En effet, est-il possible de retrouver une cohérence dans le rôle de la distribution de spin pour les deux processus, émission gamma et fission? Nous regardons le cas du noyau composé $^{240}\mathrm{Pu}^*$ qui est particulièrement intéressant, car il s'agit d'un noyau pair-pair, ce qui est censé *a priori* rendre le noyau décroissant plus sensible à la voie d'entrée, car un noyau pair-pair a une densité de niveaux plus petite qu'un noyau pair-impair ou impair-impair. Les réactions de diffusion inélastique $^{240}\mathrm{Pu}(\alpha, \alpha'\gamma \text{ ou f})^{240}\mathrm{Pu}^*$ vont permettre d'exciter le noyau $^{240}\mathrm{Pu}^*$ à des énergies élévées et équivalentes à $^{239}\mathrm{Pu}(n, \gamma/f)$.

La probabilité d'émission gamma ou de fission sera extraite expérimentalement (voir formule (3)) en mesurant le nombre d'éjectiles détectés $N_s(E^*)$ correspondant (particule b fig. 1), à une énergie d'excitation donnée E^* et après correction de l'efficacité de détection ε_χ, au nombre de noyaux composés formés dans la réaction, et le nombre de coïncidences (éjectile+gamma ou éjectile+fission) $N_\chi(E^*)$ correspondant au nombre de noyaux ayant décru par la voie de désexcitation regardée, $\chi = \gamma$ ou f.

$$P_\chi(E^*) = \frac{N_\chi(E^*)}{N_s(E^*) \cdot \varepsilon_\chi(E^*)} \tag{3}$$

L'expérience proposée a eu lieu en 2017 au tandem de l'IPN d'Orsay [24]. Un faisceau d'ions ^4He a été envoyé avec une énergie cinétique de 30 MeV sur une cible de $^{240}PuO_2$ électrodéposé sur une feuille très fine, 100 μg/cm^2, de carbone. Le dispositif expérimental utilisé, décrit en détail dans une publication récente [24], comprenait :

- des détecteurs de particules chargées, des semiconducteurs Si segmentés de 100 μm d'épaisseur et SiLi (de 2 et 5 mm d'épaiseur) montés en télescope ΔE-E, pour identifier, mesurer les énergies et sélectionner les éjectiles $N_s(E^*)$, signaux de la réaction choisie. L'énergie d'excitation du noyau composé sera déduite de ces mesures en tenant compte en plus de l'angle de détection;
- des détecteurs de gamma, 4 scintillateurs C_6D_6 et 6 HPGe, pour compter le nombre de coïncidences entre les détecteurs gamma et les télescopes N_γ;
- des détecteurs de fission, des cellules photovoltaïques, pour compter les coïncidences entre les détecteurs de fission et les télescopes N_f;
- un porte cible positionnable ("Target airlock") avec des cibles de $^{240}PuO_2$, de carbone, de ^{208}Pb et un trou pour laisser passer le faisceau.

La figure 2 montre le dispositif expérimental dans son ensemble avec la chambre à réaction (fig. 2a) et en particulier les détecteurs de particules et de fission (fig. 2b et 2c). Le positionnement des télescopes offre une ouverture angulaire de 119° à 157°, à l'arrière fig. 2b.

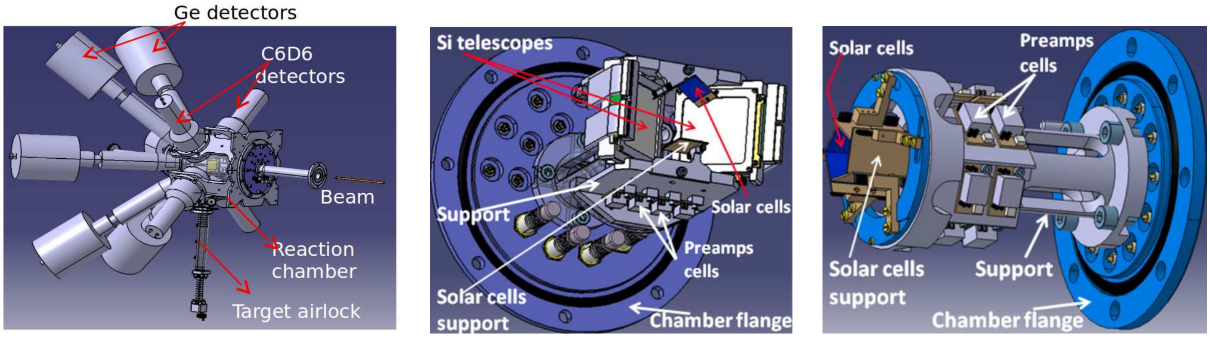

(a) Vue de l'ensemble du dispositif.

(b) Détecteurs à l'intérieur de la chambre à réaction (angles arrière).

(c) Détecteurs à l'intérieur de la chambre à réaction (angles avant).

Figure 2: Modèles 3D de l'extérieur et de l'intérieur du dispositf expérimental.

L'étalonnage des télescopes a été réalisé en utilisant une réaction de diffusion inélastique, $^{208}\mathrm{Pb}(\alpha,\alpha')^{208}\mathrm{Pb}^*$, afin d'obtenir des particules chargées d'énergies très proches de celles rencontrées dans la réaction regardée. Connaissant les états excités du ^{208}Pb, la cinématique de la réaction est bien reproduite pour chaque état excité. Les énergies des éjectiles sont bien connues ainsi que les pertes d'énergies attendues dans les télescopes ΔE-E obtenues avec le code Kaliveda [25]. Elles permettent par comparaison avec celles mesurées d'étalonner finement les détecteurs dans le domaine d'énergie de mesures à étudier (plus de détails dans le chapitre 3).

L'étalonnage des détecteurs gamma est standard et important jusqu'à des énergies de l'ordre de 2 MeV, énergie des cascades gamma à détecter. Le nombre N_γ sera obtenu avec les scintillateurs C_6D_6 et les détecteurs HPGe après correction de l'efficacité. Cette efficacité de détection gamma ε_γ est déterminée avec une méthode validée dans des travaux précédents [1],[2], appelée la méthode EXEM ("EXtrapolated Efficiency Method"). Elle repose sur l'hypothèse que la variation de l'efficacité de détection avec E^* est la même en-dessous et au-dessus du S_n, ou du seuil de fission dans le cas du ^{240}Pu. En dessous du seuil de fission et du S_n, puisque la probabilité d'émission gamma doit être égale à $P_\gamma = 1$, l'efficacité dans cette région d'énergie s'écrit $\varepsilon_\gamma = N_\gamma / N_s$. Ensuite, la variation de l'efficacité obtenue est extrapolée à des énergies d'excitation plus élevées $\sim S_n + 1.5$ MeV.

Le dernier point important à propos du dispositif est l'efficacité de détection des fragments de fission. Les détecteurs sont composés de 8 plans de cellules photovoltaïques, 5 aux angles à l'avant et 3 aux angles à l'arrière. Chaque plan étant composé de deux cellules de taille differente pour pouvoir mesurer différents angles des fragments de fission, les cellules à l'avant sont positionnées à differents angles entre 20^o et 60^o, et à l'arrière entre 115^o et 155^o. L'anisotropie angulaire des fragments de fission a été aussi étudiée afin de bien déterminer l'efficacité de détection de fission. Un code Monte Carlo simulant l'émision des fragments a été écrit pour compléter les mesures réalisées avec une source de ^{252}Cf. Le nombre d'événements de fission N_f va dépendre fortement de cette efficacité de détection des fragments cellule par cellule.

Parmi toutes les corrections appliquées (bruit de fond, soustraction des contaminants,...) aux données mesurées pour extraire les probabilités d'émission gamma et de fission, nous noterons ici une particulièrement intéressante : celle que nous attribuons à la contribution non négligeable de la fission ternaire. En effet, les histogrammes de coïncidence éjectile-fission ont montré des événements entre 0 et 4.5 MeV, soit en dessous du seuil théorique de fission du ^{240}Pu, même après avoir soustrait les coïncidences aléatoires. Une explication plausible est qu'il s'agit d'événements de fusion-fission ternaire avec une particule ^{4}He émise avec une énergie de l'ordre de la dizaine de MeV dans la réaction $^4\text{He}+^{240}\text{Pu}\rightarrow^{244}\text{Cm}^* \rightarrow FF1 + FF2 + \alpha$. Ces événements font donc partie de ceux sélectionnés dans nos données et constituent un bruit de fond relativement important pour l'extraction des probabilités de fission à base énergie d'excitation. Une soustraction de ces événements a donc été réalisée.

Finalement, les résultats obtenus, avec toute la statistique possible et corrigés, sont représentés par les deux courbes de probabilités d'émission gamma et de fission sur la figure 3. Malheureusement la présence inattendue de contaminants dans la cible nous a obligé à restreindre nos données à des énergies d'excitation inférieures à 8 MeV.

Si on regarde en détail la figure 3, on voit qu'entre 2 et 4.5 MeV la probabilité de fission P_f est nulle. Dans ce domaine en énergie, la probabilité d'émission gamma P_γ est égale à 1, car c'est la seule voie ouverte pour la désexcitation du noyau composé. À partir de 4.5 MeV d'énergie, la voie fission est ouverte et est en compétition avec la voie gamma. Lorsque P_f augmente, P_γ diminue, et jusqu'au S_n, on vérifie que $P_f + P_\gamma = 1$. Quand $E^* > S_n$, le noyau a assez d'énergie pour émettre des neutrons, qui ne sont pas mesurés avec notre dispositif. Le noyau a alors le choix entre les trois voies P_f, P_γ et P_n pour émettre son énergie d'excitation, et donc l'ouverture de la voie neutron a des

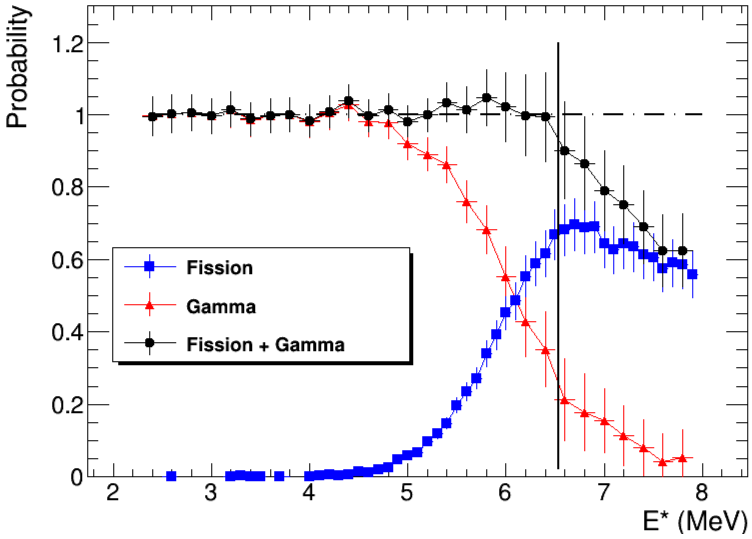

Figure 3: Probabilités de désexcitation du ^{240}Pu* en fonction E^*, moyennées sur l'angle de l'éjectile, en prenant en compte la soustraction du fond de fission ternaire supposé. La ligne verticale noire répresente l'énergie de séparation du neutron $S_n = 6.534$ MeV. Le seuil de fission est autour de 4.5 MeV.

répercussions sur les autres voies.

Pour interpréter ces résultats, il faut s'intéresser aux différents termes des équations (1) et (2). Dans l'équation (2), les éléments non mesurés sont la distribution en spin et parité $F(E^*, J^\pi)$ et les rapports d'embranchement $G_\chi(E^*, J^\pi)$. Plusieurs chemins d'interprétation sont possibles. A partir des probabilités mesurées $P^{mes.}_{\gamma fission}(E^*)$, en déterminant l'un des deux termes, l'autre peut être déduit. Si les rapports d'embranchement $G_\chi(E^*, J^\pi)$ sont calculés, alors la distribution en spin $F(E^*, J^\pi)$ pourra être extraite en s'ajustant sur les résultats expérimentaux, c'est le premier chemin emprunté. Si la distribution en spin est calculée ainsi que les rapports d'embranchement, les probabilités de désexcitation pourront être extraites et comparées aux résultats expérimentaux, c'est le deuxième chemin suivi. Un troisième chemin pourrait être l'ajustement des rapports d'embranchement sur les probabilités mesurées.

Si l'on se reporte à l'équation (1) dans le cas bien connu de la capture neutronique sur le ^{239}Pu, les valeurs des différents sections efficaces de fission, de diffusion élastique et inélastique, de capture radiative et de transmission existent expérimentalement ainsi que la section efficace de réaction grâce au modèle optique. La distribution en spin dans le cas de réactions induites par neutron peuvent être calculées avec confiance. Il reste donc les rapports d'embranchement $G_\chi(E^*, J^\pi)$ à déterminer grâce aux modèles de réaction. Néanmoins, les valeurs de $G_\chi(E^*, J^\pi)$ dépendent fortement des paramètres des modèles pour la désexcitation du noyau composé ^{240}Pu*. Ces paramètres intègrent par exemple les schémas de niveaux discrets, les densités de niveaux dans le continuum et les fonctions de force gamma. Ces paramètres régissant la compétiton entre les différentes voies de désexcitation du noyau vont devoir être ajustés sur les données nucléaires existantes. Ce processus de calcul pour déterminer un bon jeu de paramètres, avec un code de calcul de réactions comme TALYS 1.9 [26], s'appelle une évaluation. Ici, il ne s'agira pas d'une évaluation de référence mais d'une évaluation adaptée à notre problème, suffisamment précise pour expliquer nos résultats dans le domaine en énergie $E_n = 0.03 - 6$ MeV. Les sections efficaces $^{239}\mathrm{Pu}^*(n,f)$ et $^{239}\mathrm{Pu}^*(n,\gamma)$ seront prises en compte ainsi que les sections efficaces de diffusion élastique et de transmission et le valeur de la largeur radiative.

La première étape de l'évaluation est le calcul avec le modèle optique de la section efficace de réaction. Le calcul effectué utilise le potentiel optique de l'évaluation japonaise JENDL 4.0 [27]. Il est réalisé en voies couplées pour un noyau déformé, avec la formulation de Soukhovitskii *et al.* [28]. Cette section efficace représentant la probabilité maximum que la réaction de capture neutronique $^{239}\mathrm{Pu}(n,x)$ se produise, va se décomposer en toutes les autres voies déterminant les rapports d'embranchement. L'étape suivante consiste essentiellement à reproduire en ajustant les paramètres des modèles (densité de niveaux, fonction de force gamma, barrières de fission, états de transition et de classe II) les sections efficaces de capture radiative et de fission. Sur la figure 4 sont comparées les sections efficaces expérimentales utilisées dans JENDL 4.0 et celles issues des calculs réalisés.

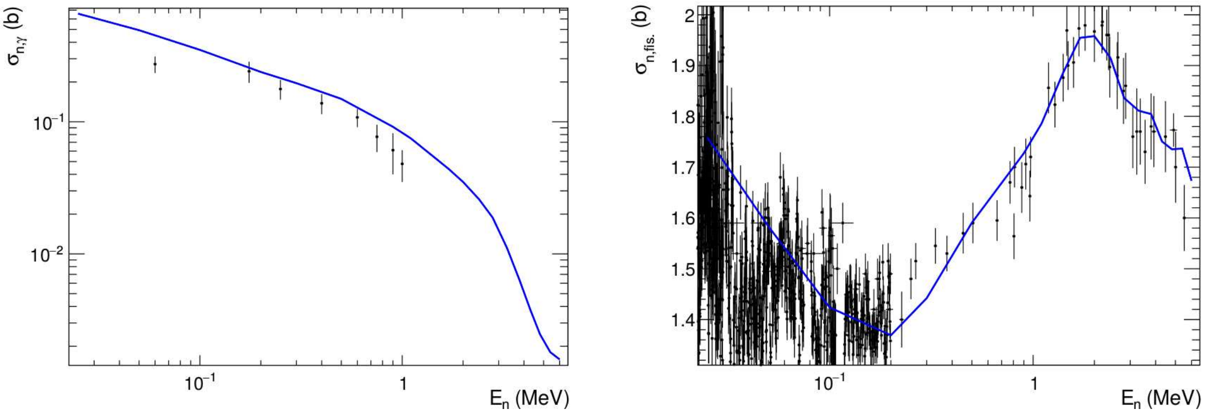

(a) Section efficace de capture $^{239}Pu(n,\gamma)$.

(b) Section efficace de fission $^{239}Pu(n,f)$.

Figure 4: Sections efficaces induites par neutron calculées (lignes bleues), comparées aux données expérimentalles (points) utilisées par l'évaluation JENDL 4.0 [27].

On voit que pour la capture, figure 4a, l'accord avec les données est plutôt bon comme dans le cas de la fission, figure 4b. Le processus est fastidieux car un ajustement plus précis pour la fission en ajustant seulement les paramètres du modèles pour la fission entraine des modifications des autres voies. Par exemple, de légers changements de la hauteur des barrières de fission induisent une grande variation sur la section efficace de capture radiative. Plusieurs règles ont été surveillées, par exemple la largeur moyenne radiative dans le cas de la réaction $^{239}\mathrm{Pu}(n,x)$ est gardée au plus près de la valeur expérimentale $< \Gamma_\gamma >= 43 \pm 5$ meV. Cette valeur dépend à la fois de la densité de niveaux et de la fonction force gamma du noyau se désexcitant. Avec une technique d'essai-erreur, un jeu de paramètres a été fixé permettant de calculer les sections efficaces de la figure 4. Avec ces paramètres, les rapports d'embranchement $G_\chi(E^*, J^\pi)$ du noyau composé $^{240}\mathrm{Pu}$ pour chaque spin et parité à différentes énergies d'excitation ont été déterminés. Dans ce cas, un calcul des probabilités d'émission gamma et de fission est effectué pour les réactions en neutron induit. La comparaison avec les résultats expérimentaux pour les réactions de substitution montre que ni l'émission gamma, ni la fission ne donnent des probabilités identiques aux réactions de capture neutronique, montrés sur la figure 5. Ceci nous indique que les distributions en spin sont très différentes, nous les déterminerons dans la suite.

Une autre conclusion est que l'hypothèse de W.E. n'est pas applicable à la fission comme pour l'émission gamma.

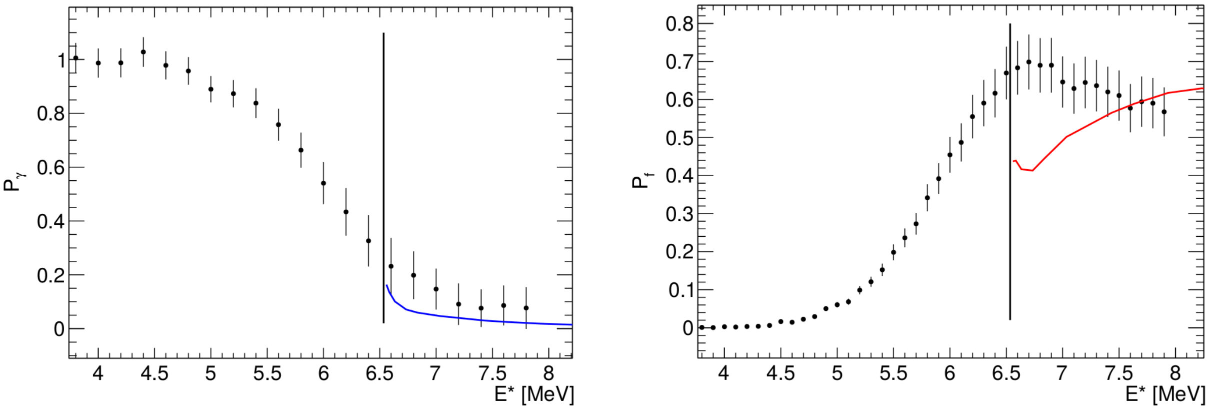

(a) Probabilité de capture $^{239}Pu(n,\gamma)$.

(b) Probabilité de fission $^{239}Pu(n,f)$.

Figure 5: Probabilités de désexcitation induites par neutron calculées (traits pleins), comparées à nos données expérimentalles (points).

La distribution en spin $F(E^*,J^\pi)$ est alors déduite à partir des probabilités mesurées et des rapports d'embranchement calculées en utilisant une procédure d'ajustement adéquate. La distribution de spin est modélisée par une fonction dérivée d'une fonction Gaussienne (4) dont les paramètres sont obtenus par la procédure d'ajustement.

$$F(E^*,J,\Pi) = P(E^*,J,\Pi)\frac{2J+1}{2\sigma^2}exp\left[-\frac{(J+1/2)^2}{2\sigma^2}\right] \tag{4}$$

où $P(E^*,J,\Pi)$ est un facteur pour garantir que la parité soit naturelle (0^+, 1^-, 2^+...). En effet, seulement ces états de parité naturelle sont peuplés lors de la réaction ^{240}Pu$(\alpha,\alpha')^{240}$Pu* en respectant les lois de conservation du moment angulaire et de la parité. La distribution de l'équation (4) provient du modèle d'excitons. Le paramètre σ est supposé suivre une forme linéaire $\sigma = a\cdot(E^*-4.1)+b$. Les paramètres ajustés ont été trouvés égaux aux valeurs : $a = 0.73\ MeV^{-1}$ et $b = 2.88$ en tenant compte des rapports d'embranchement précédemment calculés, et donnent des distributions comme celles de la figure 6.

L'ajustement des probabilités d'émission gamma et de fission du ^{240}Pu expérimentales donne des distributions en spin identiques. Ceci prouve que la distribution en spin et parité pour l'émission gamma et la fission est bien la même et que celle-ci évolue en fonction de l'énergie d'excitation dû au plus grand spin transféré lors que l'énergie transférée augmente.

Une autre façon d'obtenir la distribution de spin et parité $F(E^*,J^\pi)$ est de réaliser un calcul théorique. Pour cela, M. Dupuis du CEA/DAM/DIF a utilisé un modèle de réaction [29] [30], pour obtenir les distributions de pré-équilibre du noyau de recul lors de la réaction ^{240}Pu(α,α'). Le potentiel optique pour la réaction (α,α') est celui de Jeukenne-Lejeune-Mahaux dit JLM. Ceci est combiné avec des informations de structure nucléaire issues d'un calcul QRPA ("Quasi-particle Random Phase Approximation"). Cette approximation donne les états de tête de bande K^π sur lesquels sont construites des bandes de rotation. Une fois tous les états de la QRPA générés, un code de calcul de réaction directe en voies

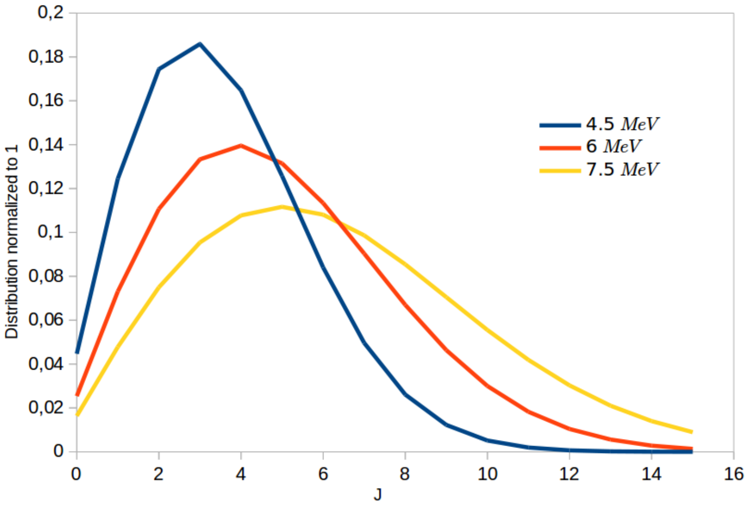

Figure 6: Distributions extraites à partir des donées expérimentales de spin pour trois valeurs de E^*. La parité des distributions est naturelle.

couplées fournit la section efficace de formation de chaque état. La somme de ces sections efficaces pour une énergie et un J^π donnés divisée par la section efficace totale donne la distribution en spin $F(E^*, J^\pi)$ recherchée. Dans la figure 7, les distributions de spin du noyau composé ^{240}Pu pour la réaction de substitution obtenues par ajustement sur les résultats expérimentaux ou par ce calcul sont représentés pour une énergie d'excitation du noyau composé de 7.5 MeV. Elles sont comparées aussi à celle de la réaction $n+^{239}\mathrm{Pu} \rightarrow ^{240}\mathrm{Pu}$ à $E_n = 1\ MeV \sim E^* \approx 7.5$ MeV. La distribution en spin pour la réaction en neutron induit (courbe bleue) est centrée autour d'un spin moyen $\overline{J}_n \approx 1.0\hbar$, tandis que les distributions obtenues pour la réaction $^{240}\mathrm{Pu}(\alpha, \alpha')^{240}\mathrm{Pu}^*$ expérimentales $\overline{J}_{exp} \approx 6.3\hbar$ et calculées le sont à des spins $\overline{J}_{th} \approx 5.7\hbar$. Ce résultat montre que le calcul de la distribution en spin du noyau composé formé dans la réaction (α, α') est valide. Ceci marque une avancée importante pour les réactions de substitution et cette réaction (α, α'), car cela permet de bien comprendre les mécanismes sous-jacents aux mesures des probabilités d'émission gamma et de fission. La preuve en est qu'un calcul complet des probabilités d'émission gamma et de fission est possible en utilisant cette distribution en spin et parité calculée et les rapports d'embranchement calculés précédemment, avec un ajustement sur les données neutroniques.

La comparaison de ces calculs de probabilités avec les résultats expérimentaux est présentée sur la figure 8. L'accord est très bon entre la théorie et l'expérience. Autour de 5.3 MeV et de 6.2 MeV, le calcul théorique est en léger désaccord avec l'expérience, montrant certainement l'implication différente d'états de classe II dans la fission induite par neutron et par réaction de substitution.

Le résultat de la figure 8 est remarquable car il montre que l'introduction d'une distribution en spin calculée, à l'aide d'un modèle JLM+QRPA, permet de reproduire les probabilités expérimentales. Ceci démontre la bonne compréhension du mécansime de réaction mis en jeu, et rend possible l'utilisation des probabilités mesurées dans une évaluation. Un calcul des rapports d'embranchement plus fin aurait permis d'aboutir à des conclusions plus précises sur les différences entre les réactions induites par neutron et par substitution à partir de ces probabilités d'émission gamma et de fission mesurées.

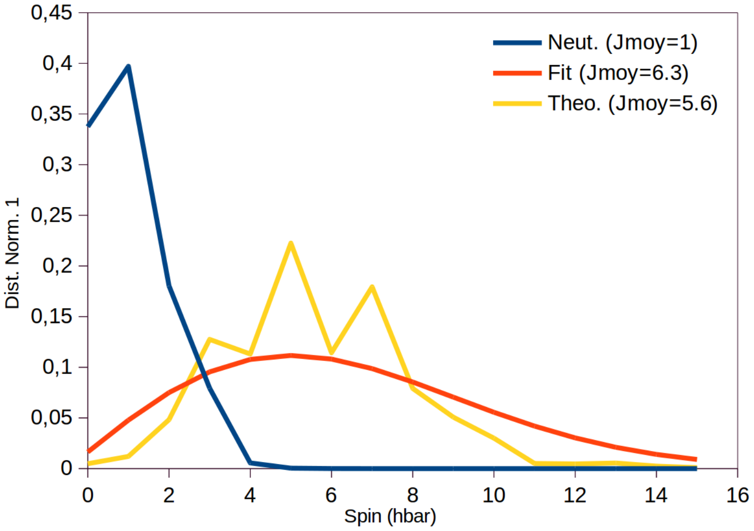

Figure 7: Distribution de spin à $E^* = 7.5$ MeV, induite par neutron (bleu), ajustée aux données de substitution (rouge), et avec un calcul microscopique pour la réaction inelatique (jaune). La parité de la réaction (α, α') est naturelle.

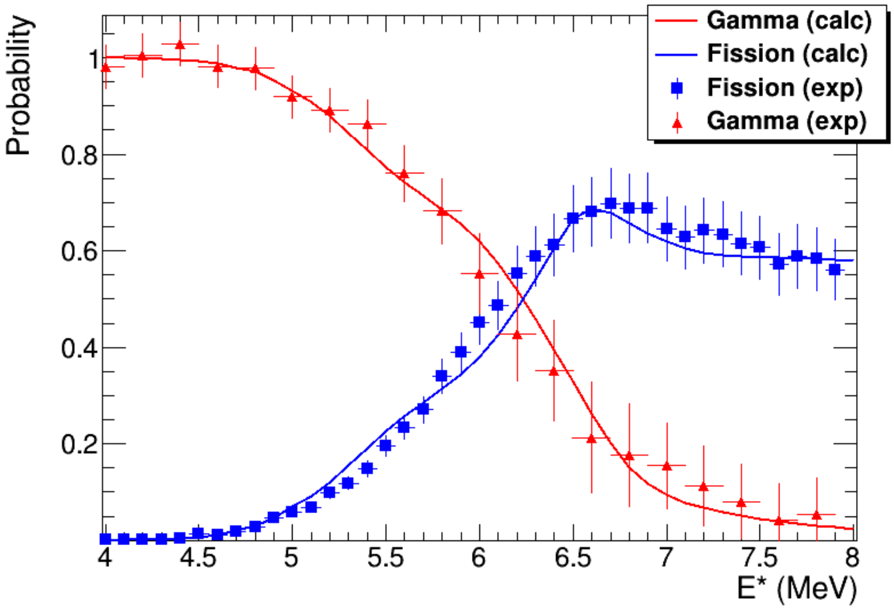

Figure 8: Probabilités de désexcitation expérimentales (symbols) comparées à celles calculées (lignes), probabilité gamma en rouge et fission en bleu.

L'évaluation effectuée a aussi montré combien ce processus est complexe et demande un grand nombre de données expérimentales lorsque la fission est ouverte. Si la fission est bien connue, un ajustement des densités de niveaux et des fonctions de force gamma doit permettre de reproduire la seule probabilité d'émission gamma à la manière des très récents résultats de Ratkiewicz *et al.* [23], et d'améliorer significativement les prédictions pour la section efficace de capture radiative induite par neutron, qui est souvent extrêmement difficile à mesurer. Lorsque la fission n'est pas bien connue, les réactions de substitution permettent d'apporter des informations précieuses sur les hauteurs de barrières, les profondeurs de puits ou les états de classe II. Ces informations sont essentielles pour réaliser une évaluation de la section efficace neutronique de fission.

La sensibilité de chaque ingrédient des modèles de réaction fixés dans l'évaluation en neutron induit pour reproduire ces probabilités d'émission gamma et de fission a été testée. Ces tests montrent comme attendu qu'une évaluation standard (paramètres par défaut de TALYS) avec la distribution de spin et parité calculée ne permet pas de reproduire ces probabilités. Dans le cadre de cette thèse, une étude de sensibilité systématique n'a pas pu être effectuée. Cela reste une perspective de déterminer l'incertitude des paramètres ajustables par la méthode de substitution. En faisant varier aléatoirement ces paramètres dans les limites d'incertitude, un calcul de sections efficaces et l'incertitude associée pourra être réalisé. Ce travail de thèse ouvre donc sur des perspectives très intéressantes d'utilisation des réactions de substitution pour l'évaluation des processus de capture radiative et de fission induits par des neutrons.

En conclusion ce travail a apporté des éléments très précis à la fois expérimentaux et théoriques pour expliquer les probabilités d'émission gamma et de fission du ^{240}Pu obtenues par la réaction de substitution (α, α'). Les distributions en spin du noyau composé formé lors de la réaction (α, α') a été déduite expérimentalement et décrite théoriquement. Ceci ouvre clairement la possibilité d'utiliser cette voie de réaction dans le futur pour étudier la sensibilité de la méthode pour reproduire des sections efficaces en neutron induit et aussi pour d'autres noyaux moins accessibles (décalant la masse du noyau cible de 1).

Dans un futur proche, la collaboration envisage de réaliser une expérience avec le même dispositif expérimental présenté ici pour étudier la réaction ^{242}Pu$(\alpha, \alpha')^{242}$Pu* qui est équivalente à la réaction $n +^{241}$ Pu $\rightarrow^{242}$ Pu*. Cette réaction sera un cas intéressant parce que le ^{240}Pu et le ^{242}Pu ont des structures nucléaires similaires ce qui permettra d'appliquer les enseignements appris lors de cette thèse. Le noyau ^{242}Pu a une durée de vie très longue, ce qui rend plus facile la manipulation de la cible. Etant donné que le ^{241}Pu a une durée de vie assez courte ne facilitant pas les mesures en neutron induit, cette réaction de substitution apportera des informations pertinentes pour la réaction ^{241}Pu(n,x).

Un autre sujet d'étude est d'effectuer en cinématique inverse, où le noyau lourd est le faisceau et le noyau léger la cible, des expériences en utilisant des anneaux de stockage. Ce type de mesure semble être l'avenir de la méthode de substitution pour plusieurs raisons, dont les principales sont l'absence de contaminants, la résolution en énergie d'excitation $\sim$ 200 keV, et l'accès à un bon nombre de noyaux à courte durée de vie. La cible est formée par un jet de gaz d'hydrogène ou de deutérium pur isotopiquement, de $10^{13} - 10^{14}$ $at./cm^2$. La haute fréquence de révolution des ions dans les anneaux de stockage ($\sim$ 1 MHz) amène à des taux de réaction similaires à ceux qu'on obtient en cinématique directe. Le refroidisement par électrons ("e^- cooler") garantit et maintient l'excellente qualité du faisceau après chaque passage à travers de la cible ultrafine. Enfin, comme on détecte et on identifie le noyau lourd après son interaction avec la cible, l'efficacité de détection des différentes voies de désexcitation est quasiment de 100%.

Cette synthèse est un résumé du travail de thèse, le manuscrit en anglais comporte plus de détails et est organisé en deux parties et 7 chapitres. La première partie traite de tous les aspects expérimentaux dans les chapitres 1, 2, 3 et 4. La deuxième partie est consacrée à l'interprétation des résultats et comprend les chapitres 5, 6 et 7. Le chapitre 1 présente le contexte théorique des réactions de subsitution. Sera aussi donnée dans ce chapitre, les motivations pour étudier les réactions ^{240}Pu(α,α')^{240}Pu* et ^{240}Pu(^{3}He,α)^{239}Pu*. Le chapitre 2 détaille l'état de l'art de la discipline, en faisant mention des dernières expériences réalisées en utilisant la méthode "absolue" de substitution, la méthode SRM du "ratio", ou aussi un peu différemment avec la méthode d'Oslo. Le chapitre 3 décrit l'expérience réalisée à Orsay pendant le mois d'avril 2017. Le chapitre 4 fait le point sur l'analyse des données obtenues pendant l'expérience. Toutes les étapes, du traitement à l'extraction des observables recherchées y sont décrites : sélection des événements, étalonnage des détecteurs, soustraction des coïncidences fortuites, etc... La partie II est dédiée à l'interprétation théorique de nos résultats. Le chapitre 5 présente le contexte théorique. L'évaluation de la réaction $n + {}^{239}$Pu y est détaillée. Le chapitre 6 décrit l'interprétation des résultats expérimentaux obtenus par la méthode de substitution. Enfin, le manuscrit se termine dans le chapitre 7 avec les conclusions sur ces travaux et les perspectives qu'ils leur sont données au sein de la collaboration.

Contents

List of Figures

Part I

Experiment

Chapter 1

Introduction

There is a need for neutron induced cross sections of short-lived nuclei in nuclear technology applications and nuclear astrophysics. Unfortunately there are cases in which the neutron-induced cross sections cannot be measured directly because the target nucleus is too radioactive to produce and handle the target. In addition, neutron induced cross sections are very difficult to calculate when no data are available, specially the part concerning the de-excitation of the nucleus.

Surrogate reactions are an alternative way to obtain neutron induced cross sections when measuring them is not possible. A surrogate reaction is a transfer or inelastic scattering reaction leading to the formation of the same excited nucleus as in the case of a neutron induced (desired) reaction. Surrogate reactions can also improve the general understanding of the de-excitation process of heavy nuclei at excitation energy ranges from about 5 to 10 MeV, which is key for the development of the reaction models used in different domains. In this excitation-energy range, an excited heavy nucleus decays via different competing channels, basically γ-emission, particle emission and fission. The decay process is ruled by fundamental properties of nuclei such as level densities, γ-ray strength functions, particle transmission coefficients or fission barriers. In this context surrogate reactions prove to be a valuable source of information, which will be exploited in this work to improve our current knowledge of nuclear reactions.

Fission probabilities induced by transfer and inelastic-scattering reactions have been used since the 70s, Cramer and Britt [41], to explore the fission threshold and infer fission-barrier parameters. In particular, transfer-induced and inelastic-scattering-induced fission probabilities are the only means to obtain information on the fission barriers of fissile nuclei, i.e. nuclei whose fission barrier is lower than the neutron separation S_n. Moreover, the measured fission probabilities can be used to obtain neutron-induced fission cross sections of short-lived nuclei that cannot be measured directly [42], [18], [43].

The study of γ-decay probabilities via the surrogate reaction method has dragged an important interest in recent years. This led to the formation of a collaboration between two French laboratories, CENBG and CEA/DAM/DIF, that has resulted in several publications [1], [2], [3], [4], [5], [6], and Ph.D. thesis [7], [8], [9], [10]. However the results obtained for γ-decay are in general worse agreement with neutron induced data than in the case of fission. Trying to understand this difference is one of the motivations of this work and we will return to this point later on.

Figure 1.1 schematically represents the surrogate reaction method. The left hand side of the figure shows a neutron-induced reaction, i.e. a neutron n is captured by a target

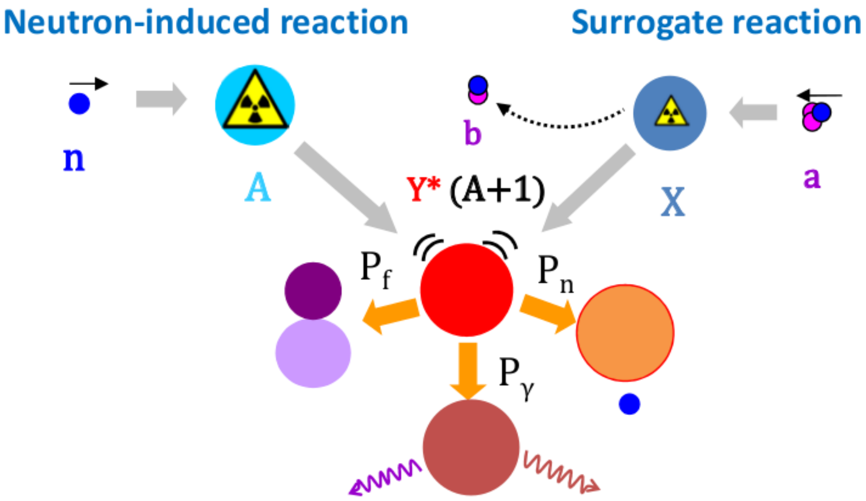

Figure 1.1: Schematic representation of a neutron induced reaction $n + A \rightarrow Y^*$ and a surrogate of this reaction. The surrogate reaction is $X(a,b)Y^*$ where the most probable decay paths of the compound nucleus are fission (P_f), gamma decay (P_γ) and neutron emission (P_n).

nucleus A which leads to the formation of a compound nucleus Y^* of $A+1$ nucleons at an excitation energy E^*. The right hand side of the picture depicts a surrogate reaction in which a charged particle a impinges on a target nucleus X leaving, after the reaction process, the same compound nucleus Y^* and a scattered particle b. The detection and identification of this scattered particle b, or ejectile, enables to select the mass and the charge of the decaying nucleus Y^* in addition to knowing its excitation energy. The formed nucleus Y^* will then tend to release this energy E^*, typically by emitting a neutron (P_n), γ-rays (P_γ) or fissioning (P_f), in the case of actinides. In equation (1.1), $P_\chi^{Y,surr.}$ stands for the probability of the nucleus Y^* to decay through one of these paths χ. Experimentally these probabilities are obtained as a function of excitation energy $P_\chi^{Y,surr.}(E^*)$,

$$P_\chi^{Y,surr.}(E^*) = \frac{N_\chi(E^*)}{N_s(E^*) \cdot \varepsilon_\chi(E^*)} \tag{1.1}$$

where

- $N_s(E^*)$ is the so-called "singles spectrum", in other words the total number of detected particles b as a function of the excitation energy E^* of Y^*.
- $N_\chi(E^*)$ is the "coincidence spectrum" corresponding to the number of detected particles b in coincidence with the observable that identifies the decay mode, in this case a fission fragment or a γ-ray cascade.
- $\varepsilon_\chi(E^*)$ is the detection efficiency to detect the χ decay path.

Measuring the number of coincidences between the ejectiles and the decay products, see figure 1.1, one may determine the experimental decay probability $P_\chi^{Y,surr.}$, induced by the surrogate reaction, for the corresponding decay channel χ. Assuming that the decay probabilities are independent from the spin, the neutron-induced cross section for the nucleus A is given by the equation:

$$\sigma_{\chi}^{A}(E_n) \cong \sigma_{CN}^{A+1}(E_n) \cdot P_{\chi}^{Y,surr.}(E^*) \tag{1.2}$$

where $\sigma_{CN}^{A+1}(E_n)$ is the compound nucleus (CN) formation cross section of the desired, neutron-induced, $n + A$ reaction at a neutron incident energy E_n. In chapter 5 it will be explained how to calculate this cross section. Applying momentum and energy conservation, the input energies are related via formula (1.3):

$$E^* = S_n + E_n \cdot \frac{A}{A+1} \tag{1.3}$$

where S_n is the neutron separation energy. Equation (1.2) is the most simple expression of the surrogate reaction method, in the following we will discuss its validity.

1.1 Validity of the Surrogate Reaction Method

The method relies on Bohr's compound nucleus hypothesis [11] and that $P_{\chi}^{surr.} = P_{\chi}^{n}$, in this section we will discuss in which situations are these conditions true.

1.1.1 Compound Nucleus Hypothesis

Bohr's hypothesis states that nuclear reactions go through an intermediate step in which the formed nucleus loses the "memory" on how it was formed, or in other words that the exit channel is independent from the entrance channel. This is based on the idea that the energy introduced in the system by the projectile is distributed among all the nucleons. This process of *thermalisation* is of the same order of magnitude as the time it takes a light projectile to traverse the target nucleus $10^{-18} - 10^{-22}s$, which is much shorter than the half-life of the compound nucleus $10^{-15}s$. Therefore the information about the formation of the compound nucleus would be lost during this process.

The first experimental verification of Bohr's compound nucleus hypothesis was performed in 1950 by S. N. Ghoshal [44]. To prove this Ghoshal studied two different systems, $^{60}Ni +^4 He \to {}^{64}Zn^*$ and $^{63}Cu + p \to {}^{64}Zn^*$ to form the same compound nucleus $^{64}Zn^*$, or using a general nomenclature $A + a \to C^* \to B + b$. Under the hypothesis that the decay of C^* is independent from its formation the cross section reads:

$$\sigma(a, b) = \sigma_a(E_a)P_b(E^*) \tag{1.4}$$

where $\sigma_a(E_a)$ is the cross section for the absorption of the particle a, with energy E_a, by the target nucleus A to form C^* at an excitation energy E^* and P_b is the probability that the compound nucleus decays into the final state $B + b$. If the C^* is now formed by a different process $A' + a'$ the disintegration cross section into the same final state:

$$\sigma(a', b) = \sigma_{a'}(E_{a'})P_b(E^*) \tag{1.5}$$

where $E_{a'}$ is the kinetic energy of a'. Because of the different binding energies, the kinetic energies must be different $E_a \neq E_{a'}$ to form C^* at the same E^*, while $P_b(E^*)$ is the same in both cases by hypothesis. If C^* decays into a different state $D + d$ the corresponding cross sections to $a + A$ and $a' + A'$ will respectively be:

$$\sigma(a, d) = \sigma_a(E_a)P_d(E^*) \tag{1.6}$$

$$\sigma(a', d) = \sigma_{a'}(E_{a'})P_d(E^*) \tag{1.7}$$

Hence taking the ratio of (1.4) over (1.6), and the ratio of (1.5) over (1.7), one may write:

$$\frac{\sigma(a, b)}{\sigma(a, d)} = \frac{P_b(E^*)}{P_d(E^*)} = \frac{\sigma(a', b)}{\sigma(a', d)} \tag{1.8}$$

The experimental proof of equation (1.8) is a direct test of Bohr's compound nucleus hypothesis. Since Ghoshal's article, which validates the hypothesis for fusion reactions, there have been several works that ratify this hypothesis and others that question it.

1.1.2 Equivalence of the Decay Probabilities

Neutron induced reactions and surrogate reactions produce a compound nucleus with the same (Z,A) at an excitation energy E^*. In contrast, as proven in previous works of the collaboration [8] [10], the angular momentum and the parity distributions (J^π) populated by the surrogate reactions are in general different from those populated by neutron induced reactions. Decay probabilities strongly depend on J^π, and it is at E^* just above the neutron separation energy S_n, that the differences between the spin-parity distribution of the neutron-induced and surrogate reactions are most important. The reason of these differences is that in neutron induced reactions when the neutron energy is low, the orbital momentum transfered is low, and conversely this orbital momentum transfer is higher for surrogate reactions because the impinging particle has a much higher energy than a neutron, as equation (1.3) reflects. It also depends on the spin of the target nucleus which can significantly vary from one isotope to the other, for example the ground state of ^{240}Pu is a 0^+ state, while in the case of ^{241}Pu it is $5/2^+$. If the nucleus A^* is in a compound state, then by definition the entrance channel and the exit channel are not correlated. Thus the n-induced cross section can be factorized into the product of the CN cross sections and the decay probability, which leads to eq. (1.2). The decay probabilities are given by:

$$P^n_\chi(E^*) = \sum_{J^\pi} S(E^*, J^\pi) \cdot G_\chi(E^*, J^\pi) \tag{1.9}$$

$$P^{surr.}_\chi(E^*) = \sum_{J^\pi} F(E^*, J^\pi) \cdot G_\chi(E^*, J^\pi) \tag{1.10}$$

where the super-indexes n and $surr.$ stand for neutron-induced and surrogate reactions, respectively. The functions $S(E^*, J^\pi)$ and $F(E^*, J^\pi)$ represent the probability that the compound nucleus is formed in the state J^π by the neutron-induced or the surrogate reaction, respectively. The function $G_\chi(E^*, J^\pi)$ is the branching ratio for a given decay channel χ. In two limiting situations equations (1.9) and (1.10) are equal:

1) If the J^π distributions in both kinds of reactions are the same:

$$S(E^*, J^\pi) = F(E^*, J^\pi) \tag{1.11}$$

Unfortunately equation (1.11) is seldom verified, [22] [18].

2) If the branching ratios are independent of J^π:

$$G_\chi(E^*, J^\pi) = G_\chi(E^*) \tag{1.12}$$

If (1.12) is met, then the branching ratios can be taken out from the summations in equations (1.9) and (1.10). And since:

$$\sum_{J^\pi} S(E^*, J^\pi) = 1, \; \sum_{J^\pi} F(E^*, J^\pi) = 1 \tag{1.13}$$

then,

$$P_\chi^n(E^*) \approx P_\chi^{surr.}(E^*) = G_\chi(E^*) \tag{1.14}$$

and if (1.14), then the cross section of the desired reaction takes the form of equation (1.2). This second hypothesis, illustrated by equation (1.12), is known as the Weisskopf-Ewing approximation [12] and is justified for high excitation energies ($E^* > S_n + 3$ MeV) where level densities are extremely high.

1.2 Limitations of the Method

There are some assumptions that limit the applicability of the method. Firstly, the assumption that the interaction of the beam particles with the target nucleus always forms a compound nucleus is not true, in spite of Ghoshal's experiment, because a pre-equilibrium or a direct reaction can take place too, which would make equation (1.2) not valid. Some efforts have been done to account for them, the first, six years after Ghoshal's article, was an insightful discussion on the topic by V. Weisskopf [45], in which he already pointed out the limitations of Bohr's hypothesis. However as we will show in chapter 5, the pre-equilibrium and direct components amount for $10\% - 20\%$ of the reaction cross section for excitation energies up to $\sim 10MeV$ and can be neglected for relatively low excitation energy, which is the scope of this work.

Secondly, deducing the J^π distribution of the compound nucleus formed with the surrogate reaction is a challenging task. It is necessary to account for the difference between it and the one of the desired reaction. In chapter 2, some state of the art calculations of this distribution done in previous works will be shown. As a matter of fact, the most recent works on the surrogate reaction field are focusing on correctly calculating the J^π distribution [22], [23].

Finally, one should take into account the existing correlations between the entrance channel and the exit channel, which is something that is neglected in Bohr's hypothesis. These are accounted for by introducing the so-called width fluctuation corrections (WFC) factors, which tend to enhance the elastic channel, hence they have impact on all of the decay probabilities. The WFC factors have an important role when the compound nucleus is formed at an excitation energy lower than S_n+1 MeV, but they tend to one as excitation energy increases [46].

1.3 Application of the Surrogate Reaction Method to ^{240}Pu

In previous works of the collaboration even-odd or odd-odd decaying systems were studied [5], [7], [10]. When applying equation (1.2) to fission, the obtained cross sections with the surrogate method were in good agreement with neutron induced data. This was not the case for γ-decay as shown in [8], [10], [5]. One explanation is that due to the different spin distributions in each reaction, the neutron emission is inhibited and that most of this flux is absorbed by the γ-decay path rather than fission. However, this is not well understood and for this reason in this work we study an even-even decaying nucleus Y^*, i.e. ^{240}Pu, as opposed to even-odd or odd-odd. It is known that even-even nuclei have lower level densities than odd nuclei. Hopefully this will permit to test whether this has an impact on the behavior of these two kinds of decaying systems.

Another motivation for this thesis is to better understand surrogate reactions. To this end studying ^{240}Pu via this method will be helpful for several reasons. First of all, its neutron separation energy is above the fission threshold, therefore the excitation energies under this threshold energy cannot be studied when ^{240}Pu* is formed through the reaction $n +^{239}$ Pu, but when this compound nucleus is formed via a surrogate reaction one has access to parameters relevant for fission. In addition, neutron induced reactions on ^{239}Pu are relatively well known and there are plenty of data with which to adjust the structure parameters of the compound nucleus ^{240}Pu. This will make the comparison between the desired reaction and the surrogate one more meaningful, and optimistically we will be able to account for the differences between them.

In chapter 2 a review of past experiments using the surrogate reaction method and the Oslo method is done. When revisiting previous articles, it becomes evident that there is still an important effort to be done, which justifies this thesis. In it three reactions are explored $^{240}Pu(^3He,^3He')$, $^{240}Pu(^3He,^4He)$ and $^{240}Pu(^4He,^4He')$, although only the results of the last one will be interpreted in detail. The experimental methodology followed will be exposed in chapter 3 and the analysis of the data collected described in chapter 4.

To compare the experimental results obtained with the theoretical prediction, it is necessary to deduce the structure model parameters of ^{240}Pu*. We detail in chapter 5 how they were obtained from the evaluation of the reaction $n+^{239}$Pu using the existing neutron data, specially radiative capture and fission cross sections. In parallel, the J^π distribution of ^{240}Pu* was calculated theoretically, as experimentally there is no available data. This task was performed by M. Dupuis (CEA/DAM/DIF) for the $^{240}Pu(^4He,^4He')$ reaction. He used the quasi-particle random phase approximation (QRPA) to generate the final states of the nucleus, and a direct reaction model to calculate the cross sections to populate them [30]. With these two ingredients, the model parameters and the calculated J^π, the decay probabilities (gamma-emission and fission) as a function of excitation energy were calculated as detailed in chapter 6. In this same chapter we show that the differences between the calculations and the experimental results are within error bars. This is a really important result as it means that surrogate data can help to constrain evaluation parameters. Finally, in chapter 7 we will conclude by commenting the results obtained in this work and discussing the perspectives of the method for the future.

Chapter 2

State of the Art

The surrogate reaction method has been used since the 70's, when it was first applied to infer fission cross sections. Since then several improvements have been done to it, from both experimental and theoretical points of view. The goal is in general to measure the γ-decay probability P_γ, the fission probability P_f, or both as in this work. In the last years the method is regaining interest because it is the most promising alternative to infer neutron induced cross sections of short-lived nuclei. In this chapter we will go through some of the most relevant works in the field of the past years.

2.1 Absolute Surrogate Method (ASM)

This is the same method as the one described in chapter 1, the adjective "absolute" is added to distinguish it from the "ratio" approach described in the following section. As discussed in the first chapter, this method has several limitations, and eq. (1.2) is only valid under certain circumstances. However, the renewed interest in the method has provoked big improvements. In the last two decades a wealth of experimental data and theoretical interpretations of them have been published.

2.1.1 The ASM Applied to Fission

The method was first successfully applied to deduce neutron induced fission cross sections by Cramer and Britt [41] [13] and a bit later by Back *et al.* [47]. In Cramer and Britt's papers they investigated the (t, pf) reactions, beam energy 18 MeV, on different actinide targets, from ^{232}Th to ^{242}Pu. Although the data was contaminated by background reactions in the target support, they were able to provide fission probabilities, and deduce from them fission cross sections multiplying them by the compound nucleus formation cross section. They reported an uncertainty of 10% for fission probabilities and 20% for n-induced compound nucleus formation cross section. Some years later Back and his collaborators used (d, p) and (p, p') surrogate reactions to again study the fission of actinides. Later, Britt and Wilhelmy [48] used $(^3He, d)$ and $(^3He, t)$ reactions to infer (n, f) cross sections of different isotopes from protactinium to einsteinium from $E_n = 0.5$ to 6 MeV, for which they used a constant compound nucleus formation cross section of $3.1b$ in this energy region. When neutron induced data were available there was a good agreement of these and the surrogate data, except for neutron induced energies below 1 MeV. In this region the Weisskopf-Ewing limit is not valid due to the spin-parity mismatch and the so called width-fluctuation correction factors, as it was discussed in chapter 1. These first works set the bases of the surrogate method.

More recently, in 2003, W. Younes and H. Britt [49] [42] investigated whether nuclear structure models can be used to correct the J^π distribution mismatch between neutron induced and transfer reactions. They did a theoretical work based on the data of Cramer and Britt [13], and Back et al. [50], improving the calculation of the compound nucleus formation cross section, which lead to slight variations of the previous data.

In 2004, the CENBG collaboration [15] used the ASM to measure fission cross sections of reactions relevant for the thorium cycle, like ^{231,233}Pa. The experiment was performed in the tandem accelerator at the IPN of Orsay, where a 24 MeV ^3He beam impinged on a target of $100\mu g$ ^{232}Th deposited on a $50\mu g/cm^2$ C^{nat} backing. The ejectiles were detected with two silicon telescopes at 90^o and 130^o with respect to the beam axis. The fission-fragment detector was made out of 15 solar cells placed at different angles to measure fission fragment angular distributions. Their results using a Weisskopf-Ewing approximation are given in figure 2.1. Their results for $^{231}Pa(n,f)$ are in better agreement with previous data and evaluation than the ones for $^{233}Pa(n,f)$, but in any case at high energies there are important differences between the different sets of data.

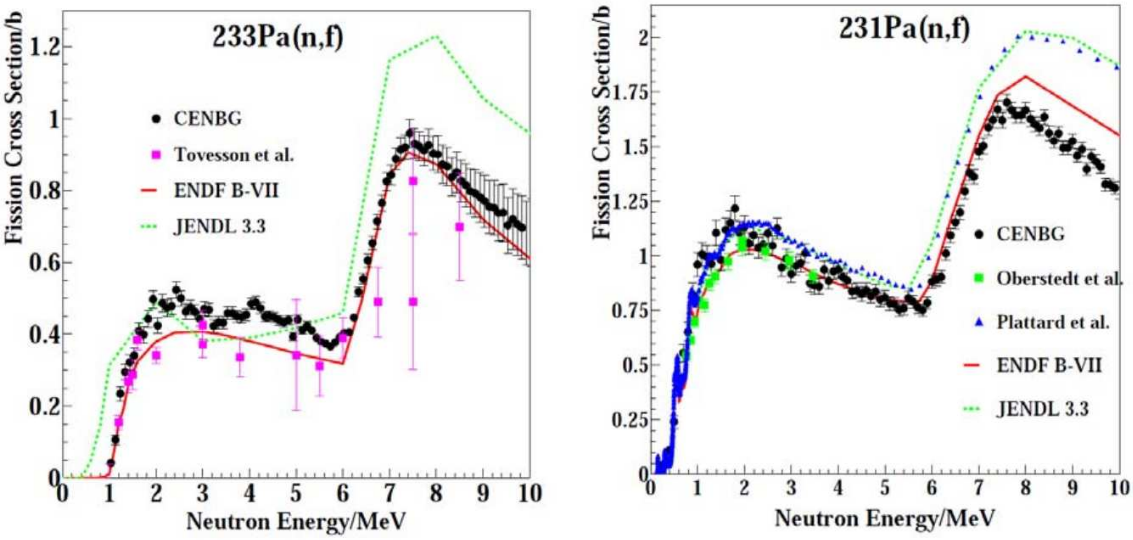

$^{232}Th(^3He,pf)^{234}Pa^*$ $^{232}Th(^3He,tf)^{232}Pa^*$

Figure 2.1: Fission cross section as a function of the neutron energy of two protactinium isotopes. The black dots are the measured data by CENBG (surrogate), as compared to other data (neutron-induced) and evaluations [15].

In 2007, B. Lyles *et al.* [51] used the $^{238}U(^3He,\alpha)^{237}U$ reaction to deduce the $^{236}U(n,f)$ cross section. They used a 42 MeV ^3He beam produced by the cyclotron at Lawrence Berkeley National Laboratory. The scattered particles were detected with an array of silicon telescopes. In their article they could remark big differences between their data and the neutron-induced evaluated data for energies below 1.5 MeV. They found that their data was sensitive to the ejectile angle, which implies a dependence on the transfered spin, and they interpreted this as a failure of the Weisskopf-Ewing limit in this energy range.

More or less simultaneously, the CENBG collaboration continued investigating the fission of actinides, americiums and curiums, via the surrogate-reaction method. This work lead to a Ph.D. thesis by G. Kessedjian [7] and an article [16]. A ^{3}He beam impinged on a target of ^{243}Am enabling to study the compound nuclei $^{242}Am^{*}$, $^{243}Cm^{*}$ and $^{244}Cm^{*}$ In this work they compared the surrogate data to neutron-induced data, and found that both are in very good agreement as figure 2.2 proves.

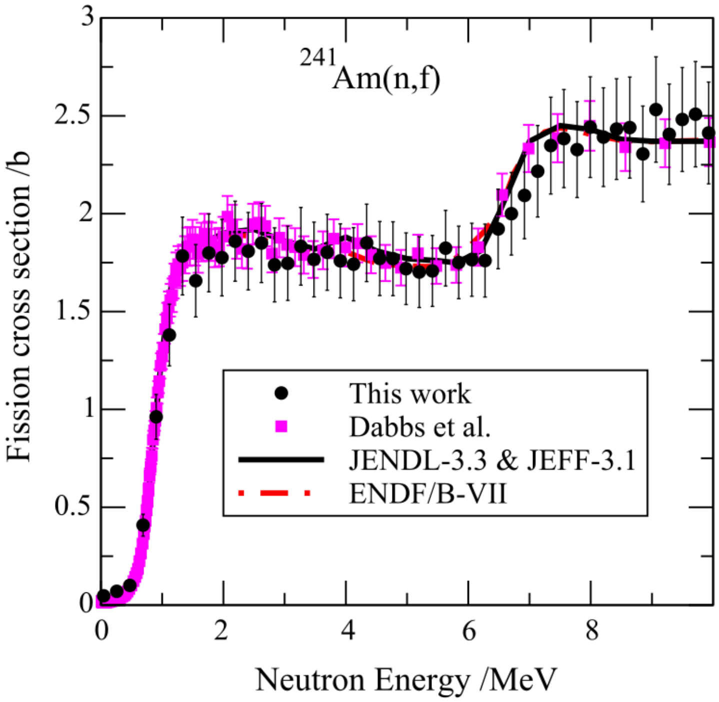

Figure 2.2: Cross section of the reaction $^{241}Am(n,f)$ as a function of the neutron energy. The black dots are the measured data by CENBG ("This work"), as compared to neutron induced data (pink points) and two evaluations for the neutron induced fission cross section (lines) [16].

The results published in [16], in combination with the ones obtained for γ-decay discussed later, encouraged the CENBG collaboration to continue investigating fission with the surrogate reaction method, which lead in 2015 to the Ph.D. thesis of Q. Ducasse [10] and in 2016 to an article [3]. In this work they aimed to measure simultaneously the fission probability and the γ-decay probability of several uranium and neptunium isotopes. To that end, they performed an experiment with the SiRi-CACTUS set-up at the Cyclotron of the University of Oslo. The measurement was done with a ^{238}U target and two beams: ^{2}H at 15 MeV and ^{3}He at 24MeV. The experimental set-up included an array of telescopes with a ring shape, which covered azimuthal angles θ between 126^{o} and 140^{o}. In coincidence with the scattered particles the fission fragments were detected with Parallel Plate Avalanche Counters (PPACs), and the γ-rays with 27 NaI, thallium-doped scintillators.

Figure 2.3 represents the fission probability of $^{237}U^{*}$ as a function of excitation energy, compared to the one deduced from the evaluation of the $^{236}U(n,f)$ reaction published in JENDL 4.0. The surrogate data is in good agreement with the evaluation up to high excitation energies. This is another proof that, in general, applying the ASM to fission gives good results when compared to neutron induced data.

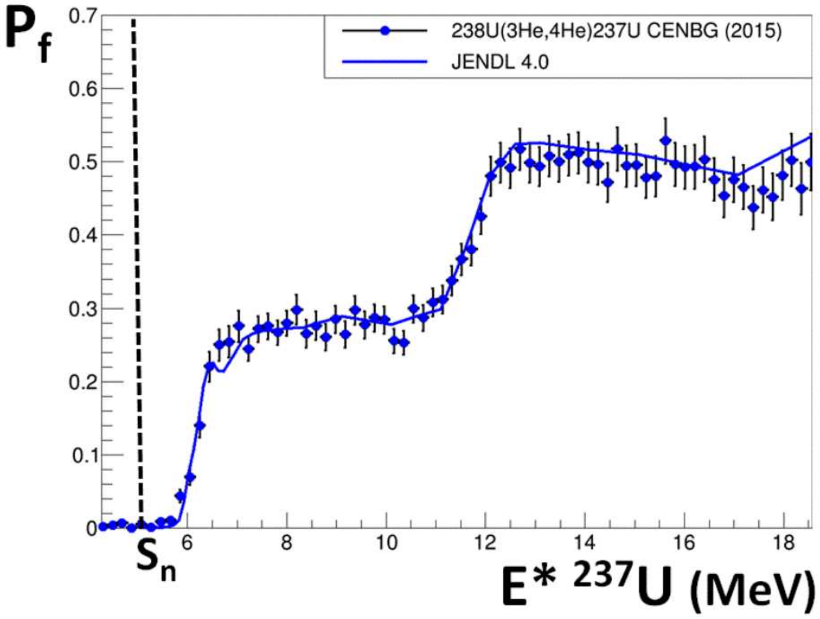

Figure 2.3: Fission probability of ${}^{237}U^*$ as a function of excitation energy, obtained with the surrogate reaction ${}^{238}U({}^3He, {}^4He){}^{237}U$ compared to JENDL 4.0 [10]. The dashed black line represents the neutron separation energy.

2.1.2 The ASM Applied to γ-Decay

Using the surrogate reaction method to determine radiative capture cross sections is more difficult than in the case of fission. Firstly, in all previous experiments the γ-decay probability has always been more sensitive to changes in spin-parity distributions than fission. Secondly, in the energy region in which the method can be applied, the radiative capture probability represents a small percentage of the decay, hence small variations due to the J^π mismatch can induce big differences in this probability. Additionally, the radiative capture probability is much more complicated to measure than the fission one. As explained in chapters 3 and 4, it involves knowing the γ-cascade detection efficiency correctly, distinguishing γ-rays from neutrons, for higher excitation energies than the neutron separation energy, and several background subtractions including fission-fragment-γ-rays coincidences, when studying nuclei that undergo fission. Although the γ-decay probabilities can also be studied by selecting specific gamma transitions, which requires an array of Ge detectors, in general the detection efficiency is much lower than when detecting any gamma of the cascade.

The first measurement of a radiative capture with a surrogate reaction was performed by the CENBG collaboration and published in 2006 [19]. They measured the gamma decay probability of ${}^{234}Pa$ formed through the reaction ${}^{232}Th({}^3He, p){}^{234}Pa$ and a beam energy of 24 MeV. The experimental set-up consisted of four silicon telescopes set at backward angles, and four C_6D_6 liquid scintillators to detect the γ-rays in coincidence with the scattered particles. There are no cross section data of the ${}^{233}Pa(n, \gamma)$ reaction to compare with, however the surrogate data transformed to neutron energy are included in the EXFOR data bank as derived data.

In the same year, 2006, Bernstein *et al.* [20] used the surrogate reaction $^{238}U(\alpha,\alpha')$, with 55 MeV α-particles from the 88-Inch Cyclotron at the Lawrence Livermore National Laboratory, to deduce the $^{237}U(n,\gamma)$ cross section. They placed the scattered particle detectors at forward angles and a γ-detector array consisting of five high-purity germanium detectors. In this case the analysis was done by selecting γ-ray transitions corresponding to low-lying levels. The cross sections deduced in this article are systematically higher than evaluations.

Scielzo *et al.* [21] used in 2010 the surrogate $^{154,156,158}Gd(p,p')$ reactions to infer $^{153,155,157}Gd(n,\gamma)$ cross sections. The gadolinium targets were bombarded with 22 MeV protons produced in the same cyclotron and with the same set-up as in Bernstein's *et al.* [20]. In this article the authors compare their experimental results to neutron-induced ones. The measured cross sections were overestimated by a factor of three with respect to the neutron-induced ones. They also performed Hauser-Feshbach calculations with different Gaussian spin distributions. The calculations done with a higher mean spin, $J_{avg} = 5 - 8\hbar$, are in better agreement with the surrogate data, whilst the one done for $J_{avg} = 2\hbar$ is in better agreement with neutron induced data. For a same excitation energy, in a surrogate reaction the angular momentum transfered is higher than in the case of neutron induced reactions, which explains their calculations.

In 2011 a detailed study of the surrogate reactions of figure 2.4 was done by the CENBG collaboration, in the frame of Boutoux's Ph.D. thesis [8] and an article [4]. From the five reactions listed in figure 2.4, the inelastic scattering $^{174}Yb(^3He,^3He')$ could not be used because the scattered ^3He particle had not enough energy to be detected with the telescopes. The results of the other four studied reactions show the same discrepancy between neutron induced probabilities and surrogate probabilities. In figure 2.5 the experimental γ-decay probability of the compound nucleus $^{173}Yb^*$ is plotted as a function of excitation energy measured via the surrogate reaction $^{174}Yb(^3He,^4He\gamma)$ and is compared to the probability obtained with the neutron-induced $^{172}Yb(n,\gamma)$ and γ-induced $^{173}Yb(\gamma,\gamma)$ reactions. In this study theoretically calculated branching ratios were used to fit the gamma decay probabilities with a Gaussian spin distribution by varying its parameters. The authors found that the distribution that best fitted the results was centered at a higher average spin than the neutron induced ones, which is in agreement with the previous results.

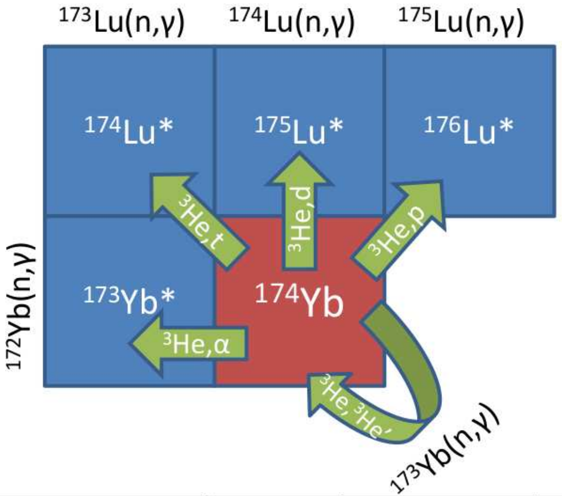

Surrogate reaction	CN	$\sigma(n,\gamma)$	$T_{1/2}$
$^{174}Yb(^3He,p\gamma)$	$^{176}Lu^*$	$^{175}Lu(n,\gamma)$	stable
$^{174}Yb(^3He,d\gamma)$	$^{175}Lu^*$	$^{174}Lu(n,\gamma)$	3,31y
$^{174}Yb(^3He,t\gamma)$	$^{174}Lu^*$	$^{173}Lu(n,\gamma)$	1,37y
$^{174}Yb(^3He,{}^3He'\gamma)$	$^{174}Yb^*$	$^{173}Yb(n,\gamma)$	stable
$^{174}Yb(^3He,\alpha\gamma)$	$^{173}Yb^*$	$^{172}Yb(n,\gamma)$	stable

Figure 2.4: Surrogate reaction channels and their corresponding neutron induced reactions as described in [8]. $T_{1/2}$ is the half-life of each isotope.

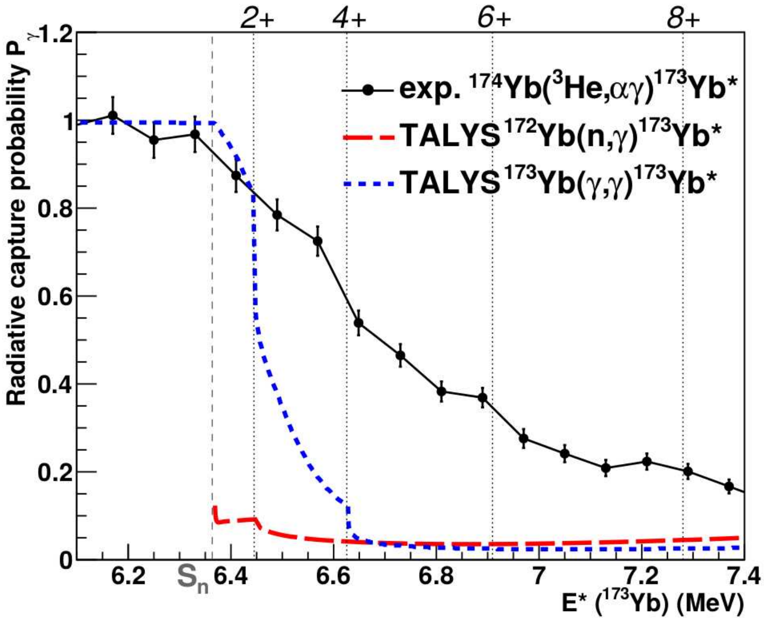

Figure 2.5: Experimental γ-decay probability of the compound nucleus $^{173}Yb^*$ as a function of excitation energy measured via the surrogate reaction $^{174}Yb(^3He,^4He\gamma)$ compared with the probability obtained with the neutron-induced $^{172}Yb(n,\gamma)$ and γ-induced $^{173}Yb(\gamma,\gamma)$ reactions [8].

The next year, 2012, Wilson *et al.* [31] studied (d,p), $(^3He,t)$ and $(^3He,\alpha)$ surrogate reactions on ^{232}Th to deduce neutron capture cross sections. The measurement was performed at the Oslo Cyclotron Laboratory using the CACTUS γ-detector array, formed by 28 NaI detectors, and Silicon Ring, which was a particle telescope. Here we will just comment the results of the (d,p) reaction, which are plotted in figure 2.6 and compared to previous neutron induced data and ENDF/B-VII.0.

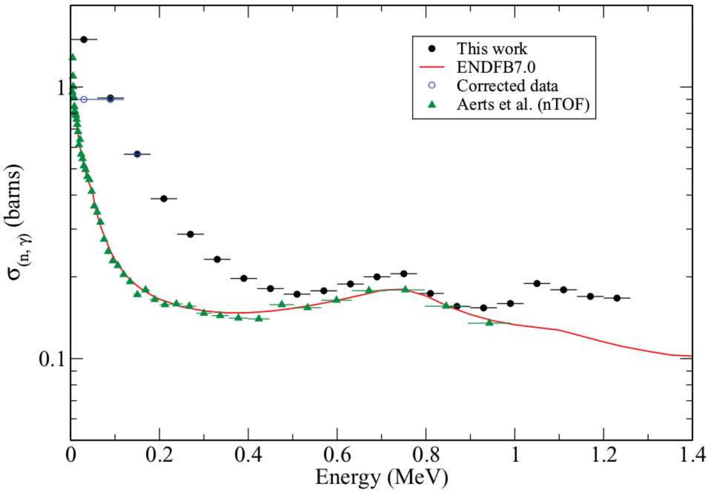

Figure 2.6: Radiative capture cross section of ^{232}Th measured by Wilson *et al.* [31] with the (d,p) transfer reaction "This work". It is compared to neutron induced data and to the evaluation ENDF/B-VII.0.

This was the first time that the (n,γ) cross section of an actinide was measured using the surrogate method and could be compared to high quality neutron induced data. As seen in figure 2.6, the surrogate data is systematically higher than the neutron induced one up to an equivalent neutron energy of 0.4 MeV, but for higher energies both sets of data are in better agreement, with a difference of $\sim 15\%$. The authors conclude that the Weisskopf-Ewing limit is reached at this point, and thus that in this situation it is possible to extract neutron induced cross sections from the surrogate data.

However, during the analysis of the experimental data they had several difficulties to overcome that may have partially flawed the conclusions. Firstly, the neutrons emitted during the $^{232}Th(d,pn)$ reaction may interact with the NaI detectors, which would produce a signal that can be mistaken with a γ-ray. The authors of the article applied a 22 ns time window to retain just γ-rays, but in fact this time window is just effective to eliminate neutrons with energies under 700 keV from the analysis. Thus neutrons probably had a small impact on the capture cross section at $E_n > 700$ keV. In addition, the deuteron beam can undergo break-up, which has the effect of increasing the number of unreacted scattered protons, thus reducing the probabilities obtained with the surrogate method. The deuteron break-up was neglected in the article, but as proven in later works it should not be [3]. Finally the experiment took place in a cyclotron facility, in which the beam energy is usually not correctly determined, affecting the energy calibration. The effect of this is particularly evident in figure 8 of [31], where the gamma decay probability starts falling 200 keV under S_n. In theory the only open decay path of the ^{233}Th nucleus is γ-emission and therefore P_γ should be 1 up to the neutron separation energy.

In the article of 2016 of Ducasse *et al.* [3] they investigated the $^{238}U(d,p)$ reaction by simultaneously measuring the fission and the γ-decay probabilities of $^{239}U^*$. With the same set-up as the one described above, they extracted these probabilities, see figure 2.7. The dependence on the angle is probably related to the differences in angular momentum transfer l. They corrected the probabilities from deuteron break-up which changed the final results, figure 2.8.

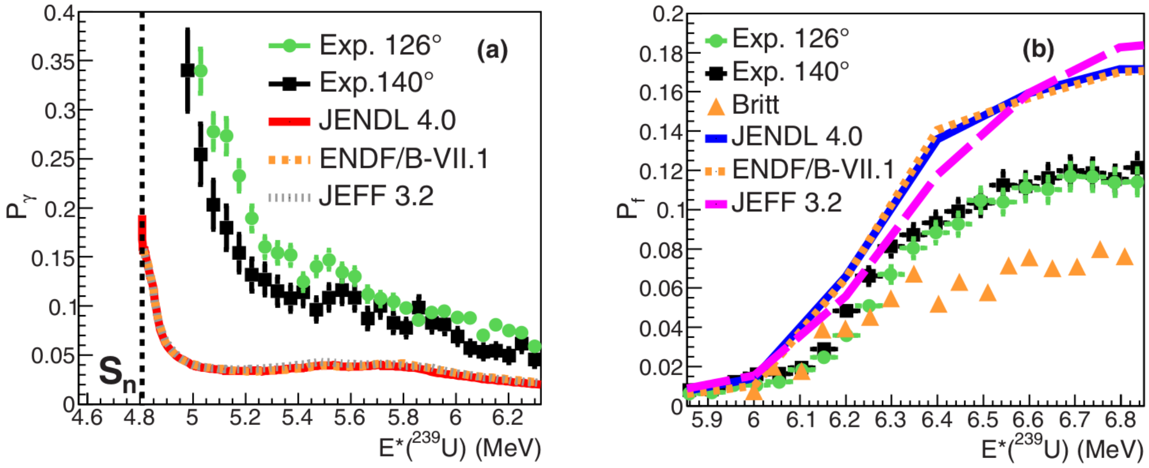

Figure 2.7: [3] Measured γ-decay (a) and fission (b) probabilities of the compound nucleus $^{239}U^*$ as a function of excitation energy measured via the surrogate reaction $^{238}U(d,p)$, at polar angles 126^o and 140^o. The decay probabilities are compared to the evaluations for the neutron induced cross sections, for fission (b) they are also compared to the surrogate data of Britt and Cramer [41].

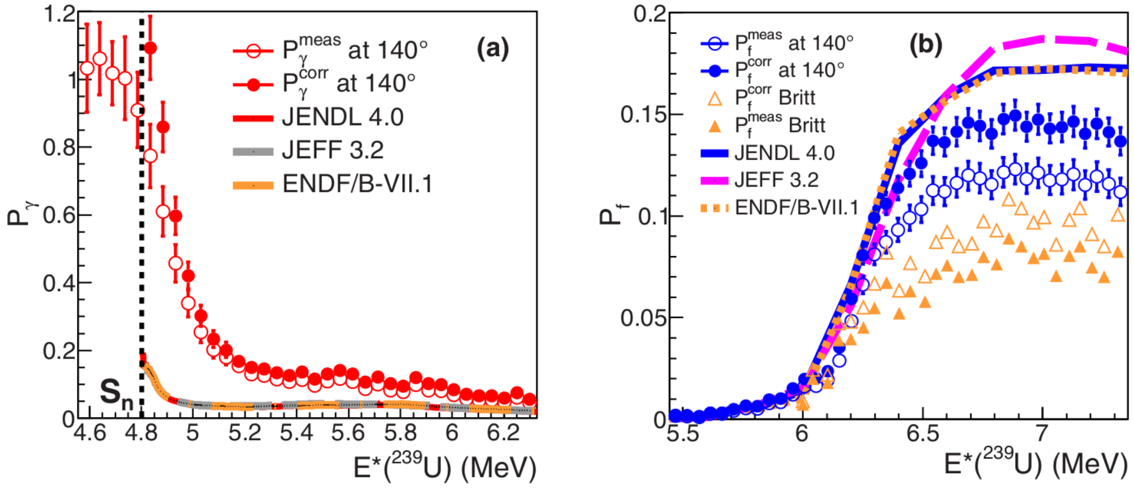

Figure 2.8: [3] Measured and corrected from deuteron break-up probabilities for γ-decay (a) and fission (b) of the compound nucleus $^{239}U^*$ as a function of excitation energy measured via the surrogate reaction $^{238}U(d,p)$, at $\theta = 140^o$. The decay probabilities are compared to the evaluations, for fission (b) they are also compared to the data of Britt and Cramer [41] and these data corrected from deuteron break-up.

After correcting for the deuteron break-up, the measured decay probabilities increase, figure 2.8. The transfered l is much higher in surrogate reactions at low equivalent neutron energy E_n than in the case of neutron-induced reactions, which explains why the γ-decay probability does not agree with neutron induced data. In the case of fission this disagreement was attributed to the presence of oxygen in the target.

In figure 2.9 both γ-decay probability and fission probability are shown with a zoom in the 5 to 6.3 MeV energy region. In this low energy region fission is in good agreement with neutron data, but $P_\gamma^{surr.} > P_\gamma^n$, which proves that P_γ is more sensitive to the J^π mismatch. No spin distribution could be found to match both decay probabilities, most likely because an equipartition of negative and positive parities was assumed, which in general is not true as it will be shown later.

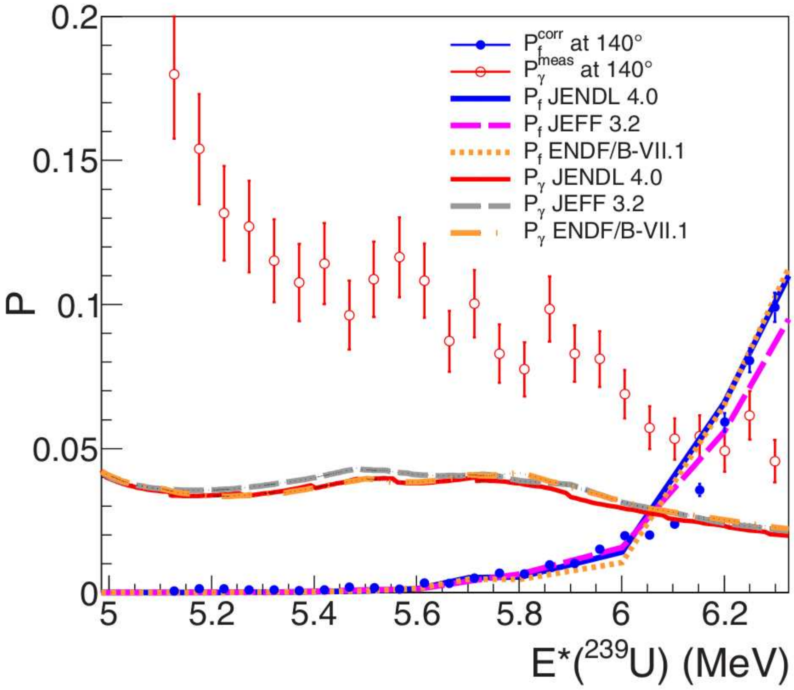

Figure 2.9: [3] Measured and corrected from deuteron break-up probabilities for γ-decay and fission of the compound nucleus $^{239}U^*$ as a function of excitation energy measured via the surrogate reaction $^{238}U(d,p)$, at $\theta = 140^o$. The decay probabilities are compared to different evaluations.

More recently, two articles in which the spin-parity distributions of the surrogate reactions were theoretically calculated were published. In the first article, of 2018, by Escher *et al.* [22], they used the $^{89}Y(p,d)^{88}Y$ reaction as a surrogate of $n + {}^{87}Y$. To validate the calculations they performed a benchmark experiment to obtain the known $^{90}Zr(n,\gamma)$ cross section with the surrogate $^{92}Zr(p,d)^{91}Zr$. The data were produced at the K250 Cyclotron at Texas A&M University, and natural ^{89}Y and enriched $^{90,91,92,94,96}Zr$ targets were bombarded with 28.5 MeV protons. The scattered particles were tagged with silicon telescopes, and the γ-rays were detected in coincidence with five HPGe. The spin distributions $F(E^*, J^\pi)$ of figure 2.10 were calculated using the two-step Distorted-Wave Born Approximation (DWBA) process of the code FRESCO [52].

The spin distributions of figure 2.10 change smoothly with energy. The branching

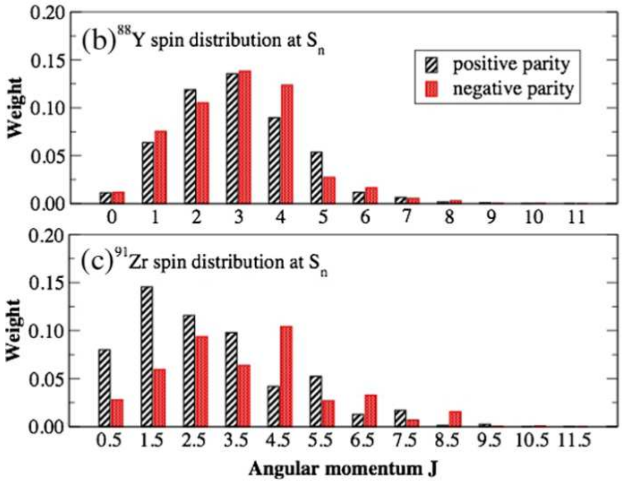

Figure 2.10: Calculated spin distributions at neutron separation energy, populated in the $^{89}Y(p,d)$ and $^{92}Zr(p,d)$ reactions [22].

ratios $G_\gamma(E^*, J^\pi)$ were obtained with standard level density functionals and strength functions, with parameters that were adjusted to reproduce the measured probabilities for specific γ-ray transitions, in an E^* region between 6 and 10 MeV. In figure 2.11 the results obtained with the surrogate data are compared to other evaluations, and although the results are not in disagreement with them, it is worth mentioning that there are no experimental data for the $^{87}Y(n,\gamma)$ reaction.

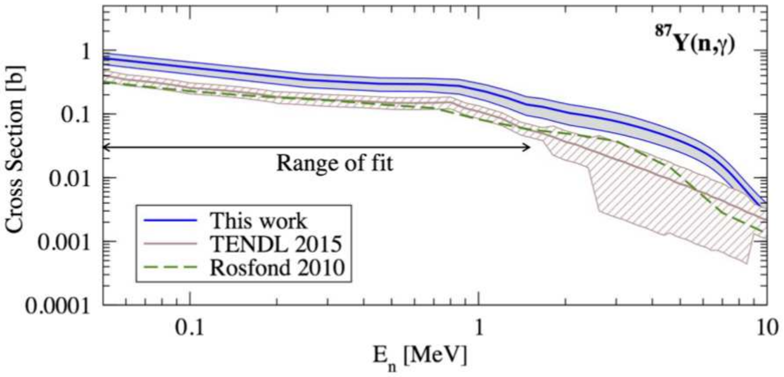

Figure 2.11: Deduced cross section $^{87}Y(n,\gamma)$ from the surrogate reaction $^{89}Y(p,d)^{88}Y$ ("This work" corresponds to [22]). The results are compared with cross sections given in TENDL 2015 and Rosfond 2010.

The year after, in 2019, Ratkiewicz *et al.* [23] used (d,p) reactions with a formalism beyond the Weisskopf-Ewing approximation, given by eq. (1.2), to produce $^{95}Mo(n,\gamma)$ cross sections, figure 2.13. Their calculations account for the break-up of the deuteron beam. They calculated the spin distributions represented in figure 2.12, which illustrates a big difference in the proportion of negative and positive parities. This is something that dismisses the usual hypothesis of supposing 50% of each parity of the distributions, [53], which in this case would flaw the results.

Figure 2.13 includes the results obtained by combining the calculated spin-parity distributions of figure 2.12 and a Hauser-Feshbach calculation with structure parameters of

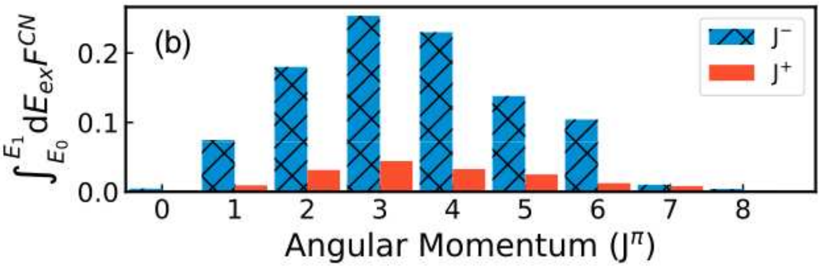

Figure 2.12: Calculated spin distribution of the $^{95}Mo(d,p)$ reaction in a an excitation energy region between 8.55 MeV and 10.65 MeV [23]. Negative parities are represented in blue and positive ones in red.

RIPL [53]. These results are in very good agreement with the neutron-induced data (red and black points), and the ENDF/B-VIII.0 evaluation. Figure 2.13 also includes cross section that would have been deduced from the surrogate data if the Weisskopf-Ewing approximation,eq. (1.2), had been assumed (gold diamonds). The difference between the results obtained with this approximation and the full calculation can be explained as part of a J^π mismatch.

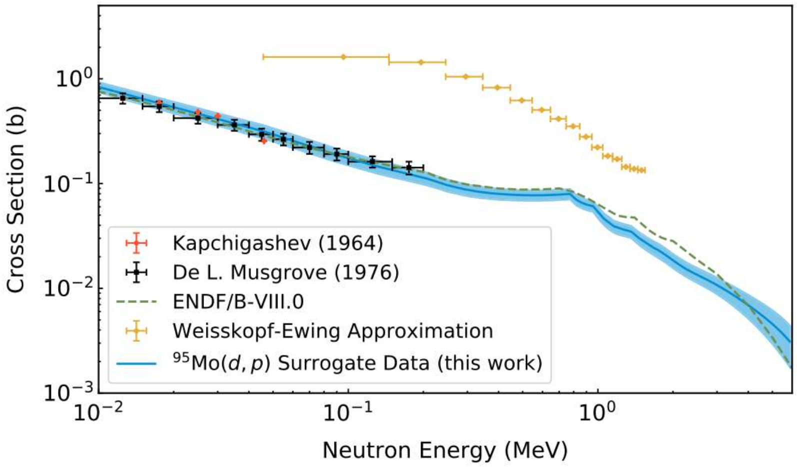

Figure 2.13: Deduced cross section $^{95}Mo(n,\gamma)$ from the surrogate reaction $^{95}Mo(d,p)^{96}Mo^*$ ("$^{95}Mo(d,p)$ Surrogate Data (this work)" corresponds to [23]). The solid line represents the cross section obtained using the spin distribution of figure 2.12 and the gold diamonds using the WE approximation [23]. The results are compared to previous neutron induced data and the ENDF evaluation.

It is a general result that the γ-decay probability deduced from the surrogate data is higher than with neutron-induced data due to the differences in J^π. This is due to the competition with neutron emission which is suppressed when the difference between the spin of the parent compound nucleus and the daughter nucleus is big. As it will be explained in the part II of this work, we aim to reproduce our experimental data in a similar way to [23] which was first proposed in [54]. This implies correctly calculating the spin distribution with a direct reaction model [29] [30]. We believe that this is the way to proceed and obtain meaningful results from the surrogate reaction experiments.

2.2 Surrogate Ratio Method (SRM)

In this section we will focus on the most relevant and recent results obtained with the SRM, which was introduced in 2005 by Plettner *et al.* [55]. In this approach, $R(E)$ is the ratio of the cross sections of two different reactions [54]:

$$R(E) = \frac{\sigma_{\alpha_1\chi_1}(E)}{\sigma_{\alpha_2\chi_2}(E)} \tag{2.1}$$

where α corresponds to the entrance channel $a + A$ and χ to the exit channel, thus $\sigma_{\alpha_1\chi_1}(E)$ corresponds to $a_1 + A_1 \to c_1 + C_1$ and $\sigma_{\alpha_2\chi_2}(E)$ to $a_2 + A_2 \to c_2 + C_2$. These ratio is determined in two surrogate experiments, thus an independent determination of one of the cross sections can be used to obtain the other. The meaning of E depends on each case, as typically a compound nucleus formation cross section is characterized by the kinetic energy of the projectile E_a, while the branching ratios are normally expressed as a function of the excitation energy of the nucleus E^*. These two energies are related by eq. (1.3). In the Weisskopf-Ewing limit the ratio $R(E)$ can be expressed as,

$$R(E) = \frac{\sigma^{CN}_{\alpha_1}(E)G_{\chi_1}(E)}{\sigma^{CN}_{\alpha_2}(E)G_{\chi_2}(E)} \tag{2.2}$$

where σ^{CN} is the compound nucleus formation cross section, which is calculated in the optical model formalism, and G_χ is the branching ratio for decay channel χ. The ratio $G_{\chi_1}(E)/G_{\chi_2}(E)$ is determined with two experiments to form the corresponding compound nuclei. It is equivalent to the ratio of the probabilities determined with the absolute surrogate reaction method:

$$\frac{G^{CN}_{\chi_1}(E)}{G^{CN}_{\chi_2}(E)} = \frac{P^{CN}_{\delta_1\chi_1}(E)}{P^{CN}_{\delta_2\chi_2}(E)} = \frac{N^{CN}_{\delta_1\chi_1}(E)/[N^{CN}_{\delta_1}(E)\varepsilon_{\chi_1}(E)]}{N^{CN}_{\delta_2\chi_2}(E)/[N^{CN}_{\delta_2}(E)\varepsilon_{\chi_1}(E)]} = \frac{N^{CN}_{\delta_1\chi_1}(E)}{N^{CN}_{\delta_2\chi_2}(E)}\frac{N^{CN}_{\delta_2}(E)}{N^{CN}_{\delta_1}(E)}\frac{\varepsilon_{\chi_2}(E)}{\varepsilon_{\chi_1}(E)} \tag{2.3}$$

where δ corresponds to the entrance channel $d + D$ and ε_χ is the efficiency of detecting exit channel χ. The ratio of the detection efficiencies $\varepsilon_{\chi_1}/\varepsilon_{\chi_2}$ can be determined independently and in the case of fission it is approximately unity. During the measurement, the conditions can be adjusted in such a way that the relative number of events $N^{CN}_{\delta_1}/N^{CN}_{\delta_2}$ can be determined with the relative beam intensities, target thickness and live times of both experiments. Setting these ratios to 1 to simplify the notation, the ratio of the decay probabilities simplifies to eq. (2.4).

$$R^{exp}(E) = \frac{\sigma^{CN}_{\alpha_1}(E)N^{CN}_{\delta_1\chi_1}(E)}{\sigma^{CN}_{\alpha_2}(E)N^{CN}_{\delta_2\chi_2}(E)} \tag{2.4}$$

The main advantage of the ratio method over the absolute one is that it eliminates the necessity to accurately measure the total number of surrogate reaction events N^{CN}_δ which correspond to the number of detected ejectiles. This way one can avoid the problem of target impurities that induce a background, but it can make it worse if the contaminants are excited when measuring gamma-decay probabilities because this cannot be disentangled from the true events. In addition, it requires performing two measurements, and a very good knowledge of the reference cross section.

2.2.1 SRM Applied to Fission

In 2014, Hughes *et al.* [18] applied the SRM to infer the neutron induced fission cross sections $^{236,237,238}Pu(n,f)$ using (p,t), (p,d) and (p,p') reactions on targets of ^{239}Pu and ^{235}U. The proton beam had an energy of 28.5 MeV and was produced at the K-150 cyclotron at Texas A&M University. Figure 2.14 illustrates the experimental set-up used, named STARLiTeR. With this array they performed a measurement with the U target and another one with Pu and determined the ratio of the fission coincidences for each reaction channel. Then they converted the ratios to $^{236,237,238}Pu(n,f)$ cross section using the $^{235}U(n,f)$ cross sections as reference and compared to ENDF, figure 2.15.

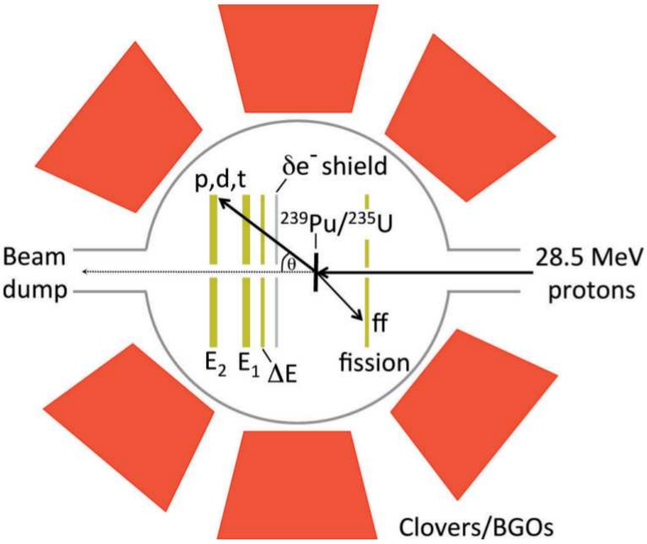

Figure 2.14: Sketch of the STARLiTeR array at Texas A&M. It consists of a position sensitive silicon telescope at forward angles, between 36^o and 67^o, for ejectiles, a fission fragment detector at backward angles, between 108^o and 135^o and six Compton-suppressed γ-ray detectors surrounding the chamber [18].

In figure 2.15 they compare their data to one published in 2011 by Ressler *et al.* [17]. Both sets of data are in agreement up to 5 MeV in equivalent neutron energy. The procedure followed by Ressler *et al.* was slightly different to that of Hughes *et al.* And the experiment was carried out in the 88-Inch Cyclotron at Berkeley and the surrogate reactions were performed with 55-MeV α particles.

Between 2013 and 2015 a collaboration based in India produced three different articles [56], [32] and [33] using the SRM to obtain fission cross sections of short lived actinides. In the first article they utilized surrogate reactions on a ^{238}U target with ^6Li and ^7Li beam to determine the $^{239}Np(n,f)$ and $^{240}Np(n,f)$ cross sections. The problem is that they considered the directly measured $^{241}Pu(n,f)$ as reference, which has not been accurately measured, thus the results are not very reliable. However, in the last two articles they used the $^{235}U(n,f)$ cross section as reference, which is a very well measured cross section. In [32] they determined $^{234}Pa(n,f)$ with the ratio of the reactions $^{232}Th(^7Li,\alpha f)^{235}Pa$ and $^{232}Th(^7Li,tf)^{236}U$, multiplied by the $^{235}U(n,f)$ cross section, figure 2.16.

In the article of 2015, Pal *et al.* [33] determined the $^{238}Pu(n,f)$ and $^{236}Np(n,f)$ cross sections applying the surrogate ratio method to $^{235}U(^6Li,df)$ and $^{232}Th(^6Li,df)$. As one

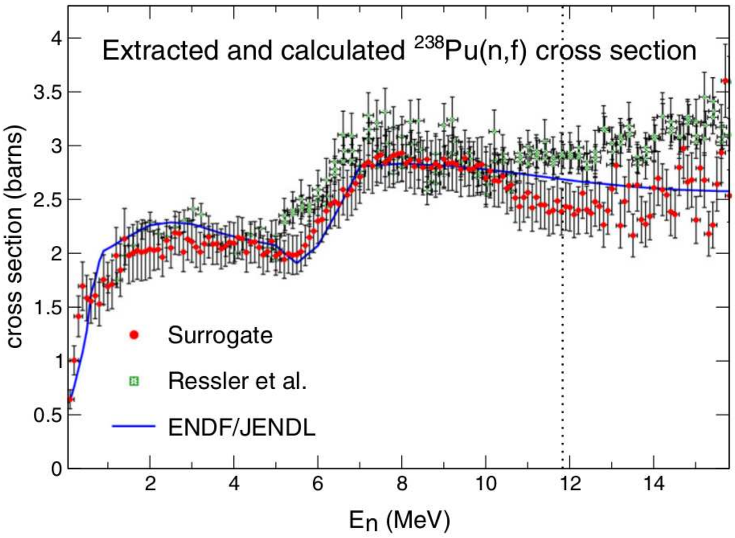

Figure 2.15: $^{238}Pu(n, f)$ cross section deduced from the surrogate ratio and the $\sigma(^{234}U(n, f))$ ENDF/B-VII evaluation (red circles), from the SRM applied by Ressler *et al.* [17] (green squares), and from the ENDF/JENDL evaluations (solid blue line) [18].

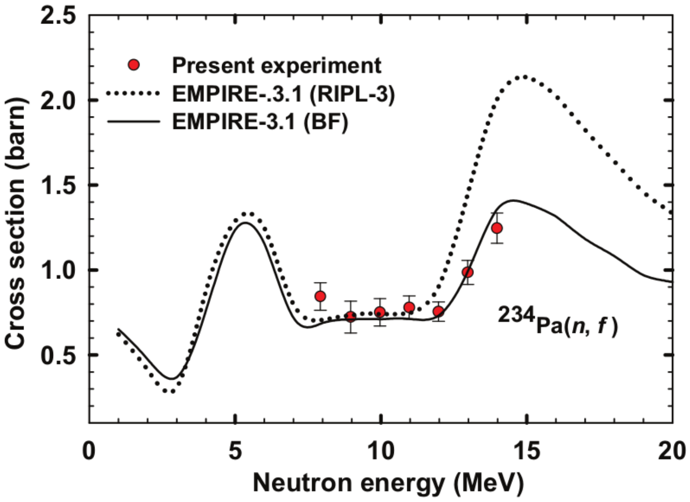

Figure 2.16: $^{234}Pa(n, f)$ cross section deduced with the surrogate ratio method (red circles "Present experiment" corresponding to [32]), compared to calculations with the EMPIRE-3.1 code, for the fission barrier formula described in the article (BF) and RIPL-3 [32].

may see in figure 2.17, the inferred $^{238}Pu(n, f)$ cross section is in agreement with that of Ressler *et al.* [17].

2.2.2 Application of the SRM to Radiative Capture

In 2010 Goldblum *et al.* [34] used the SRM to infer the $^{161}Dy(n, \gamma)$ cross section in an equivalent neutron energy range of 130-560keV. The experiment took place in the Oslo Cyclotron Laboratory using the CACTUS array which includes light-charged-particle telescopes and scintillators. They measured the γ-decay probability of $^{162}Dy^{*}$ relative to

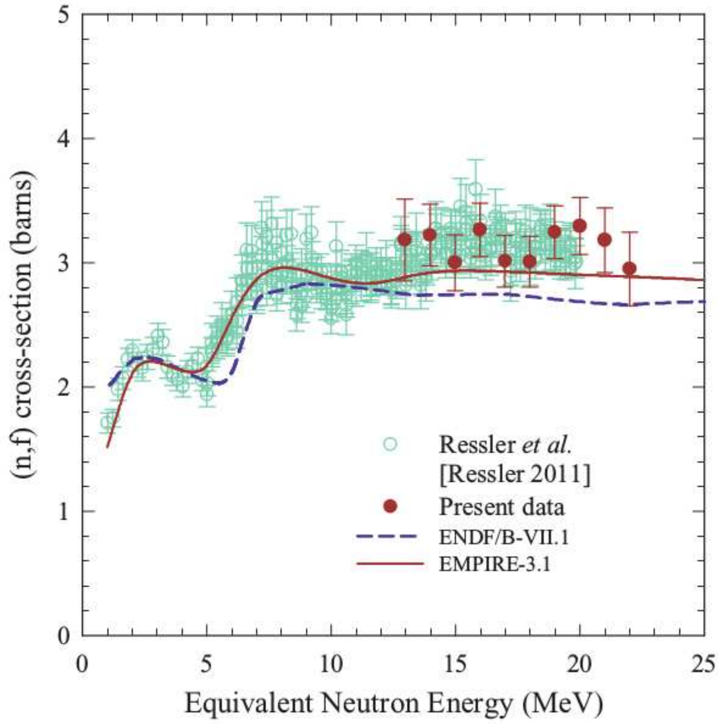

Figure 2.17: $^{238}Pu(n,f)$ cross section deduced with the surrogate ratio method (red circles "Present data" corresponding to [32]), compared to Ressler *et al.* [17] (green circles), a calculation with EMPIRE-3.1, and ENDF/B-VII.1 [33].

$^{161}Dy^{*}$ and $^{164}Dy^{*}$ residual nuclei. Figure 2.18 resumes their results.

In both figures 2.18a and 2.18b which represent the $^{161}Dy(n,\gamma)$ cross section, a better agreement is achieved with a higher γ-energy threshold. On the top part of the figures the cross sections are obtained with a threshold in γ-ray energy of 500keV and the lower part with a threshold of 2MeV. The authors link this improvement to the fact that the Weisskopf-Ewing approximation, used to infer the cross sections, works better at high energies.

In an article published in 2012 by Scielzo *et al.* [57], they contradict the hypothesis that by rising the γ-energy threshold, the angular momentum distributions do not need to be taken into account. They find no evidence for this and state that the differences in the spin-parity distribution between neutron induced and surrogate reactions have to be accounted for.

In 2016 Yan *et al.* [35] used the $^{92}Zr(^{18}O,^{16}O)^{94}Zr$ and $^{90}Zr(^{18}O,^{16}O)^{92}Zr$ reactions to test the SRM. They infer the $^{93}Zr(n,\gamma)^{94}Zr$ cross section with the experimental ratio of the coincidence events multiplied by the measured $^{91}Zr(n,\gamma)^{92}Zr$ cross section, in energy region equivalent to $E_n = 0-8\ MeV$. The deduced cross section is in good agreement with their calculations for $E_n > 3$ MeV, as figure 2.19 shows.

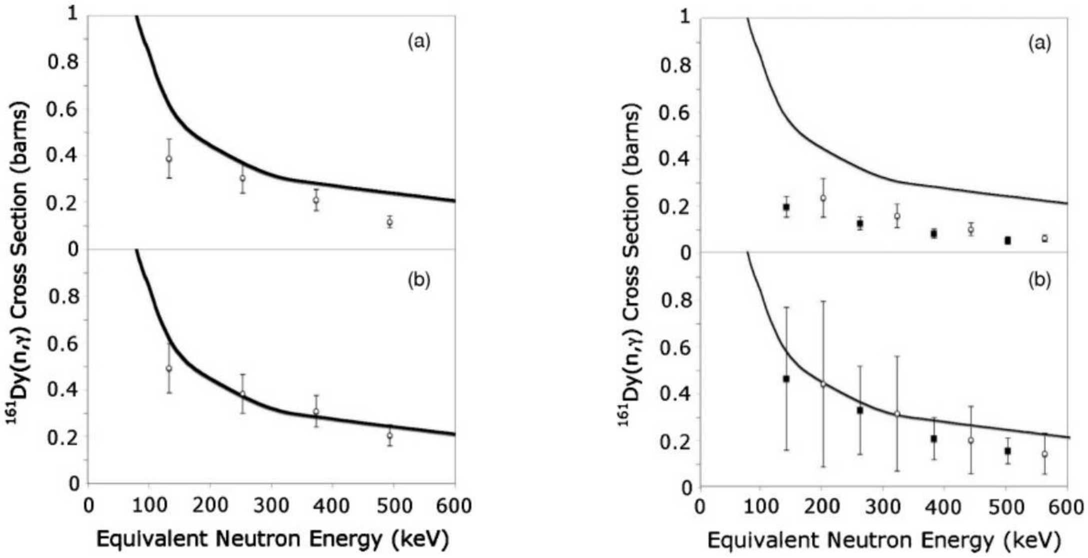

(a) Quoting from [34]: "*cross section extracted using the SRM with similar compound nuclei pairs relative to the evaluated* $^{163}Dy(n,\gamma)$ *cross section obtained from ENDF/B-VII.0 as a function of equivalent neutron energy obtained via the* $(^3He,{}^3He')$ *inelastic scattering reaction with a* γ*-ray energy threshold of (a) 500keV and (b) 2MeV. [...] For comparison, the directly measured* $^{161}Dy(n,\gamma)$ *cross section from ENDF/B-VII is denoted by the solid line.*"

(b) Quoting from [34]: "*cross section extracted using the SRM with dissimilar compound nuclei pairs relative to the evaluated* $^{160}Dy(n,\gamma)$ *cross section obtained from ENDF/B-VII.0 as a function of equivalent neutron energy obtained via the* $(^3He,{}^3He')$ *inelastic scattering reaction (open circles) and the* $(^3He,\alpha)$ *pickup reaction (solid squares) with a* γ*-ray energy threshold of (a) 500keV and (b) 2MeV. [...] For comparison, the directly measured* $^{161}Dy(n,\gamma)$ *cross section from ENDF/B-VII is denoted by the solid line.*"

Figure 2.18: $^{161}Dy(n,\gamma)$ cross section extracted using the SRM [34].

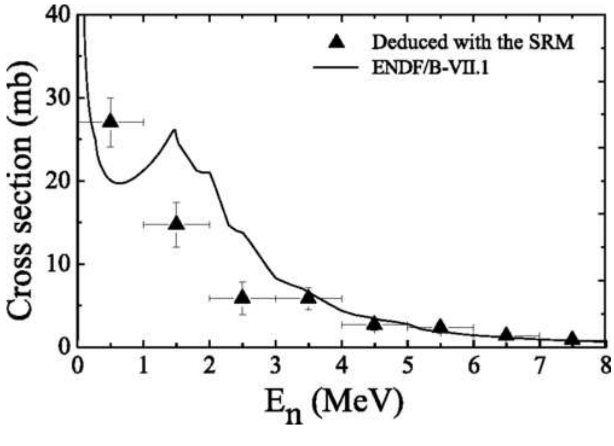

Figure 2.19: $^{93}Zr(n,\gamma)^{94}Zr$ cross section deduced with the surrogate ratio method (black triangles), compared to the neutron induced reaction from ENDF/B-VII.1 [35].

2.3 The Oslo Method

Although this method was not conceived to produce neutron induced cross sections as the surrogate method does, in some articles the authors deduce neutron radiative capture cross sections with this method, for instance Laplace *et al.* [37]. The aim of the Oslo method is to use charged particle reactions to deduce level densities and gamma strength functions (γSF) from the recoil nuclei. It is based on the measurement of γ-ray-ejectile coincidences and was developed in several steps with different contributions to it:

- First generation: extract primary γ-rays from the total gamma spectra [58] (1987).
- Unfolding: correct the gamma spectra with detector response [59] (1996).
- Simultaneous extraction of the level density and gamma strength from the matrix of primary γ-rays [60] (2000). In the article of Schiller *et al.* [60] the full procedure to extract the information from the experimental data is detailed.
- Revision of the method and the uncertainties associated with the hypothesis done [61] (2011).

There are some limitations to the model: the normalization of the level density at S_n is needed, and the only observed decay channel is γ-decay. The method has been used since its development mainly in several articles to obtain level densities (LD) and γSFs, however in this work we will cite some of the most relevant ones for the present work.

In 2013 the method was applied by Guttormsen *et al.* [36] to extract the level densities from different Th and U isotopes. They performed two experiments at the Oslo Cyclotron Laboratory on ^{232}Th and ^{238}U targets, with the SiRi particle telescope and the CACTUS γ-detector device. The Th target was bombarded with 12 MeV deuterons and 24 MeV ^{3}He nuclei, and the U one with 15 MeV deuterons. With this beam-target combinations, they had access to the level densities of $^{231,232,233}Th$ and $^{237,238,239}U$, see figure 2.20.

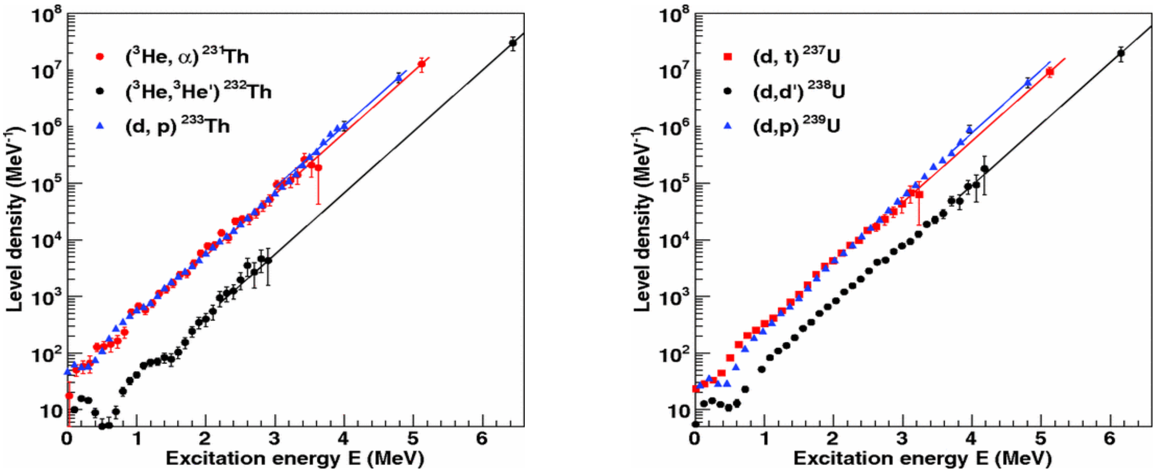

(a) LDs for $^{231,232,233}Th$, and CTM extrapolations (solid lines) with $T_{CT} = 0.40$ MeV [36].

(b) LDs of $^{237,238,239}U$, and CTM extrapolations (solid lines) with $T_{CT} = 0.40$ MeV for $^{237,238}U$ and $T_{CT} = 0.39$ MeV for ^{239}U [36].

Figure 2.20: Level densities of $^{231,232,233}Th$ and $^{237,238,239}U$ [36].

The data of Guttormsen *et al.* goes up to ~ 4 MeV and it is renormalized with the level density at S_n. This level density is obtained with neutron induced reaction data, which at low neutron energies provides the mean resonance spacing D_0, with which one can deduce the level density of the compound nucleus assuming a certain spin distribution. Between the data deduced with the Oslo method and the neutron induced data they extrapolate using a Constant Temperature Model (CTM) [62] as shown in figure 2.20. They conclude that it is the best mode to fit the data and they give thermodynamic properties of the nuclei, such as entropy and heat capacity.

In 2016 Laplace *et al.* [37] applied the Oslo method to the $^{242}Pu(d,p)$ reaction. They did a remarkable work to extract the nuclear level density (NLD) and the γSF of ^{243}Pu. However, here we will concentrate on the $^{242}Pu(n,\gamma)$ cross section they deduced from the data. They bombarded a target of $0.4 mg/cm^2$ ^{242}Pu on a Be-backing, with 12 MeV deuterons produced at the Oslo Cyclotron Laboratory, with the same set-up as [36]. Figure 2.21 shows the radiative capture cross sections they obtained, with a scissors-resonance (SR) in the γSF and with out it. Their curves are compared to neutron induced data and different evaluations, the agreement is very good up to 200 keV where the data stop. They extrapolate their calculations up to 4 MeV, and at around 1 MeV there are differences between their calculation and the evaluations.

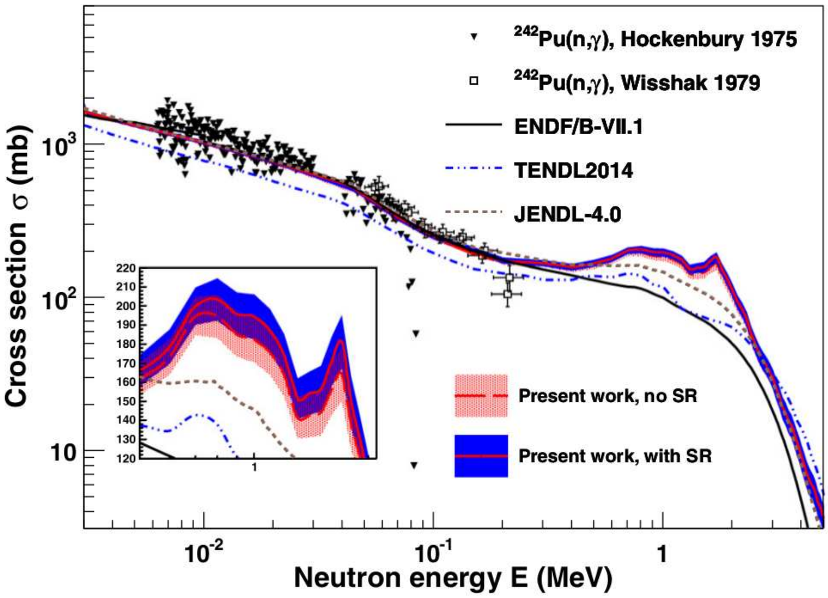

Figure 2.21: Quoting from Laplace *et al.* [37]: "*Calculated* $^{242}Pu(n,\gamma)$ *cross section using level density and* γ*SF parameters obtained in the present work, including the M1 scissors mode (continuous red curve with blue error-band) and without it (dashed red curve with red dots error-band). A zoom in the energy region 0.5 to 2 MeV, where the impact of the SR is the most important, is shown in the inset. The predictions are compared at low energy with measured data from Hockenbury et al. [63] (black triangles), Wisshak and Käppeler [64] (empty squares), and evaluations from ENDF/B-VII.1 (black curve), JENDL-4.0 (dashed grey curve), TENDL2014 (blue dotted-dashed curve)*". The references to "present work" is the work of Laplace *et al.* [37].

In 2019 Zeiser *et al.* [38] applied the Oslo method to obtain the NLD and the γSF of ^{240}Pu with the reaction $^{239}Pu(d,p)$. As in the experiment above, they bombarded the ^{239}Pu target with 12 MeV deuterons produced at the Oslo Cyclotron Laboratory, with the same set-up as [36]. Although the article has to go still through the peer review process their results seem really interesting. Figure 2.22 represents the NLD of ^{240}Pu that they obtained, the level density at S_n from the neutron induced data and CTM [62] that fits the data.

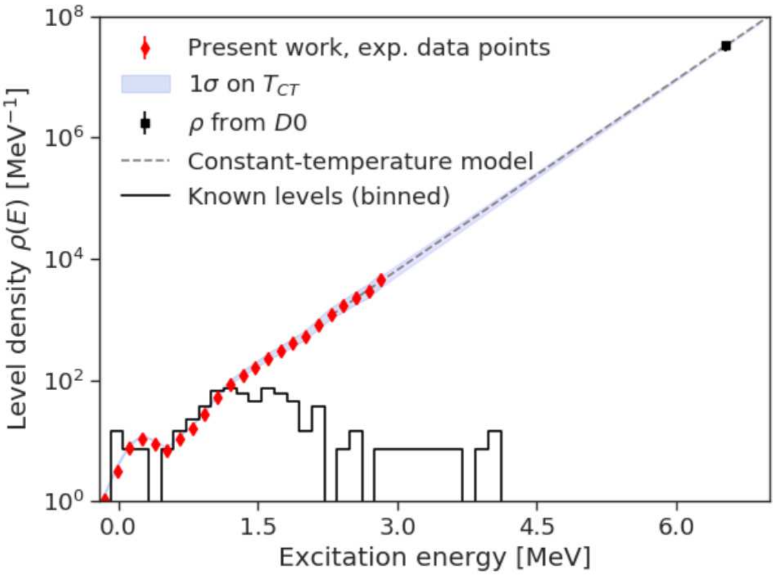

Figure 2.22: The NLD of ^{240}Pu obtained with the Oslo method compared to known discrete levels, the level density at S_n from the neutron induced data, calculated with D_0, and a curve of the CTM with $T_{CT} = 0.415$ [38]. The reference to "present work" is the work of Zeiser *et al.* [38].

As we will see in chapter 5, the level density of the CTM given in figure 2.22 is similar to what we use in our calculations, i.e. a constant CTM with the parametrization of RIPL [53]. Apart from the NLD in their article they also propose a gamma strength function for ^{240}Pu, see figure 2.23.

The γSF deduced in figure 2.23 presents a small structure between 2 and 4 MeV, which is consistent with other results [40]. As a matter of fact this "pygmy" resonance is usually related to the so-called scissors mode [65], which are collective excitations in which two particle systems rotate in opposite sense while conserving their shape. This kind of resonance is being included in neutron data evaluations to avoid having to do a renormalization between the resonance energy range and the continuum one.

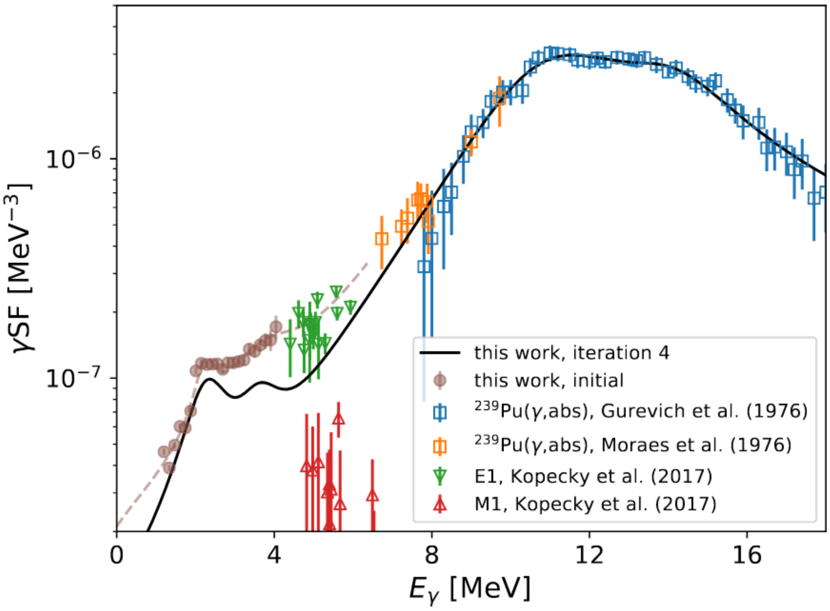

Figure 2.23: The γSF of ^{240}Pu obtained with the Oslo compared to the available data. The references to "this work" correspond to the work of Zeiser *et al.* [38].

Chapter 3

Experimental Set-Up

The CENBG/CEA-DAM collaboration has developed an experimental set-up for the simultaneous measurement of fission and γ-emission probabilities. Measuring the γ-decay probabilities of fissionable actinides is complicated because, when fission sets in, it is necessary to disentangle the γ-rays emitted by the fission fragments and those from the decaying nucleus. This is particularly difficult in the case of fissile nuclei, where the contribution of γ-rays emitted by the fission fragments is dominant when the fission probability is of the same magnitude as the γ-decay probability.

As explained in chapter 1 in this work we investigated the interaction of ^{3}He and ^{4}He beams impinging on a ^{240}Pu target. It was successfully performed at the Tandem accelerator at the Institute for Nuclear Physics of Orsay (I.P.N.O), during the last three weeks of April 2017. The beam energy was chosen to be $30MeV$ and the target was manufactured by the radiochemistry group of the I.P.N.O. The aim of this experiment was to study the decay probabilities of $^{239}Pu^{*}$ and $^{240}Pu^{*}$ by means of the following surrogate reactions,

$$^{240}Pu(^{4}He,{}^{4}He')^{240}Pu^{*} \Longleftrightarrow n+{}^{239}Pu \rightarrow {}^{240}Pu^{*}$$
$$^{240}Pu(^{3}He,{}^{3}He')^{240}Pu^{*} \Longleftrightarrow n+{}^{239}Pu \rightarrow {}^{240}Pu^{*}$$
$$^{240}Pu(^{3}He,{}^{4}He)^{239}Pu^{*} \Longleftrightarrow n+{}^{238}Pu \rightarrow {}^{239}Pu^{*}$$

where we have indicated the n-induced reaction associated to each surrogate reaction.

The experimental set-up we used revolves around equation (1.1) and the measurement of its different terms, to obtain the decay probabilities [43] [24]. In the absence of scattered particles originated from contaminant reactions, the number of single events $N_s(E^*)$ corresponds to the total number of Y^* nuclei and the number of coincidences corrected for detection efficiency $N_\chi(E^*)/\varepsilon_\chi$ to the number of Y^* nuclei that have decayed via channel χ at a certain excitation energy.

3.1 Beam Energy

Selecting the optimal beam energy is crucial to obtain the best possible results. The beam energy has an influence on the different reaction cross sections. The higher the energy above the Coulomb barrier, the lower the elastic cross section in relation to the inelastic scattering cross section. To get an estimation of the Coulomb barrier (V_C) of each pair of target and projectile, the classical formula was used:

$$V_C(Z_1, Z_2) = \frac{Z_1 Z_2 e^2}{4\pi\epsilon_0 d} \tag{3.1}$$

where ϵ_0 is the electrical permeability of the vacuum, e the electron charge, and $d = r_0(A_1^{1/3} + A_2^{1/3})$. Applying equation (3.1) to the reactions above mentioned with a value of $r_0 = 1.25 fm$, gives $V_C \approx 28$ MeV. Other formulas, see [66], give values as low as 24 MeV. However, equation (3.1) gives an upper value that has to be surpassed to reduce the elastic scattering cross section.

For that reason a beam energy of 30 MeV was chosen, for both the ^3He and ^4He beams, because the barrier values are very similar. It is a sufficiently high energy to be well above the Coulomb barrier, and to avoid to have a huge proportion of fusion-fission events, which can damage the fission detectors. The latter increases rapidly with the incident beam energy.

3.2 Overview of the Experimental Set-up

The best way of getting a first grasp of the set-up is to look at figure 3.1a, which shows a drawing with an external view of the experimental set-up. A vacuum reaction chamber is surrounded by two types of gamma-ray detectors: six high-purity germanium detectors and four C_6D_6 liquid scintillators. One also distinguishes a target airlock, which is needed to isolate the radioactive targets or sources from the environment during the transportation from a glove box, where they are mounted, to the experimental set-up. Figure 3.1b shows a photograph of the set-up taken during the measurement at the Tandem accelerator of the IPN of Orsay in France.

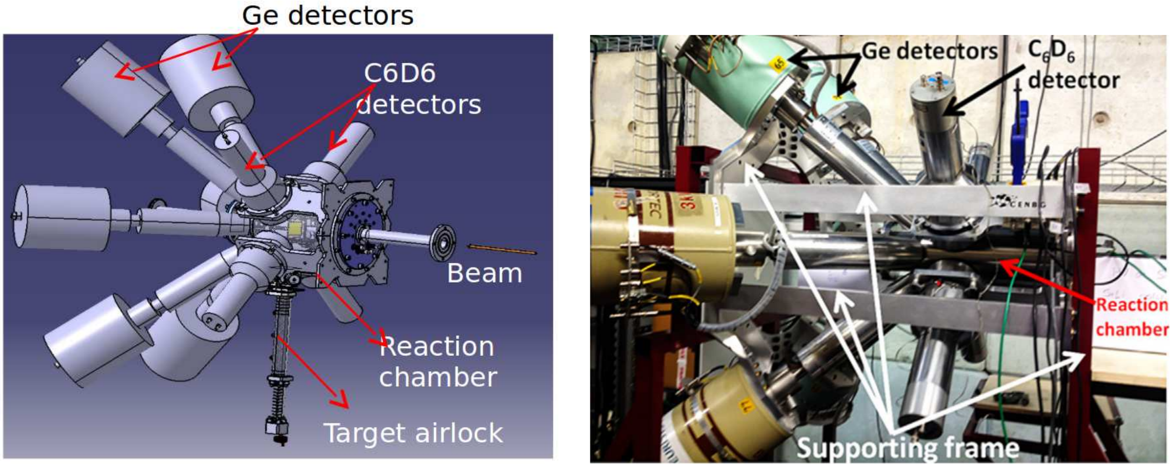

(a) Digital 3D-model of the set up.

(b) Photograph of the set-up during the measurement at the I.P.N. Orsay in France.

Figure 3.1: Overview of the experimental set-up.

The vacuum chamber houses the target, two position-sensitive particle telescopes ($\Delta E - E$) and a fission detector made out of 16 solar cells. The telescopes are used to identify the scattered particles b of the investigated two-body nuclear reactions $X(a,b)Y^*$, and to measure their kinetic energy and their polar angle. The energies of the detected particles b are converted to nuclear excitation energy of the decaying nucleus Y^* applying energy and linear momentum conservation, see equation (3.9), and accounting for energy losses in dead layers. Fission fragments and/or γ rays are detected in coincidence with the scattered particles. As explained above, with this information, the fission detection efficiency and the γ-cascade detection efficiency, it is possible to determine fission and γ-decay probabilities, see equation (1.1).

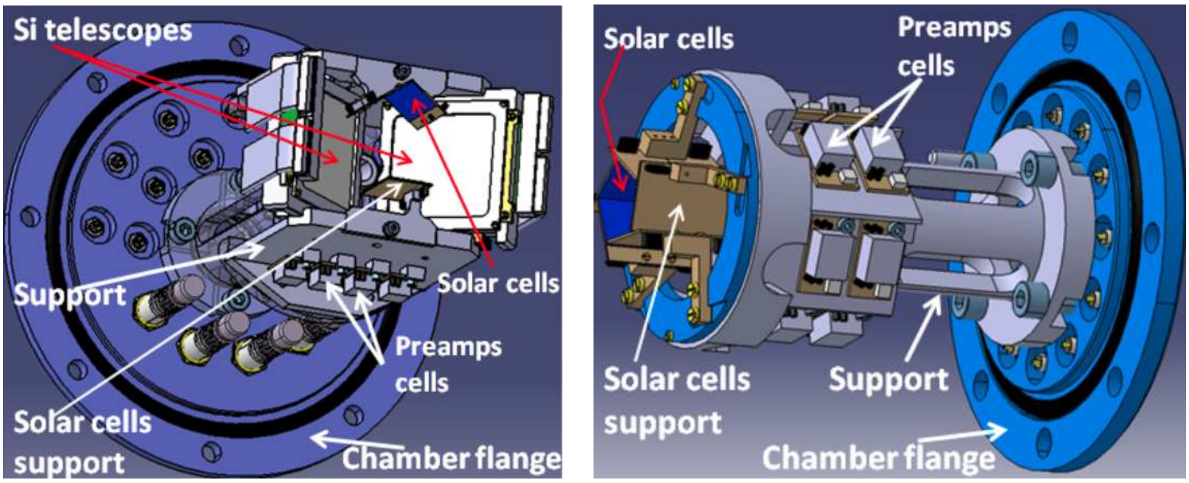

(a) The detectors located upstream the target. (b) The detectors located downstream the target.

Figure 3.2: Detectors placed inside the vacuum reaction chamber, including their supports, which are fixed to the chamber flanges.

The reaction chamber has three openings, two on the sides and one on the center. The central opening is located on the bottom of the chamber and serves to fix the airlock and insert the target ladder. The airlock includes a high-precision positioning system to place the center of the targets on the beam axis. The detectors are placed on either side of the target, they are fixed to the lateral chamber flanges. Figure 3.2 shows the detectors together with their supports and the chamber flanges. The two telescopes are located upstream from the target. The fission detector is divided into two parts, one upstream and the other downstream the target, each part is composed of several solar cells. More details will be given in the following subsections.

3.2.1 Targets

The target ladder contains four positions, see figure 3.3. One of the positions was occupied by the PuO_2 target, which had an areal density of about $100\mu g/cm^2$ and $\phi = 9$ mm, which corresponds to an α activity of 534 kBq, and a target backing made of natural carbon of the same surface density. The Pu target was manufactured at the I.P.N.Orsay by the radiochemistry group. Two other positions were occupied by a ^{208}Pb target of $200\mu g/cm^2$ over the same carbon backing of $100\mu g/cm^2$ and by the C backing alone. In the remaining position there was a hole to let the beam pass through and ensure that it was correctly aligned.

Figure 3.3: Target support and targets (photograph taken after the experiment), from left to right: hole, carbon backing, plutonium target and lead target. The Pu target was slightly detached from the support. Note the marks left by the beam on the targets.

Measurements with the C backing alone are necessary to evaluate the background spectrum induced by the reactions taking place on it, which may contaminate the singles spectrum obtained with the Pu. In the present experiment, the beam energy and the angle of the telescopes were chosen in such a way that the peaks in the singles spectrum associated to the elastic scattering of the beam on C or ^{16}O where out of the range of the E^* of ^{240}Pu of interest. However, during the experiment we noticed that there were unexpected contaminants in the Pu target. The origin of these contaminants is not fully clear, but one hypothesis is that they were acquired during the fabrication process. From the position of the peaks at different telescope angles we deduce that the contaminants are mainly Ca and Cl, but also K and S. Figure 3.4 represents the difference between the energy of the elastically scattered α particles by a ^{240}Pu nucleus and the mentioned contaminants, as a function of the polar angle $\theta[^o]$. The figure illustrates the fact that the bigger the angle, the higher the contaminant will appear in excitation energy.

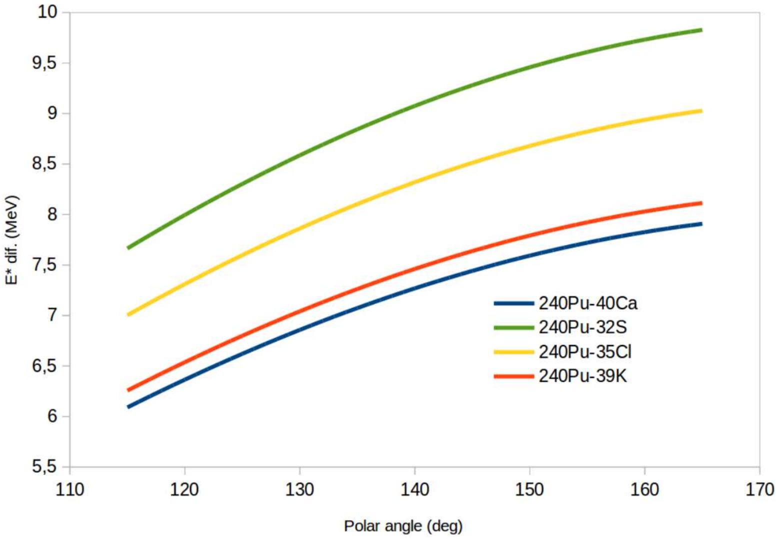

Figure 3.4: Difference in MeV between kinetic energy of an elastically scattered α particle by a ^{240}Pu nucleus and the different contaminants, as a function of the polar angle $\theta[^o]$.

The ^{208}Pb target is used for telescope calibration purposes, as the first excited states of the lead isotopes, produced by scattering or transfer reactions on it, are well separated from each other and the ejectiles have energies comparable to the ones they have after the reactions with plutonium. The measurement of the kinetic energy of the scattered particles is crucial for the determination of the E^* of Y^* and we made significant efforts to determine it as accurately as possible, more details are given in chapter 4.

3.2.2 Particle Telescopes

Each telescope is composed of a thin position-sensitive Si strip detector (ΔE) and a thick Si-Li detector (E). The thickness and the polarization voltages were different for each detector, see table 3.1. The ΔE detectors were 16x16 channels double-sided-silicon-strip detectors (DSSSD) with a surface of 25 cm^2, manufactured by Micron semiconductors [67]. The telescopes were centered at 138.5 degrees (polar angle) with respect to the beam axis at a distance of 5.5 cm from the target, see figure 3.5. The covered polar angles range from 119.4 to 157.2 degrees in steps of about 2 degrees. As seen in figure 3.5, the E detector has a smaller surface (22.1 cm^2) than the ΔE detector and defines the geometrical efficiency. The sum of the geometrical efficiency of both telescopes amounts to 8.25%. Also a 30 μm-thick aluminum foil was placed in front of each ΔE detector to stop fission fragments and the alpha particles emitted by the plutonium target. In addition, these Al foils are biased to -300V to repel the δ electrons stemming from the target.

Detector	Thk. ΔE (μm)	Pol. ΔE (V)	Thk. E (mm)	Pol. E (V)
Telescope 1	97	+9	2	+300
Telescope 2	100	+10	5	+600

Table 3.1: Thicknesses (Thk.) and polarization voltages (Pol.) of the detectors that form the particle telescopes.

The telescopes were placed at backward angles with respect to the beam direction to minimize the impact of the background coming from reactions on the target backing (natural carbon) and light target contaminants (e.g. oxygen) on the singles spectrum. Because of the kinematics of two-body reactions, at backward angles the scattered particles of these parasitic reactions have kinetic energies that correspond to excitation energies of the excited isotope Y^*, which are not of interest, thus leaving a large range of E^* in the singles spectrum free from contaminant peaks of natural carbon and oxygen. Unfortunately, as previously mentioned, there were some unexpected contaminants, S, K, Ca and Cl isotopes, which are common in tap water, probably acquired by the C backing during the fabrication of the target. The procedure followed to cope with them is detailed in chapter 4, section 4.4.1.

The kinetic energies relevant in this experiment range from few to several tens of MeV. Thus, the kinetic energies of the scattered particles can be much higher than the kinetic energies of the alpha particles originating from a standard 3-α (Am-Cm-Pu) calibration source, $\sim 5MeV$. This is the reason why the first excited states of $^{207}Pb^*$ and $^{208}Pb^*$ produced in $^{208}Pb(^3He,^4He)$ and $^{208}Pb(^4He,^4He')$ or $^{208}Pb(^3He,^3He')$ where used to calibrate the telescopes (ΔE and E) instead of the mentioned source. We have access

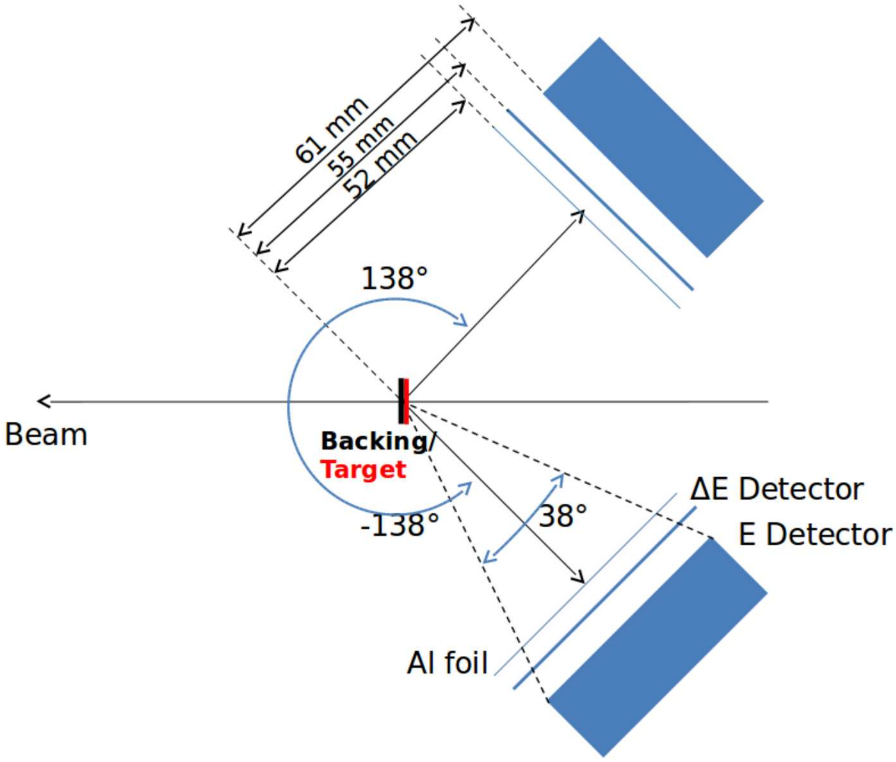

Figure 3.5: Position of the telescope detectors in relation to the beam direction and the target. View of a cut of the horizontal plane.

to the theoretical kinetic energy of the ejectile with formula (3.7), that can be used to calibrate the detectors.

In the following we derive eq (3.7). Schematically the two body reactions taking place can be described like they are in figure 3.6, where,

- $M_i, \ i = \{a, X, b, Y\}$ are the masses of the nuclei.
- $E_{ci}, \ \{i = a, b, Y\}$ are their corresponding kinetic energies.
- And $\vec{v_i}, \ \{i = a, b, Y\}$ are their velocities.

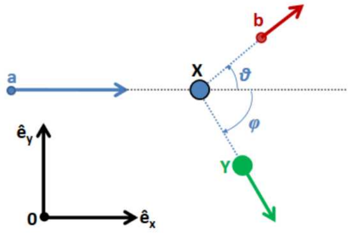

Particles	Parameters
X (target)	M_X
a (projectile)	M_a, E_{ca}, $\vec{v_a}$
b (ejectile)	M_b, E_{cb}, $\vec{v_b}$
Y (recoiling nucleus)	M_Y, E_{cY}, $\vec{v_Y}$

Figure 3.6: Left: schematic two body reaction in which a particle "a" impinges on a target nucleus at rest "X", resulting in an ejectile "b" and recoil nucleus "Y". Right: associated variables, masses, energies and velocities, to each body intervening in the reaction [8].

The principle of conservation of the total energy reads in this case:

$$E_{ca} = E_{cb} + E_b^* + E_{cY} + E_Y^* - Q \tag{3.2}$$

where E_b^* and E_Y^* are the excitation energies of the ejectile and the recoiling nucleus respectively, and Q is the Q-value of the reaction. In our case the excitation energy of the ejectile is neglected because ^3He has no bound excited states and the first excited of ^4He is at $20MeV$ which is well over the energies that we will study.

The principle of momentum conservation over the x-axis and the y-axis gives:

$$M_a v_a = M_b v_b \cdot cos(\theta) + M_Y v_Y \cdot cos(\varphi) \tag{3.3}$$

$$0 = M_b v_b \cdot sin(\theta) + M_Y v_Y \cdot sin(\varphi) \tag{3.4}$$

As we are in the non-relativistic limit $M \cdot v = \sqrt{2ME_c}$, and substituting this expression in (3.3) and (3.4) gives:

$$\sqrt{2M_a E_{ca}} = \sqrt{2M_b E_{cb}} \cdot cos(\theta) + \sqrt{2M_Y E_{cY}} \cdot cos(\varphi) \tag{3.5}$$

$$0 = \sqrt{2M_b E_{cb}} \cdot sin(\theta) + \sqrt{2M_Y E_{cY}} \cdot sin(\varphi) \tag{3.6}$$

Using equations (3.2), (3.5) and (3.6), one obtains the energy of the ejectile E_{cb}:

$$E_{cb} = \left\{ \frac{cos\theta\sqrt{M_{ca}M_{cb}E_{ca}} + \sqrt{M_{ca}M_{cb}E_{ca}cos^2\theta + (M_{cb}+M_Y)[E_{ca}(M_Y - M_{ca}) + M_y(Q - E^*)]}}{M_{cb} + M_Y} \right\}^2 \tag{3.7}$$

Using equation (3.7) we can calibrate the telescope detectors by correctly simulating their geometry and the energy losses in the aluminum foils and the ΔE detectors. We neglect the losses in the target as in this experiment it was really thin, thus the energy of the ejectile is equal to:

$$E_{cb} = E_{Al-foil} + \Delta E + E_{SiLi} \tag{3.8}$$

where $E_{Al-foil}$ is the energy loss in the Al foil, ΔE and E_{SiLi} are the energies deposited in the strip detector and in the Si-Li detector, respectively. These energy losses where calculated using three different programs: Kaliveda, Geant4 and Lise++. Each of them gave different values for the energy losses, but the variations, of some tens of keV, were less than the energy resolution we had, ~ 100 keV. Finally we chose Kaliveda, a simulation library developed in C++ by IN2P3 [25], to do the energy loss simulation. A C++ Monte-Carlo simulation was made to determine the mean angle of each strip (see appendix A).

Once the telescopes are calibrated, the deposited energy in the telescopes can be converted to excitation energy of the recoil nucleus with the formula (3.9).

$$E^* = \frac{M_Y Q - E_{ca}(M_a - M_Y) - E_{cb}(M_Y + M_b) + 2cos\theta\sqrt{M_a M_b E_{ca} E_{cb}}}{M_Y} \tag{3.9}$$

The ΔE detector has 16x16 strips but we only used the 16 vertical strips because for the heavy recoil nuclei Y considered here, the variation of the kinetic energy of the ejectile with its emission angle is very slow. Thus the position information obtained with the vertical strips was sufficient. In addition strips number 1 and 16 were not included in the analysis because the Si-Li detector was slightly smaller than the strip detector making these two strips useless. In principle it is possible to investigate the decay probabilities for each vertical strip and even each telescope independently, but it was impossible here due to the lack of statistics, for all the reaction channels. To improve it, seven groups of four strips, two from each telescope, were defined as summarized in table 3.2:

Strips	Angle #	$\theta(^o)$	$\Delta\theta(^o)$
2-3	1	156.0	3.4
4-5	2	150.6	3.0
6-7	3	144.7	2.6
8-9	4	138.6	2.2
10-11	5	132.4	1.9
12-13	6	126.3	1.7
14-15	7	120.7	1.4

Table 3.2: Average angles for each group of four strips, two from each telescope.

3.2.3 Gamma Detectors

As mentioned before there were four scintillators and six Ge detectors placed surrounding the chamber. The disposition of the detectors is detailed in figure 3.7. The upper part shows that the central axes of the C_6D_6 detectors are included in the plane containing the target. The central axes of the germanium detectors are tilted by 45 degrees with respect to this plane. The lower panel shows the angles between adjacent detectors. The distance of the C_6D_6 and Ge detectors to the target is 93 and 130 mm, respectively.

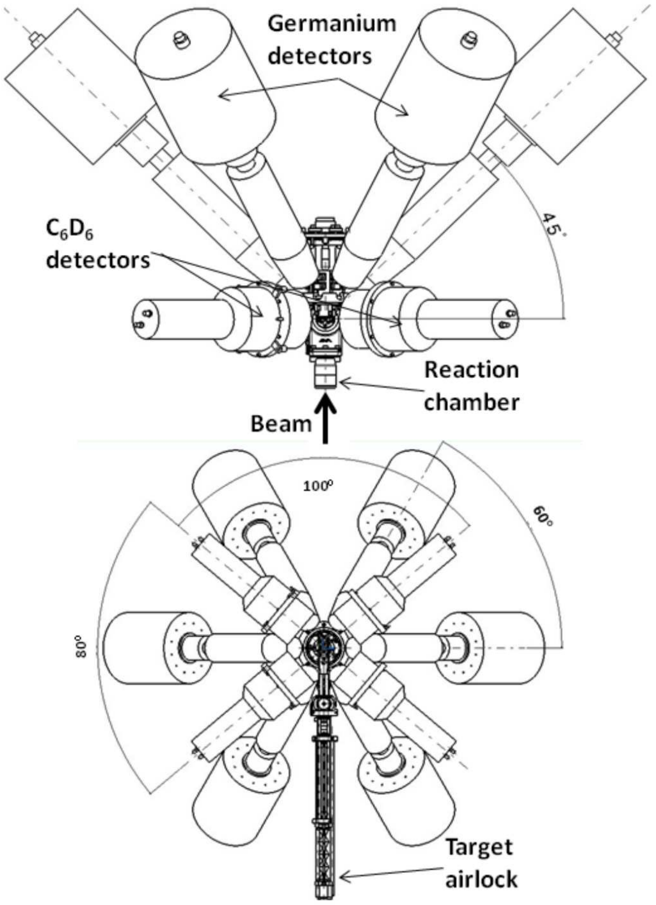

Figure 3.7: Geometrical arrangement of the γ-ray detectors. (Top) Top view of the detector arrays. The angle between the plane containing the central axes of the C_6D_6 detectors and the Ge detectors is given. (Bottom) Front view of the detector arrays. The angle between adjacent C_6D_6 and adjacent Ge detectors is given [24].

Liquid Scintillators

The detection principle of these detectors is based on the Compton scattering of photons in the liquid C_6D_6. When a photon interacts with an electron it may transfer just a fraction of its total energy and momentum. Applying the conservation rules of these two quantities, the energy transfered to the recoil electron E_{e^-} can be expressed as a function of the incident energy of the photon E_0 and the scattering angle θ, like in equation (3.10):

$$E_{e^-} = E_0 - \frac{E_0}{1 + E_0\left(\frac{1-cos\theta}{m_e c^2}\right)} \tag{3.10}$$

When $\theta = 180^o$ the energy transfer is maximal and a broad peak is formed in the spectrum with an energy $E_{e^-}^{max}$ as defined in equation (3.11), *the Compton edge.*

$$E_{e^-}^{max} = \frac{2E_0^2}{m_e c^2 + 2E_0} \tag{3.11}$$

Although photons may deposit all their energy in the detector, which makes appear in theory a well defined peak, this peak is not exploitable due to its small cross section as compared to a Compton scattering.

In figure 3.8 the energy spectrum we measured with a ^{137}Cs source is represented. This nucleus decays by emitting a γ-ray of $661.7keV$. Introducing this value in formula (3.11) gives a value of the Compton edge of $476.7keV$. In figure 3.8 the electronic threshold is visible at around 210 channels, in contrast the photo-peak, which should be at around 370 channels, is not distinguishable from the background in this image.

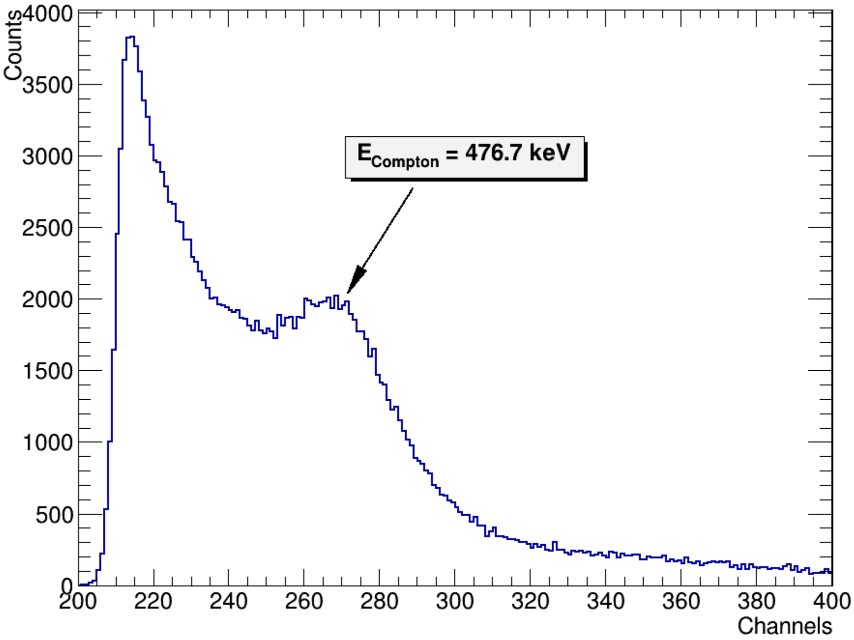

Figure 3.8: Gamma energy spectrum, in channels, of ^{137}Cs obtained with scintillator 4.

One of the main reasons to choose these detectors is that they can be used to distinguish between the signal of a neutron and that of a γ-ray. This is possible thanks to the pulse shape discrimination technique. In addition, the fact that the benzene of scintillating liquid has deuterium in its composition, instead of just being regular C_6H_6, drastically reduces the neutron captures by hydrogen, which would create an intense background of gamma rays within the detector. This makes C_6D_6 detectors perfect as γ-ray counters, even though their energy resolution is modest.

Germanium detectors

High purity germanium detectors (HPGe) can be used to accurately measure low-lying γ-ray transition intensities, and thus determine the probabilities of observing specific γ-ray transitions as a function of the excitation energy of the decaying nucleus [22]. They can also be used in the same way as C_6D_6 detectors, to count γ-rays from a few 100keV to several MeV. As a matter of fact, the HPGe had two output signals, one was amplified with a high gain (HG) to have a detailed structure of the low-lying γ-rays, the other had a low gain (LG) to be able to detect high energy γ-rays, see section 3.3.

It is possible to accurately measure low-lying γ-rays because the detection principle in the case of germanium detectors is completely different to the one of the scintillators. Within the Ge crystal, which is a semiconductor, there is a high proportion of photoelectric effect, i.e. an electron of the valence band absorbs an incoming photon, if its energy is high enough it will reach the conduction band and be detected. This process is what makes the germanium detectors have an excellent energy resolution.

Unfortunately, in our case, it was not possible to obtain the expected resolution because the energy response of the HPGe fluctuated during time, probably due to temperature changes within the detectors or the electronic chain. This problem can be encountered when using this kind of detector and can be solved by periodically re-adjusting their response to a reference value. However, during this experiment it could not be corrected. The limited energy resolution of these specific germanium detectors, which had been previously used in a neutron environment, the rapid energy shift, combined with the low statistics per time-unit during the plutonium target runs, made it impossible to account for this effect. In addition, detector number 1 did not work correctly, thus it was not used during the whole experiment, therefore the analysis was done just with five Ge detectors.

To illustrate the mentioned resolution problem, the γ-ray spectrum of $^{207}Pb^*$ obtained in this experiment will be compared with the spectra obtained in two previous ones. The focus will be one particular peak characteristic from $^{206}Pb^*$ formed after neutron emission. It is the result of the decay from the first exited state to the ground state through the transition $2^+ \to 0^+$ emitting a γ-ray of $803keV$. In figures 3.9b and 3.9c we may see two different γ-ray energy spectra obtained in previous experiments performed by the group. These spectra contrast with the one shown in figure 3.9a obtained in this experiment. In this last case, the resolution makes it almost impossible to identify the same peaks as those identified in 3.9b and 3.9c. All the spectra represented in figure 3.9 were filled in for the same reaction and range of excitation energy. The $^{208}Pb(^3He,^4He)$ gamma spectra of figure 3.9 show that the germanium detectors had a resolution that made impossible the analysis of selected gamma transitions. To confirm this the spectrum of the $^{240}Pu(^4He,^4He')$ reaction is plotted in figure 3.10, where just the peak corresponding to $511keV$ is barely distinguishable.

Despite the low resolution of the germanium detectors, they could be used as counters of γ-decay events. We used the low-gain output signal to detect the γ-rays with energies up to $\sim 8MeV$. In principle the Ge detectors can only be used up to excitation energies under S_n, because these detectors cannot distinguish between the signal of neutrons and gamma rays. Therefore the neutrons detected by these detectors would increase the gamma decay probability and make untrue the results. Nonetheless, as shown in chapter 4, the results are compatible within error bars with those obtained just with the C_6D_6. Thus, they have been very useful to increase the statistics of the gamma decay probability.

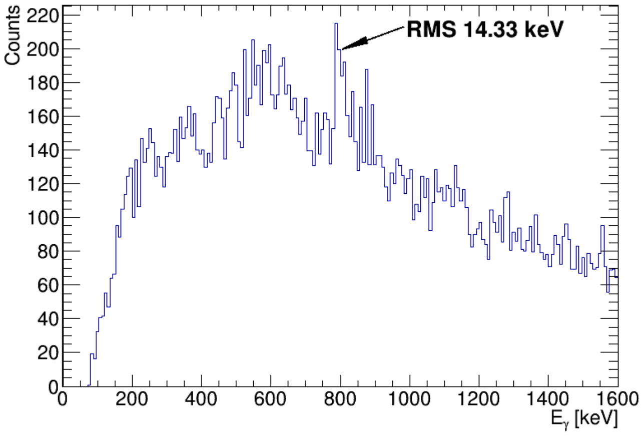

(a) Spectrum from this experiment (2017).

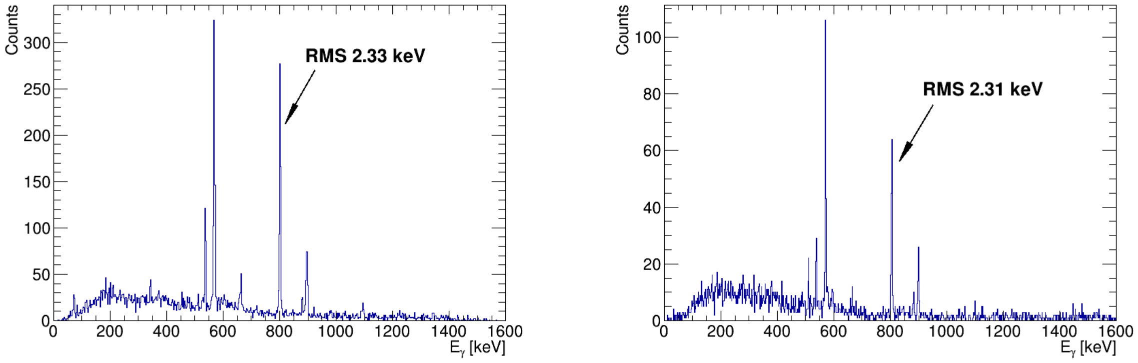

(b) Spectrum from a previous experiment (2010). (c) Spectrum from a previous experiment (2015).

Figure 3.9: Gamma energy spectra obtained with the germanium detectors during three different experiments for the reaction $^{208}Pb(^3He,^4He)^{207}Pb^*$ and similar experimental set-ups. The highlighted peak corresponds to the first excited state of ^{206}Pb at 803 keV, which is a very prominent one, with its corresponding RMS.

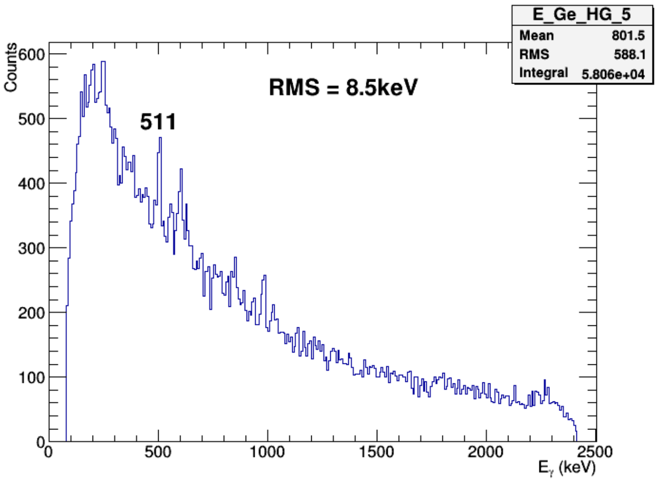

Figure 3.10: Gamma energy spectrum obtained with Ge five for reaction $^{240}Pu(^4He,^4He')$.

3.2.4 Solar Cells

The same devices that are routinely used to convert the energy of sunlight into electricity, solar cells, have been used to detect fission fragments in this experiment. They were first proposed as fission detectors by Siegert [68] and have been used as fission detectors within large γ-detector arrays as Euroball [69]. The CENBG/CEA-DAM collaboration has many years of experience using them for the measurement of fission probabilities [70] [43].

The thickness of solar cells varies between $300\mu m$ and $500\mu m$, but their depletion depth is less than $1\mu m$, therefore very small as compared to the total thickness. It cannot be increased by applying a bias voltage because this increases the electronic noise, due to their very low resistivity of a few Ohm/cm. The small depletion depth leads to a very large capacitance of the order of $40nf/cm^2$. To obtain good timing performances with such a high capacitance we use specially designed, current-mode preamplifiers [69]. The typical time resolution that can be obtained is of few ns, which makes these detectors well suited for coincidence measurements.

Because of the very thin depletion depth, most of the energy deposition occurs in the neutral substrate. The charge collection in the cell is possible thanks to the "funneling" mechanism [71] [72], where the high density of ionization produced along the fragment track locally changes the depletion region into a funnel-like shape extending to the substrate and enclosing the track. This enables the collection of a significant part of the charge produced by the fission fragments via ionization. The funneling efficiency depends strongly on the ionization density profile and it is very small for light particles. This brings the response of the cells to light nuclei into the detector noise and gives a very impressive pile-up suppression in the fission region. Therefore, solar cells are much better suited than Si detectors to investigate fission events in the presence of a high background of light charged particles. This is exactly the situation of our measurements, where the cells are located near the target and are subject to a strong flux of elastic scattered projectile nuclei. In figure 3.11 you may see a fission spectrum of ^{252}Cf, where the double-humped structure due to the different kinetic energies of the light and heavy fission fragments can be clearly distinguished, reflecting the fairly good energy resolution of solar cells.

Another advantage is that solar cells are much more resistant to radiation damage than Si detectors. In addition they are very cost effective and mechanically robust [73]. They can be cut into a wide variety of shapes (e.g. strips) without exhibiting any deterioration and are thus very well suited to build position-sensitive fission detectors within a very compact geometry. The conducting grid on the surface, which is generally made of very thin silver wires, reduces the sensitive area of the cells because the fission fragments are stopped in these wires. For the cells we use the intrinsic efficiency is $(95 \pm 2)\%$.

As one may see in figure 3.12, our fission detector is divided into two parts placed upstream and downstream the target. Each detector plane, 40 mm long and 20 mm wide, is composed of two cells. The length of the cells varies from one detector plane to the other in order to cover different mean polar angles θ_f. The downstream part has the shape of a regular pentagonal prism, see the lower part of figure 3.12. It is placed at 6.0 ± 0.4 mm from the target and the distance from each plane to the beam axis is 12.6 ± 0.3 mm. The latter distance was chosen to avoid very forward angles where the amount of elastically scattered beam particles impinging on the cells is huge. Each side of the prism is equipped with two cells whose length varies from side to side, i.e. two sides have two cells of 19.5 ± 0.5 mm each, two other sides two cells of 9.5 ± 0.5 and

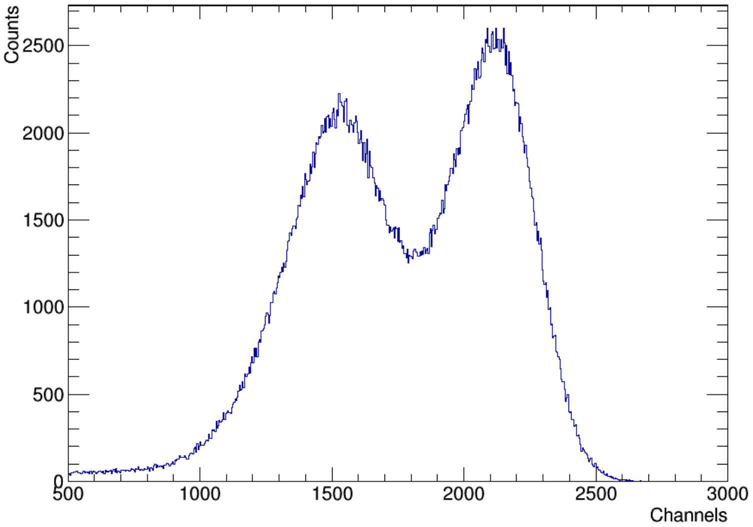

Figure 3.11: Number of counts as a function of energy, in channels, of the ^{252}Cf source obtained with cell number 2.

29.5 ± 0.5 mm, and the remaining side two cells of 29.5 ± 0.5 and 9.5 ± 0.5 mm. With this segmentation we cover polar angles θ_f from 15 to 65 degrees. The upstream part is made out of six solar cells distributed on three planes, see upper panel in figure 3.12. The distance to the target is 19.5 ± 0.2 mm. The distances to the beam axis of the upper and lower detector planes are 28 ± 0.2 and 19.5 ± 0.2 mm, respectively. These distances were chosen in order not to overshadow the Si telescopes. This geometry leads to an angular coverage $\theta_f \in (110, 155)$ degrees. Therefore, with the described segmentation it is possible to measure the fission-fragment angular distribution at forward and backward polar angles. The angular resolution ($\Delta\theta_f$, standard deviation) depends on the size of the cells and varies from 8 degrees for the smallest cells to 30 degrees for the largest ones.

In this experiment the solar cells were just used to count the number of fission events, thus an energy calibration was not needed. It was however possible to distinguish the signal of the true fission events and the signal coming from the pile-up of scattered beam particles, so they could be removed from the analysis. This way we ensure that just the fission fragments coming from the fission of ^{240}Pu are counted.

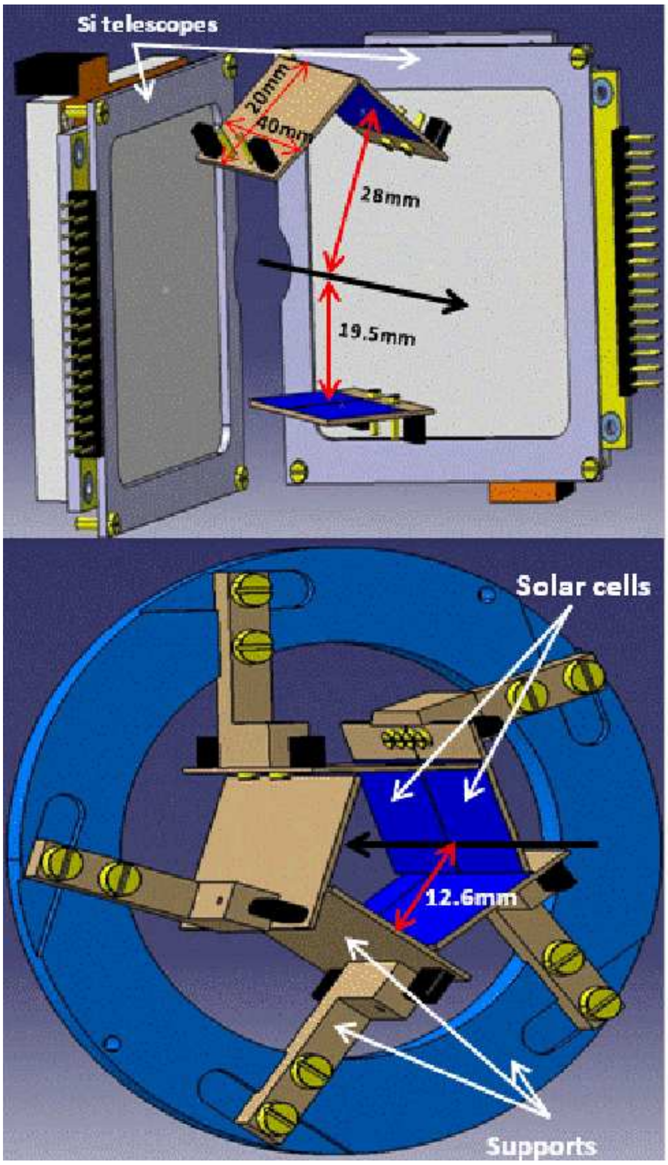

Figure 3.12: Detail of the fission detector, where the beam is represented by the black arrow and the solar cells are indicated in blue. (Top) Part of the fission detector placed upstream the target. This part is made out of three detector planes including six solar cells of various sizes, the Si telescopes are also shown for completeness. (Bottom) Part of the fission detector located downstream the target, which is composed of five detector planes including ten solar cells. The different cell sizes can be observed in blue, as well as their supports in light brown.

3.3 Acquisition and Electronics

Each type of detector had an electronic chain associated to it, preamplifiers, amplifiers, etc. The processed signal is digitalized and an integer is associated to its amplitude or its shape, which is done in the analog-digital converter (ADC). Also the time difference between the signals of two detectors are converted to an integer by the time-to-digital-converter (TDC). If the acquisition system receives a trigger, the information sent to the ADCs/TDCs is associated to an event and during a time gate of $15\mu s$ all the data received is stored.

3.3.1 Telescopes and Trigger

The telescopes permit to identify the compound nucleus formed and its excitation energy, but also they act as the trigger for the acquisition. The detectors were polarized with the voltages of table 3.1. As shown in fig. 3.13, the pulse generated in a Si-Li detector when a particle impinges on it goes to the preamplifier, which has a gain of 20mV/MeV and two outputs. One of them goes to the amplifier that transforms the shape of the signal, ideally, into a Gaussian and increases its peak value, the ADC then stores this value which is associated to the deposited energy in the detector. The other output signal goes to a fast filter amplifier to reshape the signal and from there to a constant fraction discriminator (CFD). The output of this module is a logic signal which is duplicated and that goes to two different gate generators. One that delays the signal 300 ns and is sent to a TDC, and the other increases the width of the signal used as trigger.

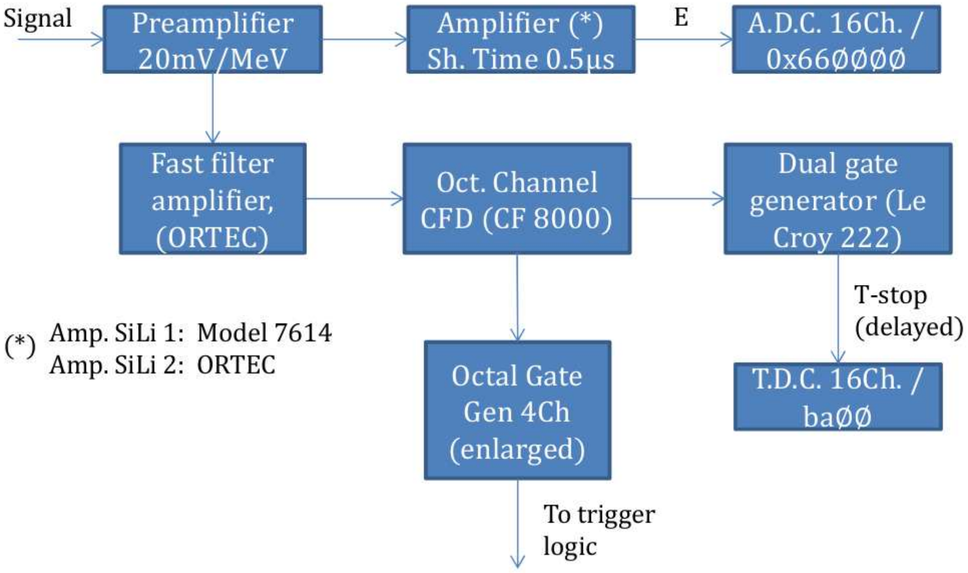

Figure 3.13: Electronic chain of the SiLi detectors.

The signals from the 16 vertical strips going out from the ΔE detector are collected by 16-channel cables and taken into Mesytec preamplifiers specific to these detectors. From these preamplifiers, the energy signals go through a Mesytec amplifier (MSCF-16) that delivers two outputs. One is the amplified energy signals that go directly into the ADC to be stored. The other is the OR signal that passes through a fan-in-fan-out (FIFO) module that duplicates it. One for the trigger logic and the other for the "scaler", which is used to control the counting rates, see figure 3.14.

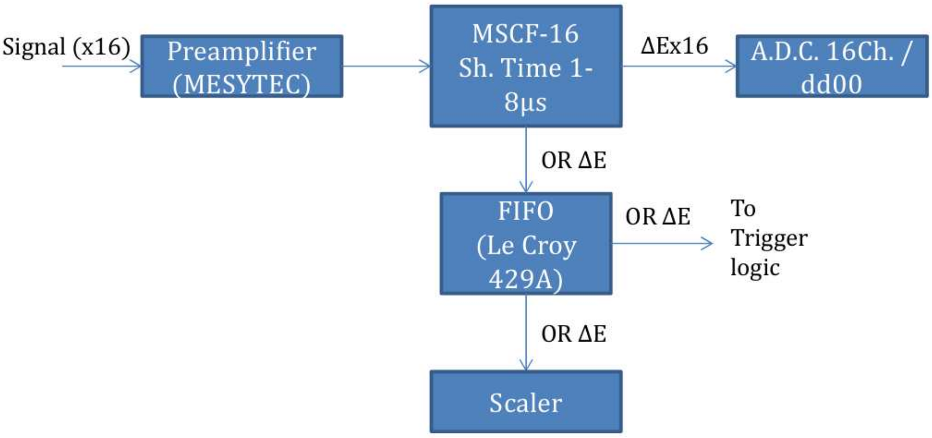

Figure 3.14: Electronic chain of the ΔE detectors.

Finally, the idea of the trigger logic is that when a particle traverses a strip and is stopped in the Si-Li detector this is the signal for the acquisition to record the information coming from all other detectors during $15\mu s$. A diagram of the logic implemented is represented in figure 3.15.

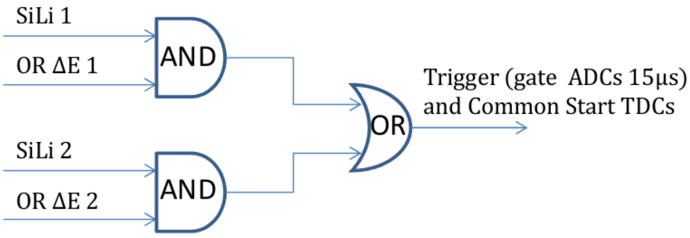

Figure 3.15: Logic implemented for the trigger.

3.3.2 Liquid Scintillators

In the case of liquid scintillators, the output signal of the built-in preamplifiers was attenuated 3 *dB* by putting a 50 Ω resistance to the mass before the Mesytec MPD-4 module. From this module the energy and the pulse shape discrimination (PSD) signals went to the ADC to be stored. The PSD amplitude is proportional to the rise time of the detector signal and enables to distinguish signals from neutrons and γ-rays. The OR of the logic signals was triplicated in two FIFO modules, two of the signals were used as triggers, and one was digitalized and delayed in a gate generator. The time difference of this signal with the telescope trigger is then recorded in the TDC.

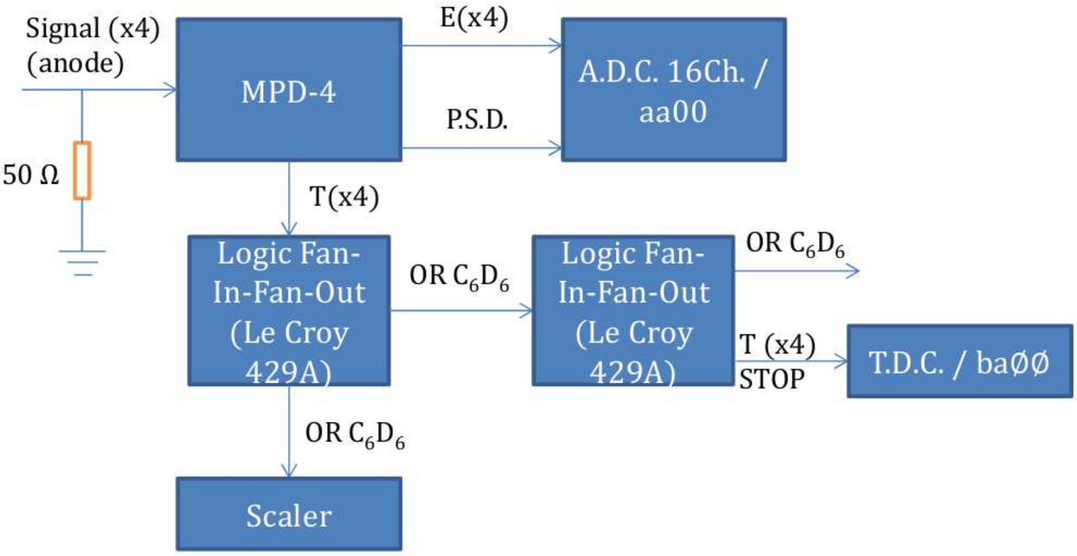

Figure 3.16: Electronic chain of the C_6D_6 detectors.

3.3.3 Germanium Detectors

As mentioned before the germanium detectors had two outputs that were previously pre-amplified within the detector, as shown in figure 3.17. Both signals went into the same Mesytec (MSCF-16) module, and each of them was set to a different gain, low gain (LG) and high gain (HG). This was possible because this module can take up to 16 input signals and allows to change the gain by groups of four channels. The OR of the logic signals of each HG/LG went into a Logic FIFO to duplicate it, this way one OR could be used as trigger for the calibration runs and the other one was sent to the scaler. The output energy signals (E_{HG}/E_{LG}) went to an ADC module to be recorded. Conversely, the time difference of the fired germanium detector with the telescope that trigger the acquisition (T_{HG}/T_{LG}) was recorded by a TDC module.

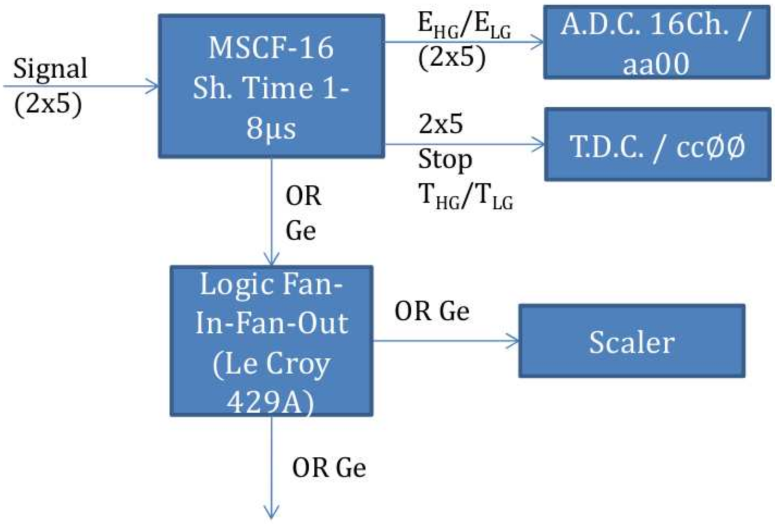

Figure 3.17: Electronic chain of the Ge detectors.

3.3.4 Solar Cells

Each solar cell has a current preamplifier, which is inside the reaction chamber and really near to the cells. The output signals of these preamplifiers go to a Mesytec module (MSCF-16) that processes the signals and gives as outputs the energy, stored in the ADC, and the time, whose time difference with the telescope coincidence that triggered the acquisition is recorded in the TDC. The logic signal OR is duplicated in a FIFO module so that it can be used as a trigger for a scaler module, see figure 3.18.

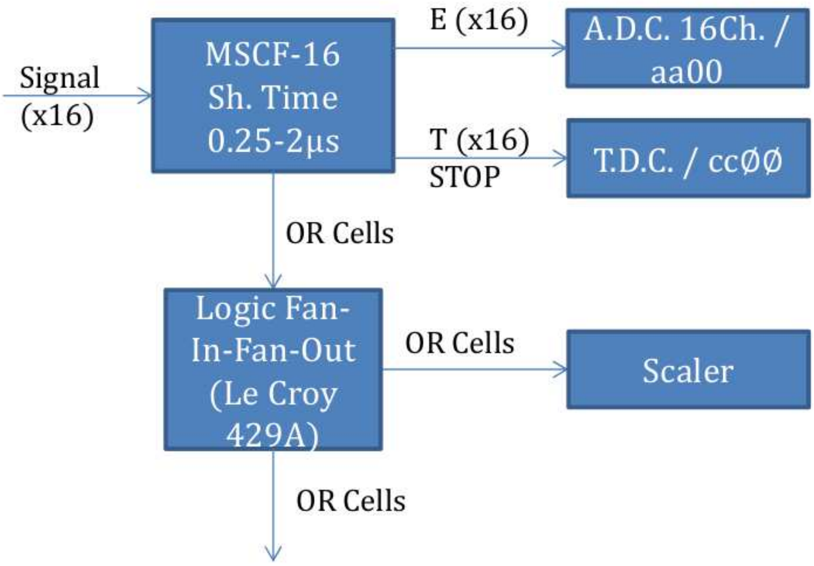

Figure 3.18: Electronic chain of the solar cells.

Chapter 4

Data Analysis

In the previous chapter a thorough description of the experiment, set-up and procedure, performed at the Tandem accelerator of the IPN of Orsay was done. The analysis of the obtained data was performed with series of C++ scripts including: data reduction, calibration, event selection, geometry simulation... These scripts made use of some of the program libraries of ROOT, a tool developed by CERN in C++ for data analysis. As mentioned in chapter 3, the experiment was designed to study the following reactions: $^{240}Pu(^{4}He,^{4}He')$, $^{240}Pu(^{3}He,^{3}He')$ and $^{240}Pu(^{3}He,^{4}He)$.

To explain the steps followed to obtain the final results we recall equation (1.1):

$$P_{\chi}(E^*) = \frac{N_{\chi}(E^*)}{N_s(E^*) \cdot \varepsilon_{\chi}(E^*)}$$

The aim is therefore to know all the quantities on the right-hand side of the above equation to deduce the probability:

I $N_s(E^*)$ is the so-called "singles spectrum", i.e. the number of detected ejectiles with the telescopes, as a function of excitation energy of the recoil nucleus. It is determined by selecting the reaction channel with the uncalibrated data. Then the telescopes are calibrated and one can convert the deposited energy into excitation energy of the recoil nucleus. Finally, the contribution of the target contaminants to this number of events is removed to keep only the desired events from the studied Pu compound nucleus.

II $N_{\chi}(E^*)$ is the "coincidence spectrum", which corresponds to the number of ejectiles detected in coincidence with the observable that identifies the decay mode χ, fission or γ. In the case of γ-decay, $N_{\gamma}(E^*)$ has to be corrected for the number of γ-rays coming from the fission fragments. This requires to subtract the triple coincidence (ejectile-γ-fission-fragment) events $N_t(E^*)$, corrected by the fission efficiency. In addition, a γ-energy threshold is imposed, to eliminate the γ-rays emitted by the daughter nucleus after neutron emission. The coincidence spectra are obtained by setting an appropriate time window. The random coincidence spectra are determined, normalized and subtracted from each type of coincidence N_{χ} spectra.

III The detection efficiencies $\varepsilon_{\chi}(E^*)$, fission and gamma, are determined. The γ-ray cascade detection efficiency is deduced from the data with the EXEM method [1], and the fission event detection efficiency is simulated with a detailed knowledge of the geometry and includes anisotropy corrections.

IV Finally, an estimation of all the sources of uncertainty of this probability was done with the error propagation formula.

4.1 Data Reduction

Before starting all the steps above mentioned the data have to be preprocessed. In fact the data recorded by the acquisition are first converted into "trees", a data structure that greatly simplifies the analysis with ROOT's built-in functions and classes. During this process of data conversion, a lower limit of 200 channels and an upper one of 4000, were imposed to every variable to eliminate most of the undesirable events.

There was an unexpected drift of the energy amplitude measured by the $Si-Li$ detectors over time, see figure 4.1a. Although this is a common phenomenon, the magnitude of the drift was important and a possible explanation is the influence of the room temperature, that changed a lot between day and night, on the gain of the used preamplifiers or amplifiers. All the events of the measurements with the ^{208}Pb target were re-adjusted to a reference, and all the ^{240}Pu ones to those that were closer in time to the reactions with Pb. This was done to minimize the time lapse, and therefore the energy drift, between the runs of lead which were used to calibrate, and plutonium. All the bi-dimensional spectra that appear in this document, obtained with the telescopes, are plotted with this correction taken into account.

A further reduction of the data was done by eliminating all the events in which more than one of the telescopes was fired, i.e. they were above a threshold of energy 420 channels for the ΔE detector and 500 channels for the E detector. The purpose of this second reduction is to ensure that the decaying compound nucleus is uniquely identified and to remove part of the events coming from the electronic noise. The thresholds were chosen in such a way that the proportion of true events removed was minimized.

The spectra represented in figure 4.2 were cleansed using this routine to remove events in which more than one strip was fired. However, in the figure there are still events, out of the contours. The events in the region of the lower left-hand corner of figure 4.2a, come from the reaction channels in which a hydrogen isotope *p, d, t* is emitted, forming a compound nucleus of Am, which were not studied because the ΔE detector of the telescope was too thin to detect them properly. The signal from these events might pile-up giving events with a different energy as it can be better seen in figure 4.2b. These pile-up events cannot be removed with the cleaning routine described above. Still they are well separated from the events of interest, which are within the contours of figure 4.2.

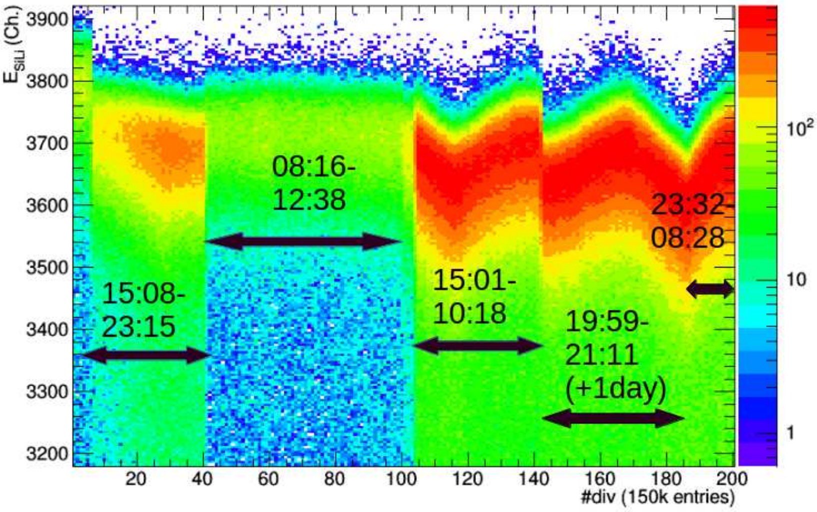

(a) Spectrum without correction and the start-stop times of the runs. The peaks usually coincide with the early morning $\sim$ 8 a.m. and the valleys with the beginning of the night $\sim$ 9 p.m.

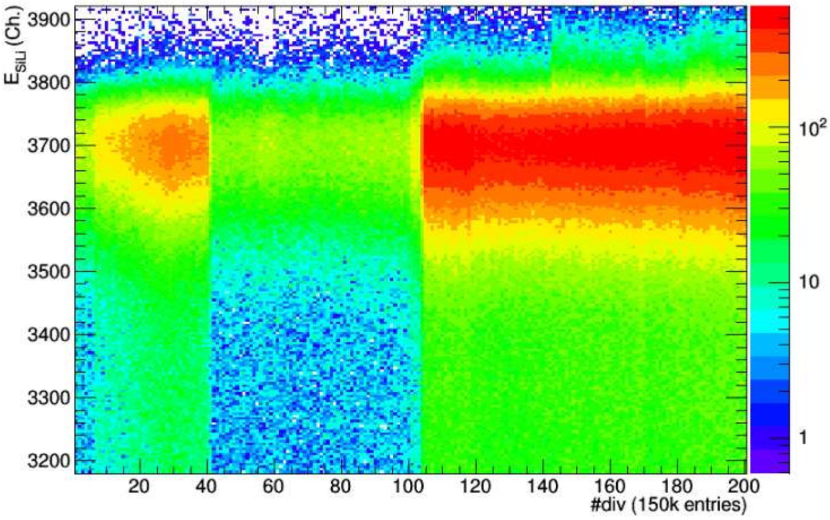

(b) Spectrum with a correction applied to each group of entries to adjust the gain of the detector to the group of events closer in time to the lead runs.

Figure 4.1: Energy response of the $SiLi$ detector number 2 in channels as a function of the event number of the ${}^{240}Pu({}^4He,{}^4He')$ reaction.

4.2 Reaction Channels Selection

To select the relevant events corresponding to each reaction to be studied, graphical cuts as the ones in figure 4.2 were done for each possible combination of target and beam. The reason why the events are selected with contours in the bi-dimensional spectra $\Delta E - E$, or identification plot, is that when a charged particle trespasses these detectors, there is a correlation between the energy deposited in each one of them. This correlation depends on the mass, the charge and the kinetic energy of the particle, and it leaves a trace with a characteristic hyperbolic shape similar to that of a "banana".

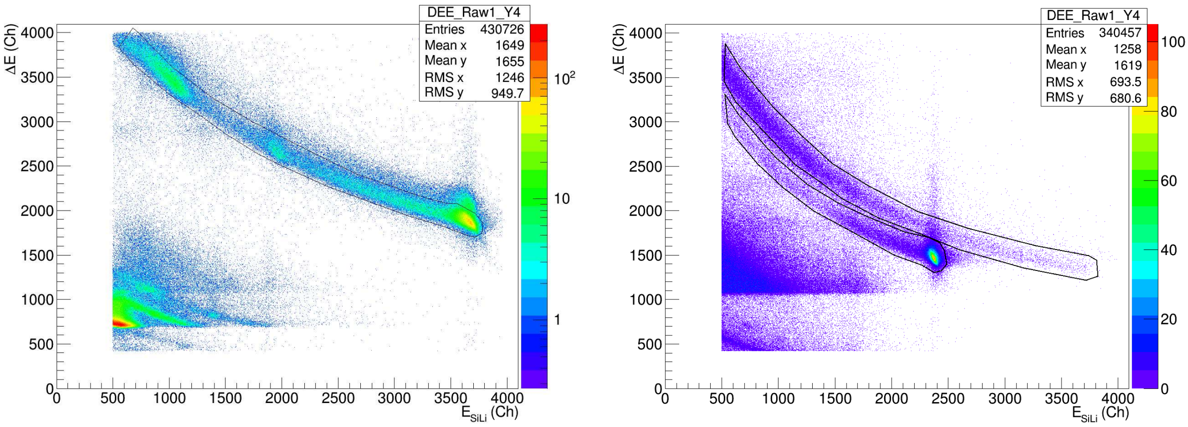

(a) Bi-dimensional spectrum from the reaction $^{4}He + ^{240}Pu$. The black line is the contour used to select the events from the reaction channel $^{240}Pu(^{4}He,^{4}He')$.

(b) Bi-dimensional spectrum from the reaction $^{3}He + ^{240}Pu$ at the same angle as 4.2a. Within the lower contour fall the events from the $^{240}Pu(^{3}He,^{3}He')$ reaction and within the upper one the events from the $^{240}Pu(^{3}He,^{4}He)$ one.

Figure 4.2: Energy loss in the ΔE versus the energy deposited in the E detector obtained with the telescope number 1 and strip number 4, $\theta_{ej} = 124.8^{o}$, plots of the reactions with the plutonium target. The solid lines are the contours to select the events of interest.

Notice that in figure 4.2a a small proportion of the events of the $^{240}Pu(^{4}He,^{4}He')$ are shifted towards higher ΔE energies. This effect appeared also in the reactions with the lead target. To identify the origin of these events we selected them with a contour to study them, see figure 4.3.

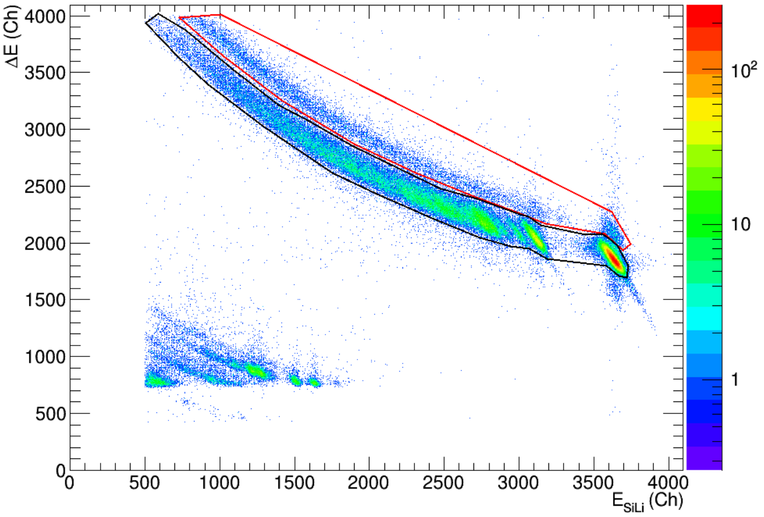

Figure 4.3: Bi-dimensional spectrum obtained with telescope number 1 for $^{4}He + ^{208}Pb$ at $\theta_{scat} \approx 154.8^{o}$. The trace within the lower contour (black) was left by the alpha particles scattered after the $^{208}Pb(^{4}He,^{4}He')^{208}Pb^{*}$ reaction. The events within the upper contour (red) are part of a noise of undetermined origin.

The events contained in the contours of figure 4.3 are represented in figure 4.4, in red the events within the upper contour and in blue the ones within the lower one. They are represented as a function of the energy deposited in the detectors, after the calibration was done, to see if some additional information could be obtained with the calibrated data.

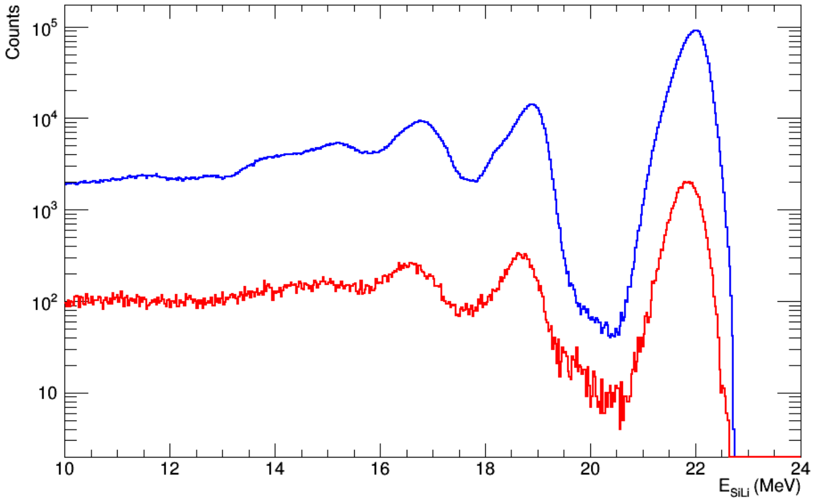

(a) Number of counts as a function of the energy deposited in the E-detector for the reaction $^{208}Pb(^4He,^4He')$.

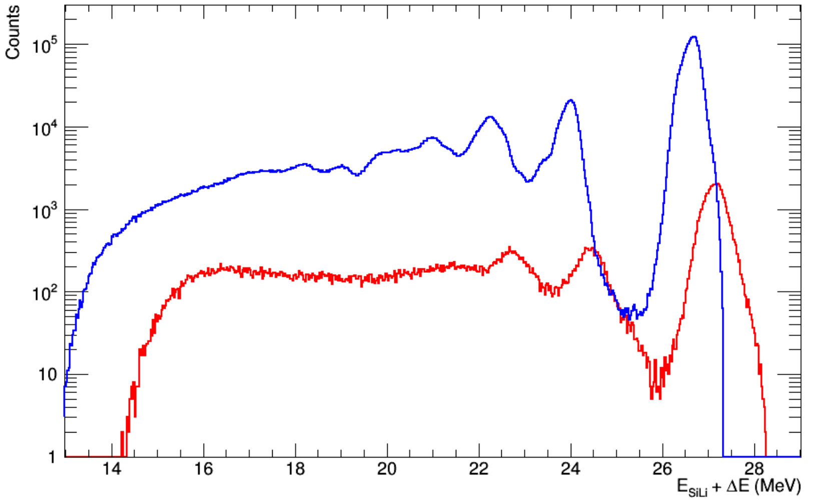

(b) Number of counts as a function of the energy deposited in the E-detector plus the energy deposited in the ΔE-detector for the reaction $^{208}Pb(^4He,^4He')$.

Figure 4.4: Number of counts as a function of the energy deposited in telescope 1. The blue spectra represent the events within the black contours of figure 4.3, the red spectra the events within the red contours of figure 4.3

As it can be deduced by comparing 4.4a and 4.4b, the energy deposited in the $SiLi$ detector is the same for the events contained in either contour. In contrast, when representing the number of events as a function of $E + \Delta E$, the red spectrum is shifted approximately $2MeV$ to higher energies. This excludes the possibility of a dead layer in the detector since in that case both E and ΔE should change. The explanation to this phenomenon is uncertain, and the only hypothesis is that every now and then the energy was wrongly coded by the ΔE-detector. In any case they just represent around 4% of the statistics and they were easily removed from the analysis with the graphical cuts.

4.3 Energy Calibration

Doing a proper energy calibration of all the detectors is of utmost importance for this kind of experiment. From it depend all the results that will be obtained and therefore the conclusions that may be deduced from them.

4.3.1 Telescopes: ΔE - E_{SiLi} Detectors

The reactions on a target of ^{208}Pb are frequently used to calibrate the telescopes. This lead isotope is a good reference because its first excited states, and those of ^{207}Pb, have well defined energies and are separated by wide energy gaps. There are two other reasons to use lead, one is that a wide range of energies may be covered, in both the ΔE and the E_{SiLi} detectors, but also that these energies are very similar to those of the true measurement if the beam energy is appropriately chosen. The reactions used and the corresponding states are listed in table 4.1.

Reaction	State (keV)
$^{208}Pb(^4He,^4He')^{208}Pb^*$	0.0
	2614.5
	3197.7
	3708.5

(a) Excitation energies of the first states of ^{208}Pb used as a reference to calibrate the telescopes with the ^4He beam.

Reaction	State (keV)
$^{208}Pb(^3He,^4He)^{207}Pb^*$	0.0
	1633.4
	2339.9
	3476.4
$^{208}Pb(^3He,^3He')^{208}Pb^*$	0.0
	2614.5
	3197.7

(b) Excitation energies of the first states of ^{207}Pb and ^{208}Pb used as a reference to calibrate the telescopes with the ^3He beam.

Table 4.1: Reactions and states used for the calibration of the telescopes.

The calibration of the telescopes was done separately for each of the two beams, ^3He and ^4He. This was so because the gain of the amplifiers associated to these detectors were changed from one type of beam to the other. In table 4.1 we may see the energy of the states that were used for each beam, sub-table 4.1a for ^4He and sub-table 4.1b for ^3He. The third excited state of $^{208}Pb^*$, $E = 3708.5keV$, formed with the $^{208}Pb(^3He,^3He')^{208}Pb^*$ reaction, was not used because the energy resolution prevented from correctly separating it from other states. For the same reason we did not use the first two excited states of $^{207}Pb^*$, which have energies of $569.7keV$ and $897.7keV$, respectively.

Once the correction of the energy drift of the $SiLi$ detectors above mentioned is taken into account, the first step to do the calibration is to obtain the identification plots of the lead target in channels, as coded by the acquisition system, see figure 4.5.

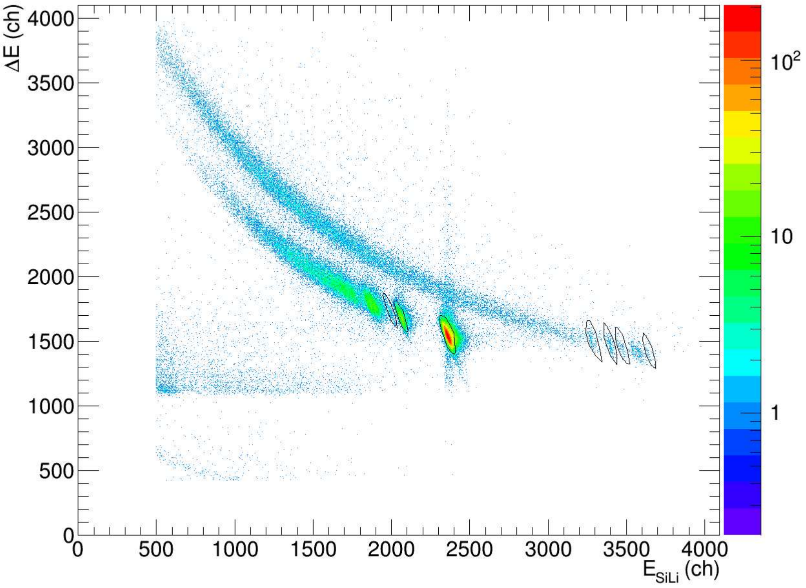

Figure 4.5: Example of identification plot obtained with the telescopes for $^{208}Pb + {}^{3}He$ at $\theta_{scat} \approx 154.8^o$. The upper trace was left by alpha particles scattered after the $^{208}Pb(^3He, {}^4He)^{207}Pb^*$ reaction, while the lower one corresponds to the scattered $^3He'$ from the $^{208}Pb(^3He, {}^3He')^{208}Pb^*$ reaction. The seven contours in black were used to select the events of the seven states (sub-table 4.1b) used for the calibration of the reactions with the ^3He beam.

The peaks used for the calibration were selected with contours as shown in figure 4.5. Apart from selecting these events, a calculation of their corresponding energy was done, taking into account the kinematics of the scattered particle and the energy losses in the detectors and the aluminum foils that protected them, see equations (3.7) and (3.8). These calculations were done using Kaliveda [25], within our simulation scripts. The coefficients obtained with the calibration lines for all the strips, see figure 4.6, are given in appendix B.

These same coefficients are then used to obtain the ejectiles' energy in the reactions with the ^{240}Pu. To transform the energy deposited by the scattered particles on these detectors into excitation energy of the recoil nucleus, we recall formula (3.9):

$$E^* = \frac{M_Y Q - E_{ca}(M_a - M_Y) - E_{cb}(M_Y + M_b) + 2cos\theta\sqrt{M_a M_b E_{ca} E_{cb}}}{M_Y}$$

It is then possible to represent the number of detected ejectiles as a function of excitation energy, see figures 4.7 and 4.8, which will often be referred to as the *singles spectrum*, *single events* or simply *singles*. The peaks used for the calibration, and the corresponding J^π of each state, are marked in these figures. It is worth mentioning that three of the peaks in the ^{207}Pb spectrum, figure 4.8b, were not included in the calibration. The two at low excitation energies, 570 and 898 keV, and the peak created by the pile-up of the elastic scattering of the ^3He beam. The excitation energy resolution obtained with our set-up corresponds to a root-mean-squared deviation (RMS) of the peaks associated to

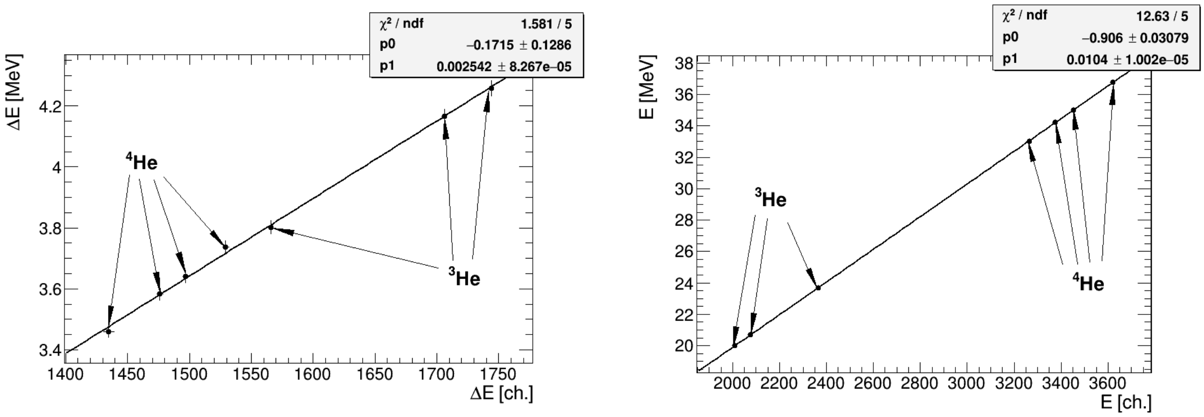

(a) Strip detector ΔE.

(b) Si-Li detector E.

Figure 4.6: Calibration lines of the ^3He beam with their parameters for strip no. 13, telescope no. 2.

the first states of the Pb isotopes and varies from $100keV$ for the ^4He beam, to $120keV$ for the ^3He beam.

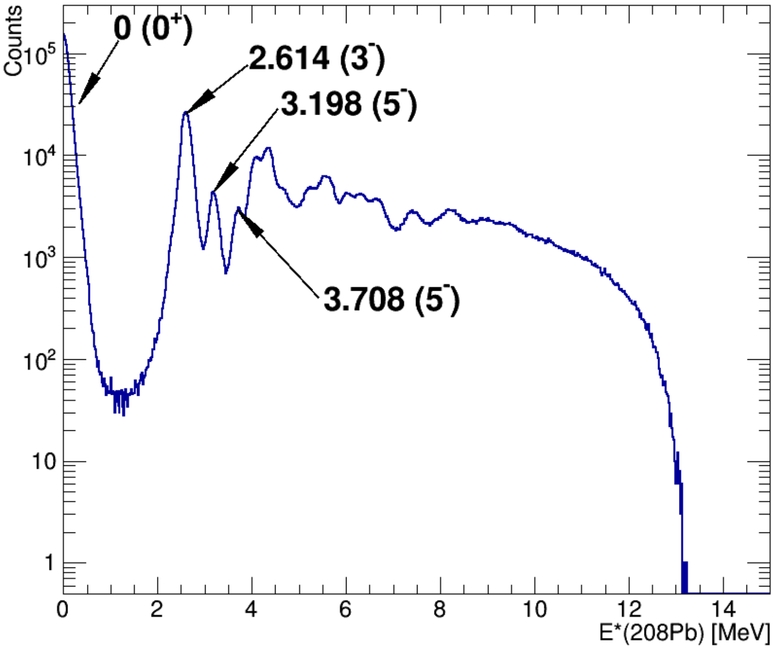

Figure 4.7: Number of detected alpha particles as a function of the excitation energy of the recoil nucleus $^{208}Pb^*$ formed with the reaction $^{208}Pb(^4He, ^4He')$ (singles spectrum) obtained with all the strips of telescope number 1.

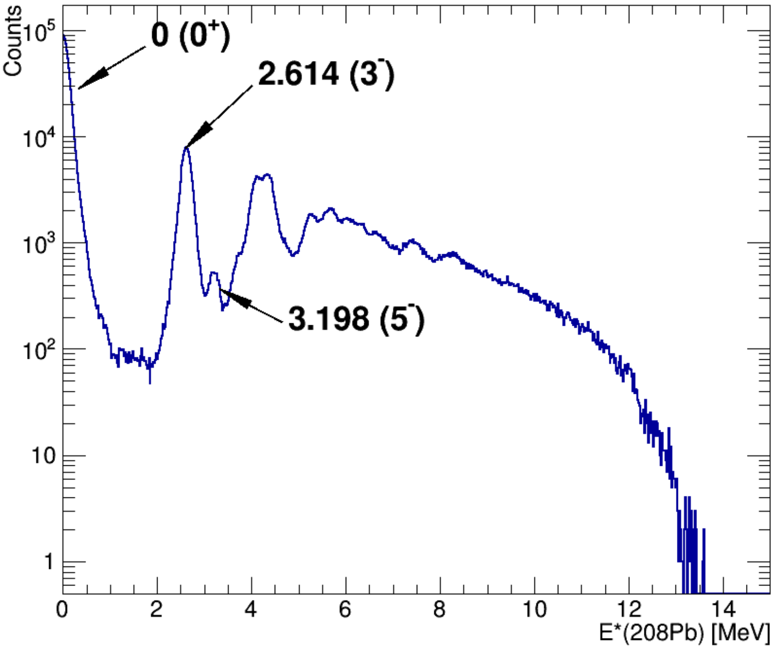

(a) Spectrum of the (^3He,$^3He'$) channel.

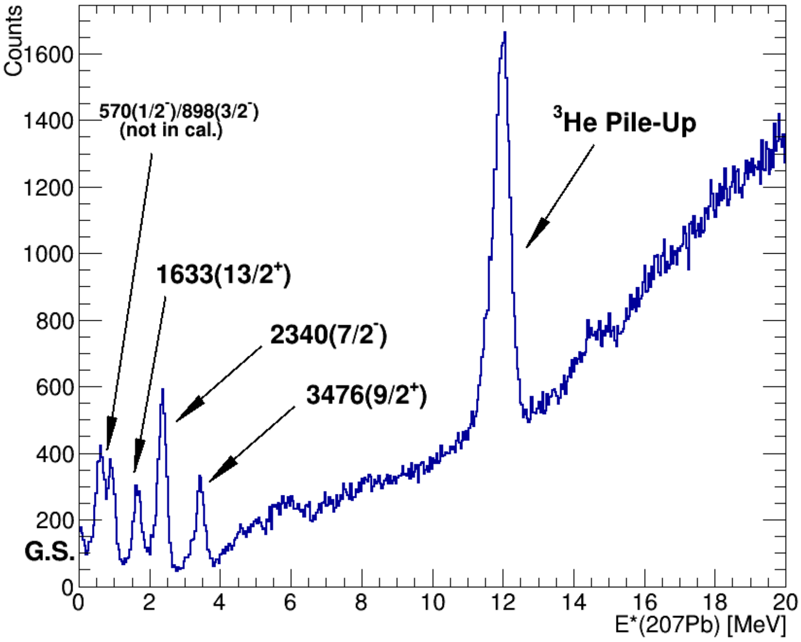

(b) Spectrum of the (^3He,^4He) channel.

Figure 4.8: The same as figure 4.7 but for a beam of ^3He impinging on the ^{208}Pb target.

4.3.2 Liquid Scintillators

The calibration of the liquid scintillators is crucial up to gamma energies of $\sim 2MeV$ because the gamma-emission decay of the $^{239}Pu^*$ and $^{240}Pu^*$ will be studied up to an excitation energy of $E^* = S_n + 1.5MeV \approx 8MeV$. Above the neutron binding energy the recoil nucleus has enough energy to emit a neutron and form a nucleus of $N-1$ neutrons which would be formed at a certain excitation level, and thus emit γ-rays to decay into its ground state. Therefore, one needs to be sure that γ-rays coming from the nucleus formed after neutron emission are removed from the analysis. This is done by setting thresholds in γ-energy to not include these events at $E^* > S_n$, thus the importance to correctly calibrate these detectors. To clearly define the position of the Compton edge (chapter 3), the use of mono-energetic gamma-sources, or with two peaks with clearly separated energies, is necessary (table 4.2).

Source	γ-Energy (keV)	Compton edge energy (keV)
^{22}Na	511	340.7
^{137}Cs	661	476.7
^{22}Na	1274	1061.2
^{232}Th	2608	2375.3

Table 4.2: Gamma sources used for the calibration of the scintillators, the energies of their characteristic γ-rays, and the energy of the Compton edge associated to these.

The criterion to choose the position of the Compton edge was to pick the position of the bin at 80% of the maximum. The reasons to proceed this way are thoroughly described in the thesis of G. Boutoux [8]. The main idea is that this percentage takes into account the resolution of the scintillators and thus gives better calibration parameters (appendix B).

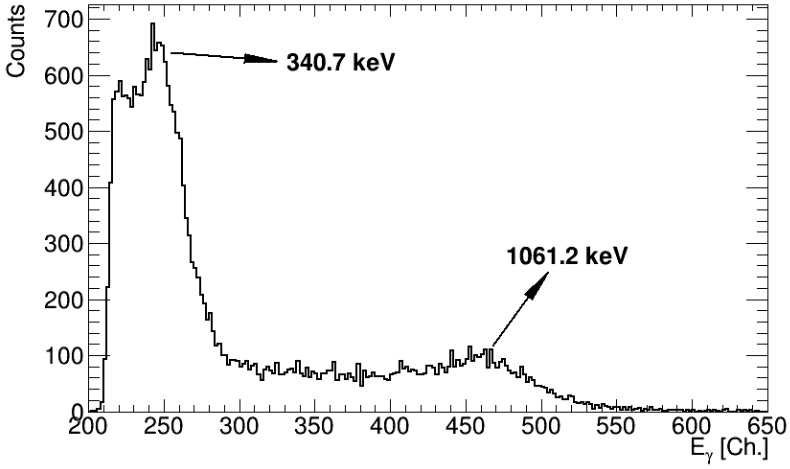

Figure 4.9: Spectrum of the ^{22}Na source obtained with the C_6D_6 detector number one. The arrows indicate the position and energy of the two Compton edges that can be resolved with this source.

Figure 4.9 represents the response function from one of the scintillators to a ^{22}Na source. The arrows indicate the position and energy of the two Compton edges obtained with this source that were used for the calibration of the liquid scintillators.

4.3.3 Germanium Detectors

An ^{152}Eu source was used to calibrate these detectors as it gives several well defined peaks covering an energy from about 100 keV to 1.4 MeV, thus within the energy range in which the γ-energy thresholds are placed. As explained in chapter 3 each germanium had two outputs, one of the signals was multiplied by a big amplification constant (high-gain), figure 4.10a, while the other one was amplified by a smaller constant (low-gain), figure 4.10b. When comparing these two figures it is evident that the energy scales are not the same, but the energy thresholds where set in both cases to 200 channels during the data reduction step. This is the reason why the two low energy peaks in figure 4.10a are cut in 4.10b. Therefore, different peaks were used for the calibration of each output. The calibration coefficients are given in appendix B.

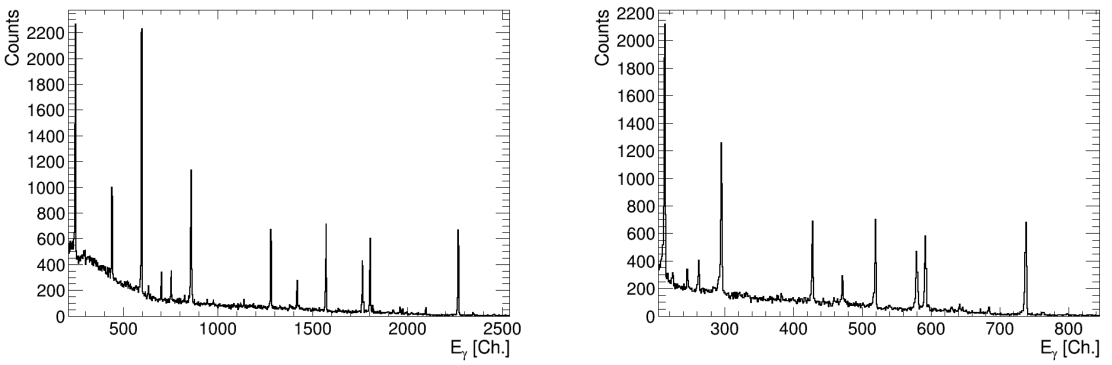

(a) Spectrum of the ^{152}Eu source obtained with the germanium (High-Gain) detector no. 2.

(b) Spectrum of the ^{152}Eu source obtained with the germanium (Low-Gain) detector no. 2.

Figure 4.10: Europium spectra obtained with Ge number 2

The energy resolution of the Ge detectors obtained with the spectra depicted in figure 4.10, are around 5 keV for the high-gain and 10 keV for the low gain. These were the approximate resolutions during the Europium runs, which lasted a few minutes. During longer runs, like the plutonium ones, the resolution was even worse due to the energy drift, around 30 keV. This forbade from using the Ge detectors to study selected transitions, as mentioned in chapter 3.

4.4 Singles Spectra

In the case of the PuO_2 target, the scattered particles after the reaction with a nucleus of ^{240}Pu, true events, have to be distinguished from the ones scattered after the reaction with the target contaminants. These true events $N_S(E^*)$ will be from now on referred to as *singles*. The spectrum drawn in figure 4.11 represents the number of alpha particles detected with the telescopes as a function of the E^* of $^{240}Pu^*$, equation (3.9). The events were selected with identification plots done for each strip, as described in section 4.2.

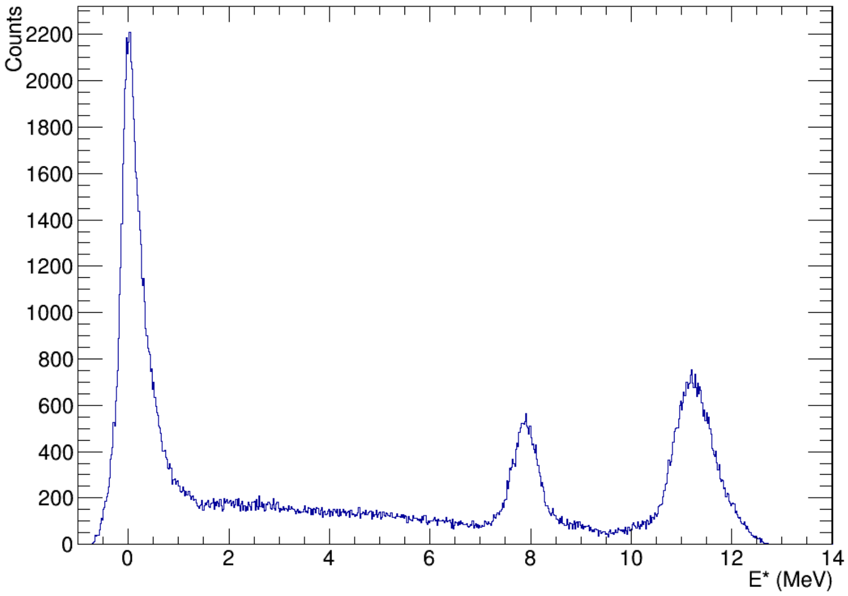

Figure 4.11: Number of alpha particles as a function of the excitation energy of $^{240}Pu^{*}$, from the reaction $^{240}Pu(^{4}He, ^{4}He')$ and scattering angle $\theta_{scat} \approx 154.8^{o}$.

In figure 4.11 three peaks can be clearly distinguished. The one centered at $E^{*} = 0MeV$ mainly corresponds to the elastic scattering of the α particles from the $^{240}Pu(^{4}He, ^{4}He)$ reaction, but also to the first excited states of $^{240}Pu^{*}$. The one in the middle $E^{*} \approx 8MeV$ corresponds to the ground states of the contaminants present in the target, which are supposed to mainly be ^{nat}S, ^{nat}Cl, ^{nat}K and ^{nat}Ca. The third peak $E^{*} \approx 11MeV$ corresponds to the first excited states of these contaminants and some other lighter elements. Had it not been for these contaminants, the number of detected $^{4}He'$ would have directly represented $N_{S}(E^{*})$.

4.4.1 Contaminants Fitting

$^{240}Pu(^{4}He, ^{4}He')$

To remove the contaminant peaks, different functions between the non-contaminated zones of the spectra were tried. These contaminant-free regions could be determined by comparing the spectra of the target and the spectra of the carbon backing. Figure 4.12 illustrates several aspects of the contaminants present in the C backing:

i The peaks are approximately placed at the same energies when the alpha particles scattered by the target backing are represented as a function of the "E^{*} of ^{240}Pu*".

ii The position of the peaks in relation to the rest of the spectrum depends on the scattering angle. The reason is the smaller mass of the contaminant nuclei as compared to that of $^{240}Pu^{*}$, this makes them more sensitive to the angle of the scattered particles for kinematic considerations.

iii There is an energy region, between the peak of the ground state of Ca/K and the excited states / lighter contaminants peak, in which the number of counts due to sulfur and chlorine amount to $\sim 5\%$ of the elastic peak's maximum.

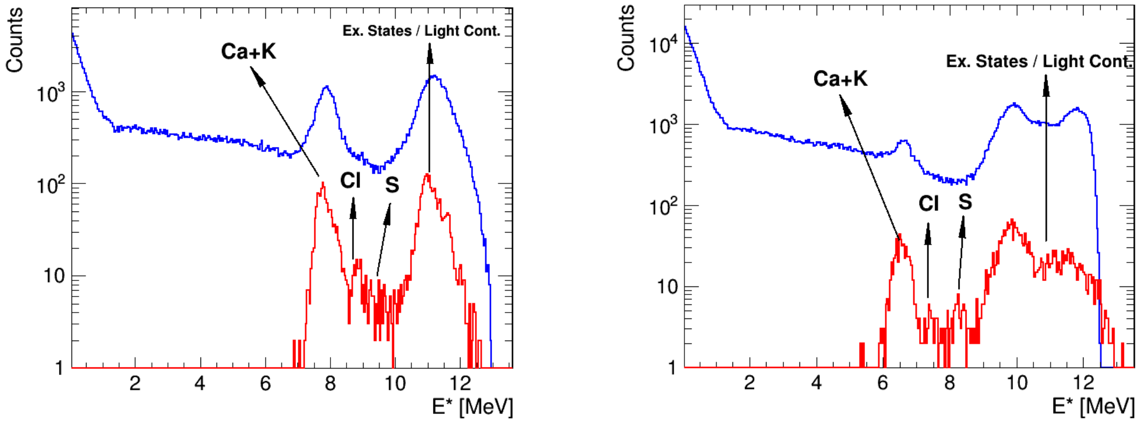

(a) Detected alpha particles at $\theta_{scat} \approx 154.8^o$ (b) Detected alpha particles at $\theta_{scat} \approx 124.8^o$

Figure 4.12: Blue spectra: number of alpha particles as a function of the excitation energy of $^{240}Pu^*$, from the reaction $^{240}Pu(^4He, ^4He')$. Red spectra: alpha particles of events as a function of the excitation energy of $^{240}Pu^*$ from the reactions with the carbon backing.

Having done the comparison of the spectra obtained with the plutonium target and the carbon backing, the next step is to remove the contaminants from the plutonium spectra. The first attempt was to subtract the renormalized carbon backing spectra to the plutonium ones. Although for some of the angles this subtraction was satisfactory, for others it did not work. This was expected because, even if the process to obtain the carbon backing foils was the same in both cases, with or without PuO_2 deposition, nothing guarantees that the proportion of contaminants is the same in both carbon layers. On top of that, the layer of PuO_2 modifies the shape of the contaminant peaks.

For these reasons, the contaminants were removed using linear functions, done strip by strip, based on two assumptions. First, that the shape of the singles spectrum in the energy region of the contaminants is linear, similarly to the region of lower excitation energies, which is free from contaminants. Second, that the region between the calcium peak and the peak of the excited states is almost free from contaminants, except for some counts coming from Cl and S. Therefore, the probabilities given will go up to $E^*(^{240}Pu) \leq$ 8 MeV, because for the smallest angles, where the contaminant peaks start at lower energies, the valley between the big contaminant peaks is at 8 MeV. The procedure to do a linear interpolation between the low energy region before the contaminants and the valley, fig. 4.12a, was the following:

i The proportion between the number of counts within the Ca/K peak and the valley, S/Cl, was calculated to be between 5-10%, figure 4.12.

ii Two points were chosen to define the interpolation, "fit start" and "fit stop" in figure 4.13

iii The number of events in the valley after the subtraction of the background, gives the point through which the linear interpolation should pass, black spectrum in figure 4.13.

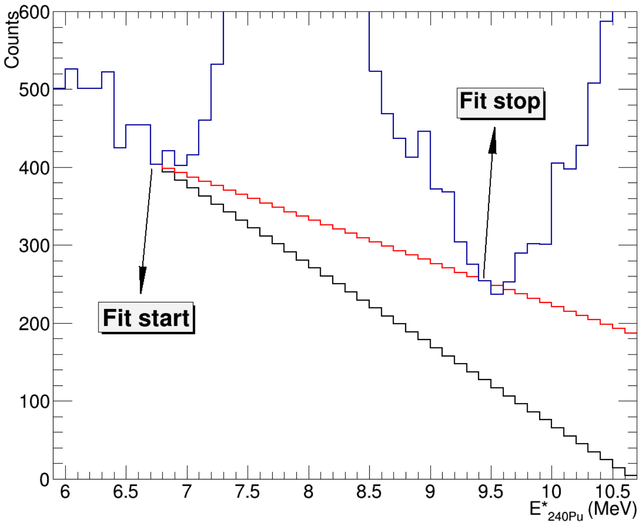

Figure 4.13: Number of events as a function of the excitation energy of $^{240}Pu^{*}$, around the first contaminant peak, from the reaction $^{240}Pu(^{4}He,^{4}He')$ and scattering angle $\theta_{scat} \approx 154.8^{o}$. The blue spectrum represents the detected events, the red spectrum is a linear fit between the two signaled points, the black spectrum is a linear fit between the starting point and the stopping point passing through the 50% of the counts in that energy bin.

Figure 4.13 illustrates the difference between the measured spectrum (blue), a linear (red) fit supposing that there are no contaminants between the two contaminant peaks in figure 4.12, and a linear function (black) taking into account the proportion of events in the valley including the resolution. For this angle, the fit passed through the 50% of the number of counts in the bin at $E^{*}(^{240}Pu) = 9.4MeV$.

This proportion of peak to valley events was calculated for each strip. It was slightly re-adjusted to take into account the worsening of the resolution due to the PuO_2 layer. For this reason, an effective coefficient was used to obtain the interpolations, which varied between 0.6 to 0.9 depending on the strip. The upper energy limit of the measured singles spectra ($\sim$ 13 MeV) is defined by the detection limit of the telescopes, as a higher excitation energy means a lower ejectile's energy, and at some point scattered particles cannot trespass the ΔE detector and the event is not recorded.

$^{240}Pu(^{3}He,^{3}He')$

In the case of the $^{240}Pu(^{3}He,^{3}He')$ reaction, the contaminants could not be removed. The reason is that the scattered particles are nuclei of ^{3}He instead of ^{4}He, which are lighter. Thus, the ^{3}He particles lose in proportion less kinetic energy after colliding with a light nucleus than with a heavy one, than in the case of ^{4}He. Therefore the contaminant peaks are shifted to lower excitation energies and are more spread out after interacting with the different isotopes of ^{nat}Ca, ^{nat}K, ^{nat}Cl and ^{nat}S.

The differences between the spectra obtained with the ^{3}He and the ^{4}He beams are clear when comparing figures 4.14a and 4.14b. In these figures the spectra are represented using all the strips because in the case of the ^{3}He beam, the statistics was not enough to represent individual strips. The reasons of this poor statistics are firstly, that the intensity of the ^{3}He beam was lower than the one oh the ^{4}He beam, and secondly that the Tandem accelerator broke down two days before the end of the beam-time. All in all, the reactions for the case of the $(^{3}He, ^{3}He')$ reaction lead to a widespread background which could not be removed. For this reason the data of the $^{240}Pu(^{3}He, ^{3}He')$ reaction were not exploited.

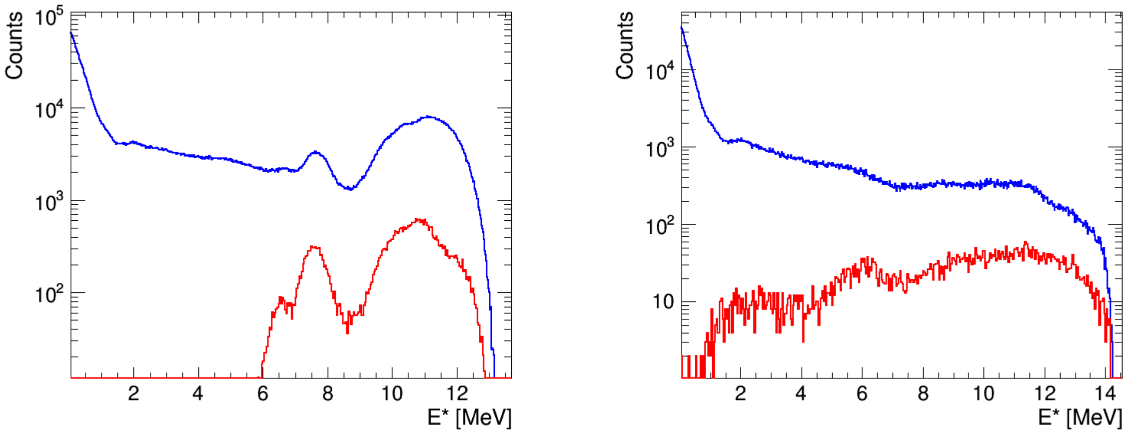

(a) Spectra obtained with the ^{4}He beam. (b) Spectra obtained with the ^{3}He beam.

Figure 4.14: In blue, number of scattered beam particles after the interaction with the ^{240}Pu target. In red, number of scattered beam particles after the interaction with carbon backing, both as a function of the excitation energy of ^{240}Pu. The represented spectra were obtained adding the statistics from all the strips of telescope no. 2.

$^{240}Pu(^{3}He, ^{4}He)$

In this last case, the contaminants are not an issue up to an excitation energy of $14MeV$, as seen in figure 4.15.

However, when looking into figure 4.15, there is a peak around $13MeV$ excitation energy, that is not in the contaminant spectrum. Indeed it is not produced by the contaminants, but rather by some of the events of the elastic scattering peak of the $^{240}Pu(^{3}He, ^{3}He)$ reaction that pile-up. These events fall into the ^{4}He contour as seen in figure 4.2b and therefore the data for this reaction will be given up to $E^{*}(^{239}Pu) = 10.5MeV$, where this peak starts. We did not do an interpolation of the singles spectra as in the case of the ^{4}He beam because the error associated to it would be too high and make the results meaningless.

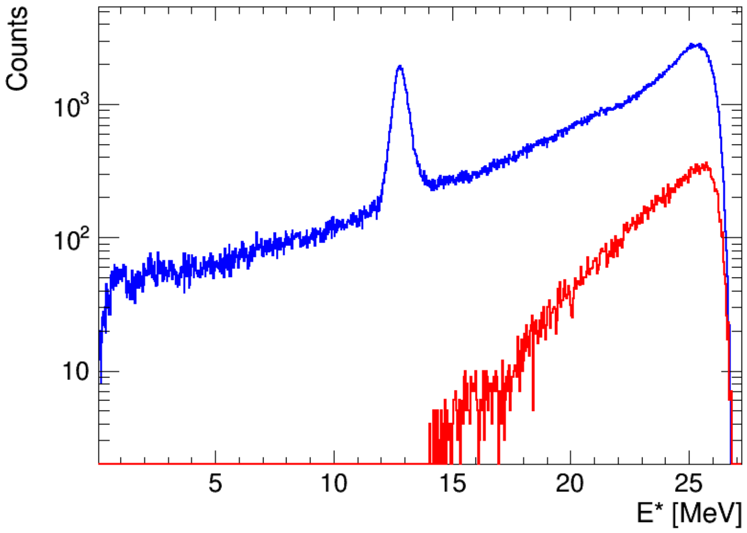

Figure 4.15: In blue, number of scattered beam particles after the interaction with the ^{240}Pu target. The peak in the spectrum is caused by the pile-up of the inelastic scattering of the ^3He, some of these events fall within the contour of the ^4He trace in the identification plots, see figure 4.2b. In red, number of scattered beam particles after the interaction with the carbon backing, both as a function of excitation energy, with all the statistics of telescope number 2.

4.5 Coincidence Spectra

In this section we will distinguish between three different types of coincidence spectra, *gamma coincidences*, *fission coincidences* and *triple coincidences*, and explain how they were obtained.

4.5.1 Fission Coincidences

To study the fission probability of $^{239}Pu^*$ and $^{240}Pu^*$ it is necessary to obtain histograms of the number of events detected with the telescopes, in coincidence with an event detected with the solar cells. These events are only considered once, when one of the cells is touched, and not twice, as at least two fragments are emitted during a fission event.

The first step to do this is to represent the time difference between the cells and the telescopes (figure 4.16). With it, we can determine the time limits between which the fission coincidences fall in, vertical black lines in fig. 4.16. In addition to these time windows, an energy threshold was imposed on certain cells at forward angles to remove from the analysis the signals produced by the scattered beam. The blue vertical lines represent the limits to fill the random coincidence histograms that will then be subtracted from the coincidence spectra. These histograms are first re-normalized multiplying their integral by the ratio $(T^{coin.}_{sup} - T^{coin.}_{inf})/(T^{bkgd.}_{sup} - T^{bkgd.}_{inf})$, where:

- $T^{coin.}_{inf}$ is the lower limit of the coincidence time window.
- $T^{coin.}_{sup}$ is the upper limit of the coincidence time window.

- $T_{inf}^{bkgd.}$ is the lower limit of the random coincidence time interval.
- $T_{sup}^{bkgd.}$ is the upper limit of the random coincidence time interval.

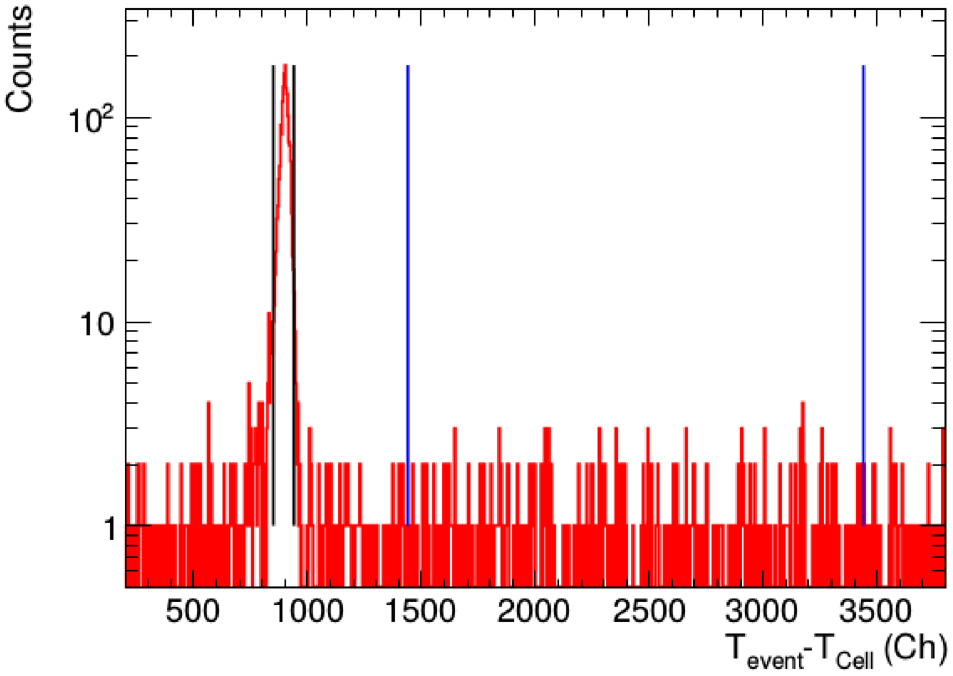

Figure 4.16: Number of counts as a function of the time difference between telescope 1 and cell 15. The black vertical lines delimit the coincidence window and the blue ones the random coincidence ones.

In the case of fission the coincidence windows range between $30 - 65ns$ depending on each cell, and the time window of the random coincidences spans $600ns$. Once the renormalization of the background histograms is done, the renormalized random-coincidences histograms are subtracted from the coincidence ones. The resulting histograms have the true number of coincidence events.

In figure 4.17 we may see the scattered particle spectrum, the raw fission coincidence spectrum, the random coincidence spectrum of the cells and the coincidence spectrum after the random coincidences subtraction. It is worth noting that the background spectrum has the same shape as the singles spectrum, this is logical as the random events are decorrelated in time with the true events, thus they are merely proportional to the singles. When subtracting the fission random coincidence spectra to the fission coincidences spectra, the peak at $E^* = 0$ MeV, corresponding to the random coincidence elastic scattering of alpha particles, is almost completely suppressed. This indicates that the subtraction was correctly done. From figure 4.17 it is also important to realize that even after subtracting the random coincidences, the fission coincidence spectrum (black solid line) has counts under $4.5MeV$, which is the theoretical fission energy threshold. This is something which was just observed for the $^{240}Pu(^4He, ^4He')$ reaction. Under $E^*(^{240}Pu) < 4.5MeV$ the probability for the compound nucleus to decay by fissioning should be much smaller than what was measured.

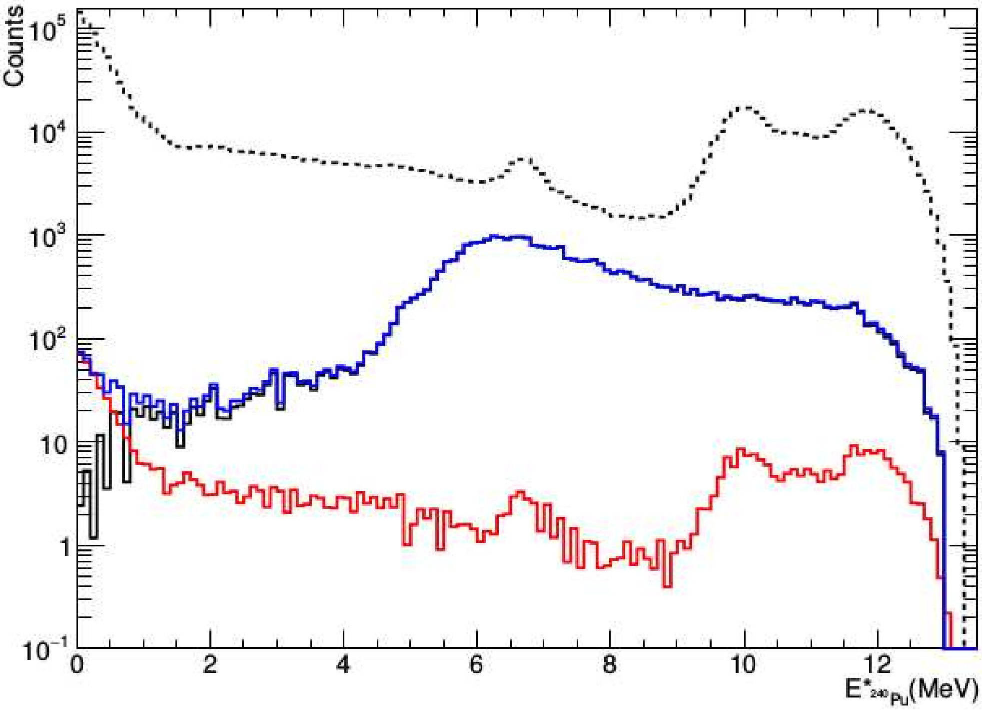

Figure 4.17: Number of events as a function of the excitation energy of $^{240}Pu^*$, for the reaction $^{240}Pu(^4He,^4He')$ and a scattering angle $\theta_{scat} \approx 126.3^o$. The dotted line represents the singles spectrum without the subtraction of the contaminant peaks, the blue line the fission coincidences, the red line the normalized random coincidences and the black solid line the fission coincidences after the subtraction of the random coincidences spectrum.

Fission Coincidence Events below the Fission Threshold

The only hypothesis we had to explain this phenomenon, is that these events are part of a background induced by the ternary fission of ^{244}Cm. This nucleus can be formed by the fusion of an alpha particle of the beam with a nucleus of ^{240}Pu of the target, which has a cross section $\sim 850\ mb$. If this happens, the $^{244}Cm^*$ is very likely to undergo fission because it is formed with an excitation energy of $24MeV$. In approximately 1 in 300 fission events, the curium nucleus will undergo a ternary fission in which an alpha particle is formed [74]. This alpha particle may then be detected by our telescopes and thus cause the sub-threshold events in our fission coincidence spectra.

As measured by Wagemans *et al.* [74], at excitation energies $S_n(^{244}Cm^*) \approx 6.8$ MeV, approximately every one in 316 fissions emits an alpha particle with a kinetic energy that follows a Gaussian distribution centered at $16.14 \pm 0.06MeV$ and $\sigma = 4.39 \pm 0.05MeV$. However at $E^*(^{244}Cm) = 0$ MeV these parameters of the Gaussian distribution become $15.99 \pm 0.08MeV$ and $\sigma = 4.24 \pm 0.11MeV$, respectively. Thus, the average energy of the alpha particles gently increases with excitation energy. Doing a linear extrapolation to $E^* = 24MeV$ results in an average kinetic energy of $16.52 \pm 0.10MeV$, which converted into excitation energy of $^{240}Pu^*$, is equivalent to $E^* \in (11.3, 11.8)MeV$ depending on the polar angle. Similarly the standard deviation can be extrapolated to $E^* = 24MeV$ resulting in $\sigma = 4.77 \pm 0.21MeV$. This value was further increased to $\sigma = 5.1MeV$ to account for the energy resolution of the telescopes and the losses in the target.

Figure 4.18 illustrates the effect of the subtraction of the presumed ternary fission spectrum on the fission coincidence spectra. When comparing the spectra in figures 4.18a and 4.18b, one may see that the counts between 0 and 4MeV excitation energy were eliminated after the subtraction of the supposed Gaussian ternary background. It is worth noting that in figure 4.18a at $E^* \approx 12$ MeV the supposed ternary background becomes higher than the actual fission coincidences. The reason is that at some point alpha particles have not got enough energy to trespass the detectors, but this was not taken into account when doing the subtraction because, as said before, we will only consider the results with $E^* \leq 8$ MeV. The background Gaussian distribution was obtained with slightly modified parameters, as described above, to those of [74], and then renormalized to fit the observed spectrum at low excitation energy.

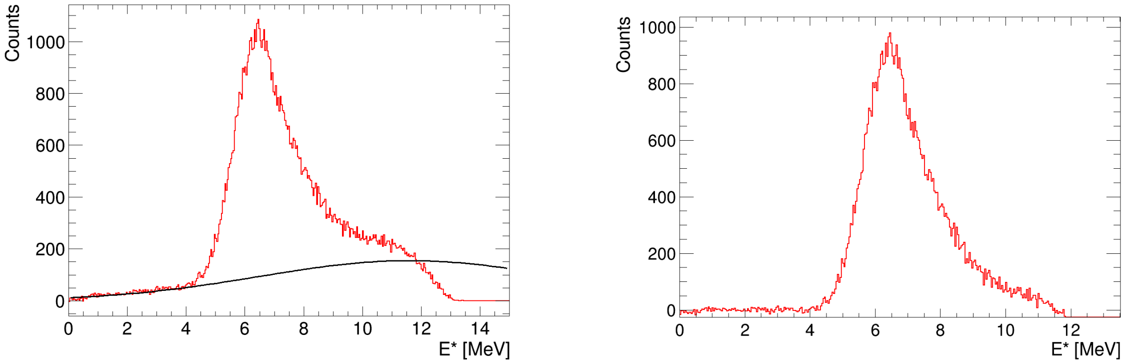

(a) Fission events obtained in coincidence with telescope no. 1 (red) and a Gaussian distribution that represents the ternary fission background (black).

(b) Fission events obtained in coincidence with telescope no. 1 after the subtraction of the assumed ternary fission background.

Figure 4.18: Fission coincidence spectrum before (left) and after (right) ternary fission background subtraction.

In addition to subtracting this background to the fission coincidences, it should also be subtracted from the singles spectra as these are not true events. To subtract them, the ternary background events were rescaled dividing them by the fission detection efficiency, for each excitation energy bin. In principle the detection efficiency of the ternary fissions could be different from the one of the normal fission events, because in the first case the ternary alpha particle is emitted in a direction forming approximately 92^o with the fission fragments. This value can slightly fluctuate depending on the masses of the fission fragments and the energies of these and the alpha particle. This angular correlation implies that only some specific combinations of strip-solar-cell can be fired simultaneously, thus affecting the detection efficiency of these events. However, when simulated, the fission detection efficiency of a normal fission event and a ternary fission are similar.

As this hypothesis to explain the fission coincidence events under the fission threshold cannot be confirmed with certainty, the final results for the fission probabilities will be presented with the ternary fission background subtraction and without it in section 4.9. In the case of the $^{240}Pu(^3He,^4He)$ this hypothetical background is not a problem because the $Q_{reac.} \approx 14$ MeV.

4.5.2 Gamma Coincidences

As mentioned before, the γ-decay probability P_γ measures the probability that the nucleus Y^* decays exclusively through a γ-ray cascade. Above the neutron separation energy, this probability rapidly decreases with excitation energy E^* because of the competition with the neutron emission channel. Therefore the P_γ is typically measured up to $E^* \approx S_n + 1MeV$. The used gamma detector array has a small solid angle and generally only one of the γ-rays of the cascade is detected. In a small proportion of the cases more than one γ-ray of the same cascade is detected, a random γ-ray is selected among all the events to fill the coincidence and γ-ray spectra. This way the number of coincidences corresponds to the number of detected γ-ray cascades.

The procedure to obtain the γ-decay coincidences has similitudes and differences to the one used for fission. In this case, not only gamma-coincidence and random coincidences histograms have to be obtained, but also, in the case of C_6D_6 detectors, an additional condition has to be set to ensure that the signal was generated by a γ-ray and not a neutron. A gamma decay event is therefore associated to a detected γ-ray coming from the compound nucleus formed in studied the reaction and will only be counted once. Finally, to subtract the γ-rays emitted after neutron emission, a threshold is imposed on the detected γ energy E_γ.

Liquid Scintillators

The first step to obtain the γ-coincidences is to remove the signals coming from the interaction of neutrons with the liquid scintillators. This can be done by virtue of the pulse shape discrimination (P.S.D.) technique, using a module that can differentiate between the shapes of the signals generated by gamma rays and neutrons, each signal has a different rise time. This module assigns a discrete value to the detected signal in the detector that depends on the fall time of the signal. By representing this value (PSD on the following) as a function of E_γ, a separation between the detected neutron events and the gamma events can be done. In figure 4.19, two distinct regions may be observed. The events within the black contour are the gamma events, and the ones above them are the neutrons.

Once the γ-rays have been selected as shown in figure 4.19, the next step is to fill the excitation energy spectrum with the events that are within the coincidence window in the spectra of the time difference between a telescope and a C6D6 detector.

Represented in figure 4.20 there is the number of detected γ-rays in scintillator number 1 as a function of the time difference with telescope 1. The black vertical lines represent the time limits that were chosen for this C_6D_6 to consider a coincidence, $\approx 20ns$. The blue vertical lines represent the limits to fill the random coincidence histograms. An analogous procedure to that of subsection 4.5.1 was followed to remove the random coincidences from the raw gamma-telescope coincidence spectra.

Gamma-ray Energy Thresholds

For an excitation energy E^* of nucleus (Z, N), the γ-rays emitted after neutron emission, i.e. the ones emitted by the nucleus $(Z, N-1)$, have a maximum energy $E^* - S_n$. Therefore, to remove these γ-rays, we fill the γ-coincidence spectrum imposing that E_γ is above an energy threshold E_{th} such that $E_\gamma > E_{th} = E^* - S_n$ MeV.

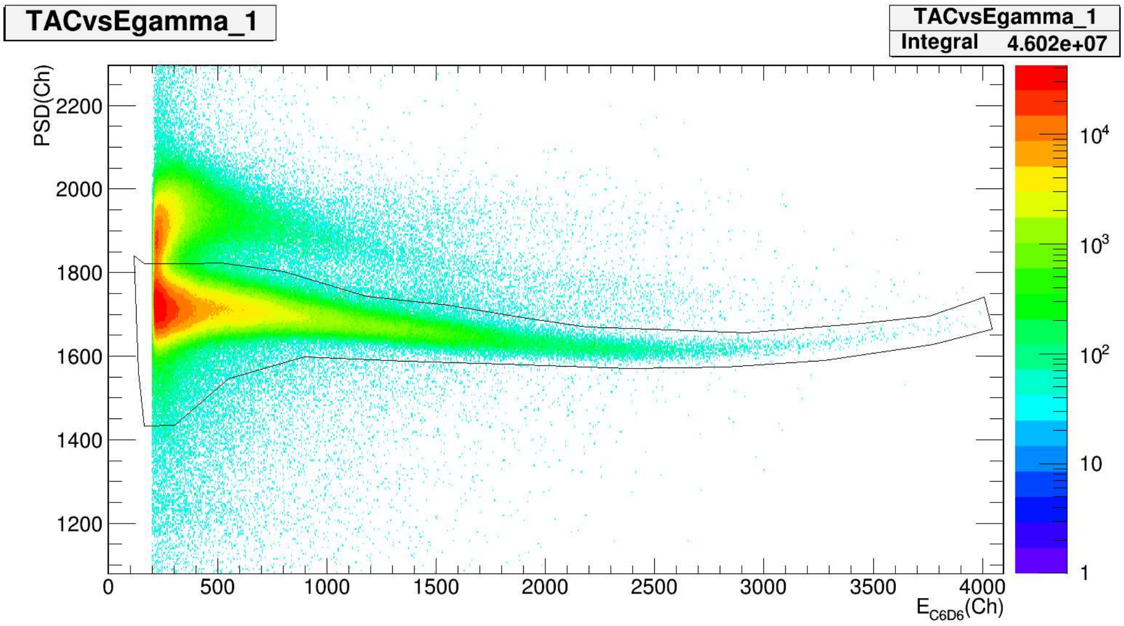

Figure 4.19: Value given by the PSD module vs E_γ from C_6D_6 no. 1, and the contour to select gamma events.

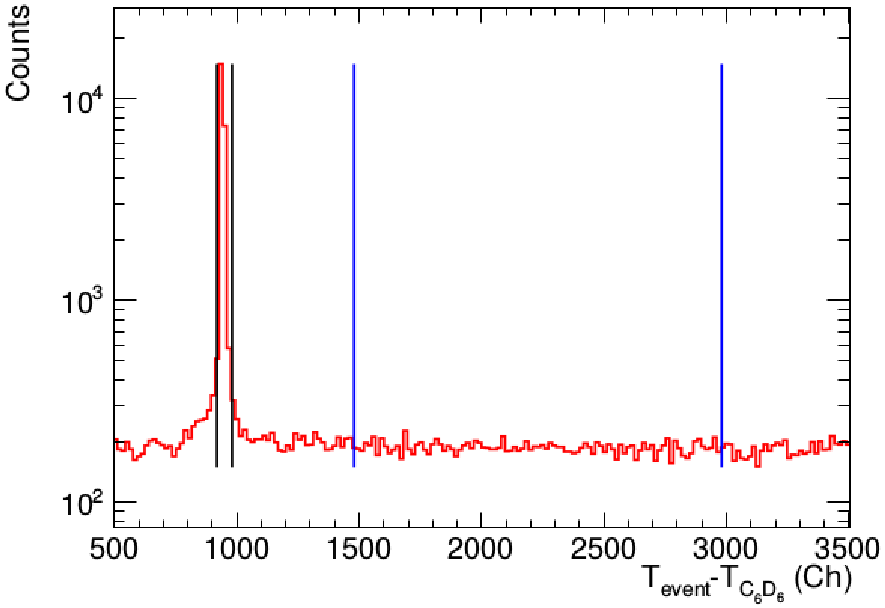

Figure 4.20: Number of counts as a function of the time difference between telescope number 1 and scintillator number 1 in channels. The black vertical lines delimit the coincidence window and the blue ones the random coincidence ones.

As seen in table 4.3, the values change from one compound nucleus to the other. This is because the limits were chosen to have access to excitation energies $E^* = S_n + E_{th}$ that were multiples of $200keV$, as that is bin energy width for the gamma-decay probability. In addition, by changing the threshold for each energy bin more statistics is included as less gamma rays are discarded.

For each threshold we will evaluate the γ-cascade detection efficiency (see section

Reaction	Threshold Energies keV						
$^{240}Pu(^4He,^4He')$	266	466	666	866	1066	1266	1466
$^{240}Pu(^3He,^4He)$	254	554	854	1354	1854	2354	2854

Table 4.3: Thresholds in gamma energy for the studied plutonium reactions.

4.6.2). The γ decay probability will be evaluated for each E^* energy bin by determining the ratio of the coincidences obtained with the corresponding threshold over the singles events and correcting for the associated efficiency.

Ge Detectors

As said before, even though the gain changed over time and the resolution of 20 keV of the best Ge detector in figure 3.10 made impossible to do a spectroscopic analysis of the Plutonium, this resolution was enough to use the germaniums as γ-ray counters. The thresholds in table 4.3 can also be applied to the analysis including germanium detectors to eliminate gammas after neutron emission.

In principle, the germanium detectors can only be used to obtain the gamma decay probabilities up to the neutron separation energy of the studied nuclei because the neutrons emitted can be captured by the Ge material leading to the emission of γ-rays that generate a signal. Unfortunately the PSD technique cannot be used with Ge detectors. In addition, the time resolution of these detectors and their distance to the target is too short to separate neutrons from gamma rays using a time of flight technique. Note that during a fission event of a ^{240}Pu nucleus, the average neutron multiplicity, for the energies relevant in this work, is $\overline{\nu} \approx 2.8$ per fission [75]. However, the neutrons emitted during the fission process are removed from the analysis when subtracting the triple coincidences, as explained in subsection 4.5.3.

When comparing the results of the γ-decay probability obtained with the liquid scintillators and the Ge detectors, there is no significant difference between both probabilities (section 4.9). This implies that neutron captures within the detectors' crystals are negligible within error bars. Therefore, we used the Germanium detectors in combination with the C_6D_6 to calculate the decay probabilities.

Figure 4.21 illustrates the measured gamma coincidence spectrum (blue) obtained with the statistics of all the strips of both telescopes and all the gamma detectors (C_6D_6 and Ge) with $E_\gamma^{th} = 266$ keV. In the same figure one may see the random coincidence gamma spectrum (red), and the black spectrum is the blue one after the subtraction of the random coincidences, which follows the shape of the singles spectrum. A careful look to the black spectrum reveals that the number of coincidences at $E^* = 0$ MeV is close to zero, although some counts remain due to the resolution of the telescopes. This indicates that the subtraction of the random coincidences is correctly done. As the energy increases the number of coincidences does so due to the higher multiplicity of the γ-decay cascades. At $E^* \sim 6$ MeV, before S_n, the number of counts starts decreasing due to the competition with fission, in spite of the fission-fragment γ-rays. The number of coincidences continues to decrease, speeding up for $E^* > S_n$, until $E^* \approx 9$ MeV. Indeed at this point the first excited states of the contaminants appear, see figure 4.12.

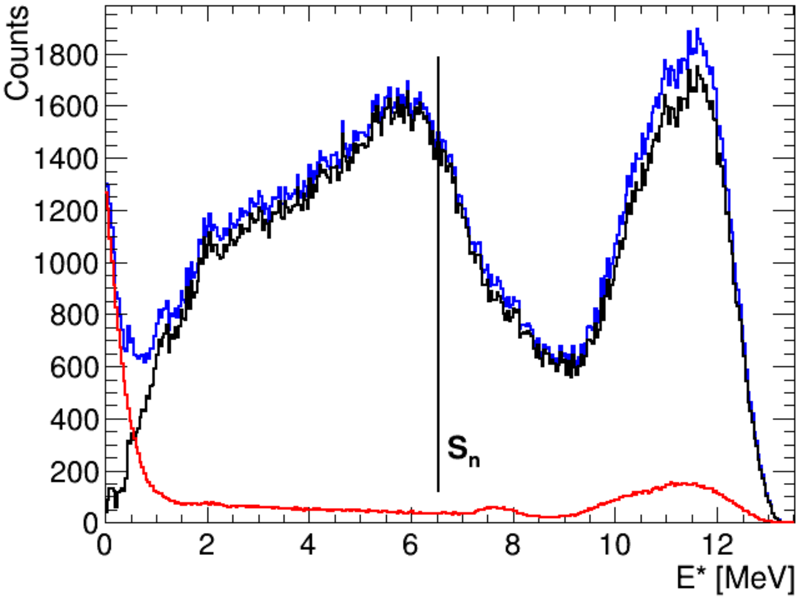

Figure 4.21: Events of the $^{240}Pu(^{4}He,^{4}He')$ reaction detected with telescope no. 1, including the statistics of all the strips, in coincidence with a cell and one of the gamma detectors, a scintillator or a germanium (blue spectrum). In red, the random coincidence spectrum. In black the gamma-coincidence spectrum after subtracting from it the random coincidences.

4.5.3 Triple Coincidences

A coincidence between a telescope, a gamma detector, and a fission detector will be called a triple coincidence. These events are representative of the gamma-rays emitted by fission fragments. To obtain the γ-rays emitted by the studied compound nucleus, it is necessary to subtract these events, re-normalized by the fission detection efficiency, eq. (4.1)

$$N_{\gamma}^{C}(E^{*}) = N_{\gamma}^{C,tot}(E^{*}) - \frac{N_{\gamma,f}^{C}}{\varepsilon_{f}} \tag{4.1}$$

where:

- N_{γ}^{C} is the final number of coincidences needed to evaluate the γ-emission probability according to equation (1.1).
- $N_{\gamma}^{C,tot}$ is the total number of measured γ-scattered particle coincidences after the application of the energy threshold E_{th}.
- $N_{\gamma,f}^{C}$ is the number of the triple fission-fragment-γ-scattered particle coincidences.
- ε_{f} is the fission detection efficiency.
- $N_{\gamma,f}^{C}/\varepsilon_{f}$ is the number of detected γ-rays emitted by the fission fragments.

More details on this correction can be found in [3], [10], [24]. Determining the triple coincidence spectrum $N_{\gamma,f}^{C}$ implies having sufficiently high detection efficiencies for all detectors, which is challenging and requires a very compact geometry. At the same time it is necessary to determine the fission detection efficiency with a good precision, in turn rather complicated due to the compactness of the detector.

The triple coincidence spectra are obtained by filling the histograms with the detected scattered particles in coincidence with the solar cells and the gamma detectors, see figures 4.16 and 4.20, respectively. The triple coincidence spectra have the same shape as the fission coincidence ones, figure 4.22.

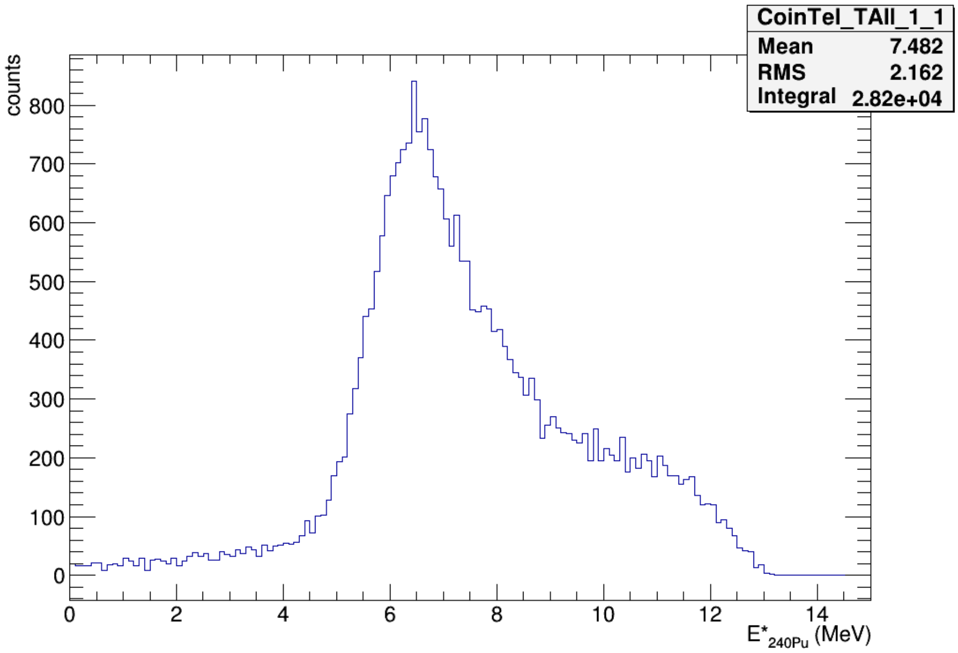

Figure 4.22: Events of the ${}^{240}Pu({}^{4}He, {}^{4}He')$ reaction detected with telescope no. 1, including the statistics of all the strips, in coincidence with a cell and one of the gamma detectors, a scintillator or a germanium. The triple random coincidences have been subtracted from the plotted spectrum as described below.

As with the other two types of coincidence spectra, random coincidences have to be subtracted from the triple coincidences. To better understand how to do the subtraction of the random coincidences, we will look into details of a spectrum representing the time difference between a telescope and a cell versus the time difference between the same telescope and a C_6D_6 detector (figure 4.23).

Very valuable information is obtained from figure 4.23. The red spot represents the true triple coincidences. Nevertheless, this peak includes also a background of random coincidences that we must evaluate. The rest of the events of fig. 4.23 correspond to four different kinds of random coincidences:

i A true gamma event in coincidence with a telescope and a random coincidence in the cells (vertical line in figure 4.23 marked with a black rectangle), or $\alpha - \gamma$.

ii A true fission event in coincidence with a telescope and a random coincidence in the gamma detectors (horizontal line in figure 4.23 marked with a green rectangle), or $\alpha - f$.

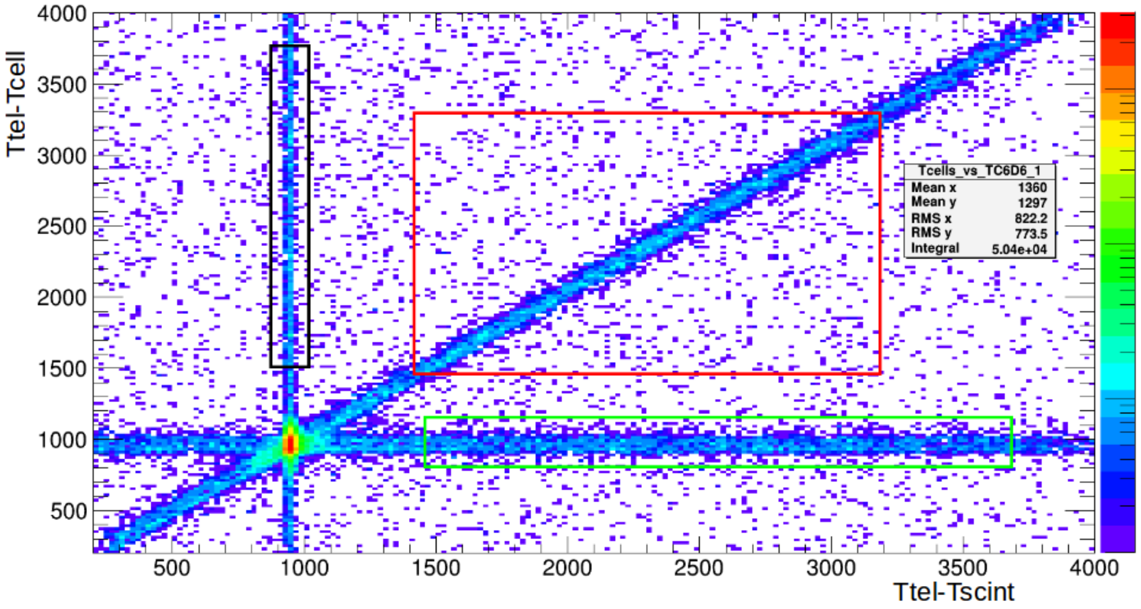

Figure 4.23: Time difference between telescope one and a cell versus the time difference between the same telescope and a C_6D_6 detector. The rectangles delimit the different kinds of random triple coincidences.

iii A fission and gamma event correlated in time, but uncorrelated with the particle that triggered the telescope (diagonal line in figure 4.23 marked with a red rectangle), or $\gamma - f$. Indeed, defining $T_1 = T_{tel} - T_{cell}$ (1) and $T_2 = T_{tel} + T_{scint}$ (2). From (2) we have: $T_{tel} = T_2 + T_{scint}$ and inserting this into (1) one gets: $T_1 = T_2 + T_{scint} - T_{cell}$. When the gamma detector and the cell are correlated, but uncorrelated with the telescope, $T_{scint} - T_{cell} = constant$ but T_1 and T_2 can take any value.

iv A random coincidence in both, the fission and gamma detectors (scattered dots in figure 4.23), or $\alpha{-}\gamma{-}f$. The contribution of these events to the random coincidences was neglected as they are very rare.

Figure 4.24 represents the number of alpha particles as a function of the E^* of ^{240}Pu for the events within the rectangles that appear in figure 4.20. The red spectrum has the shape of the γ-coincidence spectrum because it is obtained with events in the coincidence window of a gamma detector and in the random-coincidence time window of a solar cell $(\alpha - \gamma)$. Conversely, the black spectrum resembles to the fission coincidence spectrum $(\alpha - f)$. Finally, the blue spectrum has the same shape as the singles spectrum, as it corresponds to an event within the coincidence time windows of the cells and γ-ray detectors but uncorrelated with the trigger $(\gamma - f)$.

From the comparison of figures 4.22 and 4.24, the number of counts of the random coincidence spectra is really small taking into account that it comprises all the statistics, but they were however subtracted from the triple coincidences spectra. To take into account every possible combination of detectors-thresholds-random-coincidence: $2telescopes{\cdot}14strips{\cdot}16cells{\cdot}(4C_6D_6{+}5Ge){\cdot}7E_{th} = 28224$ random-coincidence histograms were subtracted from the triple coincidence spectra.

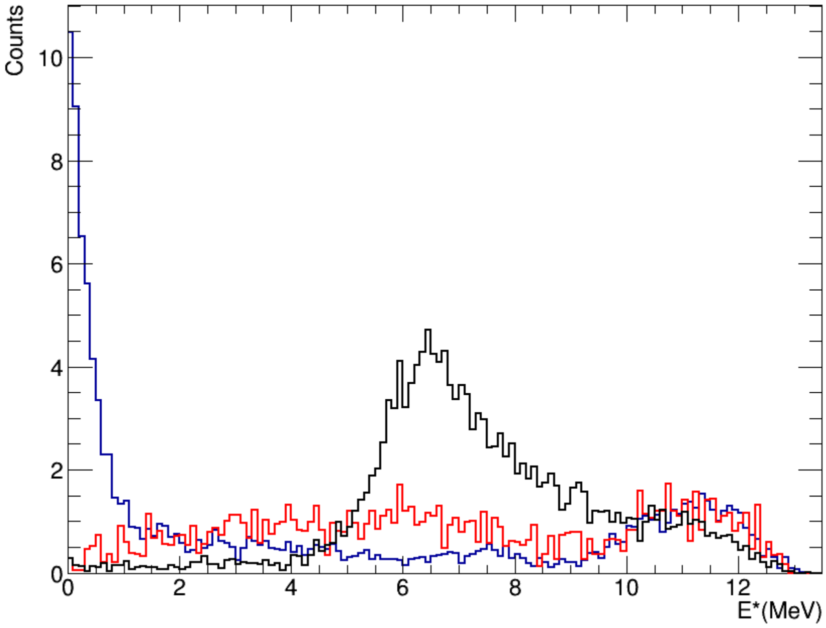

Figure 4.24: Number of counts as a function of E^* of the compound nucleus formed with the $^{240}Pu(^4He,^4He')$ for three types of random coincidences: red $\alpha-\gamma$, black $\alpha-f$, blue $\gamma-f$.

4.6 Detection Efficiency

Correctly calculating the fission detection efficiency and the γ-cascade detection efficiency is key to obtain good results as it has a strong influence on the obtained probabilities.

4.6.1 Fission-Event Detection Efficiency

The fission efficiency depends on the geometrical efficiency of the fission detector, the intrinsic efficiency of the solar cells, and the angular anisotropy of the fission fragments, which is due to two effects. First, the angular anisotropy of the fission fragments in the center of mass reference frame, which is determined by the angular momentum distribution of the fissioning nucleus. Second, the kinematic focusing of the fission fragments in the direction of the fissioning nucleus, which depends on the velocity of the latter.

A combination of experiment and simulation was used to determine the fission efficiency. The simulation was done with a Monte Carlo code in C++ developed in-house, the fission fragment yields and their energies were based on the output of the GEF code [76]. Five steps were followed to obtain the efficiency:

1 To measure the efficiency with a ^{252}Cf source of known activity placed at the same position, by hypothesis, as the target ^{240}Pu would be. This was done before and after the experiment. Both measurements were in agreement within error bars, meaning that the efficiency had not changed significantly over the experiment time. The weighted average of these two measurements gave an efficiency $\varepsilon_f(^{252}Cf) =$

62.19±0.96%. This efficiency includes the geometrical efficiency of the cells ε_{geom} and their intrinsic efficiency $\varepsilon_{int} = 0.95 \pm 0.02$, see chapter 3, such that $\varepsilon_f = \varepsilon_{int} \cdot \varepsilon_{geom}$.

2 To reproduce with the simulation the experimental efficiency obtained with californium by adjusting the geometry and the size of the cells, and their relative position to the target. To this end, the simulation included as well the size of the target and the geometry of the support. This was necessary because the source was non punctual and the support of the ^{252}Cf (first hole starting from the left in figure 3.3) casted a shade over the closest cells and thus reduced the efficiency. In figure 4.25, there is a comparison of the efficiency of each cell obtained with the experiment and simulation. Getting such a good agreement is not evident because there are many dimensions to constrain (in addition to the effect of the shade and the shape of the source) and the geometry is very compact, small changes in the dimensions imply big changes in the efficiency. Figure 4.25 shows that the efficiency of each cell varies from less than 1% to over 9%.

3 Once the experimental efficiency $\varepsilon_f(^{252}Cf)$ is correctly reproduced for each cell, the efficiency of the cells is determined taking into account the kinematic focusing of the reactions $^{240}Pu(^4He, ^4He')$ and $^{240}Pu(^3He, ^4He)$. Indeed, the efficiency of the cells placed downstream the target is increased and vice-versa, which results in a net increase of $\sim$ 5%. The efficiency and the angular anisotropy depend on the velocities of the fission fragments and thus on the angle of the scattered particle and the excitation energy of the recoil nucleus. Therefore the efficiency is calculated for the seven angles analyzed (table 3.2) and the excitation energy of the recoil nucleus.

4 To determine the angular distribution of the fission fragments in the center of mass. To do this, first the number of counts in each cell for a certain excitation energy has to be obtained, then these counts are re-normalized dividing them by the efficiency of the corresponding cell, obtained in the previous step. These normalized counts are plotted as a function of the polar angle of the fragments with respect to the recoiling fissioning nucleus θ_f^{CM}, figure 4.26. The function of the polar angle $constant(1 + \alpha \cdot cos^2(\theta_f^{CM}))$ is fitted to the points to obtain the anisotropy parameter α [43]. This parameter depends on the ejectile angle θ and the excitation energy of the recoil too. In 1965 Britt and Plasil [77] studied the inelastic scattering of alpha particles on ^{238}U and ^{240}Pu, the same reaction as in this work. They did not apply the surrogate reaction method to their data, but they extracted the fission fragments' angular distributions. Their results are in agreement with previous (d, p) measurements and with our anisotropy parameters, extracted from fits such as the ones of figure 4.26, agree with the ones they deduce.

5 Finally, having obtained α, the efficiency is simulated again including the effect of the anisotropy on the final efficiency. The effect was a slight increase, $\sim 2 - 3\%$, of the detection efficiency. During this step the impact of considering multiplicity m, i.e. the number of fission fragments detected after a fission event, was studied: $m = 2$ events in which two cells are fired; $m = any$ events in which one or two strips are fired, but only one event of the two is counted; $m = 1$ events in which only one strip is fired, explicitly discarding events with $m = 2$. The simulation was done for

$m = any$ because it gives the fission-event detection efficiency and is the only way of not introducing a bias due to particular geometrical configurations.

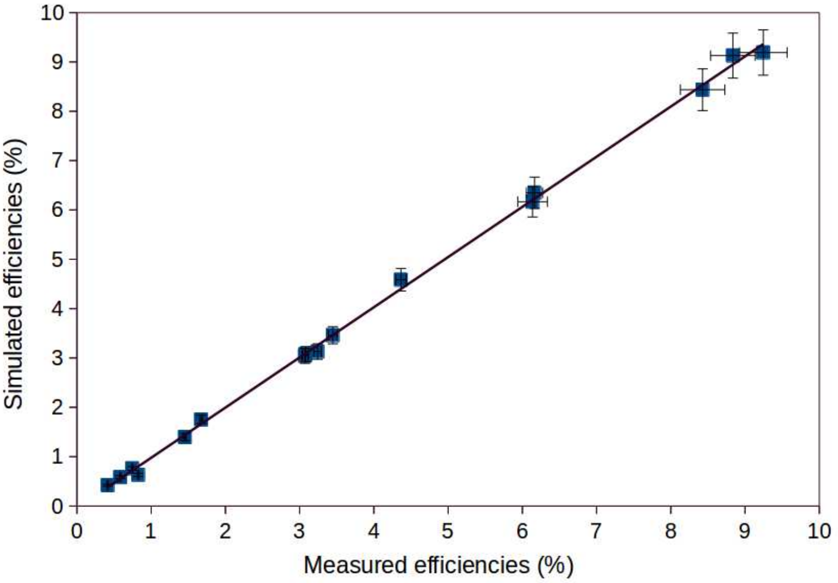

Figure 4.25: Comparison of the measured fission detection efficiency with a ^{252}Cf source and the one obtained with simulation. Each square represents a different cell and the black line is a straight line of slope equal to 1. We may see that they are almost perfectly correlated, which means that the simulation reproduces correctly the experiment.

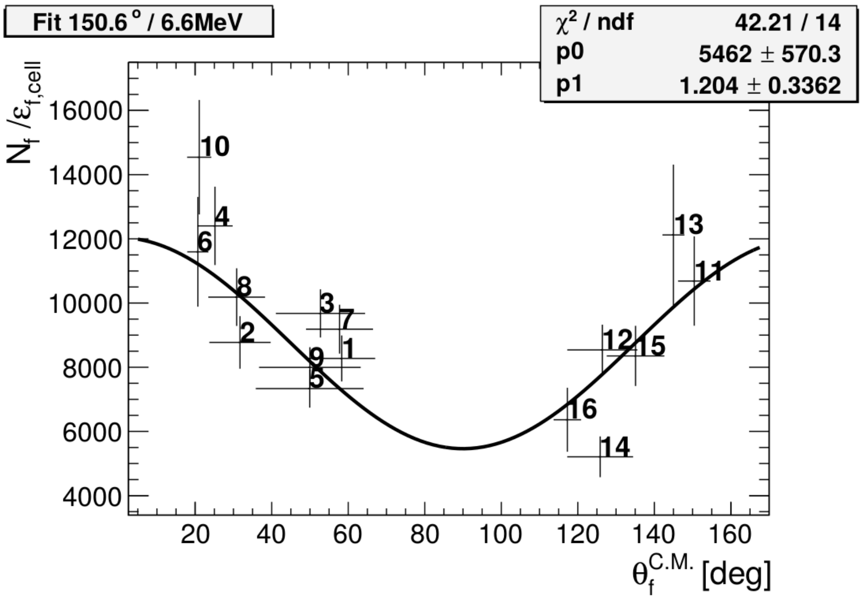

Figure 4.26: Normalized counts in the cells versus the polar angle of the fission fragments in the center of mass. The curve represents the result of the fitting points with the function $constant \cdot (1 + \alpha \cdot cos^2(\theta_f^{CM}))$. Parameter zero (p0) is the scaling constant and parameter one (p1) in the figure corresponds to the anisotropy parameter.

To verify that the geometry of the simulation was correct, we studied the events of multiplicity equal to two ($m = 2$), in which two cells were fired, by comparing the cells fired during these events in the simulation and in the data. This served not only as a debug of the programs, but also to improve our understanding of the experimental conditions. Figures 4.27a and 4.27b were obtained using the data and the simulation, respectively, and they represent the correlation between the cells two by two, or the number of events in which two cells where fired simultaneously as a function of the number of both cells (see section 3). When comparing these two figures there is a general good agreement between them, despite some small differences, which means that the geometry of the cells was correctly defined.

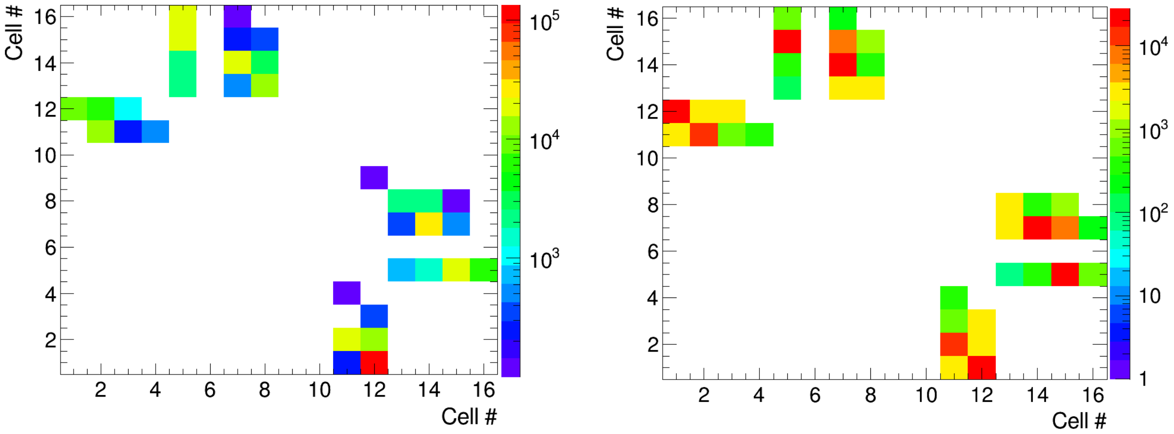

(a) Data.

(b) Simulation.

Figure 4.27: Bi-dimensional histogram of the fired cells in events with multiplicity strictly equal to two.

Still, there were differences between the experiment and the simulation when comparing the number of events with multiplicity m two and events with any multiplicity ($m = any = 1\ or\ 2$). To do this comparison the following ratio of ratios was calculated for each cell, except for the cells that are not geometrically in opposition to another one, see equation (4.2). This ratio of ratios, experimental/theoretical, as defined in equation (4.2), is plotted with the corresponding error bars for each cell in figure 4.28.

$$Multiplicity\ Ratio: \ MR = \frac{[N_f(m=2)/N_f(m=any)]_{exp}}{[N_f(m=2)/N_f(m=any)]_{sim}} \tag{4.2}$$

If the simulation would have perfectly reproduced the experimental fission detection efficiency, the ratio in equation (4.2) would be equal to one. But in this case a simple constant fit gives a value of 0.71. The origin of this mismatch in the runs with the plutonium target is still uncertain, there are several hypothesis but the most plausible one is the target quality. Energy thresholds were set on the cells during the preparation of the experiment using a californium source, which was a surface depot. In contrast, during the measurement with the beam on-line, fission fragments had to trespass the PuO_2 matter, if they were emitted backwards, and the carbon backing on top of that if they were emitted forward. This decreases the total kinetic energy of the fission fragments, especially the energy of the heavy ones which can lose up to 20% of their energy in this process (as simulated with LISE++). In addition, the energy response of the cells could have drifted during the experiment, due to the changes in room temperature and to the impact of the intense scattered beam. This caused a slight worsening of the resolution of the cells downstream the target. All these considerations were not taken into account in the simulation, and the direct consequence of this is a reduction of the intrinsic efficiency of the cells.

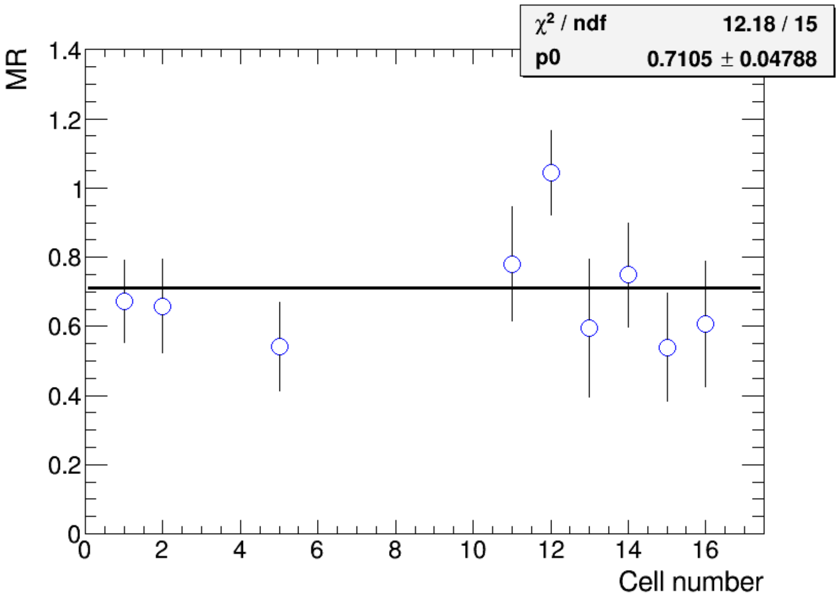

Figure 4.28: Ratio of ratios as defined in equation (4.2). Some cells were removed because the statistics of the experiment was too weak or because it was not possible geometrically for them to be in coincidence with another cell.

The effect of the energy loss in the target is a shift to lower energies of the cells spectra that can therefore appear to be cut thus losing some events. In figure 4.29 we compare the spectra obtained with cell number one, which is one of the cells most abruptly cut, for the plutonium runs and the californium ones. Other cells have a smoother cut at lower energies, but all of the fission-fragment spectra of Pu are shifted to lower energies.

To account for this effect the fission detection efficiency was reduced by multiplying it by a coefficient. The value was calculated following two different criteria: to make the ratio of figure 4.28 closer to one, which implies multiplying the intrinsic efficiency by ≈ 0.71, or to make the total decay probability, γ-decay plus fission, between the fission threshold and the neutron separation energy equal to one, which gives a value of ≈ 0.8, see figure 4.30. As we will see in section 4.7, reducing ε_f means increasing the calculated fission probability but also reducing the γ-decay probability, resulting in a diminution of the total probability.

The reason why these coefficients are not the same, 0.71 and 0.8, is that a global correction coefficient has a stronger impact on the reduction of multiplicity 2 events than one for the cells downstream and the other for the upstream ones. In fact the correction should be individual for each cell for two reasons. First, because the carbon backing of the target which was placed facing downstream, as a consequence the cells place in the forward direction of the beam will be more affected by the energy loss. Second, that the

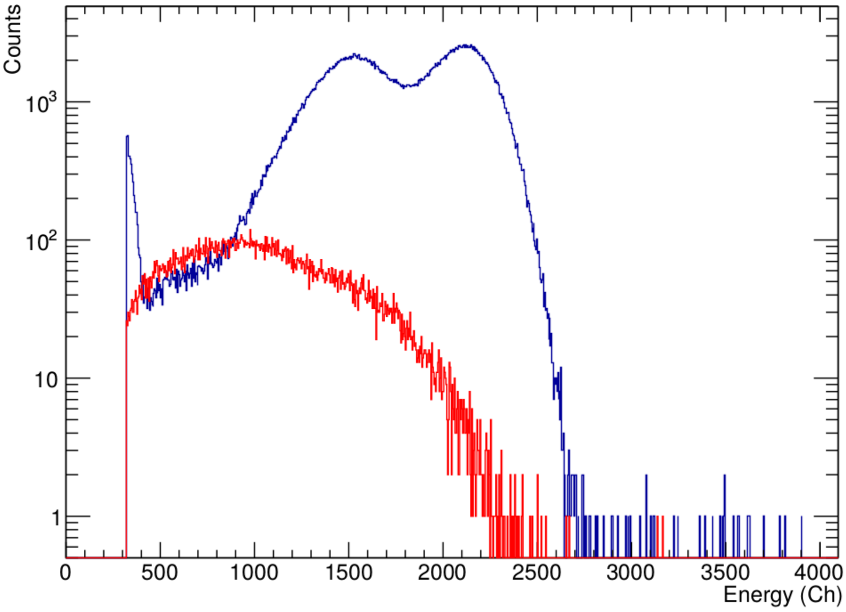

Figure 4.29: Energy spectra obtained with cell number 1 with the californium source (blue) and the $^{240}Pu(^4He,^4He')$ reaction obtained during the measurement (red).

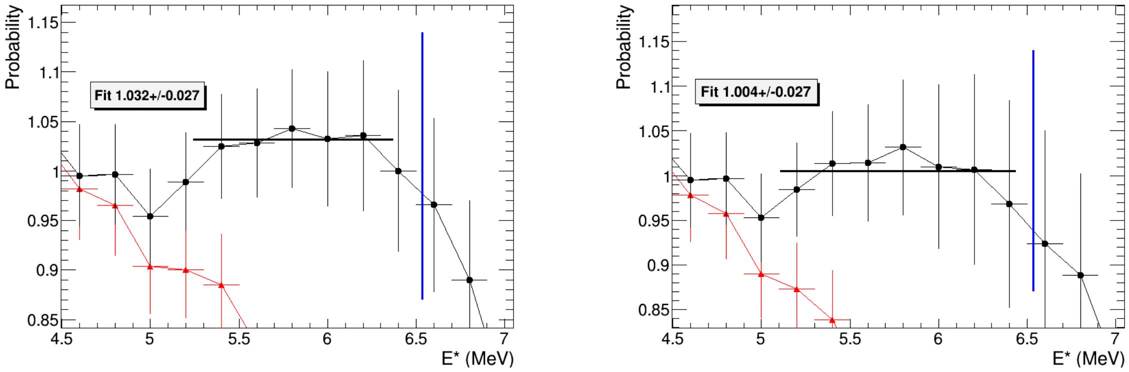

(a) Probabilities obtained with the calculated efficiency.

(b) Probabilities obtained with the calculated efficiency multiplied by 0.8.

Figure 4.30: Comparison of the total decay probability (black circles) = gamma-decay (red triangles) + fission (not in the images) and constant fit between 5.2 and 6.4 MeV. The vertical blue line represents the neutron separation energy.

elastically scattered particles of the beam are emitted at small polar angles with a much bigger cross section, which can induce a dead time on the cells placed downstream. This individualized correction per cell could not be done and a global coefficient was applied.

When trying to use the correction coefficient of 0.71, the gamma decay probability took negative values because of the subtraction of the normalized triple coincidences. As a consequence, the criterion adjusting the prob to 1 below S_n was adopted as shown in figure 4.30. Therefore the fission detection efficiency obtained with the simulation was multiplied by 0.8, a value that ensured physical probabilities, i.e. $P_f + P_\gamma \approx 1$. In figure 4.31 we represent the global fission detection efficiency $\varepsilon_f(E^*)$ as a function of $E^*(^{240}Pu)$.

The error bars of this efficiency include the uncertainty in the geometry of the cells, the uncertainty in the angular anisotropy correction, and the uncertainty due to the correction coefficient.

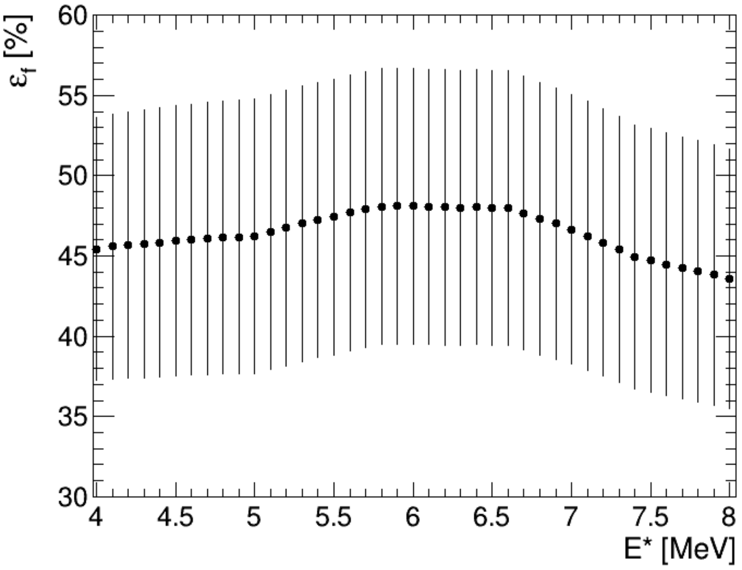

Figure 4.31: Final fission detection efficiency as a function of the excitation energy of $^{240}Pu^*$ formed through the $(^4He,^4He')$ reaction.

As a general comment, the collaboration usually proceeds following the five steps described at the beginning of the section. The problem encountered with the determination of the intrinsic efficiency, having to do a global correction to explain the multiplicity, was unattended. In fact the fission-fragment spectra of actinides are double humped, as seen with the Cf source, but not when studying the fission of Pu as it should be. This illustrates the poor quality of the target, which has increased the uncertainty of the final decay probability results.

4.6.2 Gamma Cascade Detection Efficiency

The procedure to obtain the gamma cascade detection efficiency is completely different to the one used for fission, as it is based on the EXtrapolated Efficiency Method (EXEM) [1] [2], a method developed by the collaboration and based on two main ideas. Firstly, that in the energy region under S_n, or the fission threshold for fissile nuclei, the probability for the nucleus to decay emitting γ-rays is the unity, because it is the only open decay path (neglecting proton and alpha emission). Therefore: $P_\gamma = 1 = N_{coin.}/(N_{sing.} \cdot \varepsilon_\gamma)$. Under these conditions the detection efficiency can be deduced from the data using equation (4.3):

$$\varepsilon_\gamma = N_{coin.}/N_{sing.} \tag{4.3}$$

Secondly, that the obtained efficiency may be extrapolated to higher excitation energies, which is based on the assumption that the level density and the gamma strength-function of the compound nucleus will continue to vary with excitation energy in the same manner as below the fission threshold or S_n. This assumption was validated in [1] [2].

Therefore to obtain the gamma-cascade detection efficiency, first the ratio coincidences over singles is done, then this ratio is fitted in energy region free from fission and neutron emission events and then the fit is extrapolated to higher energies.

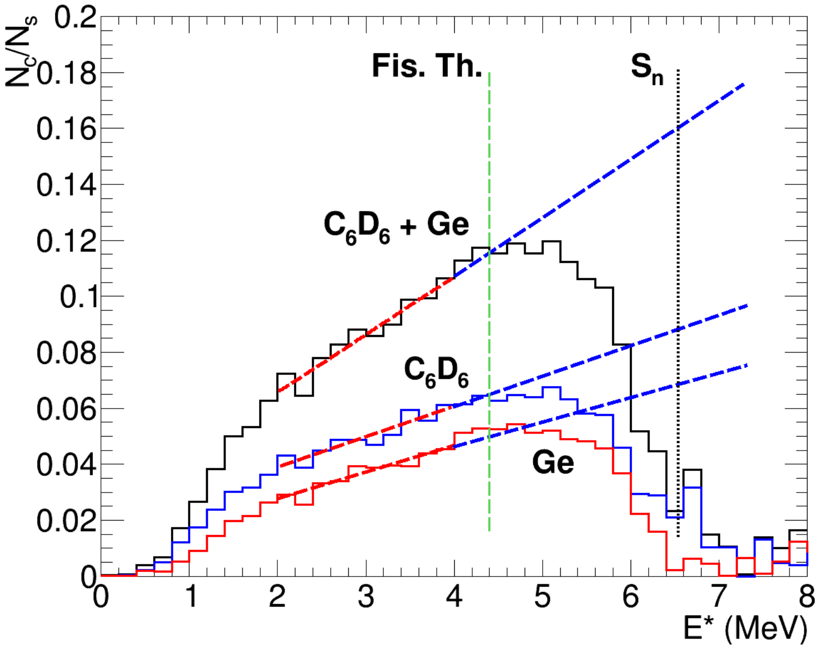

Figure 4.32: Ratio of the number detected gamma rays, with an energy over $266keV$, in coincidence with four strips $\theta_{ej} \approx 145^o$, over the total number of scattered particles as a function of the excitation energy. The red solid line was obtained with the germanium detectors, the blue one with the liquid scintillators and the black one with the sum of both. The red dashed lines represent fits of each spectra in an energy region between $2.2MeV$ and $4.2MeV$, and the blue dashed lines are an extrapolation of them. The black vertical dotted line marks the neutron separation energy of the ^{240}Pu and the green one the fission threshold.

Figure 4.32 represents the mentioned ratio obtained with germanium detectors, scintillators and both. The red dashed lines represent the fits in energy regions well in the continuum but under the fission threshold (see figure 4.33 for details). The blue dashed lines in figure 4.32 are extrapolations to higher excitation energies that will be used as the gamma detection efficiency as a function of excitation energy.

Similar fits to the ones presented in figures 4.33 and 4.32, were done to obtain the gamma cascade detection efficiency. They were done for each angle defined in table 3.2, to study the dependency of the probabilities with the angles, and for each threshold defined in table 4.3. The uncertainties associated to the detection efficiency are given by the uncertainty on the fit parameters. The efficiencies and the associated uncertainties depend on E_γ^{th}. For example, at 151^o and $E^* = 4$ MeV when using the Ge plus the scintillators with $E_\gamma^{th} = 266keV$, the efficiency $\varepsilon_\gamma = 0.1012 \pm 0.0199$ (19.7% relative uncertainty), whilst with $E_\gamma^{th} = 866keV$ the efficiency $\varepsilon_\gamma = 0.0522 \pm 0.0135$ (25.7% relative uncertainty).

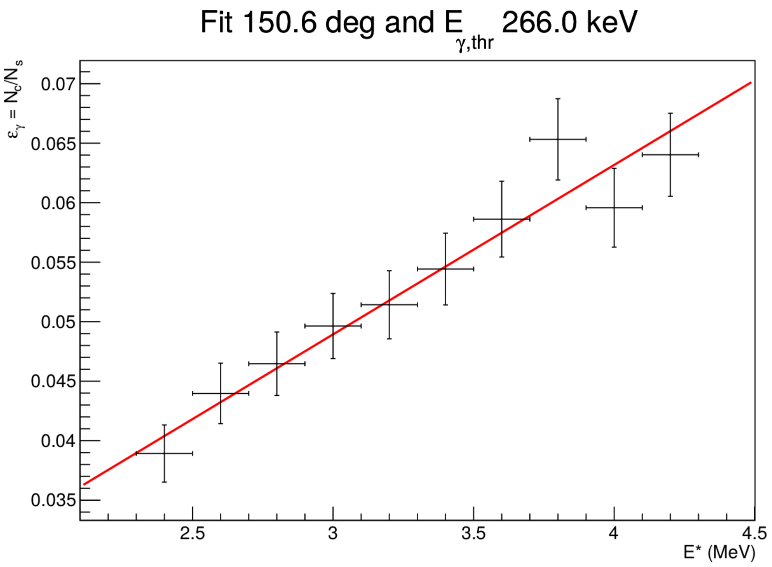

Figure 4.33: Fit of the efficiency (eq. (4.3)) for the $^{240}Pu(^4He,^4He')$, at a scattering polar angle of 150.6^o and with a threshold in gamma energy of $266keV$. The points represent the ratio $N_{coin.}/N_{sing.}$ and the error bars include the statistical error and the energy resolution. The red line is the fit result.

4.7 Determination of the Decay Probabilities

To sum up, several steps were taken before it was possible to determine the decay probabilities:

1. Select the reaction channel in the bi-dimensional spectra obtained with the telescopes.
2. Calibrate the energy of the telescopes and the gamma detectors.
3. Fill the singles, fission, gamma and random coincidence histograms.
4. Account for random coincidences, subtract the random coincidence histograms conveniently renormalized.
5. Obtain the detection efficiencies.

After completing these milestones, one can obtain the specific formulae of the decay probabilities with the general equation (1.1), which is re-written in the case of fission probability as:

$$P_f = \frac{N_f - N_{ter}}{N_s \varepsilon_f} \tag{4.4}$$

where P_f is the fission probability, N_f is the number of fission events in coincidence with an ejectile, N_{ter} is the number of presumed ternary fission events deduced from the low energy part of the fission spectra of the $^{240}Pu(^4He,^4He')$ reaction, see subsection 4.5.1, N_s is the number of ejectiles coming from the studied reaction after fitting the background, see subsection 4.8.1, and removing the presumed contribution of ternary fission events, and ε_f is the fission detection efficiency. All of these variables have a dependency on excitation energy which was not written explicitly for the sake of simplicity.

Similarly, equation (1.1), in the case of the gamma decay probability, transforms into equation 4.5:

$$P_\gamma = \frac{N_c - N_t/\varepsilon_f}{N_s \varepsilon_\gamma} \tag{4.5}$$

where P_γ is the gamma decay probability, N_c is the number of gamma cascades detected in coincidence with a scattered particle, N_t is the number of fission events detected in coincidence with a gamma ray and an ejectile, N_s and ε_f are the same quantities as in equation (4.4), and ε_γ is the gamma cascade detection efficiency. Again, all the variables depend on the excitation energy. The results are presented in section 4.9 and interpreted theoretically in chapter 6.

4.8 Uncertainty Analysis

Correctly estimating the uncertainty of a measurement is of paramount importance as it defines the quality of the data. There are usually several sources of uncertainty that contribute to the total one and that are added up using the following error propagation formula. Equation (4.6) relies on the assumption that errors are small enough that a function $f(x_1, ..., x_n)$ can be approximated by order one Taylor expansions $f \approx f(x_0) + f'(x_0) \cdot (x - x_0)$:

$$(\Delta f(x_1, ..., x_n))^2 = \sum_{i=1}^{n} \sum_{j=1}^{n} \frac{\partial f}{\partial x_i} \frac{\partial f}{\partial x_j} \sigma_{x_i} \sigma_{x_j} \rho_{ij} \tag{4.6}$$

The task will be then to replace f by the probabilities of equations (4.4) and (4.5), and evaluate each term of equation (4.6), particularly difficult to obtain are the correlation coefficients $\rho_{ij} = Cov(x_i, x_j)/\sqrt{Var(x_i) \cdot Var(x_j)}$, with $\rho_{ii} = 1$.

4.8.1 Uncertainties Due to Background Subtraction

The uncertainties induced by the interpolation of the contaminants, subsection 4.4.1, and the presumed ternary fission events, subsection 4.5.1, are calculated independently to simplify the treatment of the uncertainties. The number of singles N_s used in equations (4.4) and (4.5) sections is in fact:

$$N_s = N_{det} - N_{cont} - N_{ter}/\varepsilon_f \tag{4.7}$$

Where N_{det} is the number of ejectiles detected with the telescopes, N_{cont} is the estimated number of events induced by the contaminants in the carbon backing and N_{ter} is the number of ternary fission events deduced from the low energy part of the fission spectra.

The procedure followed to include the error due to the backgrounds was the same as detailed in section III of Kessedjian *et al.* [43]. It is valid in the case in which the shape of the background and the position are correctly known, and the background spectrum has been measured independently. In this work we use the same formulas described in the reference, even though the background was interpolated and not subtracted. In addition, to account for this and for the fact that there were two contaminant peaks, and thus the shape of the peaks was not perfectly known, in the energy region of interest, the error given by the formulas at [43] were multiplied by 2, which is a conservative way to include these errors. The errors are then added to formulas (4.8) and (4.9).

An alternative analysis to estimate these errors was done, based exclusively on equation (4.6), is described in appendix C. It gives very similar results to the ones presented in this section.

4.8.2 Uncertainty in the Fission Probability

We recall equation (4.4) used to calculate the fission probability:

$$P_f = \frac{N_f - N_{ter}}{N_s \varepsilon_f}$$

As one may see, this probability depends on four variables. Table 4.4 illustrates the covariances to take into account between these variables.

Variable	N_f	N_{ter}	N_s	ε_f
N_f	$Var(N_f)$	0	$Cov(N_f, N_s)$	≈ 0
N_{ter}		$Var(N_{ter})$	0	0
N_s			$Var(N_s)$	0
ε_f				$Var(\varepsilon_f)$

Table 4.4: Covariance table for the fission probability.

From all the possible covariance terms only the covariance between the number of fission coincidences and scattered particles has been retained. The covariance terms concerning the efficiency could be neglected because although the data was used to determine the fission fragment anisotropy (see section 4.6.1), the correlation is minimum because the impact of the anisotropy on the fission detection efficiency is lower than 10%. The terms of covariance with the ternary fission were also neglected because the proportion of these events is small. They have an impact on the background subtraction errors that will later be detailed. Taking all of this into account, equation (4.6) in the case of the fission probability takes the following explicit form:

$$\begin{aligned}\Delta P_f^2 = & \frac{1}{N_s^2 \varepsilon_f^2} \left[N_f + N_{ter} + \frac{(N_f - N_{ter})^2}{N_s} + (N_f - N_{ter})^2 \left(\frac{\Delta \varepsilon_f}{\varepsilon_f} \right)^2 \right. \\ & \left. -2 \frac{(N_f - N_{ter})}{N_s} \sqrt{N_f \cdot N_s} \cdot \rho_{fs} \right]\end{aligned} \tag{4.8}$$

where we have used $\Delta N_i = \sqrt{N_i}$. In (4.8) the first four terms to the right side correspond to the variance terms of each variable, and the fifth one to the covariance between N_f and N_s, see table 4.4. The value of the correlation coefficient ρ_{fs} was determined experimentally as explained in [10] [3]. The experimental data was divided into smaller groups of data to see how for each group of data the fluctuations in N_s affected N_f. A 2D-histogram (figure 4.34) was constructed to obtain the correlation of these two variables.

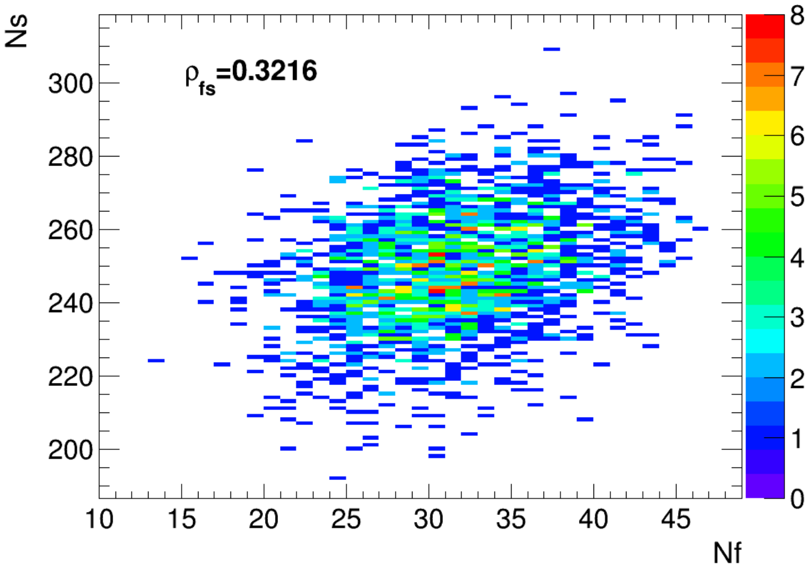

Figure 4.34: Bi-dimensional spectrum from the $^{240}Pu(\alpha, \alpha')$ reaction. The horizontal axis represents the number of fission events in coincidence with a scattered alpha particle detected with telescope number 1, N_f, and the vertical axis the total number of these events, N_s. The histogram is filled with events within the excitation energy range of 4 to 8 MeV. The correlation coefficient obtained is $\rho_{fs} = 0.3216$.

The histogram of figure 4.34 was constructed using a "event limit" that was randomly sampled during the analysis, using a normal distribution centered at 250 events and with standard deviation $\sqrt{250}$. While analyzing the data, a N_s counter is incremented when an event corresponds to a $^{239}Pu^*$ or $^{240}Pu^*$ nucleus at an excitation energy between 4 and 8 MeV, until the "event limit" is reached. Similarly, the corresponding fission events are counted for this excitation energy range. Once the limit of random events is reached, the value of both numbers of counts is stored in a bi-dimensional histogram and the process is repeated until all the events are analyzed. In theory a histogram like this one should be filled for each energy in which the probability is obtained, but in practice this is not possible due to the lack of statistics. Therefore, an average value of the correlation coefficients was used.

4.8.3 Uncertainty in the Gamma Decay Probability

The case of the gamma decay is similar to the fission one, although more complicated because there are more variables that intervene and more covariance terms have to be included, recall equation (4.5):

$$P_\gamma = \frac{N_c - N_t/\varepsilon_f}{N_s \varepsilon_\gamma}$$

The covariance terms taken into account are shown in table 4.5. The terms of covariance with the fission efficiency are zero as this efficiency was not determined with these variables. So was the covariance with the gamma detection efficiency because it is sufficiently small as shown in [10]. Although the setup is not exactly the same as in reference [10], the gamma detection efficiency is lower in our case, and therefore we may suppose this correlation is negligible.

Variable	N_c	N_t	N_s	ε_γ	ε_f
N_c	$Var(N_c)$	$Cov(N_c, N_t)$	$Cov(N_c, N_s)$	≈ 0	0
N_t		$Var(N_t)$	$Cov(N_t, N_s)$	0	0
N_s			$Var(N_s)$	≈ 0	0
ε_γ				$Var(\varepsilon_\gamma)$	0
ε_f					$Var(\varepsilon_f)$

Table 4.5: Covariance table for the gamma decay probability.

Developing equation 4.6 for the *gamma*-decay probability and taking into account the covariances of table 4.5, we obtain the following formula for the uncertainty:

$$\begin{aligned}\Delta P_\gamma^2 =& \frac{1}{N_s^2\varepsilon_\gamma^2}\Bigg[N_c + \frac{N_t}{\varepsilon_\gamma^2} + \frac{(N_c - N_t/\varepsilon_f)^2}{N_s} + (N_f - N_t)^2\left(\frac{\Delta\varepsilon_\gamma}{\varepsilon_\gamma}\right)^2 + \frac{N_t^2\Delta\varepsilon_f^2}{\varepsilon_f^4} \\ & -2\frac{\sqrt{N_c \cdot N_t}}{\varepsilon_f}\cdot\rho_{ct} - 2\frac{(N_c - N_t/\varepsilon_f)\sqrt{N_s \cdot N_c}}{N_s}\cdot\rho_{cs} + 2\frac{(N_c - N_t/\varepsilon_f)\sqrt{N_s \cdot N_t}}{N_s\varepsilon_f}\cdot\rho_{ts}\Bigg]\end{aligned} \tag{4.9}$$

where in equation (4.9) the first five terms inside the brackets are the ones associated to the variance of each variable in equation (4.5), from left to right: total number of γ-rays detected coincidence with an ejectile N_c, triple coincidences γ-ray-fission-fragment-ejectile N_t, number of scattered particles detected or *singles* N_s, gamma detection efficiency ϵ_γ and fission detection efficiency ϵ_f. The other three terms are covariance terms associated to: $Cov(N_c, N_t)$, $Cov(N_c, N_s)$ and $Cov(N_t, N_s)$, respectively. As in the case of fission, we followed the same strategy to estimate the correlation coefficients, a 2D-histogram was built for each set of two variables.

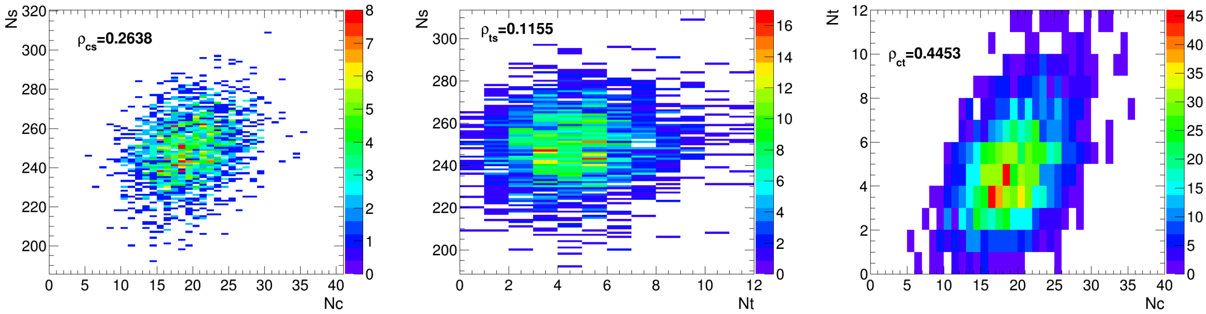

(a) $N_c - N_s$. (b) $N_t - N_s$. (c) $N_t - N_c$.

Figure 4.35: Histograms obtained with telescope number 1 with different variables selected to determine the correlation terms of the P_γ uncertainty.

The histograms of figure 4.35 were constructed in a similar way to the one of figure 4.34, i.e. by sampling a random number of events in which a $^{240}Pu^{*}$ is formed with an excitation energy between 4 and 8 MeV, following a normal distribution centered at 250 events and with standard deviation equal to the square root of this number of events. Due to the lack of statistics, averaged correlation factors, over the mentioned E^{*} range, were used instead.

The excitation energy averaged correlation coefficients used to obtain the errors in the probabilities are resumed in table 4.6. The values are the average of the results obtained with each telescope and for several runs.

ρ_{fs}	ρ_{ct}	ρ_{cs}	ρ_{ts}
0.31 ± 0.02	0.45 ± 0.03	0.26 ± 0.03	0.12 ± 0.02

Table 4.6: Average values of the correlation coefficients between the different experimental variables.

4.9 Results

After all the previous considerations the results are presented for the $^{240}Pu(^{4}He,^{4}He')$ reaction. In theory the results should be obtained for each strip, but as explained before this was not possible and they were studied forming groups of four strips to form 7 different angles, see table 3.2. Thus, in this section we give the weighted average of the probabilities calculated for each angle. The results by angle, along with results for the $^{240}Pu(^{3}He,^{4}He)$ reaction are given in appendix D, as they will not be interpreted theoretically.

In figure 4.36a we compare the gamma decay probabilities obtained at three representative angles $\theta_{ej} \approx 156^{o}/139^{o}/121^{o}$ in an energy interval without contaminants, figure 4.36b is equivalent but for fission. Doing a weighted average is justified because when comparing the decay probabilities for different angles, fig. 4.36, they agree within error bars. This was done to reduced the uncertainties, which makes more meaningful the interpretation of the results done in the second part of the thesis.

In figure 4.37, we compare the gamma decay probability obtained with the C_6D_6 detectors and the one obtained using these detectors plus the Ge detectors. The results are compatible within error bars, which means that the neutrons captured/scattered in the Ge crystals do not have a distinguishable effect on the gamma decay probability.

Therefore in the following we give the results using all the gamma detectors but we distinguish between two cases, one without subtracting the hypothetical ternary fission background as explained in subsection 4.5.1, figure 4.38, and the other one with it subtracted, figure 4.39. In these figures, the fission and the gamma decay probabilities are represented as a function of excitation energy, as well as the sum of both. The vertical solid black line represents the neutron separation energy and the horizontal striped line is set to one. Until the fission sets in at about 4.5 MeV, the $^{240}Pu^{*}$ can only release its energy excess by emitting γ-rays. From that point onwards the competition between γ-decay and fission starts up to the neutron separation energy S_n at about 6.5 MeV, but the sum of both is still one. At excitation energies $E^{*} > S_n$, it is possible for the compound nucleus to emit neutrons to release energy, thus the sum of fission and γ-decay is no longer 1.

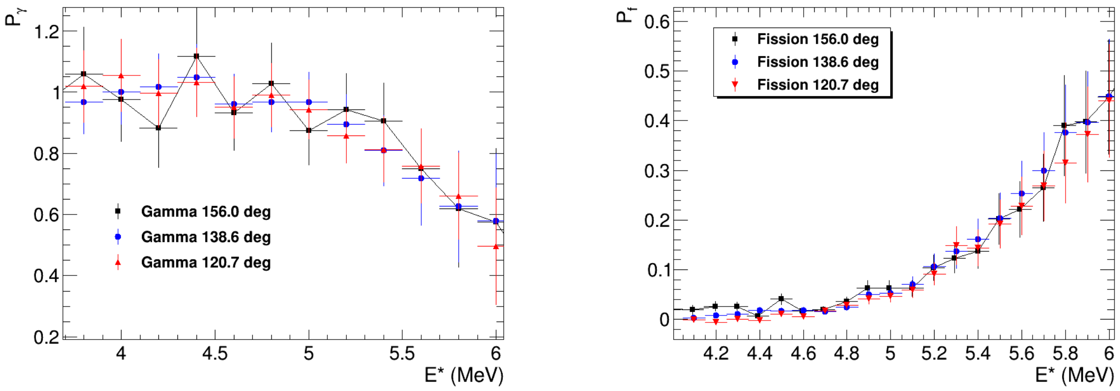

(a) γ-decay.

(b) Fission.

Figure 4.36: Comparison of the decay probabilities obtained at 3 different ejectile angles in an energy region free from contaminants.

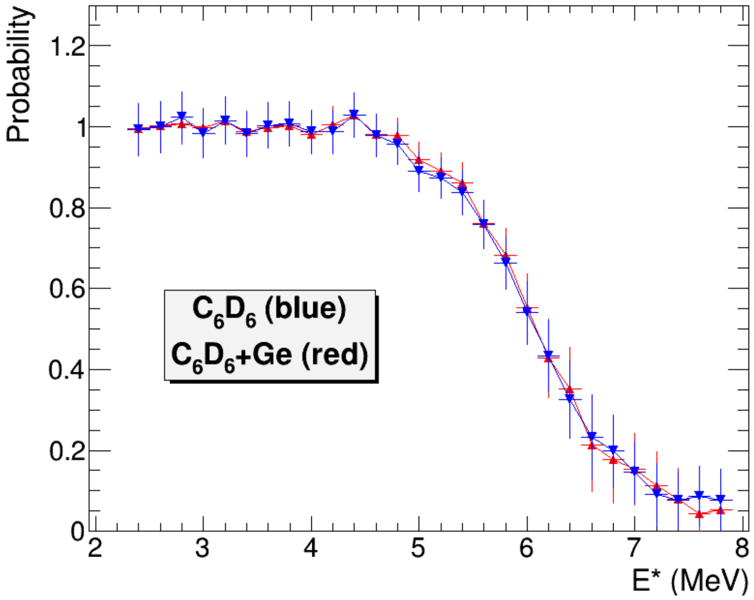

Figure 4.37: Gamma decay probability of $^{240}Pu^*$ obtained with scintillators compared to the one obtained with C_6D_6 and Ge detectors.

When looking in detail at these two figures, 4.38 and 4.39, and comparing them, one may see the difference in the fission probability under 4.5 MeV. Indeed the subtraction of the supposed background induced by the alphas generated in the ternary fission events of ^{244}Cm has a big impact in this energy region. There is also a slight effect at excitation energies of above 7 MeV, because the alpha particle distribution is peaked at excitation $E^* \sim 12$ MeV, see figure 4.18

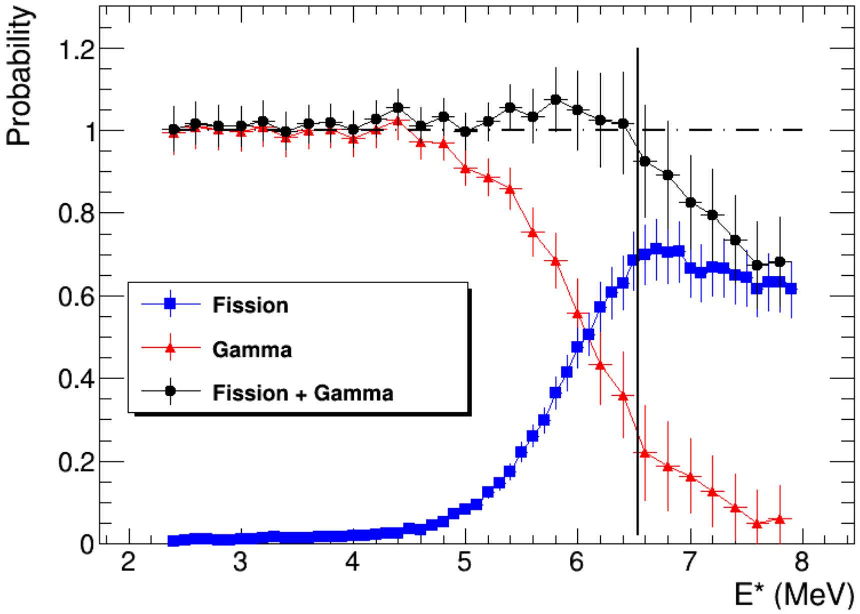

Figure 4.38: Weighted average of the decay probabilities of $^{240}Pu^{*}$ obtained per angle, without ternary fission subtraction. The vertical solid line represents the neutron separation energy.

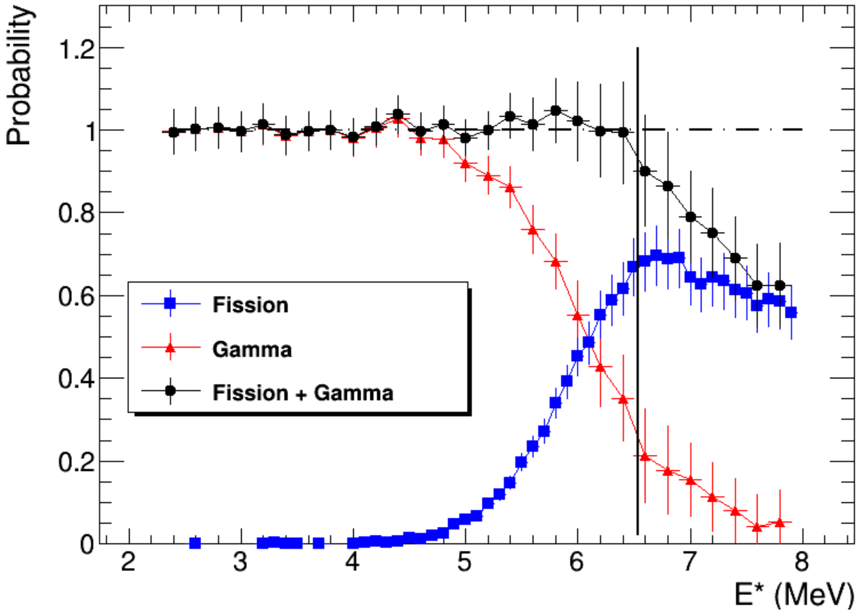

Figure 4.39: Weighted average of the decay probabilities of $^{240}Pu^{*}$ obtained per angle, after the ternary fission background was subtracted. The vertical solid line represents the neutron separation energy.

.

In figure 4.40 we compare our results obtained for the fission probability as a function of E^* of ^{240}Pu (blue squares) to previous results found in literature. Our data is in good agreement with all previous ones for $5.6 \leq E^* \leq 6.4$ MeV, which is a region which is free of contaminants for all the data sets. The results of Cramer and Britt [41] for the $^{240}Pu(t,p)$ and $^{240}Pu(p,p')$ have to be taken with caution out of the mentioned energy region because there were peaks induced by the carbon baking on their singles spectra which they had to subtract. The data of Back *et al.* [14] were affected by the deuteron break-up at excitation energies above S_n. At around 5 MeV all the data show a structure, which indicates that there is a resonance, a group of class-II states, that favors fission.

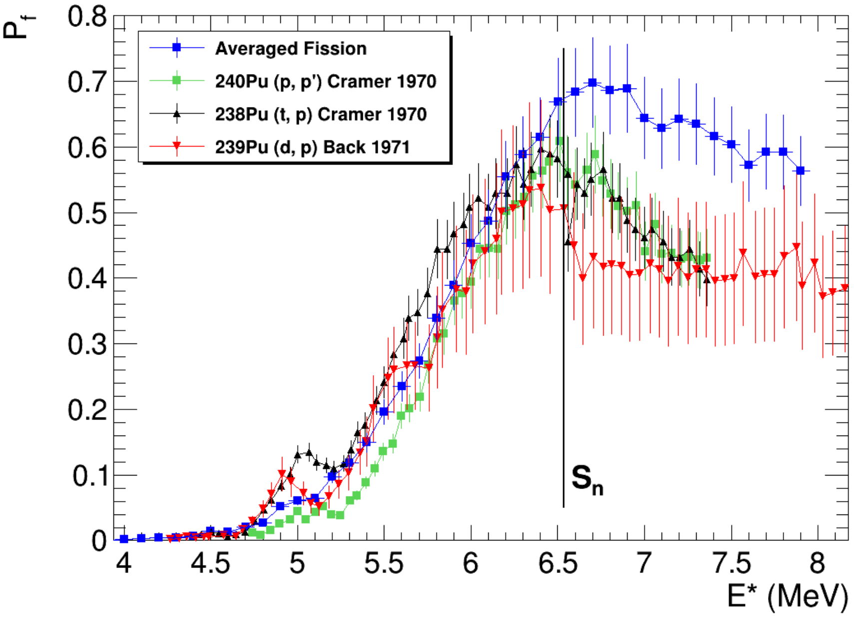

Figure 4.40: $^{240}Pu^*$ fission probability after the presumed ternary fission background was subtracted (blue squares), compared to previous data from Cramer and Britt [41] and Back *et al.* [14].

There is no γ-decay data to compare with our data. However, the comparison to previous fission data gives us confidence in our results. Even though there are differences at certain energy regions, this could be explained by the effect of the interpolation of the background in both our data and the previous ones. Another explanation is that as different reactions were used to form $^{240}Pu^*$, the spin distributions are likely to be different in each case, which as we will show in chapter 6 has a strong impact on the decay probabilities.

Finally, in figure 4.41, we compare our data to a calculation of the neutron induced probabilities, courtesy of P. Romain (CEA/DAM/DIF). The n-induced probabilities are the quotients $\sigma_n^\gamma/\sigma_n^{CN}(E_n)$ and $\sigma_n^f/\sigma_n^{CN}(E_n)$. Further details on the calculation of these cross sections will be given in chapter 5.

The calculations and the surrogate data of figure 4.41 do not compare well. This was expected for the gamma decay probability, as it is found to be a general result of previous works in the field, see chapter 2. There is an important disagreement in the case of fission too, specially at low neutron energies E_n, i.e just above the S_n. It is the first time that

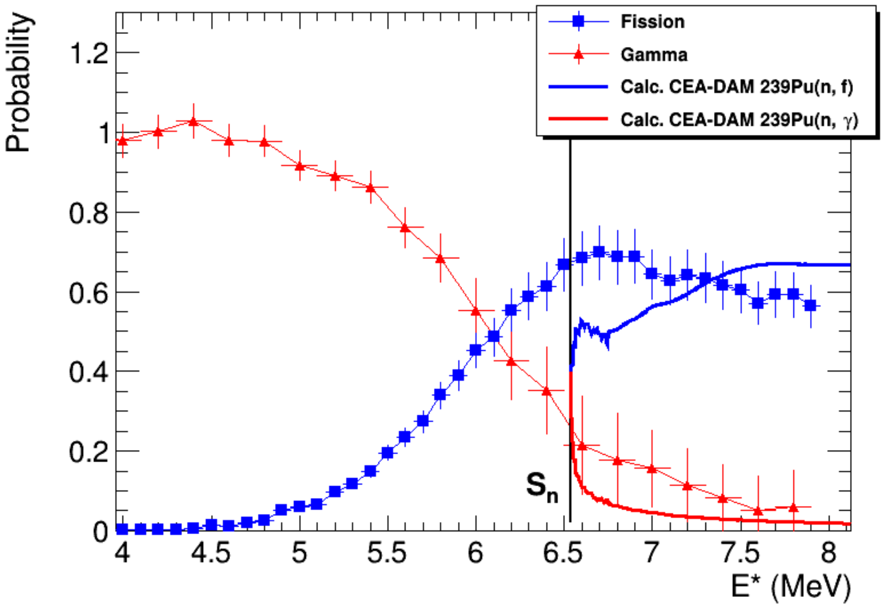

Figure 4.41: $^{240}Pu^{*}$ decay probabilities after the presumed ternary fission background was subtracted (symbols), compared to a neutron induced probability calculation, courtesy of P. Romain (CEA/DAM/DIF).

the collaboration finds such a difference for fission, and it was one of the motivations of this thesis, to test the agreement between surrogate data and neutron induced data in an even-even fissioning system like ^{240}Pu. The most plausible explanation is the spin-parity mismatch, which is meant to have a stronger impact on fission in the case of even-even decaying nuclei than in the one of odd systems. This fact proves the importance of knowing the J^{π} of the decaying nucleus. Thus, in the second part of this thesis we describe our approach to account for the differences between surrogate and n-induced data seen in figure 4.41.

Part II

Interpretation

Chapter 5

Evaluation of the Reaction n + ^{239}Pu

The ultimate goal of the surrogate reaction method is to deliver neutron induced cross sections deduced from the surrogate data. This was at first done with a Weisskopf-Ewing approximation, eq. (1.1), and more recently with approaches that go beyond it. In any case one should be able to correctly interpret the results presented in chapter 4, which implies having a thorough knowledge of the method. This requires to estimate the reaction model parameters of the $^{240}Pu^*$ CN decay. These parameters are needed to calculate the branching ratios $G_\chi(E^*, J^\pi)$ that appear in the decay probability equation (5.1), which we will use in combination with two different spin distributions $F(E^*, J^\pi)$ in the next chapter to reproduce our data.

$$P_\chi^{surr.}(E^*) = \sum_{J^\pi} F(E^*, J^\pi) \cdot G_\chi(E^*, J^\pi) \tag{5.1}$$

In this chapter we will describe the evaluation procedure, i.e. to adjust the model parameters with the $n + {}^{239}Pu$ reaction data. This process includes an optical model calculation of the reaction to the *total cross section* σ_T, which is the sum of the *shape-elastic cross section* $\sigma_{S.E.}$ and the *reaction cross section* σ_R. Having this cross section, the rest of them are deduced from it, including the fission $\sigma_{n,f}$ and capture $\sigma_{n,\gamma}$ cross sections which we will use to deduce the structure parameters of the compound nucleus $^{240}Pu^*$.

The process to interpret our data is summarized in figure 5.1. In this chapter we will focus on the first two blocks, optical model and parameters, and we will describe the theoretical ingredients needed. The rest of the interpretation will be part of chapter 6.

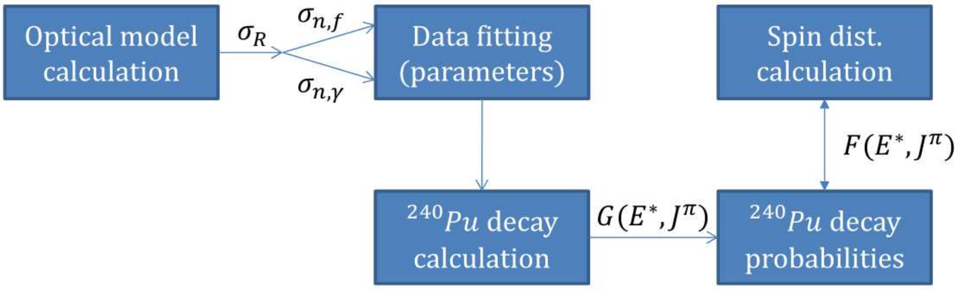

Figure 5.1: Scheme of the interpretation process

5.1 Reaction Mechanisms

Nuclear reactions can be classified depending on the reaction time, or emitted particle energy, as depicted in figure 5.2, where the labels C, P and D stand for *compound*, *pre-equilibrium* and *direct*, respectively.

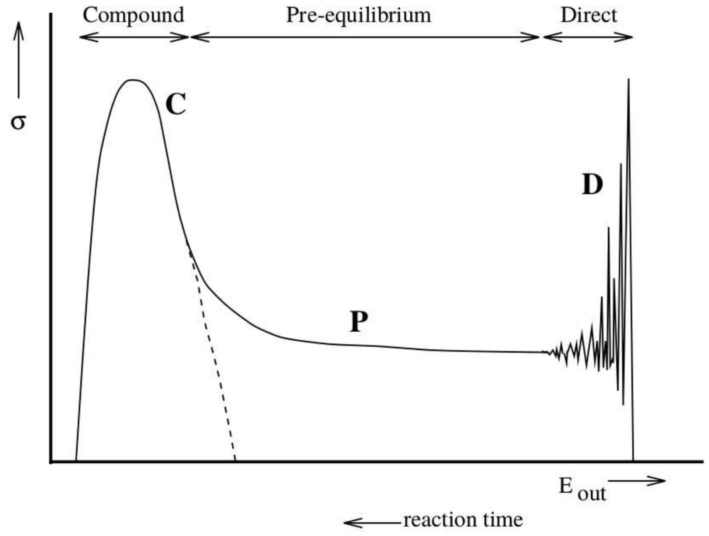

Figure 5.2: Nuclear reaction cross section as a function of the energy of the particle of the exit channel, and reaction mechanisms defined as a function of the reaction time [26].

Direct reactions are those which take place in a time interval comparable to the time it takes a particle to cover the size of a nucleus (typically $10^{-22} - 10^{-18}s$). This reaction mechanism accounts for processes in which the ejectile causes individual particle excitations, like a particle-hole (p-h) pair. In contrast, compound reactions are those in which the energy of this excitation is distributed among all the other nucleons achieving statistical equilibrium, i.e. the energy is equally distributed among all nucleons, resulting in multiple p-h pairs, and forming a compound nucleus [11], this process lasts for around $10^{-18}s$. Between these two processes there is the pre-equilibrium phase, an intermediate step between them in which the initial p-h excitation passes from one nucleon to the others, see figure 5.3.

The process depicted in figure 5.3 can be understood from a thermodynamic's perspective. The nucleus formed with $1p-0h$ after the reaction is not in equilibrium because it is in a state of minimum entropy. Boltzmann introduced a fundamental principle of statistical mechanics which states that isolated systems evolve to maximize entropy. Entropy (S) is directly connected to the number of possible ways in which energy is distributed among the particles of a system (W), through Boltzmann's formula [78]:

$$S = k_B \cdot ln(W) \tag{5.2}$$

where $k_B \approx 1.38 \cdot 10^{-23} J/K$ is Boltzmann's constant. On the one hand, from equation (5.2) it follows that the bigger W, the higher the entropy. On the other hand it is logical that the most probable configuration is the one in which there are more possibilities, or equivalently W is higher. Therefore a system will tend to distribute energy among its

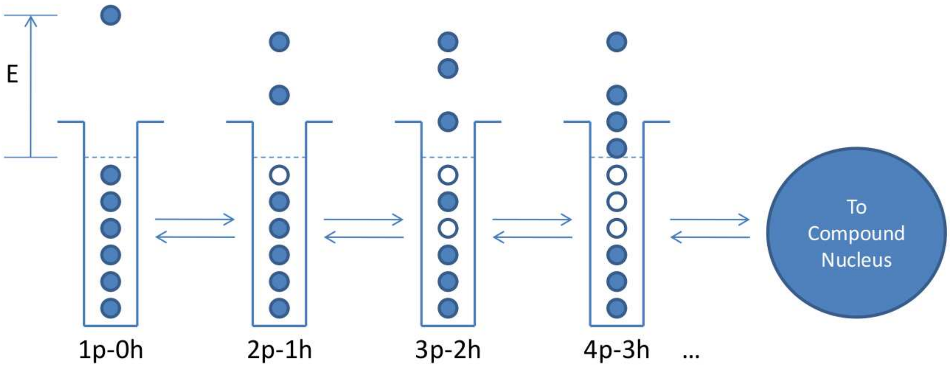

Figure 5.3: Schematic representation of the process of redistribution of excitation energy that can eventually form a CN [79] [8].

components in a way that entropy is maximized, following a similar process to the one depicted in figure 5.3.

With all this in mind, one can classify nuclear reactions depending on the result of the interaction between the projectile and the target nucleus. In general there will be several possible outcomes and intermediate stages as illustrated in figure 5.4.

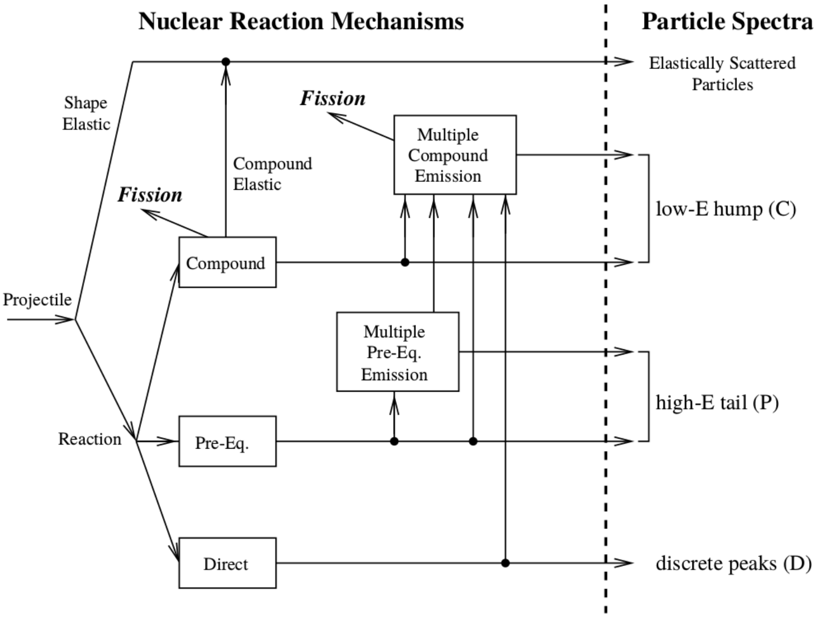

Figure 5.4: Scheme of the different reaction mechanisms that can take place when a projectile interacts with a target nucleus [26].

Figure 5.4 synthesizes all the possibilities of an arbitrary nuclear reaction, when a particle (neutron, proton, α...) impinges on a nucleus. The projectile can be either elastically scattered or it may be emitted after a compound nucleus is formed, during the pre-equilibrium state or following a direct reaction. The projectile is re-emitted with the same incident energy when it undergoes a shape-elastic scattering, which can be imagined as a classical collision between two rigid objects, or after a compound nucleus is formed, leaving the target nucleus in its ground state, compound elastic. The compound nucleus can also be left in an excited state, and can undergo fission before or after a multiple compound emission. The pre-equilibrium and direct reactions always leave the nucleus in an excited state. In this work we will focus on the compound nucleus reactions, specially on fission and radiative capture ones. The direct and pre-equilibrium components will be neglected because in the energy region of our data $E_n \sim 1$ MeV, more than 80% of the reaction cross section is given by the compound nucleus one. In addition the direct and pre-equilibrium entrance channels will predominantly contribute to the (n,n') channel which has a small impact on the evaluation.

5.2 Cross Sections

Cross sections are one of the most important observables when studying nuclear reactions. Usually denoted by σ, and with dimensions of area, cross sections between two particles can be defined as the area transverse to their relative motion within which they must meet in order to scatter from each other. When a cross section is specified as a function of some final state variable, such as the particle's angle, it is called *differential cross section.*

$$\frac{d\sigma}{d\Omega} = |f(\mathbf{p}', \mathbf{p})|^2 \tag{5.3}$$

where $|f(\mathbf{p}', \mathbf{p})|^2$ is the so called scattering amplitude. The derivation of equation (5.3) as well as an explicit form of $|f(\mathbf{p}', \mathbf{p})|^2$ will be given in appendix E.

The *total cross section* σ_T is the result of integrating the differential cross section over 4π and represents the probability of any kind of interaction taking place when a projectile with energy E approaches a nucleus. It can be unfolded into two cross sections, the *shape-elastic cross section* $\sigma_{S.E.}$ and the *reaction cross section* σ_R. The former can be understood as the collision of two particles without inner structure, while the latter measures the probability of the projectile acting on the inner structure of the target nucleus:

$$\sigma_T = \sigma_{S.E.} + \sigma_R \tag{5.4}$$

The reaction cross section itself is the sum of two cross sections:

$$\sigma_R = \sigma_{N.E.} + \sigma_{C.E.} \tag{5.5}$$

In equation (5.5), $\sigma_{N.E.}$ is the *non-elastic cross section*, or the cross section that the recoil nucleus is not left in its ground state, and $\sigma_{C.E.}$ is the *compound-elastic cross section*, which accounts for the possibility that the recoil is left in its ground state after a projectile-like particle is re-emitted. Using $\sigma_{C.E.}$ the *elastic cross section* σ_E, which is related to the probability that both particles interacting are left in their corresponding ground states after interacting, can be written as:

$$\sigma_E = \sigma_{S.E.} + \sigma_{C.E.} \tag{5.6}$$

And with this definition of elastic cross section, the total cross section can be re-written in the form:

$$\sigma_T = \sigma_E + \sigma_{N.E.} \tag{5.7}$$

Fortunately the quantities σ_T and σ_E of equation (5.7) can be measured experimentally. However to extract some meaningful information from a measurement, the experimental data has to be compared to a theoretical calculation to constraint parameters and discard models. This calculation is split into two parts, firstly an optical model with coupled channels calculation that yields σ_T, σ_R and $\sigma_{S.E.}$, secondly a compound nucleus decay calculation. In this work both were performed with Talys 1.9, although this program incorporates the code ECIS06 [80] to do the part of the calculation dependent on the optical model.

5.3 Optical Model

Making use of the optical model (OM) is the simplest way to calculate the cross sections σ_T, σ_R and $\sigma_{S.E.}$, which will then be the base to calculate the cross sections of the other mechanisms presented in figure 5.4. Doing a correct calculation is a crucial point as it influences on all the other cross sections. To calculate σ_R, ideally one should solve the Schrödinger equation of the system formed by the nucleus plus the projectile, see eq. (5.8), to calculate these cross sections.

$$\left(\frac{-\hbar^2}{2m}\nabla^2 + U\right)\Psi = i\hbar\frac{\partial\Psi}{\partial t} \tag{5.8}$$

However solving the above equation is very complicated. To attempt to simplify the problem the optical model was introduced in the 50's, by Le Levier and Saxon [81] and by Feshbach, Porter and Weisskopf [82]. The main idea developed by these authors is that the scattering of particles when interacting with nuclei can be treated in a similar way to light passing from one material to another with a complex refractive index, thus the name *optical*. Under this hypothesis the nucleon-nucleus potential U($\mathbf{r}$) is assumed to be complex and takes the form:

$$U(\mathbf{r}) = V(\mathbf{r}) + iW(\mathbf{r}) \tag{5.9}$$

where V($\mathbf{r}$) and W($\mathbf{r}$) are the real and the imaginary parts of the potential, respectively. In analogy with optics, the imaginary part of this potential (W in equation (5.9)) removes part of the flux from the shape-elastic channel to the reaction channels which are not calculated directly. For instance, in a two body reaction $a + X$, as the one in figure 5.5, U(r) is the nuclear potential that acts on a.

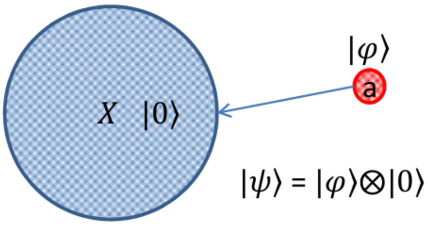

Figure 5.5: Schematic representation of a particle "a", with wave function $|\varphi\rangle$, impinging on a nucleus "X" in state $|0\rangle$. The state of the system is defined by $|\psi\rangle = |\varphi\rangle \otimes |0\rangle$.

In this formalism the incoming beam is supposed mono-energetic and is represented by a plane wave (see appendix E for details). Since the first theories of the optical potential were formulated in the 50s, a wealth of different formulations and improvements to the model have appeared.

5.3.1 Central Potentials

If the scattering potential U has a dependency on the radial coordinate such that U(r) $\rightarrow 0$ quicker than $1/r^3$ when $r \rightarrow \infty$, then it is possible to represent the stationary wave function as:

$$\Phi(r) = \sum_{l=0}^{\infty} \sum_{M=-l}^{l} R_{lM}(r) Y_l^M(\theta, \phi) \tag{5.10}$$

where $Y_l^M(\theta, \phi)$ are the spherical harmonics ans $R_{lM}(r)$ is a radial function that depends as well on the quantum numbers $l,\ M$. In general when $r \rightarrow \infty$ this function can be approximated taking into account the asymptotic behavior of Bessel's functions to:

$$R_{lM}(r) \sim \frac{C_{lM}}{r} sin\left(kr - \frac{\pi l}{2} + \delta_l\right) \tag{5.11}$$

where C_{lM} and δ_l are independent from r, but depend on the indexed quantum numbers and on the energy $E = \hbar^2 k^2/2m$. The quantities δ_l are real numbers that represent physically the impact of the scattering potential on the radial part of the wave functions, they are called *phase shifts* and are of paramount importance to determine cross sections. It can be proven that the relation between these phase shifts δ_l and the scattering amplitude $f(\mathbf{p}', \mathbf{p})$ is:

$$f(\mathbf{p}', \mathbf{p}) = \frac{1}{k} \sum_{l=0}^{\infty} (2l+1) f_l \cdot P_l(cos(\theta)) \tag{5.12}$$

where $P_l(cos\theta)$ are Legendre's polynomials, θ is the scattering angle between **p**' and **p**, and f_l:

$$f_l = \frac{e^{2i\delta_l} - 1}{2i} = e^{i\delta_l} sin(\delta_l) \tag{5.13}$$

The quantity f_l depends in fact on the energy and it is named the *partial waves' amplitude.* When substituting it in equation (5.3), the differential cross section becomes:

$$\frac{d\sigma}{d\Omega} = \frac{1}{k^2} \sum_{l=0}^{\infty} \sum_{l'=0}^{\infty} (2l+1)(2l'+1) \cdot f_l f_{l'}^* \cdot P_l(cos(\theta)) P_{l'}(cos(\theta)) \tag{5.14}$$

The total cross section can be written in terms of the phase shift δ_l:

$$\sigma = \frac{4\pi}{k^2} \sum_{l=0}^{\infty} (2l+1) sin^2(\delta_l) \tag{5.15}$$

By virtue of equation (5.15), the problem of calculating cross sections is reduced to calculating the phase shifts δ_l, which contain all the information about the interaction in the long distance limit ($r \rightarrow \infty$). It just remains to obtain an optical potential U(r) that is able to reproduce the experimental data.

5.3.2 Deformed Nuclei: Coupled Channels Calculation

The formalism described before is only valid for spherical nuclei. In reality just the nuclei with closed shells are spherical and thus have central potentials, i.e. that depend only on the radial coordinate. The rest of the nuclei are deformed and display low energy collective states. In the case of actinides this low energy excitations are rotational states that are easily populated by hadron scattering, and which are strongly coupled between them. This has to be taken into account quantifying the amount of flux that is transfered from the most relevant channels to the ground state. The potential has to have a dependence on the nuclear radius, which can be expanded in a series of spherical harmonics $Y_\lambda^\mu(\theta,\phi)$ and with shape parameters $\alpha_{\lambda\mu}$:

$$R(\theta,\phi) = R_\alpha \left(1 + \sum_{\lambda=1}^{\infty} \sum_{\mu=-\lambda}^{\lambda} \alpha_{\lambda\mu} Y_\lambda^\mu(\theta,\phi)\right) \tag{5.16}$$

The series (5.16) is a common parametrization of the nuclear radius, where R_α is the deformation dependent radius and can be related to the spherical one $R_0 = r_0 A^{1/3}$ by imposing a condition of volume conservation:

$$R_0 = R_\alpha \left(1 + \frac{3}{4\pi} \sum |\alpha_{\lambda\mu}|^2 + o(\alpha^3)\right)^{\frac{1}{3}} \tag{5.17}$$

where the orthogonality of the spherical harmonics ($\int Y_l^m Y_{l'}^{m'*} d\Omega = \delta_{ll'}\delta_{mm'}$) has been used to obtain eq. (5.17).

In deformed nuclei there is a strong coupling between the ground state and the first states of the rotational (or even vibrational) bands that can be built on top of it. This means that these states can feed the elastic channel after being populated, we will then say that these states are *coupled*. In theory one should take into account the coupling of all the levels energetically accessible, but in practice only a small number of levels are actually relevant, those strongly coupled to the ground state, and are included in the calculation. When coupling different levels parity and angular momentum conservation laws apply.

Figure 5.6 represents the coupling scheme of a ^{239}Pu target, as a reminder the reaction $n + {}^{239}Pu$ will be used to determine the structure model parameters of $^{240}Pu^*$. The left hand side of the image shows the ground state and the first three excited states of the rotational band built on top of it. The right hand side of the figure depicts the first four levels on another rotational band built over the vibrational state $3/2^+$. The blue arrows represent the possible couplings between the different states of these two bands. Taking these first eight levels is customary for the $n + {}^{239}Pu$ reaction, i.e. in JENDL 4.0, because they are the most strongly coupled and they are sufficient to describe the total reaction cross section. JEFF 3.3 includes another vibrational level but the impact on this cross section is minimal.

5.3.3 Parametrization of the Optical Model Potential (OMP)

In the frame of the optical model the nucleon-nucleus interaction is represented by a complex potential $U(\mathbf{r}, E)$, where r is the space coordinate and E the energy of the

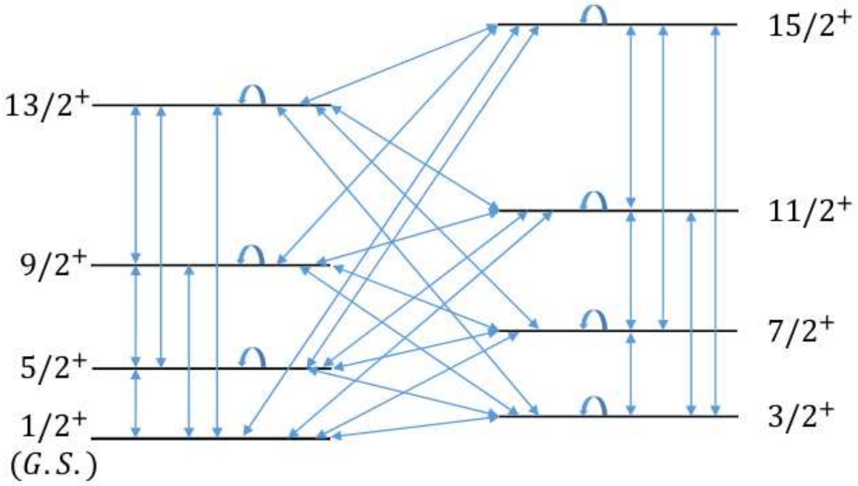

Figure 5.6: Schematic representation of the coupling scheme of ^{239}Pu. Here the first four states of the rotational band over the ground state are coupled to the four states of another rotational band built on a vibrational state. All the channels except for the ground state are coupled with themselves.

incident particle. This potential can be calculated in a microscopic way or be determined in a phenomenological way by adjusting the parameters to reproduce nuclear data. In this work we will explain the phenomenological approach to optical potentials, for which different kinds of parametrization can be found in the literature. For local potentials, in which the interaction is considered punctual, as the one by Koning and Delaroche [83], and for dispersive potentials, which connect the imaginary and real parts of the potential, like the ones of Soukhovitskii *et al.* [84] [28], or Romain *et al.* [85]. However the total σ_T and shape elastic $\sigma_{S.E.}$ cross sections are calculated using the parameters of JENDL 4.0. which were obtained using the parametrization Soukhovitskii *et al.*, as detailed in appendix F.

5.3.4 Calculation of the Total, Shape-Elastic and Reaction Cross Sections

A calculation with ECIS06 was done for the neutron induced reaction $n + {}^{239}Pu$ with the optical model, and its parametrization, described above. The code ECIS06 is ran by Talys and it calculates the total σ_T, shape elastic $\sigma_{S.E.}$ and reaction σ_R cross sections, recalling equation (5.4):

$$\sigma_T = \sigma_{S.E.} + \sigma_R$$

Because of the relative simplicity to measure the total cross section, it is enough to measure the flux of particles before and after the target, there are abundant high-quality measurements of it. The parameters of the optical model given in appendix F were adjusted by the JENDL 4.0 collaboration in the low neutron-energy range up to 10 keV, with the data of Harvey *et al.* [86], and for energies between 48 keV to 20.9 MeV with the data of Poenitz *et al.* [87], [88]. In this work we use a neutron energy between 25 keV and 6 MeV to do the evaluation for two reasons. First, our data, obtained with a surrogate reaction of $n + {}^{239}Pu$, have an energy resolution of 100 keV, therefore it is useless to adjust the parameters in the resonance energy range. Second, our data is just exploitable up to an excitation energy of the ${}^{240}Pu^*$ of 8 MeV, which is equivalent to 1.5 MeV in incident neutron energy. The evaluation range was extended up to 6 MeV to make it more congruent and because the second chance fission of the CN starts at 5.65 MeV. In figure 5.7 we compare the experimental data of Poenitz *et al.* to our calculation with Talys and the parameters of JENDL 4.0 and the evaluation JEFF 3.3.

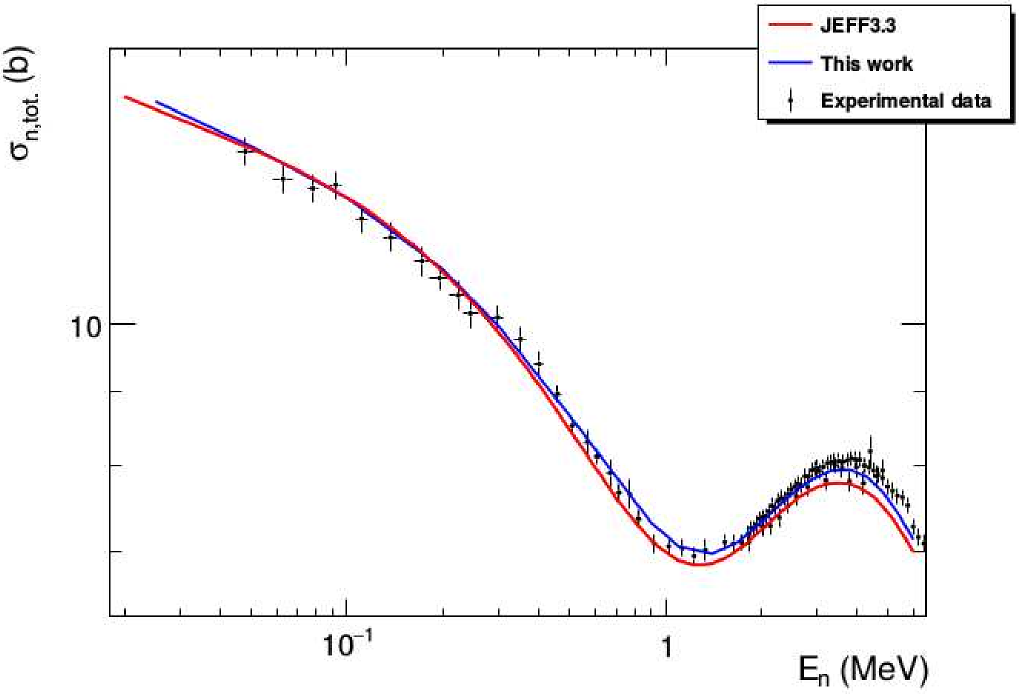

Figure 5.7: Total cross section as a function of incident neutron energy for the reaction $n + {}^{239}Pu$. The blue solid line is the calculation with Talys and the parameters of JENDL 4.0, the red solid line is from JEFF 3.3 and the experimental data is from [87] and [88].

From the total cross section one has to remove the contribution of the shape elastic cross section, to obtain the reaction one. In figure 5.8 the contribution of these cross sections to the total one is illustrated. The problem is that neither the reaction cross section, nor the shape-elastic one are measurable, thus $\sigma_{S.E.}$ cannot be compared directly to experimental data to constrain further the OMP parameters.

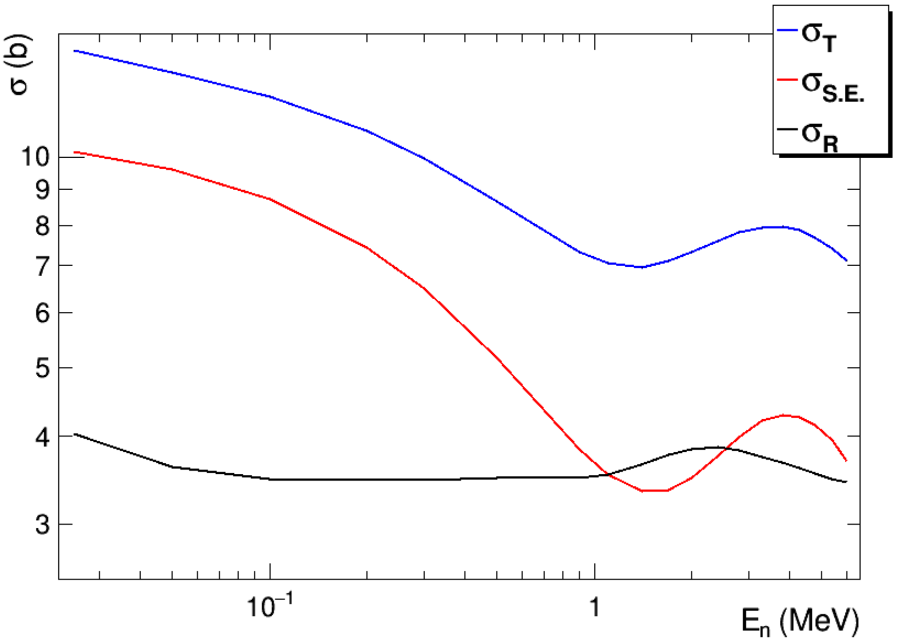

Figure 5.8: Calculation of the total σ_T, shape elastic $\sigma_{S.E.}$ and reaction σ_R cross section as a function of incident-neutron energy for the reaction $n + {}^{239}Pu$.

5.4 Compound Nucleus Reactions

To determine the branching ratios $G_{n,\chi}$ that will be used in chapter 6 it is necessary to understand which are the ingredients involved in the decay of a compound nucleus. This way the parameters of the model can be adjusted and optimized to reproduce the cross sections.

5.4.1 Hauser-Feshbach Theory

In the energy domain of this work, the ${}^{240}Pu^*$ compound nucleus is in the statistical energy regime and thus its decay is studied within the Hauser-Feshbach formalism [82]. The formation of a compound nucleus after a reaction $X(a,a')X'$, as described in section 5.1 obeys the following energy, spin and parity conservation rules:

$$E_a + S_a + E_x = E_{a'} + S_{a'} + E'_x = E^{tot} \tag{5.18}$$

where E_a is the projectile's energy, S_a is its separation energy, E_x is the excitation energy of the target nucleus, $E_{a'}$ is the ejectile's energy, $S_{a'}$ its separation energy, while E'_x is the excitation energy of the recoil nucleus and E^{tot} is the total energy of the system.

$$s + I + l = s' + I' + l' = J \tag{5.19}$$

where s is the projectile spin and l its orbital angular momentum, I is the spin of the target nucleus, s' is the spin of the scattered particle and l' its orbital angular momentum while I' is the spin of th recoil nucleus and J is the total angular momentum of the system.

$$\pi_0 \Pi_0 (-1)^l = \pi_f \Pi_f (-1)^{l'} = \Pi \tag{5.20}$$

where π_0 is the parity of the projectile, Π_0 is the parity of the target, π_f is the parity of the ejectile, Π_f is the parity of the recoil nucleus and Π is the parity of the compound system.

Knowing that equations (5.18), (5.19) and (5.20) must hold true, the compound nucleus formula for the binary cross section, can be expressed in the form of eq. (4.174) of Talys's Manual [26]:

$$\begin{aligned}\sigma^{comp}_{\beta\beta'} =& D^{CN}\frac{\pi}{k^2}\sum_{J=mod(I+s,1)}^{l_{max}+I+s}\sum_{\Pi=-1}^{1}\frac{2J+1}{(2I+1)(2s+1)}\sum_{j=|J-I|}^{J+I}\sum_{l=|j-s|}^{j+s}\sum_{j'=|J-I'|}^{J+I'}\sum_{l'=|j'-s'|}^{j'+s'} \\ &\times \delta_\pi(\beta)\delta_\pi(\beta')\frac{T^J_{\beta lj}(E_a)\langle T^J_{\beta' l' j'}(E_{a'})\rangle}{\sum_{\beta'',l'',j''}\delta_\pi(\beta'')\langle T^J_{\beta'' l'' j''}(E_{a''})\rangle}W^J_{\beta lj\beta' l' j'}\end{aligned} \tag{5.21}$$

where in (5.21): D^{CN} is the depletion factor that accounts for direct and pre-equilibrium effects, k is the wave number, l_{max} is the maximum l-value for projectile, α designates the system of the projectile and target nucleus $\beta = \{a, s, E_a, E_x, I, \Pi_0\}$, where a is the projectile, $\delta_\pi(\beta) = 1$ if $\pi_0\Pi_0(-1)^l = \Pi$ and 0 otherwise. The system of the ejectile and the recoil is designated by $\beta' = \{a', s', E_{a'}, E'_x, I', \Pi_f\}$, where a' is the ejectile, $\delta_\pi(\beta') = 1$ if $\pi_f\Pi_f(-1)^{l'} = \Pi$ and 0 otherwise. The summation of the denominator with doubly primed variables, accounts for all the possible exit channels. The coefficients T are the transmission coefficients of the entrance channel, while the transmission coefficients of the outgoing channels are denoted by $\langle T\rangle$. This notation indicates that this transmission coefficients are calculated differently depending on whether the channels β' and β'' correspond to a discrete state or a state of the continuum. Finally, the W's are the width fluctuation correction (WFC) factors, which account for the correlations that exist between the incident and outgoing waves.

A very clear and detailed review of the Hauser-Feshbach theory was done by Hodgson [91]. In section 2 of the article he details step by step the deduction of a very similar equation to (5.21), including the WFC factors. For further detail on how to compute the different terms that intervene in the general formula (5.21) we refer to [26].

Compound Nucleus Formation Cross Section

The compound nucleus formation cross section can be deduced from equation (5.21) as described in [26] and it depends on the entrance channel β. In the case of interest, $n + {}^{239}Pu \rightarrow {}^{240}Pu^*$, the entrance channel is $\beta = \{n, 1/2, E_n, 0, 1/2, +\}$. Thus the cross section to form a ${}^{240}Pu^*$ CN in a state of spin J and parity Π and total energy E^{tot} is:

$$\sigma^{CN}_{J\Pi}(E^{tot}) = D^{comp}\frac{\pi}{k^2}\frac{2J+1}{(2I+1)(2s+1)}\sum_{j=|J-I|}^{J+I}\sum_{l=|j-s|}^{j+s}T^J_{\beta lj}(E_n)\delta(\beta) \tag{5.22}$$

The cross section in eq. (5.22) must be summed over all the possible combinations J and Π to obtain the compound nucleus cross section $\sigma_{CN}(E_n)$, recalling that $E^{tot} = E_n + S_n + E_x$, is plotted in figure 5.9.

The optical model calculation produces the total cross section as well as the reaction cross section, which can be defined as the sum of the direct, pre-equilibrium and compound-nucleus reaction cross sections. None of these is an observable so it has to be

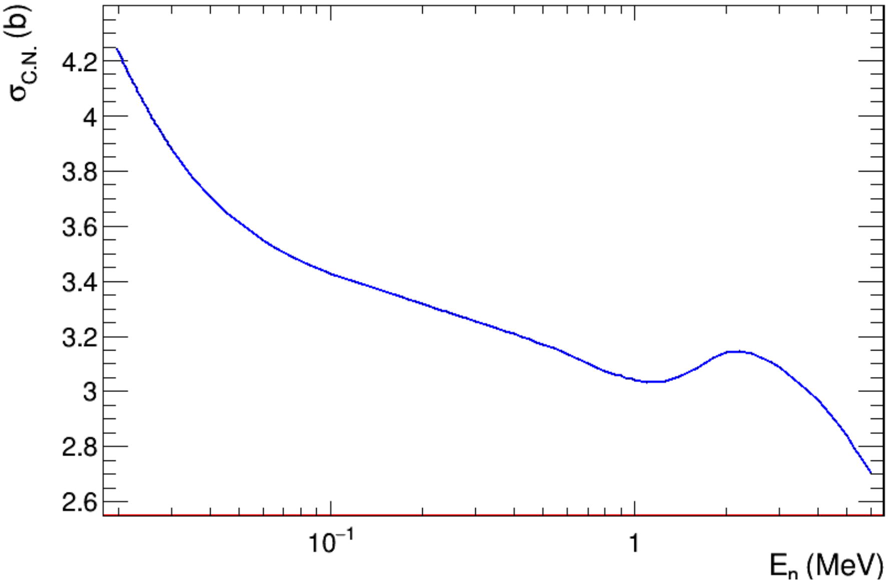

Figure 5.9: Calculation of the compound nucleus (C.N.) cross section as a function of incident neutron energy on a ^{239}Pu target.

deduced theoretically. Figure 5.10 illustrates the importance of determining correctly the compound nucleus cross section. At $E_n = 1.5MeV$, which is the energy to which we have access experimentally in which the ratio is the lowest, $\sigma_R = 3.64\ b$ and $\sigma_{C.N.} = 3.06\ b$, thus the compound nucleus cross section amounts for 84% of the reaction one.

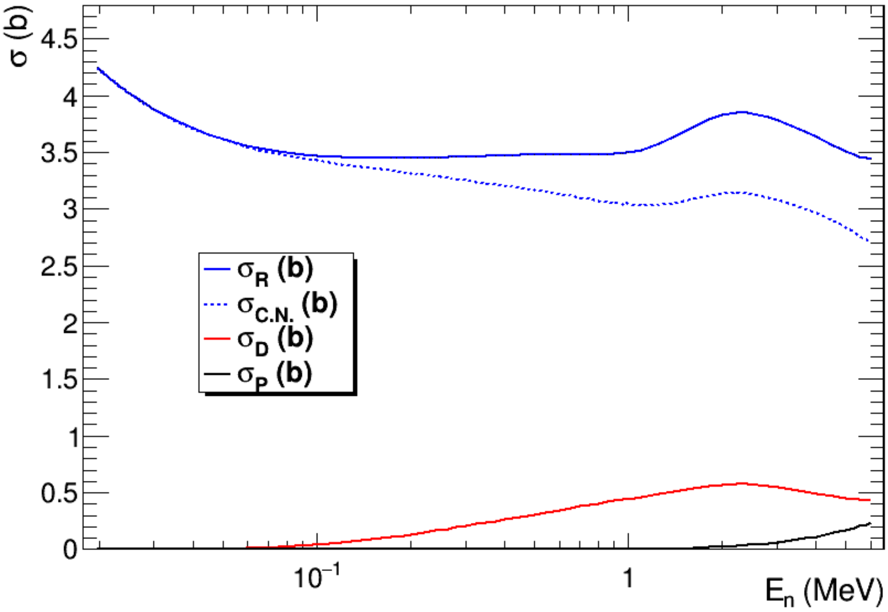

Figure 5.10: Calculation of the reaction (R), compound nucleus (C.N.), direct (D) and pre-equilibrium (P) cross sections as a function of incident neutron energy on a ^{239}Pu target. The reaction cross section (blue solid line) is the sum of the other three.

In figure 5.11 we compare the elastic cross section $sigma_E$ to the experimental data. This cross section is the sum of the shape elastic cross section $\sigma_{S.E.}$ and the compound elastic one $\sigma_{C.E.}$. There are no experimental data of $\sigma_{S.E.}$, however in the energy range of this study $\sigma_{S.E.} \sim 0.9\sigma_E$, as it can be seen in figure 5.11, thus comparing the calculation to elastic scattering data is useful to check that there are no big issues with the OM parameters.

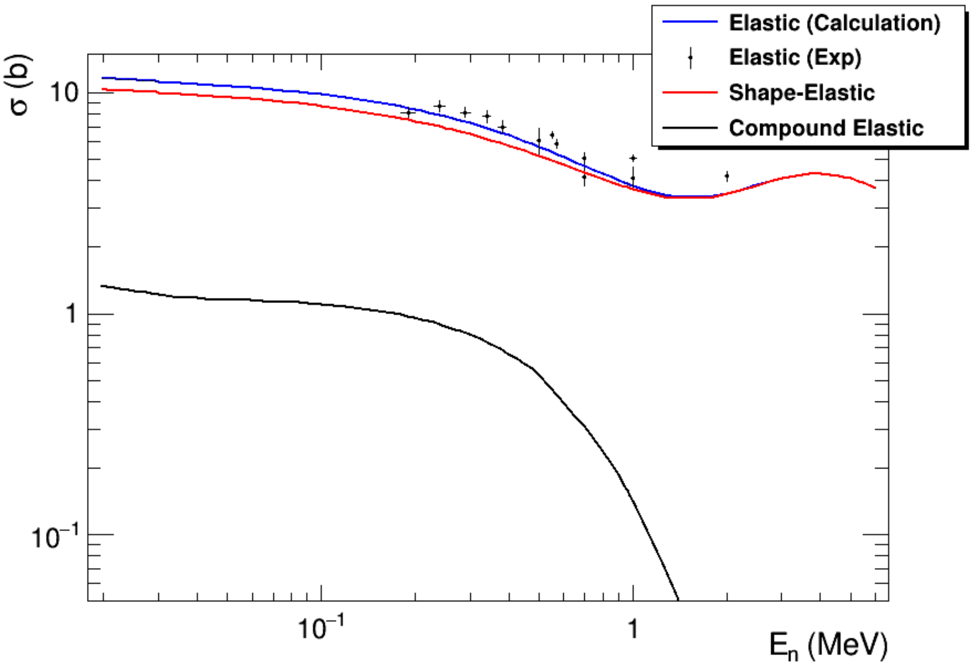

Figure 5.11: Calculation of the elastic cross section σ_E as a function of incident-neutron energy on a ${}^{239}Pu$ target, compared to the experimental data from Cranberg (report from LANL 1959), Yue *et al.* [89] and Knitter and Coppola [90]. The red solid line represents the calculated shape elastic cross section $\sigma_{S.E.}$ and the black line the compound elastic one $\sigma_{C.E.}$.

Compound Nucleus Decay Cross Sections

The quantity $\sigma_{C.N.}$ is calculated theoretically to produce cross sections from surrogate reaction experiments as we recall from equation (1.2):

$$\sigma^{A}_{n,\chi}(E_n) \cong \sigma^{A+1}_{CN}(E_n) \cdot P^{surr.}_{\chi}(E^*)$$

which is related to the equation:

$$\sigma^{A}_{n,\chi}(E_n) = \sigma^{A+1}_{CN}(E_n) \sum_{J^\pi} S(E^*, J^\pi) G_{n,\chi}(E^*, J^\pi)$$

where $S(E^*, J^\pi)$ is the usual nomenclature of the spin-parity distribution of the compound nucleus $A+1$ in the case of neutron induced reactions, which is equivalent to $F(E^*, J^\pi)$ for surrogate reactions. The radiative capture $\sigma_{n,\gamma}$ and fission $\sigma_{n,f}$ cross sections are directly related to $G_{n,\chi}$ through the above equation.

All the open decay channels should be deduced from σ_R but under the hypothesis that the reactions $\alpha + {}^{240}Pu \rightarrow \alpha' + {}^{240}Pu^*$ and $n + {}^{239}Pu \rightarrow {}^{240}Pu$ lead to the same CN ${}^{240}Pu^*$ as explained in chapter 1, these decay channels are deduced from equation (5.22). The gamma-decay, the neutron emission and the fission cross sections are calculated imposing that they are the only three possible decay paths, thus proton and other particles emission cross sections are neglected.

Therefore to obtain the cross sections of interest, it will be necessary to determine the transmission coefficients that appear in eq. (5.21), which is equivalent to knowing the model's structure parameters of the compound nucleus, as described in the next section.

5.4.2 Properties of the Compound Nucleus

Level density

It is of paramount importance to correctly determine the level structure and level density of the compound-nucleus because they have an influence in almost all of the observables. For example, small differences in the shape of these densities can have a big impact on the neutron capture cross section by favoring or inhibiting gamma-decay as compared to fission or neutron emission. Similarly neutron emission, when $E^* \geq S_n$, depends on the level scheme of the residual nucleus. Discrete levels are well known at low excitation energies E^* and near to the neutron separation energy S_n thanks to the resonances measurement in neutron induced reactions, but even in these cases the properties of these levels, like spin and parity, cannot be resolved.

In the energy range of this study, $4 \leq E^* \leq 8$ MeV, the compound nuclei will be formed in the *energy continuum*, or *statistical regime*. In this regime discrete levels cannot be distinguished from one another, either because the experimental resolution prevents from it or because the average level spacing $\langle D \rangle$ becomes smaller than the level width Γ. The object of this study is ${}^{240}Pu$ which is a deformed heavy nucleus and thus it early attains this statistical regime. At an excitation energy $E^* \sim 1.2 MeV$ the experimental level density starts to diverge from the theoretical ones because all the existing discrete levels cannot be measured. In cases like this it is convenient to define the *total level density* as a function of excitation energy $\rho(E^*)$:

$$\rho(E^*) = \frac{dN(E^*)}{dE^*} = \frac{1}{\langle D \rangle} \tag{5.23}$$

where $dN(E^*)$ is the number of levels within an energy interval dE^* around the excitation energy E^*, and $\langle D \rangle$ is the average level spacing in this energy region. It follows from equation (5.23) that to obtain the total number of levels $N(E^*)$, one should integrate $\rho(E^*)$ from 0 to E^*. This total level density $\rho(E)$ is in fact the sum over spin J and parity Π of the level density $\rho(E^*, J, \Pi)$ [92]:

$$\rho(E^*) = \sum_J \sum_\Pi \rho(E^*, J, \Pi) \tag{5.24}$$

The level density $\rho(E^*, J, \Pi)$ in the summation 5.24 can be factorized if it is given by analytical expressions such as:

$$\rho(E^*, J, \Pi) = P(E^*, J, \Pi) R(E^*, J) \rho(E^*) \tag{5.25}$$

where $P(E^*, J, \Pi)$ is the parity distribution and $R(E^*, J)$ is the spin distribution. In this work the parity equipartition is assumed for the used phenomenological model, eq. (5.26), which is a good assumption for excitation energies higher than a few MeV.

$$P(E^*, J, \Pi) = \frac{1}{2} \tag{5.26}$$

The nuclear levels are degenerate in the magnetic quantum number M, i.e. there are $(2J+1)$ states per level, therefore to obtain the *total state density* $\omega(E^*)$:

$$\omega(E^*) = \sum_J \sum_\Pi (2J+1)\rho(E, J, \Pi) \tag{5.27}$$

One of the best known analytical expressions of the level density is the Fermi gas model (FGM). It was first derived by Bethe [93] and it is based on two assumptions, that the single particle states which construct the nucleus are equally spaced, which is true if nucleons do not interact between them, and that there are no collective levels. For a system of protons and neutrons the total Fermi gas state density is:

$$\omega_F(E^*) = \frac{\sqrt{\pi}}{12} \frac{\exp\left[2\sqrt{aU}\right]}{a^{1/4}U^{5/4}} \tag{5.28}$$

where $a = \frac{\pi^2}{6}(g_p + g_n)$ is the level density parameter, with g_p/g_n the spacing of the proton/neutron single particle states near the Fermi energy. In contemporary models a depends on excitation energy, see for further detail [92] [94]. In equation (5.28) also appears the effective excitation energy U:

$$U = E^* - \Delta \tag{5.29}$$

where Δ is an empirical parameter related to the pairing energy and which is included to account for the odd-even effects in nuclei. The underlying idea is that Δ accounts for the fact that pairs of nucleons must be separated before each component can undergo a single particle excitation. In practice this energy shift is an adjustable parameter to reproduce observables.

Under the assumption that the projections of the total angular momentum are randomly coupled, it can be derived [93] [95] that the Fermi gas level density is:

$$\rho_F(E^*, J, \Pi) = \frac{1}{2} \cdot \frac{2J+1}{2\sqrt{2\pi}\sigma^3} \exp\left[-\frac{(J+1/2)^2}{2\sigma^2}\right] \cdot \frac{\sqrt{\pi}}{12} \frac{\exp\left[2\sqrt{aU}\right]}{a^{1/4}U^{5/4}} \tag{5.30}$$

where the first factor $1/2$ is given by eq (5.26) and σ^2 is the spin cut-off parameter, which represents the width of the angular momentum distribution. It depends on excitation energy as it will be shown when fitting our data. Equation (5.30) is a particular case of the factorization of equation (5.25), where the spin distribution $F(E^*, J)$ takes the form:

$$F(E^*, J) = \frac{2J+1}{2\sigma^2} \exp\left[-\frac{(J+1/2)^2}{2\sigma^2}\right] \tag{5.31}$$

Summing $\rho_F(E^*, J, \Pi)$ over parity and spin gives the total level density for the Fermi gas model,

$$\rho_F(E^*) = \frac{1}{\sqrt{2\pi}\sigma}\frac{\sqrt{\pi}}{12}\frac{\exp\left[2\sqrt{aU}\right]}{a^{1/4}U^{5/4}} \tag{5.32}$$

This level density however does not explicitly account for collective levels, although it is well known that these exist as a result of coherent excitations of the fermions that constitute the nucleus. These can be included in an effective way with the level density parameter a, and even though its energy dependence is conceived to handle shell effects, in most cases this parametrization is sufficient. However, in calculations involving strongly deformed nuclei it is convenient to introduce enhancement factors, rotational K_{rot} and vibrational K_{vib} (for further details see [26] [92]), therefore the deformed Fermi gas level density $\rho_{F,def}(E^*, J, \Pi)$ reads:

$$\rho_{F,def}(E^*, J, \Pi) = K_{rot}(E^*)K_{vib}(E^*)\rho_{F,int}(E^*, J, \Pi) \tag{5.33}$$

where $\rho_{F,int}(E^*, J, \Pi)$ is the intrinsic Fermi gas level density that should just describe single-particle excitations, with a different, smaller, level density parameter a than before. For the calculations performed in this work the collective enhancement was explicitly included in the level density used.

In this work we used the constant temperature model (CTM), proposed by Gilbert and Cameron in the 60's [62]. It is a hybrid between the FGM at high excitation energies, and an exponential function at low ones. The function is deduced from the experimental data, that suggest that at low E^* the cumulated number of levels $N(E^*)$ follows the so-called constant temperature law:

$$N(E^*) = \exp\left(\frac{E^* - E_0}{T}\right) \tag{5.34}$$

where the nuclear temperature T and the energy E_0 are adjustable parameters that serve to reproduce data. Applying to this expression the definition of level density (5.23):

$$\rho_T(E^*) = \frac{dN(E^*)}{dE^*} = \frac{1}{T}\exp\left(\frac{E^* - E_0}{T}\right) \tag{5.35}$$

This expression is matched with FGM at a certain matching E_M such that both densities are equal at this energy,

$$\rho_T(E_M) = \rho_F(E_M) \tag{5.36}$$

and that their derivatives are also equal:

$$\frac{d\rho_T}{dE^*}(E_M) = \frac{d\rho_F}{dE^*}(E_M) \tag{5.37}$$

From these conditions two expressions can be found for the temperature T and the energy E_0. However in this work they are considered as adjustable parameters. As a matter of fact, the level density may have a discontinuous derivative in contrast with equation (5.37), as seen in previous works [96] [46].

To predict the shape of the level density $\rho(E)$ there are different statistical models, but we chose the CTM because it works well for heavy deformed nuclei, like Pu, and there is experimental evidence that supports this choice as detailed in [36], [97] and [38].

It is worth mentioning that currently a big effort is being done to improve microscopic models, specially the work done by S. Hilaire *et al.* [98] to produce a level density using the Gogny force in a Hartree-Fock-Bogoliubov (HFB) temperature-dependent formalism.

Experimental data is used to constrain the models, i.e. to adjust their parameters or to rescale the predictions of the microscopic approach. At low excitation energies, where all levels have been measured, the level density should reproduce the discrete levels of the nucleus. For an excitation energy around the neutron separation S_n, the mean energy resonance spacing of low energy *s-wave* ($l = 0$) neutrons, $\langle D_0 \rangle$, is used to constrain the density of states that can be populated from $l + s$ coupling of the impinging neutron and the ground state of the target nucleus:

$$\frac{1}{D_0} = \sum_{J=I-1/2}^{J=I+1/2} \rho(S_n, J, \Pi) \tag{5.38}$$

where I is the spin of the target nucleus. Recalling that the parity is conserved, equation (5.20), then in the case of neutrons impinging on ${}^{239}Pu$:

$$n(l = 0, s = 1/2) + {}^{239}Pu(I^{\pi} = 1/2^{+}) \rightarrow {}^{240}Pu(J^{\pi} = 0^{+}, 1^{+}) \tag{5.39}$$

Taking into account the possible coupling shown in expression (5.39), from equation (5.38) the mean resonance spacing can be deduced $\langle D_0 \rangle = 1/[\rho(S_n, 0^{+}) + \rho(S_n, 1^{+})]$. For this reaction, neutron experimental data gives a value $\langle D_0 \rangle = 2.20 \pm 0.05 eV$ [99]. In figure 5.12 we compare the level density $\rho(E, 0^{+}) + \rho(E, 1^{+})$ of ${}^{240}Pu$ obtained with the Gilbert-Cameron model and with the microscopic model of Hilaire *et al.*:

Figure 5.12 perfectly illustrates the discrepancies between the existing models. As a matter of fact, it is extremely difficult to predict the shape of the level density for intermediate and high excitation energies. During the evaluation process of the reaction $n + {}^{239}Pu \rightarrow {}^{240}Pu$, we explored the possibility of using the microscopic level density calculated by Hilaire *et al.* with the HFB formalism, but the results obtained for the radiative capture cross section were not satisfactory. The reason is that the microscopic calculation is consistently higher than the CTM between $1.5 MeV$ and $6 MeV$, which implies that, when the compound nucleus is formed, its decay via gamma emission is favored as compared to fission for example, reason why in this work the Gilbert-Cameron model was chosen. This choice seems to be supported by the results obtained in a recently published work on the level density and gamma strength function of ${}^{240}Pu$ [38].

In figure 5.13 we compare the cumulative number of levels $N(E^{*})$ of ${}^{240}Pu$ over its ground state, which matches the experimental number of levels up to $1.35 MeV$, to the level density of the 1^{st} barrier (blue solid) and the 2^{nd} barrier (blue dotted). Looking at figure 5.13 it is immediate to remark the difference between the number of levels over the barriers and over the ground state. This stems from the different deformation and temperature of the ${}^{240}Pu$ nucleus over the barriers [100].

Gamma Strength Function

To describe the γ-decay process, apart from the level density, the gamma strength function (γSF) is introduced. It is a fundamental ingredient that, in combination with level density and fission parameters in fissile nuclei, rules the competition between the different open

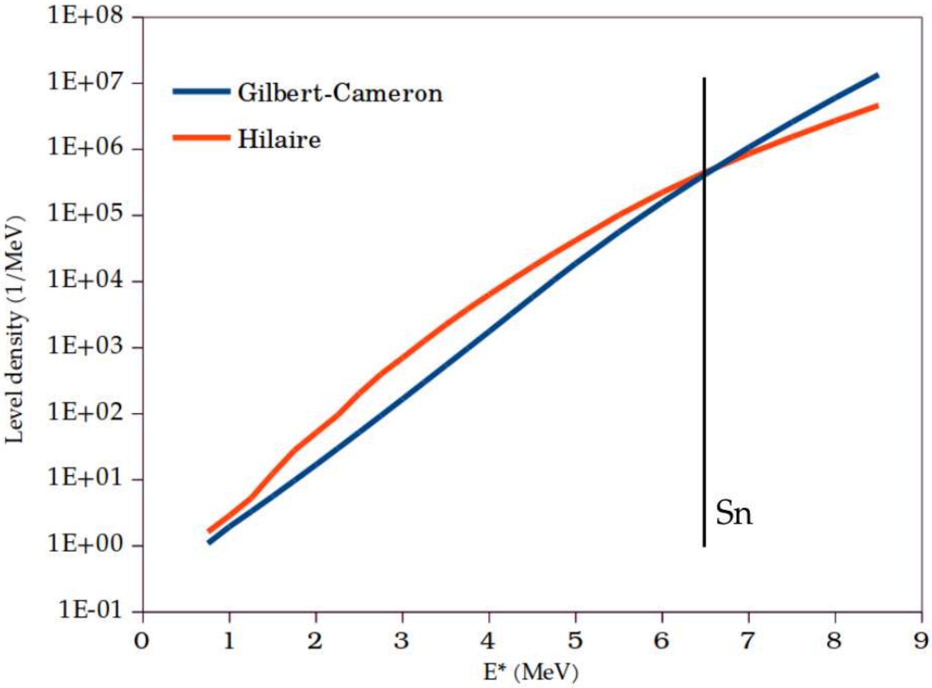

Figure 5.12: Level density $\rho(E, 0^+)+\rho(E, 1^+)$ of ^{240}Pu obtained with the Gilbert-Cameron model (blue) and with Hilaire *et al.* model (red). The black vertical line represents the neutron separation energy, at which both cross because they are adjusted to fit the experimental data $\rho(S_n, 0^+/1^+) = 1/\langle D_0\rangle = 1/2.2\ [eV^{-1}] \approx 455000\ [MeV^{-1}]$.

decay channels. Thus this function is intimately related to the γ-emission probability of the decaying nucleus. For a multi-pole transition of the type "Xl", with $X = E, M$ and l the momentum of the transition, the γSF f_{Xl} is defined as the average reduced width partial radiation $E_\gamma^{-(2l+1)}\langle\Gamma_{Xl}(E_\gamma)\rangle$, per energy interval as:

$$f_{Xl}(E_\gamma) = E_\gamma^{-(2l+1)}\langle\Gamma_{Xl}(E_\gamma)\rangle/D \tag{5.40}$$

where E_γ is the gamma energy, and D is the average spacing of the resonances. The transmission coefficient $T_{XL}(E_\gamma)$ can be expressed as:

$$T_{Xl}(E_\gamma) = 2\pi E_\gamma^{-(2l+1)} f_{Xl}(E_\gamma) \tag{5.41}$$

Equation (5.41) shows the relation between transmission coefficients and the γSF and eq. (5.40) of this function with D, which is related to the level density by $\rho = 1/D$. This is the reason why the level density ρ, together with the γSF, plays a crucial role to calculate the γ-cascade decay. The multipolarity of the transitions is defined by the selection rules, but in practice only the $E1$, $M1$ and $E2$ transitions are relevant, being $E1$ the strongest one and usually referred to as the giant electric dipole resonance (GDR).

In the 50s a great interest on the strength function developed, and a big step forward was done with Brink's hypothesis [101]. D. M. Brink proposed in his PhD thesis (1955) that the photoabsorption cross section of the GDR is independent of the detailed structure of the initial state. This hypothesis was extended in 1962 by P. Axel [102] to include absorption and emission of γ-rays between resonant states. The combination of both is

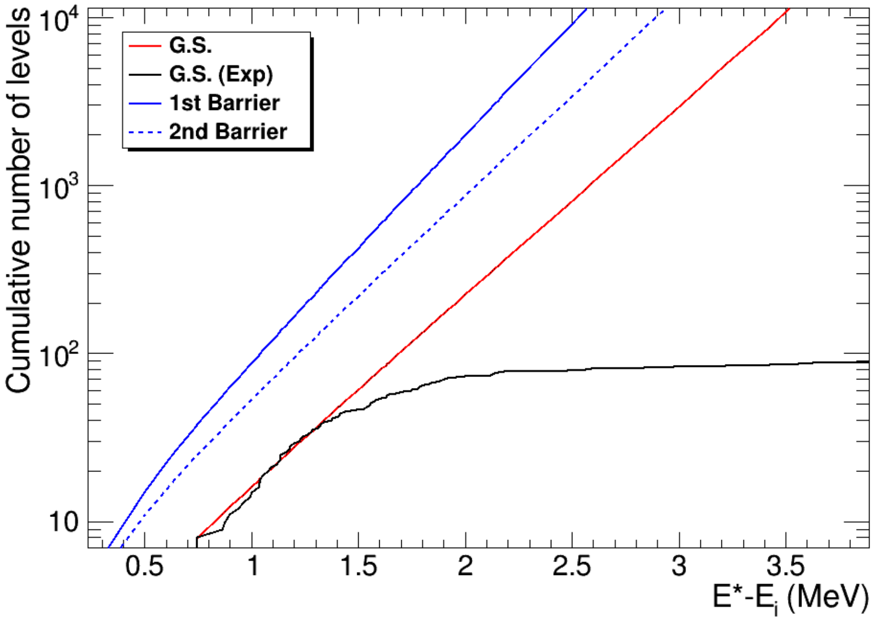

Figure 5.13: Cumulative number of ^{240}Pu levels obtained with the Gilbert-Cameron model over the ground state ($E_i = 0MeV$) compared to the experimental value ($E_i = 0MeV$), and the 1^{st} ($E_i = 5.97MeV$), and 2^{nd} ($E_i = 5.1MeV$) barrier.

known as the generalized Brink-Axel hypothesis, and it implies that the dipole γ-decay strength has no explicit dependence on excitation energy, spin or parity, apart from the usual selection rules.

The Brink-Axel hypothesis is widely used as it simplifies a lot the problem of determining the shape of the γSF, and it leads to a function related to a standard Lorentzian:

$$f_{Xl}(E_\gamma) = K_{Xl}\frac{\sigma_{Xl}E_\gamma\Gamma^2_{Xl}}{(E^2_\gamma - E^2_{Xl})^2 + E^2_\gamma\Gamma^2_{Xl}} \tag{5.42}$$

where σ_{Xl} is the peak cross section, E_{Xl} is the energy and Γ_{Xl} the width of the giant resonance. There have been several works to improve and extend eq. (5.42) to make it more consistent with the available data, specially relevant is the work of Kopecky and Uhl [103] which is included in Talys calculations by default.

In this work we tried three different parameterizations of the γSF's in combination with two different level densities:

1. Model 1: Level density from the Hilaire *et al.* [98] HFB calculations, combined with a Kopecky and Uhl's parametrization of the γSF. We added a pygmy M1 resonance associated with the rotation of protons and neutrons in opposite directions, i.e. scissors mode [65].

2. Model 2: Level density from the same HFB model, combined with Goriely's hybrid model of the γSF [26].

3. Model 3: Level density from the Gilbert-Cameron model, combined with the γSF oh Hilaire *et al.* [26]. We added an up-bend, which is a straight line that plays

an important on the E1 strength function as it permits to adjust its shape at low energies.

It is always necessary to ensure that the mean radiative capture width $\langle\Gamma_\gamma\rangle$ obtained with the calculations, is in agreement with the experimental value. The value of $\langle\Gamma_\gamma\rangle$ depends on the level density and on the γSF. Table 5.1 resumes the different values given by the considered models.

	Experiment	Model 1	Model 2	Model 3
$\langle\Gamma_\gamma\rangle$ meV	43 ± 5	43.5	43.6	38.8

Table 5.1: Experimental total radiative width for $l = 0$ compared to the one given by the different theoretical calculations performed, all of them fall within the experimental error bars.

After several tests we decided to retain model 3, because it was the one with which we could reproduce capture and fission simultaneously, also it is purely a microscopic calculation except for the up-bend correction [104]. Indeed a big progress has been done lately in this type of microscopic calculations, and there are now different approaches. In figure 5.14 we represent the gamma strength function used for E1 and M1 transitions. The M1 strength functions has a similar shape to the one extracted using the Oslo method given in [38].

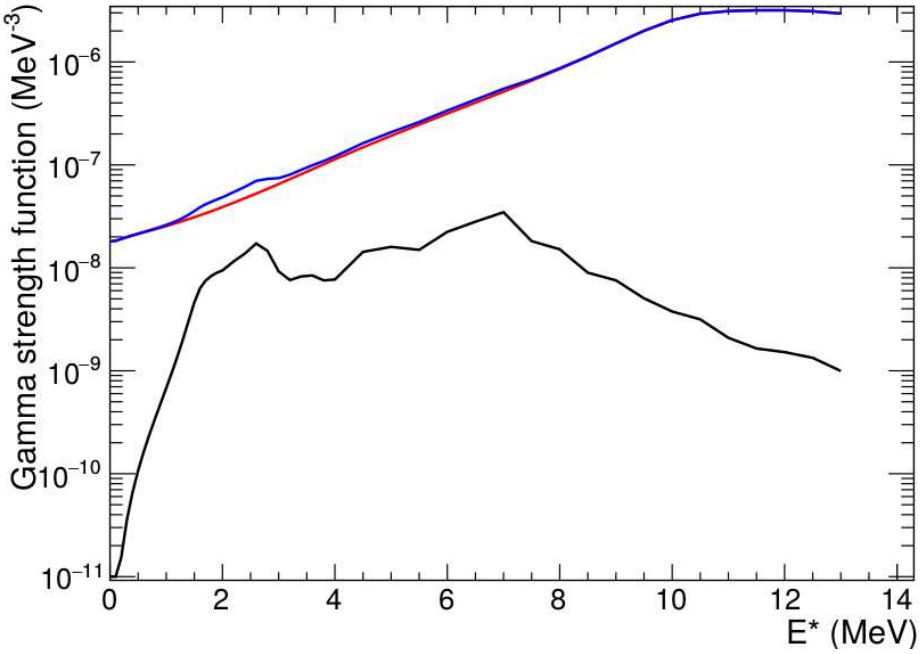

Figure 5.14: Gamma strength functions from microscopic calculations: E1 (red curve), M1 (black curve) and sum of both (blue curve).

Fission Barriers, Transition States and Class-II States

Up to now we have shown how the parameters that have a direct influence on the branching ratios $G_{n,\gamma}(E^*, J^\pi)$ and $G_{n,n'}(E^*, J^\pi)$. To be able to do a complete calculation of the competition between the different decay paths the $G_{n,f}(E^*, J^\pi)$ branching ratios are need as well, which means determining several fission parameters.

This is not easy because fission is a really complex process that depends on many variables which can have very different outcomes for a same fissioning nucleus. For instance a fissioning nucleus may split into two identical fragments, or into a heavy one, a light one and an alpha particle, a ternary fission. Figure 5.15 illustrates these differences in the fission fragment mass distribution for different fissioning nuclei. In addition, the excitation and kinetic energies of the fragments can vary a lot from one fission event to another, and these fragments can emit neutrons or γ-rays during their decay.

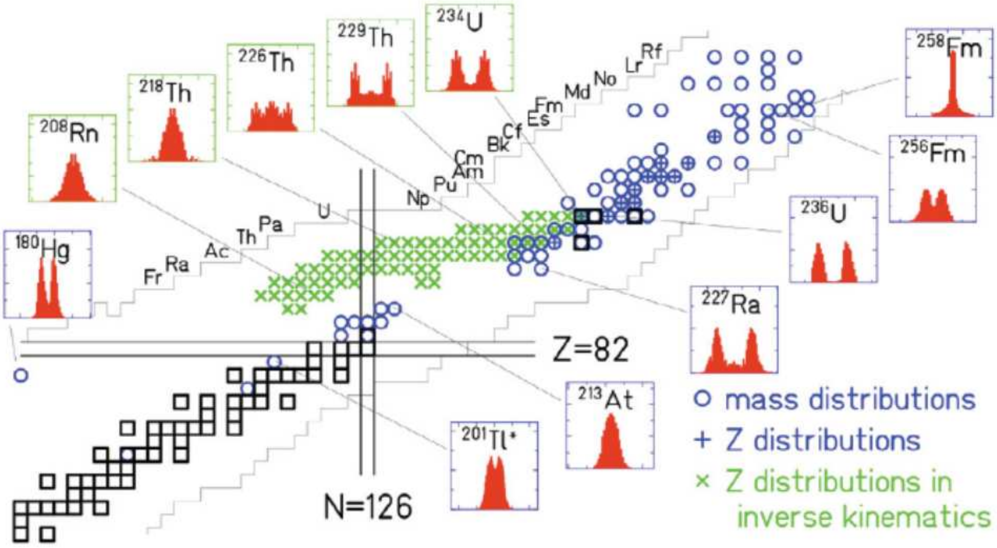

Figure 5.15: Fission fragments' mass distribution for different fissioning systems of the nuclear chart [39]. The nuclei for which the mass distributions of the fragments have been measured are marked with blue circles, those for which the charge distributions have been measured are marked with blue + signs, and the green × marks denote those measured in inverse kinematics.

To account for all these possibilities there are different ways to tackle the fission process. Modern approaches usually involve calculating a potential energy surface as a function of the different multipolar deformations. Typically this will be a two dimensional topological map of quadrupole Q_{20} and octupole Q_{30} deformation, see figure 5.16. Although other degrees of freedom are being added they need too much computation power to provide precise calculations.

These microscopic calculations could provide in theory the fission probability of the compound nucleus. However this has a very high computational cost even though several approximations and truncations have to be done. In practice for evaluations the potential energy is represented as a function of 1D-deformation, as described by Bohr and Wheeler who in 1939 developed the first theory of nuclear fission based on the liquid drop model [100]. Figure 5.17 (fig. 3 in their article) perfectly illustrates this approach to fission.

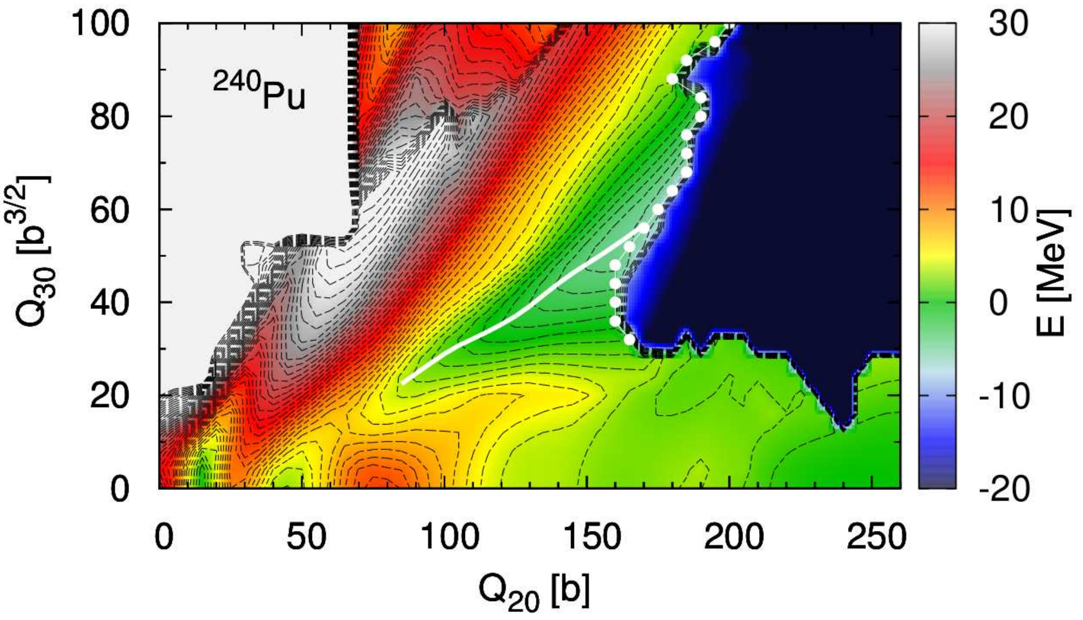

Figure 5.16: Potential energy surface of ^{240}Pu in MeV, as a function of quadrupole Q_{20} and octupole Q_{30} deformation obtained with a HFB calculation (courtesy of Anna Zdeb (CEA/DAM/DIF)). The white line represents the minimum energy decay path, the most probable, and the white dots represent other possible scission points

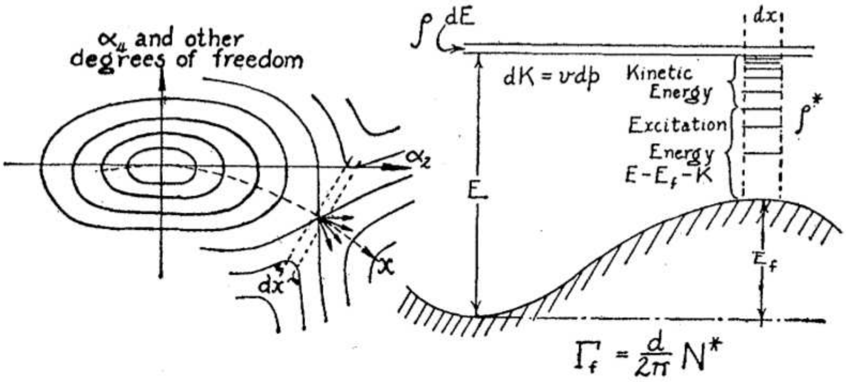

Figure 5.17: (Fig. 3 in[100]) The left part of the figure represents a topological map of potential energy. The striped line represents the path that the nucleus would follow until scission. The right part of the figure represents how the potential energy varies along this line. The saddle point defines the height of the fission barrier. Just above it transition states appear and for higher energies they can be described by level densities, figure 5.13.

In their paper Bohr and Wheeler already developed the liquid drop model (LDM) from which it follows that the potential energy surface can be plotted as an arbitrary deformation, and that the saddle point corresponds to an unstable equilibrium. They give an intuitive classical representation of the neutron induced fission process by a ball lying around the well, that if put out of equilibrium, will move over the surface. If the energy is high enough, it will trespass the saddle point, passing through the excited states on top of it, and fissioning. During this process the nucleus could lose some energy by re-emitting the neutron or by emitting gamma-rays.

Their LDM of fission also predicted that the nucleus would be cooler over the saddle point, and therefore the level density lower and discrete states appear over the barrier, *transition states*, as illustrated in the right part of figure 5.17. The LDM was extended in the 70s to include shell corrections [105] [106]. After these corrections are applied, structures appear around the LDM barrier, which becomes a double humped or even triple humped barrier. Each barrier has its own characteristic height E_B, width $\hbar\omega$, transition states and level density. If there is more than one fission barrier, between them there are wells in which the so-called Class-II states are formed. Figure 5.18 from [46] perfectly illustrates the current 1D approach used for the evaluation of the fission cross section.

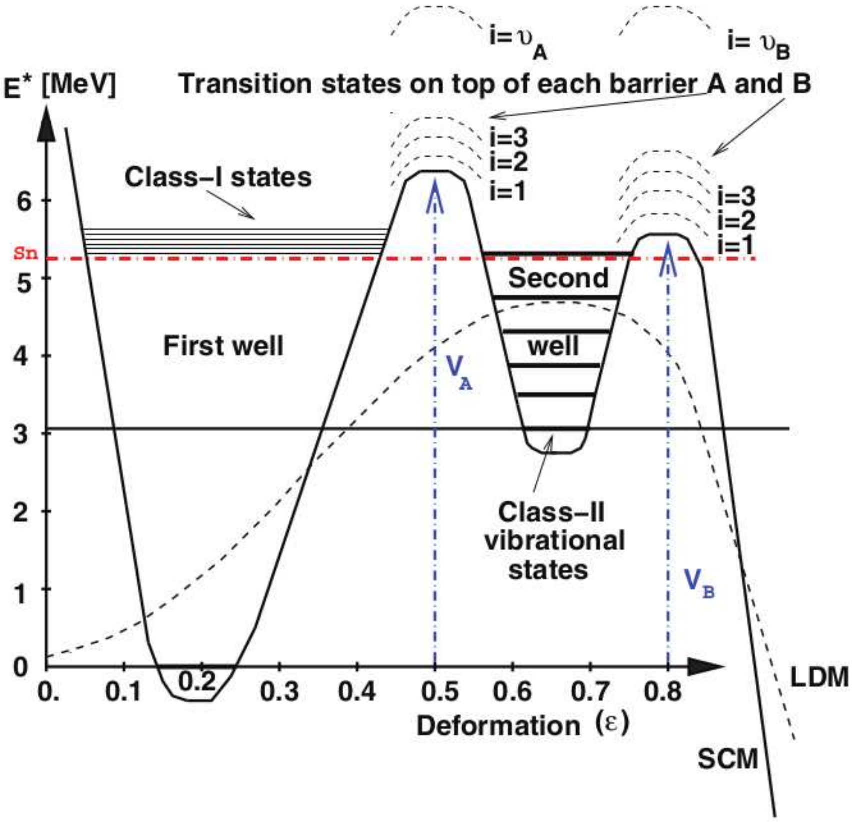

Figure 5.18: Schematic representation of the potential energy as a function of deformation ε obtained with the liquid drop model (LDM) plus the shell model corrections (SCM) [46]. The dotted curve represents the 1D potential with the LDM, to be compared with the right hand side of figure 5.17. The excited states built over the ground state lie within the first well, ie Class-I states. The ones built over the second well, between the inner barrier A of height V_A and the outer barrier B of height V_B, are the Class-II states.

The probability of the nucleus at en excitation energy E_x to tunnel through a fission barrier is given by the Hill-Wheeler formula (5.43).

$$T_f(E_x) = \frac{1}{1 + \exp\left[-2\pi\frac{(E_x - B_f)}{\hbar\omega_f}\right]} \tag{5.43}$$

where B_f is the height of the barrier and $\hbar\omega_f$ is its width. For a transition state with excitation energy ε_i above the top of this barrier:

$$T_f(E_x, \varepsilon_i) = \frac{1}{1 + \exp\left[-2\pi \frac{(E_x - B_f - \varepsilon_i)}{\hbar\omega_f}\right]} \tag{5.44}$$

To obtain the total fission transmission coefficient, one must sum all the individual transmission coefficients for each barrier through which the nucleus may tunnel. For a nucleus with excitation energy E_x, spin J and parity Π, the total transmission coefficient reads:

$$T_f^{J,\Pi}(E_x) = \sum_i T_f(E_x, \varepsilon_i) f(i, J, \Pi) + \int_{E_{th}}^{E_x} \rho(\varepsilon, J, \Pi) T_f(E_x, \varepsilon) d\varepsilon \tag{5.45}$$

where $\rho(\varepsilon, J, \Pi)$ is the level density of fission channels with spin J and parity Π for an excitation energy above the barrier ε, and $f(i, J\Pi) = 1$ if the spin and parity of the transition state is equal to that of the compound nucleus and 0 if not. The summation runs over all the discrete transition states on top of the barrier and E_{th}.

In the case of a double humped barrier, as ^{240}Pu, one has to calculate an effective transmission coefficient T_{eff}:

$$T_{eff} = \frac{T_A T_B}{T_A + T_B} \tag{5.46}$$

where T_A and T_B are the transmission coefficients, calculated with equation (5.45) for barriers A and B respectively.

Class II states have an influence in the fission transmission coefficients, specially when the excitation energy of the compound nucleus is lower than that of the barriers. They are responsible for the appearance of resonant structures in the fission probability. To include this effect in the case of the double humped barriers, the effective transmission coefficient T_{eff} has to be multiplied by a factor $F_{AB}(E^*)$:

$$T_{eff} = \frac{T_A T_B}{T_A + T_B} \cdot F_{AB}(E^*) \tag{5.47}$$

This correction factor takes the following empirical form [26]:

$$F_{AB}(E^*) = \frac{4}{T_A + T_B} + \left(\frac{E - E_{II}}{0.5\Gamma_{II}}\right)^2 \times \left(1 - \frac{4}{T_A + T_B}\right) \tag{5.48}$$

if $E_{II} - 0.5\Gamma_{II} \leq E \leq E_{II} + 0.5\Gamma_{II}$ and $F_{AB} = 1$ otherwise, where Γ_{II} is the width of the class-II state with excitation energy E_{II}.

All in all, to obtain the fission cross section $^{239}\mathrm{Pu}(n, f)$, several parameters have to be optimized. Firstly, the height of the barriers and their width, secondly, the level density and the transition states over the barriers, and finally, the class II states. In subsection 5.4.4 we compare experimental data with our calculation.

Parametrization Summary

Table 5.2 summarizes the different cross sections that were used to adjust the parameters of the Hauser-Feshbach calculation. In this table only the parameters which have *a priori* the strongest influence on each of the cross sections are listed. However, any change of a given parameter may influence all the cross sections, as the sum of all must be equal to the reaction cross section σ_R which is given by the optical model calculation.

Optical Model	Fitted XS	Most relevant parameters
σ_R	$\sigma_{n,n'}$	LD, γSF
	$\sigma_{n,\gamma}$	LD, γSF
	$\sigma_{n,f}$	Barriers, transition/class-II states, LD

Table 5.2: Reaction channels used to fix the reaction model parameters.

To sum up, we will validate these parameters with the neutron induced data of the three reactions $\sigma_{n,n'}$, $\sigma_{n,\gamma}$ and $\sigma_{n,f}$. In chapter 6 we will use these parameters to calculate the branching ratios $G_\chi(E^*, J^\pi)$ and with them reproduce our data. The input for Talys with the details of the chosen parameters is given in appendix G.

5.4.3 Radiative Capture Cross Section

As mentioned above, the gamma-strength functions and the level density are adjusted by comparing the calculated radiative capture cross section $\sigma_{n,\gamma}$ to existing data, but respecting the experimental $\langle\Gamma_\gamma\rangle$ and $\langle D_0\rangle$. This cross section will however depend on other cross sections, in fact it competes with all the other open decay channels, and specially with inelastic scattering and fission, which are an order of magnitude bigger than the radiative capture in the studied energy region. Thus small changes in the fission or inelastic scattering cross sections can induce big changes in the (n, γ) reaction cross section. In figure 5.19 we compare the calculated cross section with the experimental data for this reaction of Hopkins [107] and Kononov [108].

As one may see in figure 5.19, $\sigma_{n,\gamma}$ varies by more than two orders of magnitude in the studied energy range. There is also a change in the slope at around 500 keV, where fission starts to rise as we will see in figure 5.21, which makes the capture cross section decrease quickly and become really small. In addition, when performing a measurement of this cross section, one has to subtract the γ-rays emitted by fission fragments, for this reasons, data for energies higher than 1 MeV do not exist. This means that here the parameters cannot be fixed with the data, thus big discrepancies between the different evaluations can occur as represented in figure 5.20. Our evaluation is systematically higher than the state of the art evaluations, for two main reasons. Firstly, the other cross sections, specially fission, fit better the data, professional evaluators manage to do this with a really fine tunning of the transition states and fission parameters. Secondly, they adjust the parameters to fit $\sigma_{n,\gamma}/\sqrt{E_n}$ in the low energy region. This fine adjustment goes beyond the scope of this work, but despite these differences we consider that our calculation delivers a sufficiently good $G_\gamma(E^*, J\pi)$ to interpret our data.

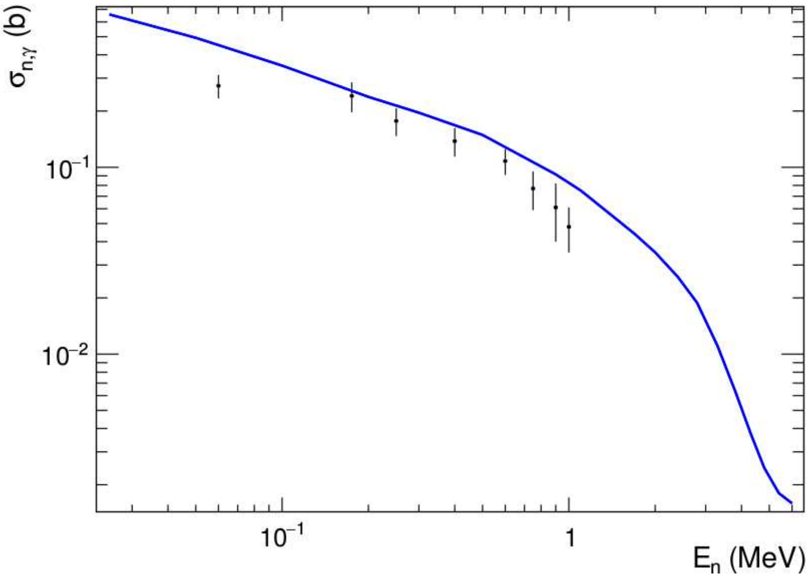

Figure 5.19: The calculated radiative capture cross section $^{239}Pu(n,\gamma)$ (blue solid line), compared to experimental data [107] [108].

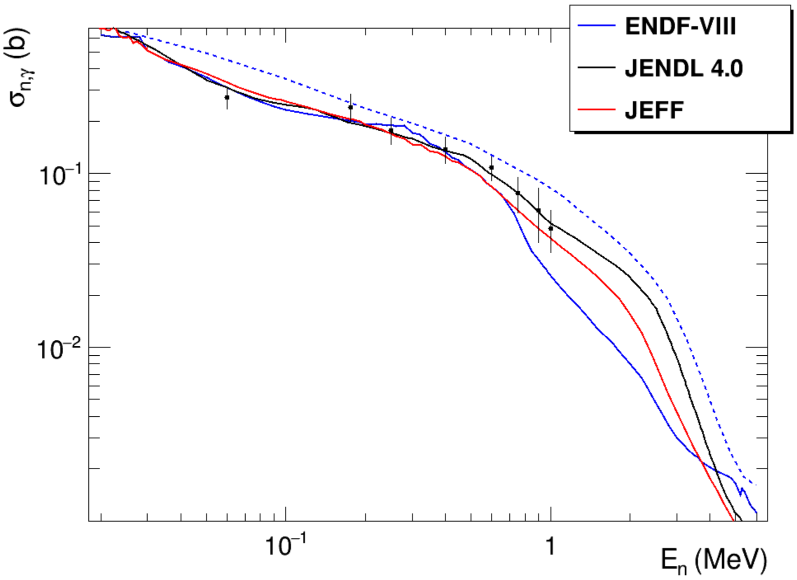

Figure 5.20: Our calculated radiative capture cross section $^{239}Pu(n,\gamma)$ (blue dotted line), compared to different evaluations, ENDF-VIII (solid blue), JENDL 4.0 (black) and JEFF 3.3 (red).

5.4.4 Fission Cross Section

As mentioned before there are a lot of parameters to adjust, barrier heights, barrier widths, transitions states and level density over each barrier and class-II states, see figure 5.18. To adjust all these parameters we used the fission cross section data [107] [108] in the region of interest, between $30keV$ and $6MeV$, and compared it to the calculation.

Figure 5.21 represents the fission cross section, for which there is a wealth of experimental data available, particularly up to 200 keV. This makes it preferable to give more importance to the parameters that will influence this cross section, rather than those that have stronger impact on capture for instance. Even though the low energy limit of 30 keV was chosen to avoid the resonance regime, the experimental data of figure 5.21, suggest that there are some structures up to a 100keV. These are in fact groups of resonances that are caused by groups of class II states. In this work we use the headband states and the class II ones given by Bouland *et al.* [40]. However to reproduce the surrogate data we removed several of the class II states and just kept some of them, as explained in the next chapter. The mentioned structures where not reproduced with our calculation but we consider it good enough to obtain the fission branching ratios $G_f(E^*, J^\pi)$.

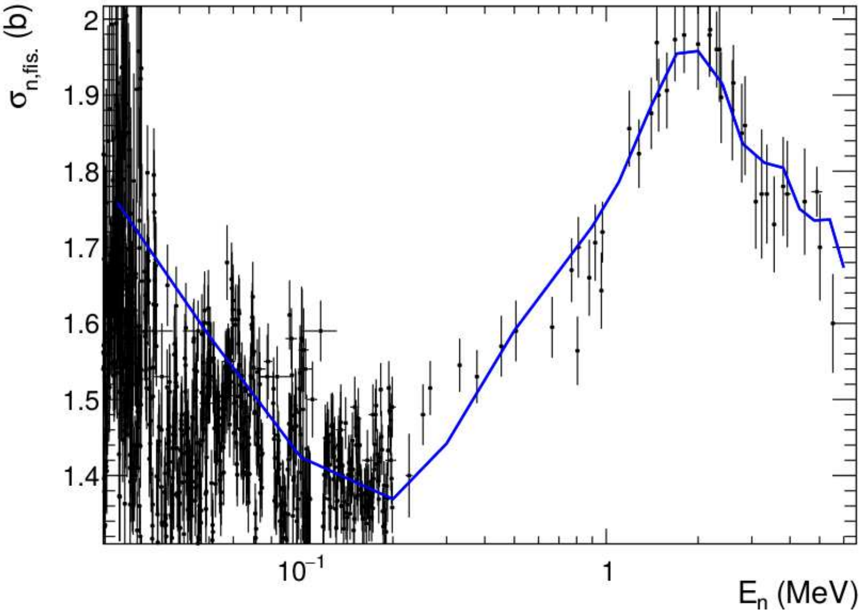

Figure 5.21: The calculated fission cross section $^{239}Pu(n,f)$ (blue solid line), compared to same absolute cross section from the experimental data used in JENDL 4.0 [27].

5.4.5 Inelastic Scattering Cross Section

Finally we calculated as well the inelastic scattering cross section $\sigma_{n,n'}$. In figure 5.22 the calculated cross section is compared with the experimental data of Batchelor [109] and Andreev [110]. Even though the error bars are large, it is a good way to check that the evaluation is congruent with other data and that there are no big flaws. However we will not use $G_{nn'}$ branching ratios to compare with our data because it was not measured directly, it can only be inferred from the sum of fission and γ-decay.

Figure 5.23 is the same as figure 5.22 but adding three evaluations JEFF 3.3, ENDF-VIII and JENDL 4.0. The first experimental point around 1 MeV is not well reproduced by our calculation, neither it is by the other evaluations except for JEFF 3.3. However our calculation is in good agreement with ENDF and JENDL which validates the evaluation procedure followed in this work.

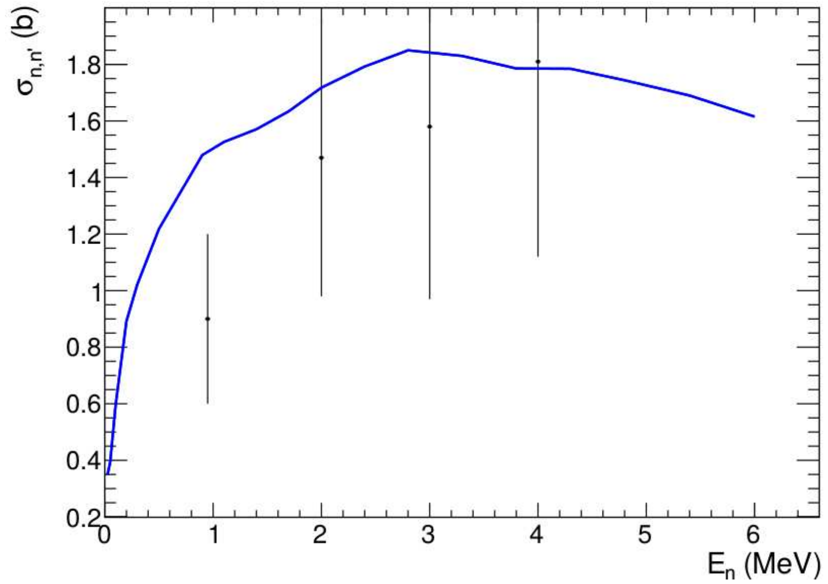

Figure 5.22: The calculated inelastic scattering cross section $^{239}Pu(n,n')$ (blue solid line), compared to experimental data [109] [110].

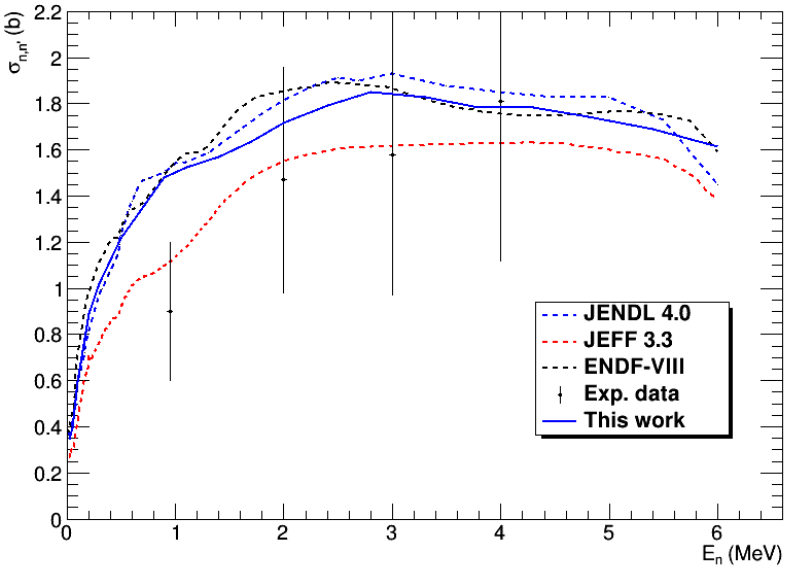

Figure 5.23: The calculated inelastic scattering cross section $^{239}Pu(n,n')$ (blue solid line), compared to experimental data [109] [110], and evaluations (dotted lines).

Chapter 6

Interpretation of our Data

This chapter is devoted to the theoretical interpretation of the $^{240}Pu(^4He,{}^4He')$ reaction experimental results and the calculations performed to reproduce these data departing from the model parameters obtained in the previous chapter. These parameters in combination with a spin-parity distribution can be used to calculate the gamma decay and the fission probabilities of $^{240}Pu^*$ as a function of excitation energy. The comparison of these calculations and the experiment, and a sensitivity test of the parameters, will be done and will be followed up by a discussion.

To describe the experimental results presented in chapter 4, the first approach was to calculate the γ-decay and fission probabilities as the quotient of their cross section over the compound nucleus formation cross section, although the calculation and the data did not compare well. The reason is that the spin distribution of the states populated with n-induced reactions is different to that of surrogate reactions, thus the spin-parity distribution has to be calculated in each case.

6.1 Branching Ratios

Having all the structure model parameters of the decaying compound nucleus (see appendix G), the calculation of the decay probabilities applying the Hauser-Feshbach formalism is quite straightforward. As explained before, it is a competition between all the possible decay paths, which is driven by the branching ratios of the decay $G_\chi(E^*, J^\pi)$. These are calculated as the ratio of the decay cross section (radiative capture or fission) over the compound nucleus formation cross section for each energy bin and each J^π:

$$G_\chi(E^*, J^\pi) = \frac{\sigma_\chi(E^*, J^\pi)}{\sigma_{CN}(E^*, J^\pi)} \tag{6.1}$$

The calculated branching ratios will then serve to deduce the spin $F(E^*, J^\pi)$ distribution from the experimental probabilities $P_\chi^{surr.}(E^*)$, we recall equation (1.10):

$$P_\chi^{surr.}(E^*) = \sum_{J^\pi} F(E^*, J^\pi) \cdot G_\chi(E^*, J^\pi)$$

The spin distribution deduced from the data is then compared to a theoretically calculated one, which was performed by M. Dupuis (CEA/DAM/DIF). This approach will be explained in detail in subsection 6.2.

The Hauser-Feshbach calculation of the compound nucleus decay was performed with Talys 1.9. This code gives the option to calculate the decay of a nucleus at a certain excitation energy E^*, spin J and parity π. However, when performing a compound nucleus decay calculation, i.e. with no incoming particle, the code does not account for the width fluctuation correction factors (WFC) of the decay channels. This can imply an error of up to 20-30% according to the calculations of O. Bouland *et al.* [46] (e.g. FIG. 3 of their article). It also implies that the decay probability through a given state can be too high. For example, if there is a 4^+ class II state at a certain excitation energy, and one performs a compound nucleus decay calculation with the nucleus in a 4^+ state, all the possible flux will pass through this state, while in theory it should be distributed among other possible outgoing channels with a weight given by the corresponding WFC factor.

The calculations of the gamma-decay and fission probabilities were done for the excitation energy interval where our data can be fitted, i.e $4 \leq E^* \leq 8$ MeV in steps of 200 keV, $0 \leq J \leq 20$, and for each parity. Figure 6.1 represents the decay probabilities as a function of excitation energy for a $^{240}Pu^*$ nucleus in different initial states J^π.

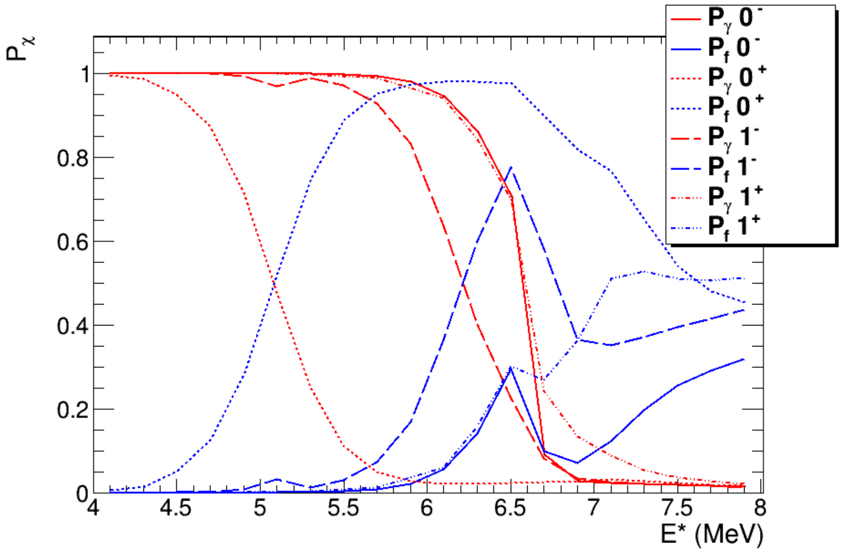

Figure 6.1: Calculated fission (blue) and gamma-decay (red) probabilities as a function of excitation energy of a compound nucleus $^{240}Pu^*$ formed at different J^π states.

The comparison of the curves in figure 6.1 illustrates the influence that spin and parity have on decay probabilities. For instance, when the CN is formed in a 0^+ state, fission grows quickly between $E^* = 4.5MeV$ and $E^* = 6MeV$ because there is a 0^+ transition state at a low energy over both barriers, as suggested in literature [40] [53].

Having obtained the branching ratios, the first attempt to reproduce our experimental data with a calculation was to use the spin-parity distribution populated by the neutron induced reaction. In figure 6.2 we compare our surrogate data, with the n-induced probabilities calculated as the quotients $\sigma_n^\gamma/\sigma_n^{CN}(E_n)$ and $\sigma_n^f/\sigma_n^{CN}(E_n)$. The calculations and the surrogate data do not compare well, which was expected for the gamma decay probability as it is a general result of previous works in the field (see chapter 2). Surprisingly, there is a major disagreement in the case of fission too, specially up to S_n+1 MeV. This is most likely due to the spin-parity mismatch, thus the importance of correctly calculating the J^π distributions, as described in the next section.

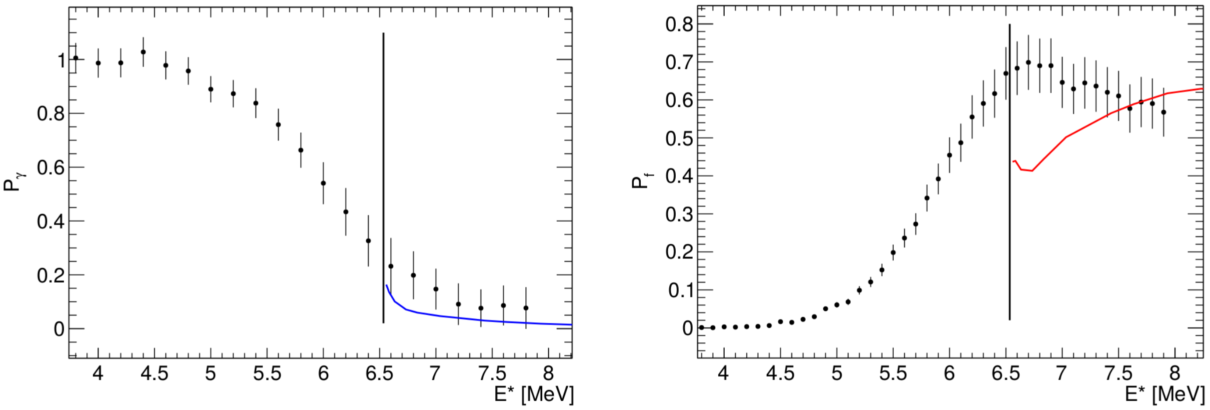

(a) Gamma decay probability.

(b) Fission probability.

Figure 6.2: Decay probabilities of the C.N. ^{240}Pu. The experimental data (points) are compared to neutron induced calculation (solid curves). The vertical line marks S_n.

6.2 Spin Distributions

In this section we compare the spin-parity distributions of the residual nucleus deduced from the data, and the one calculated with a reaction model. The compound nucleus formation must respect the spin and parity conservation rules as expressed in equations (5.19) and (5.20), respectively. This implies that in the case of the $^{240}Pu(^4He, ^4He')$ reaction, only states with a natural parity, i.e $J^\pi = 0^+, 1^-, 2^+ ...$, can be formed with direct excitations, i.e. with no intermediate coupling. When considering indirect excitations, in which intermediate strongly coupled channels intervene, a small proportion of states with unnatural parity can be formed, but it can be considered negligible as theoretical calculations show.

6.2.1 Experimental Distributions

To extract the spin distribution an iterative procedure is followed to minimize the χ^2 and fit the experimental results. Several different functional forms of the spin distributions were tried, but finally just two, a Gaussian and the derivative of a Gaussian with different proportions of parity, were retained. The reason is that this distribution arises from the Fermi Gas Model, which is still widely used in literature [79] [111]. However to reduce the number of parameters in the fit, we finally used the derivative of the Gaussian as it only depends on the spin cut-off parameter σ^2. In addition we included factor $P(E^*, J, \Pi)$ to ensure natural parities, leaving the following fitting function,

$$F(E^*, J, \Pi) = P(E^*, J, \Pi)\frac{2J+1}{2\sqrt{2\pi}\sigma^2}exp\left[-\frac{(J+1/2)^2}{2\sigma^2}\right] \tag{6.2}$$

with

$$P(E^*, J, \pm) = (1 \pm (-1)^J)/2 \tag{6.3}$$

The aim is therefore to deduce the spin cut-off parameter σ^2 from the experimental data with this constraints and the theoretical calculations of the branching ratios $G(E^*, J, \Pi)$. Assuming a linear energy dependence for σ in the energy region of interest:

$$\sigma = a \cdot (E^* - 4.1) + b \tag{6.4}$$

Only the branching ratios $G(E^*, J, \Pi)$ of states with a natural parity were considered to fit the experimental results presented in chapter 4. In figure 6.3 we show the results obtained when fitting the γ-decay and the fission probabilities independently. To achieve this however some of the class II states used in the evaluation, obtained from [40], were removed retaining the ones given in appendix G.

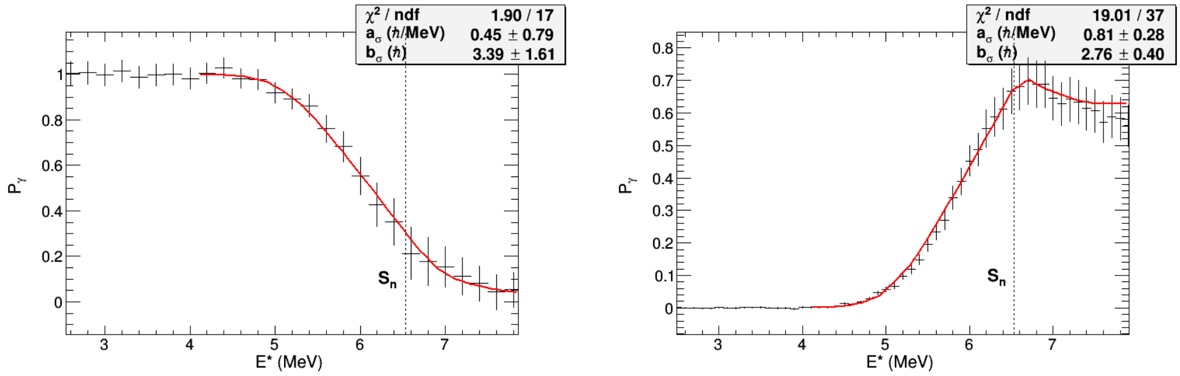

(a) Gamma decay probability.

(b) Fission probability.

Figure 6.3: Experimental γ-decay (left) and fission (right) probabilities of a compound nucleus of $^{240}Pu^*$ as a function of excitation energy, compared to the fits (solid red lines).

The parameters obtained with the fits in figures 6.3a and 6.3b are compatible within error bars, thus a weighted average of them gives: $a = 0.73 \pm 0.45 MeV^{-1}$, $b = 2.88 \pm 0.57$. The obtained distribution is plotted for different energies in figure 6.4

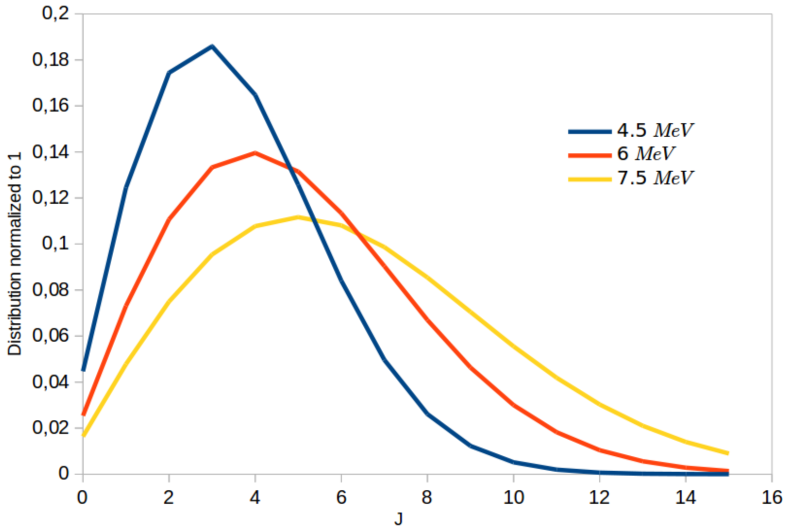

Figure 6.4: Spin distributions (eq. (6.2)) obtained with experimental parameters ($a = 0.73 \pm 0.45 MeV^{-1}$, $b = 2.88 \pm 0.57$) for different excitation energies.

The distributions represented in figure 6.4 follow the parity constraints mentioned above. This means that for even values of J a 100% of the distribution corresponds to positive parity and for odd ones a 100% corresponds to negative parity. The experimental distribution is compared to the theoretical one in figure 6.6.

6.2.2 Theoretical Distributions

The theoretical calculation of the spin distribution was performed by M. Dupuis (CEA/DAM/DIF). These calculations aim to predict the spin and parity distributions of the compound nucleus populated with the inelastic scattering reaction (α, α') using different theoretical ingredients detailed in [29] and [30].

To this end, the JLM (Jeukenne-Lejeune-Mahaux) folding model is used in combination with nuclear structure information calculated within the quasi-particle random phase approximation (QRPA), implemented with the Gogny D1S interaction. The simple folding approach for direct inelastic scattering is used to model the α particle as a punctual one. All the ingredients in the calculation are microscopic except for some parameters of the interaction that are fixed with experimental values.

This approach gives the population of excited states in the energy continuum, where the knowledge about individual states is scarce, and thus is an alternative to the usual pre-equilibrium exciton model. The first step is to produce all the possible final states of the nucleus in this case ^{240}Pu, up to a certain energy. The QRPA calculation produces the headband states K^π which are one phonon excitations, above them rotational bands are built, with approximate energies:

$$E_{\alpha K J \pi} = E_{\alpha K^\pi} + \frac{J(J+1) - K^2}{2\mathcal{I}} \tag{6.5}$$

where $E_{\alpha K^\pi}$ are the QRPA eigenvalues, and $\mathcal{I}$ is approximated by the moment of inertia of the ^{240}Pu target in its ground state.

Having the states produced with the QRPA calculation, the $F(E^*, J^\pi)$ distributions are calculated with the folding-JLM model. This model produces the cross section $\sigma_{\alpha,\alpha'}^{K_n^\pi, J}$ to populate each one of the states given by the QRPA, and the total formation cross section of the system $\sigma_{\alpha,\alpha'}$ takes the form,

$$\sigma_{\alpha,\alpha'} = \sum_{K^\pi} \sum_{n \in K^\pi} \sum_{J=J_{min}}^{J_{max}} \sigma_{\alpha,\alpha'}^{K_n^\pi, J} \tag{6.6}$$

where n distinguishes the headband states with the same quantum numbers K^π, $J_{min} = 0$ if $K^\pi = 0^+$, $J_{min} = 1$ if $K^\pi = 0^-$ and $J_{min} = K$ if $K > 0$, and J_{max} is the maximum spin up to which the calculation is performed. The probability to form the compound nucleus with a certain spin and parity $F(E^*, J^\pi)$ is calculated as follows:

$$F(E^*, J^\pi) = \frac{\sum_K \sum_{n \in K^\pi} \sigma_{\alpha,\alpha'}^{K_n^\pi, J}}{\sigma_{\alpha,\alpha'}^{pre-eq}} \tag{6.7}$$

This defines the spin distribution, which satisfies $\sum_{J^\pi} F(E^*, J^\pi) = 1$, for any given E^*. It varies with excitation energy as it may be seen in figure 6.5, which shows the preliminary results of a work that is still under improvement, the higher the energy the higher the average spin. The calculation goes up to a spin of $12\hbar$ as part of a compromise between calculation time and accuracy. At 4.5, 6 and 7.5 MeV excitation energies the average spin $\overline{J}$ is 4.5, 5.1 and 5.6 $\hbar$ respectively.

In figure 6.6 we compare de spin distributions at $E^* = 7.5$ MeV in the case of a neutron induced reaction, by fitting the experimental data, and with the microscopic

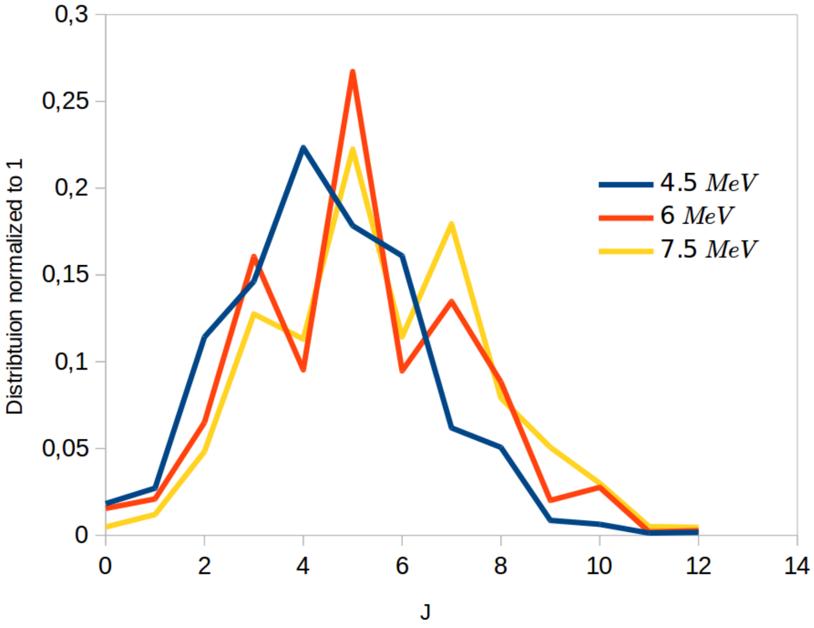

Figure 6.5: Spin distributions calculated by M. Dupuis for different energies, in which the distributions for each parity were summed. The contribution of the states with unnatural parity $\pi = (-)^{J+1}$ can be neglected. As the energy increases, so does the average spin.

calculation. The figure shows that the average spin $\overline{J}$ in the case of neutron induced reactions is much lower than in the case of the inelastic scattering of alpha particles. As previously mentioned, this was expected as the angular momentum transfered during the inelastic scattering is much higher than for the latter. A rather good agreement between the experimental distributions, eq. 5.31, and the theoretical calculation described above is observed in figure 6.6.

The big difference between the neutron induced and the two spin-parity distributions corresponding to the inelastic scattering of alpha particles means that the surrogate reaction method cannot be applied directly using equation (1.2). In the next section we will give the final calculation accounting for this spin-parity mismatch. On the contrary, the J^π distribution deduced from the experimental data is in rather good agreement with the theoretical one, which means that eventually the branching ratios $G(E^*, J^\pi)$ could be obtained by adjusting the reaction model parameters with the surrogate data.

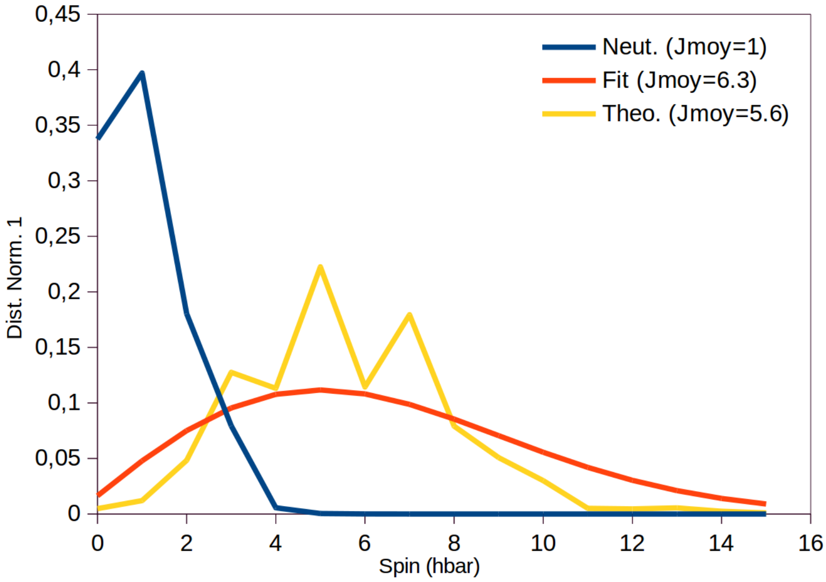

Figure 6.6: Spin distributions at $E^* = 7.5$ MeV in the case of a neutron induced reaction (blue), by fitting the experimental surrogate data (red), and with the microscopic calculation (yellow).

6.3 Decay Probabilities Calculation

The theoretical spin-parity distributions $F(E^*, J^\pi)$ and the branching ratios $G_\chi(E^*, J^\pi)$ are introduced in equation (1.10) to obtain the decay probabilities of the compound nucleus as a function of excitation energy. In figure 6.7 we compare these calculated probabilities to the experimental results.

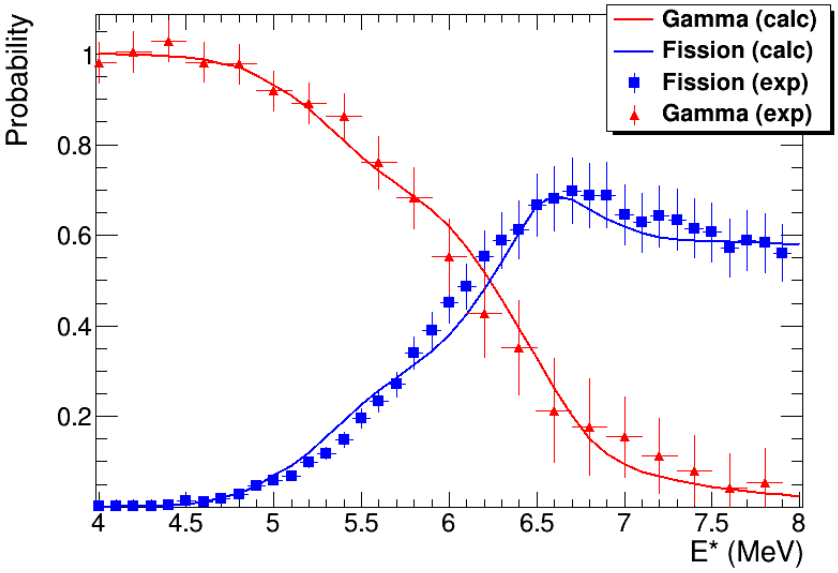

Figure 6.7: In red γ decay probability of the compound nucleus $^{240}Pu^*$, the solid line represents the calculation and the points the measurement. Fission probabilities are similarly depicted in blue.

Figure 6.7 shows a very important result, which is the good agreement between the measurement and the experiment. The discrepancies between the calculation and the experiment around 5.4 and 6 MeV may be explained with the big sensitivity of the fission probability to the barrier parameters in this energy region, as it will be shown in the next section. On the one hand a very fine tuning of the fission barrier parameters may be necessary to solve the observed discrepancies. On the other hand, further refinement of the pre-equilibrium model could account for these differences.

Calculating a spin distribution of a nuclear reaction which gives satisfying results, as those of figure 6.7, is a formidable task and a step forward in the improvement of the surrogate reaction method. Up to present, as mentioned in chapter 2, few have succeeded as Escher *et al.* [22] and Raktiewicz *et al.* [23]. In the mentioned works they studied nuclei for which just γ-decay or neutron emission was possible, thus few parameters had to be adjusted to calculate the branching ratios $G_\chi(E^*, J^\pi)$. On the contrary, doing this same process when the fission channel is open is very difficult due to the increased number of parameters. For this reason in this thesis only the sensitivity of the calculations to the input probabilities could be analyzed. In the future using a Bayesian approach all the parameters could be defined to produce neutron induced and fission cross sections.

6.3.1 Sensitivity Analysis

The sensitivity of the calculated probabilities to the input parameters to obtain the branching ratios is illustrated in figure 6.8. Here we compare the experimental probabilities to a calculation done with the theoretical spin-parity distributions of the (α, α') reaction, calculated for this work, and the branching ratios obtained with the default input parameters of Talys 1.9.

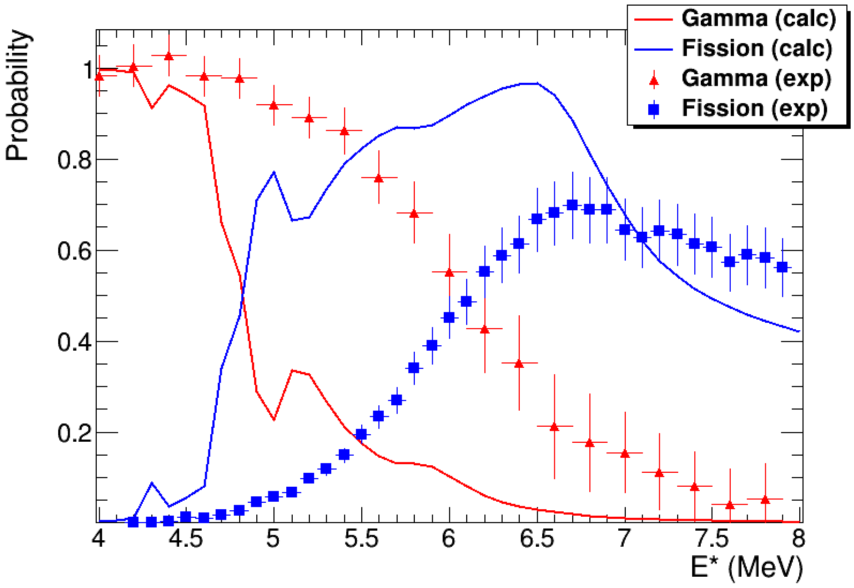

Figure 6.8: In red γ decay probability of the compound nucleus $^{240}Pu^*$, the solid line represents the calculation and the points the measurement. Fission probabilities are similarly depicted in blue. The calculations included the theoretical spin distributions, see fig 6.5, and branching ratios obtained with recommended input parameters.

The large differences between the calculations seen when comparing figures 6.7 and 6.8 suggest that the decay probabilities are very sensitive to the input model parameters. This implies that surrogate reactions can be used to fix reaction model parameters, i.e. performing an evaluation, when knowing how to calculate the spin population of the recoil nucleus.

To test the sensibility of the calculated decay probabilities to the structure model parameters, we repeated the calculations by slightly varying different parameters. The parameters were varied one by one to quantify the effect of their variations on the decay probabilities. For instance changing the fission barriers' height, the level densities, etc. All the decay probability figures contain the same data sets: calculated γ-decay probability (red solid line), calculated fission probability (blue solid line), experimental γ-decay probability (red triangles) and experimental fission probability (blue squares).

The calculated probabilities were obtained with the spin-parity distribution of M. Dupuis and with slight variations of the structure model parameters of ^{240}Pu deduced with the evaluation $n + {}^{239}Pu$. This gives an idea on how fiddling with parameters can affect the calculated probabilities for a given spin distribution. With these same changes in the parameters we calculate as well the radiative capture cross sections and the fission cross sections and compare them to the neutron induced data used for the evaluation and by JENDL 4.0.

Increase in 1st Barrier Temperature

We slightly increased, from 0.325 to 0.345 MeV the temperature of the level density over the first fission barrier (B_A), which in fact reduces the level density, see eq. (5.35). The result is a reduction of the fission probability above the neutron separation energy, see fig. 6.9. This was expected because the LD over the first barrier impacts the fission transmission coefficients at $E^* > B_A$. Equivalently the fission cross section (fig. 6.10b) is reduced and the capture cross section (fig. 6.10a) slightly increased.

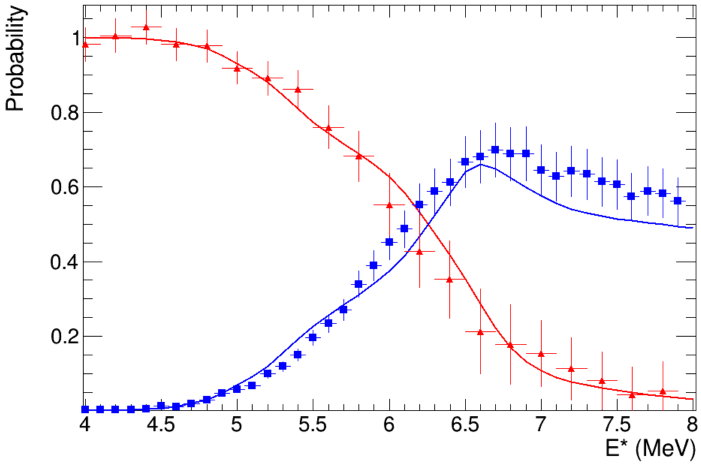

Figure 6.9: Temperature of the level density over the first barrier increased from 0.325 to 0.345 MeV.

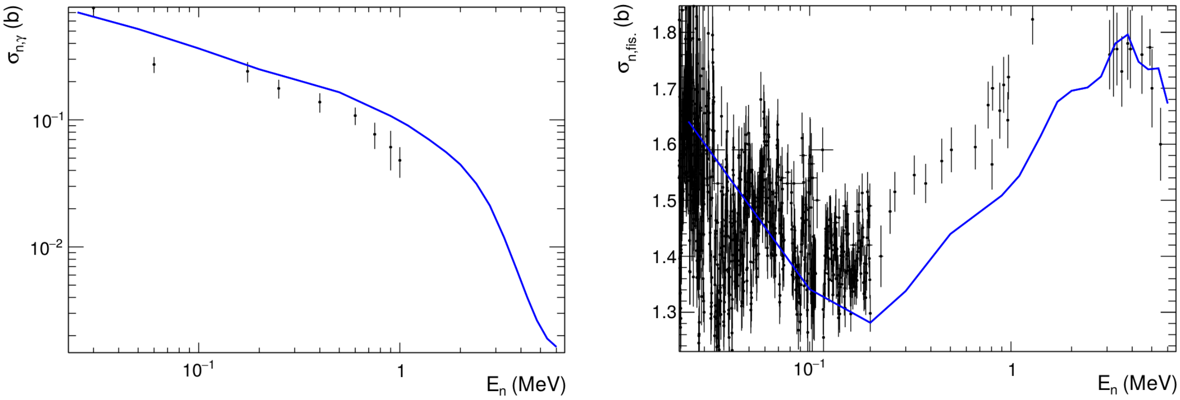

(a) Radiative capture cross section.

(b) Fission cross section.

Figure 6.10: Temperature of the level density over the first barrier increased from 0.325 to 0.345 MeV.

Higher and Wider 1st Barrier

The height of the first barrier was increased from 5.97 to 6.07 MeV and the width from 0.85 to 0.95 $\hbar\omega$. This results in a slight increase of the fission probability between 4.9 and 5.4 MeV and a reduction of the fission probability above 6.3 MeV, see fig. 6.11. The slight increase of the fission probability at low excitation energies is related to the fact that B_A is wider. When looking to the cross sections, the fission cross section (fig. 6.12b) is reduced for neutron energies up to 3 MeV but for higher energies the effect is lower. This makes the agreement with experimental data of the calculated capture cross section worse.

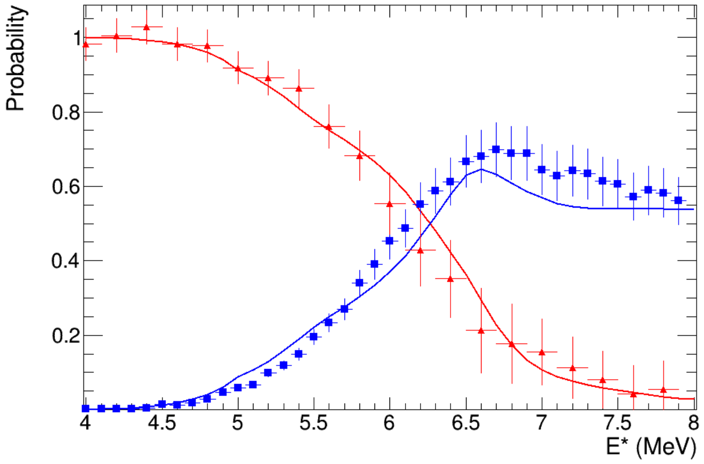

Figure 6.11: First barrier's height increased from 5.97 to 6.07 MeV and width from 0.85 to 0.95 $\hbar\omega$.

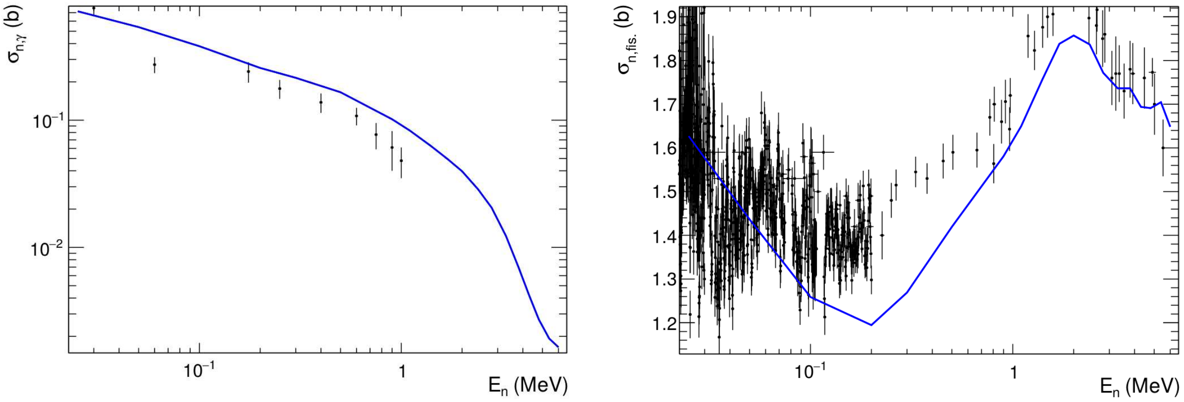

(a) Radiative capture cross section.

(b) Fission cross section.

Figure 6.12: First barrier's height increased from 5.97 to 6.07 MeV and width from 0.85 to 0.95 $\hbar\omega$.

Higher 2nd Barrier

Increasing the height of the second barrier (B_B) from 5.10 to 5.25 MeV makes the fission probability increase slightly around 5 MeV E^*. This is due to the fact that the transmission through the class-II state at 4.95 MeV is favored. The effect at higher energies is limited, figure 6.13. In contrast, the effect on the fission cross section is a reduction for $E_n > 1.5$ MeV, probably due to the effect of the lower level density over B_B. Indeed increasing the height of a barrier means shifting the LD profile in energy too, which can have an effect a high excitation energies.

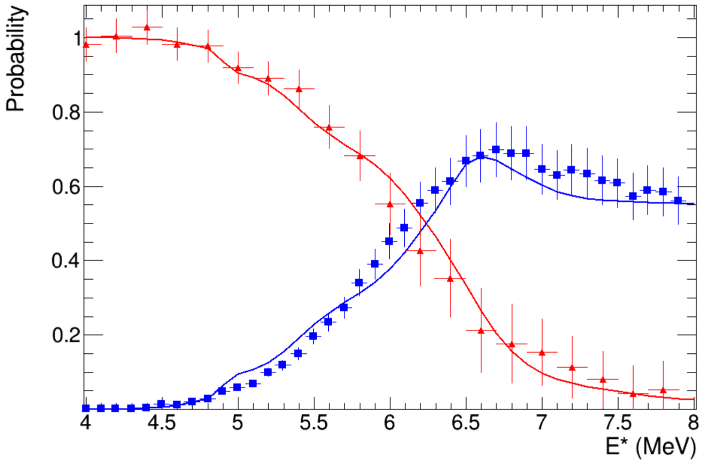

Figure 6.13: Second barrier's height increased from 5.10 to 5.25 MeV.

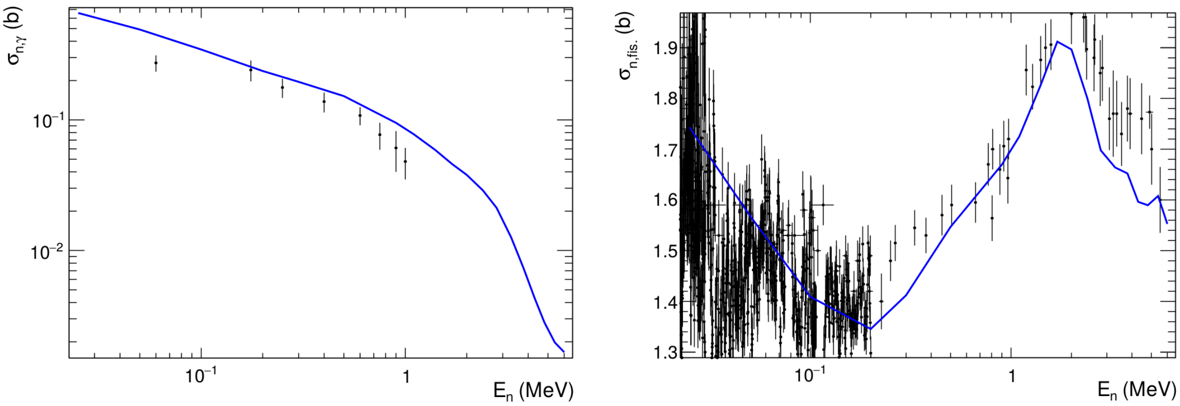

(a) Radiative capture cross section.

(b) Fission cross section.

Figure 6.14: Second barrier's height increased from 5.10 to 5.25 MeV.

Higher and Thinner 2nd Barrier

The 2nd fission barrier was increased from 5.1 to 5.2 MeV and its width reduced from 0.65 to 0.6 $\hbar\omega$. The effect is the appearance of a peak in the fission probability, and thus a descent in the γ-decay probability around 5 MeV, see fig. 6.15. This is the region where a class-II 1^- state at 4.95 MeV lies, see appendix G. This sharp increase is linked to the strong influence of the barrier thickness and class-II states on the effective transmission coefficient, equations (5.47) and (5.48). The impact on cross sections is small, besides a reduction of the fission cross section for $E_n > 2$ MeV, see figure 6.16.

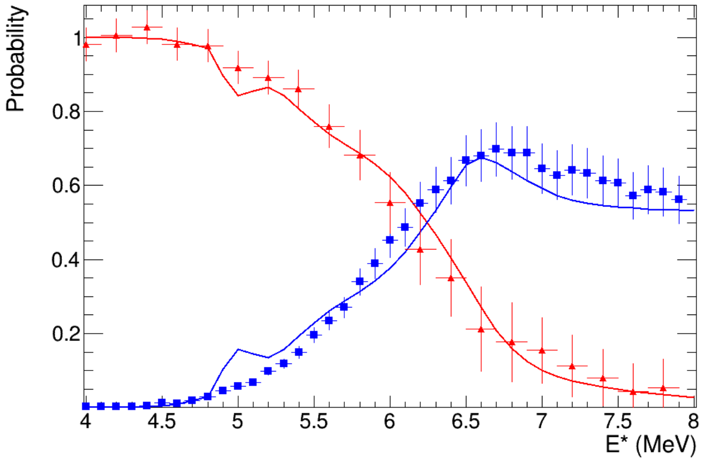

Figure 6.15: Second barrier's height increased from 5.10 to 5.20 MeV and width reduced from 0.65 to 0.6 $\hbar\omega$.

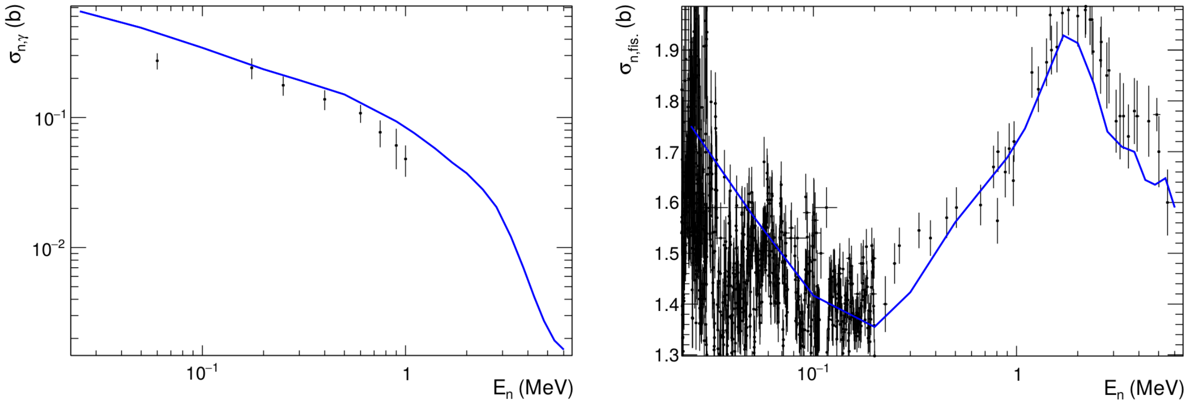

(a) Radiative capture cross section.

(b) Fission cross section.

Figure 6.16: Second barrier's height increased from 5.10 to 5.20 MeV and width reduced from 0.65 to 0.6 $\hbar$.

Default Headband States

Using the headband states over the barriers recommended by RIPL [53], which are the same as Talys 1.9 uses by default, has a big impact on the calculated probabilities, figure 6.17. There are several natural parity low-lying headband states which can favor the transmission through the barriers for both, neutron induced and surrogate reaction. The fission probability is greatly increased around 5 MeV, as in the case of thinner 2nd barrier, and it is consistently higher than the experimental probability up to $E^* \approx 7$ MeV. This results in a lower γ-decay probability and thus a lower radiative capture up to $E_n \approx 1$ MeV, fig. 6.18a. The effect on the fission cross section is a 50% increase up to $E_n \approx 1.5$ MeV, but for higher neutron energies there is almost no impact. This is due to the fact that for higher energies the transmission coefficients through the barriers are mainly ruled by the level densities over the barriers.

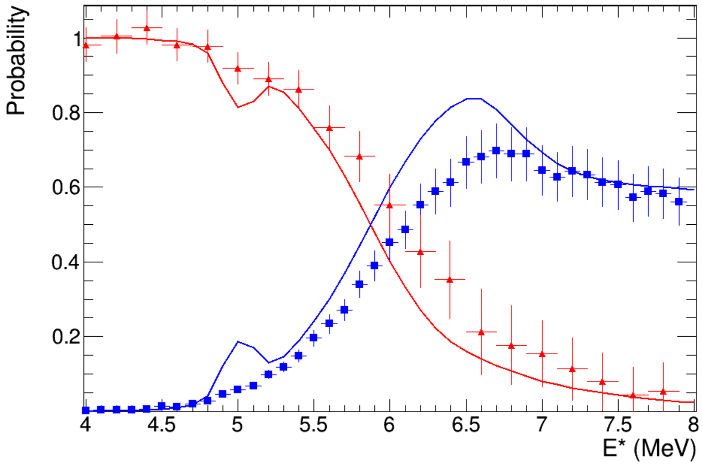

Figure 6.17: Default transition states over the fission barriers.

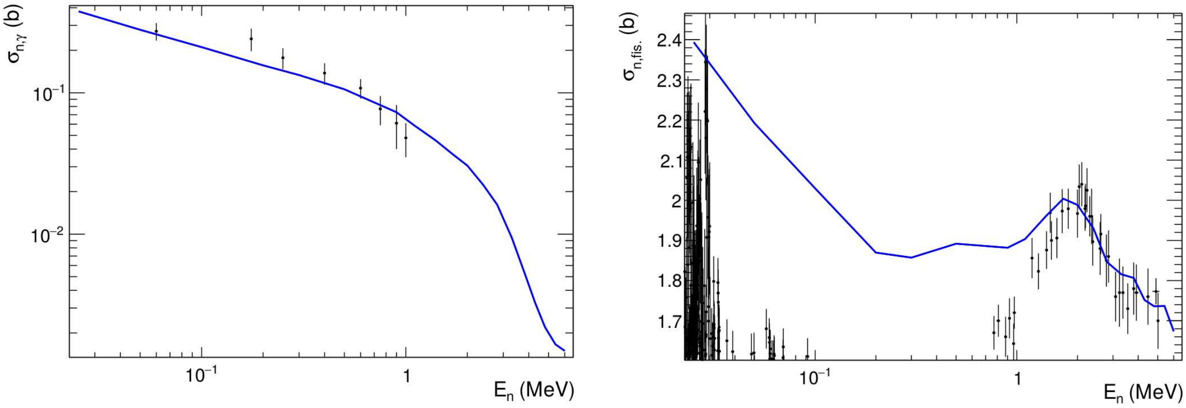

(a) Radiative capture cross section.

(b) Fission cross section.

Figure 6.18: Temperature of the level density over the first barrier increased from 0.325 to 0.345.

Class II States of Lynn *et al.*

In this case we changed our class-II states to include the ones used by Lynn et al. [40] to evaluate the plutonium isotopic family. The impact on the fission and gamma emission probabilities is clear, making several peaks appear on the calculated probabilities at the energies in which the states are placed, fig. 6.19. This is a very clear example of why surrogate data help to determine the properties of the decaying nuclei under the neutron separation energy. On the contrary, the effect on the cross sections is almost nonexistent, fig. 6.20. There are two reasons for this, one is that with neutron induced reactions one does not have access to the energy region in which these states lie, and the other is that the spin distribution is different. Thus the role of these states on neutron induced reactions and surrogate ones is not the same.

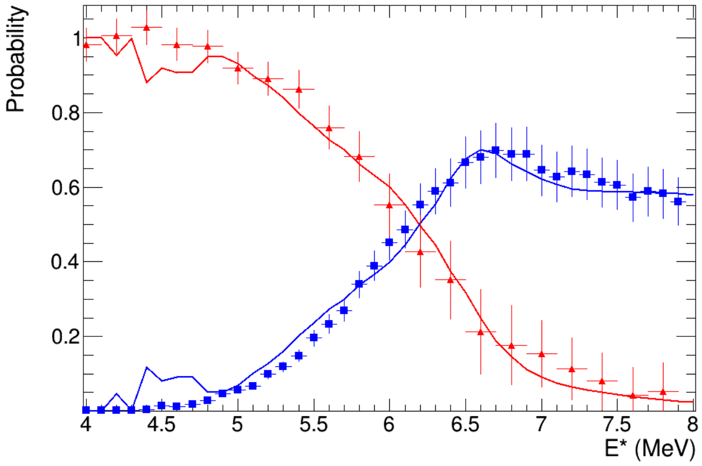

Figure 6.19: Class two states from [40].

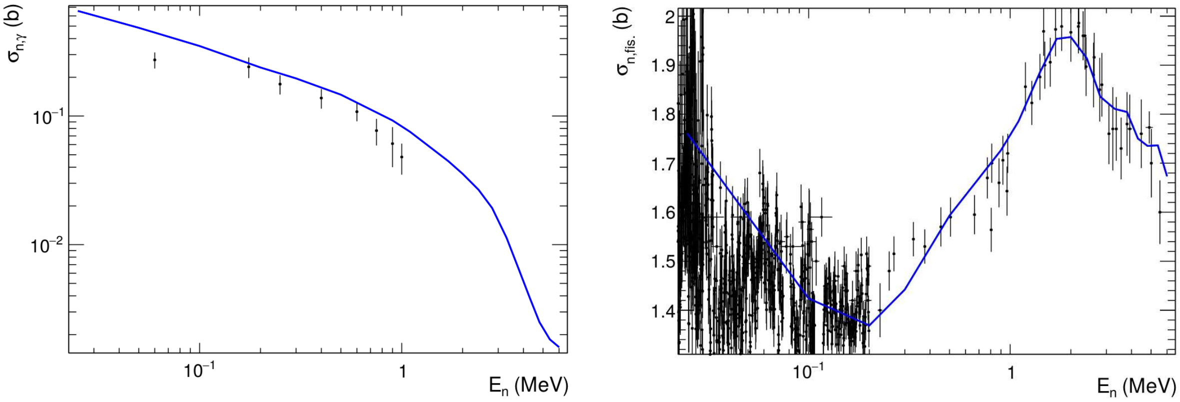

(a) Radiative capture cross section.

(b) Fission cross section.

Figure 6.20: Class-II states from [40]

Different Level Densities and γSF

Finally we changed both, the level densities and the γSF, using "model 2" as described in chapter 5, table 5.1. The result is an even better agreement of the decay probabilities up to $E^* \approx 5.7$ MeV, and then for $E^* > 6.6$ MeV there is an overestimation of the fission probability and an underestimation of the gamma decay. This however results in radiative capture in better agreement with neutron induced data, fig. 6.22a. In the case of the fission cross section the results are in good agreement up to $E_n \approx 200keV$, but at higher energies the cross section is consistently higher. The reason seems to be the different shape of the level densities obtained with the HFB calculation when compare to the CTM, see figure 5.12. The microscopic level densities, even over the barriers, have a steep slope at low excitation energies which decreases as E^* increases.

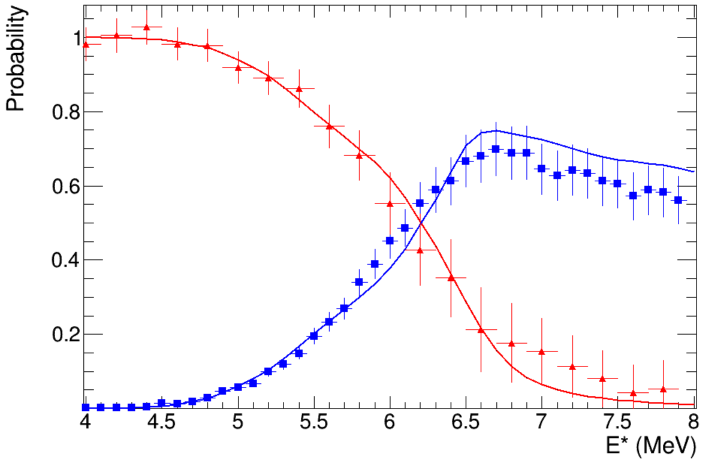

Figure 6.21: The level densities come from a QRPA/HFB calculation and Goriely's hybrid model was used for the γSF, see Talys manual [26].

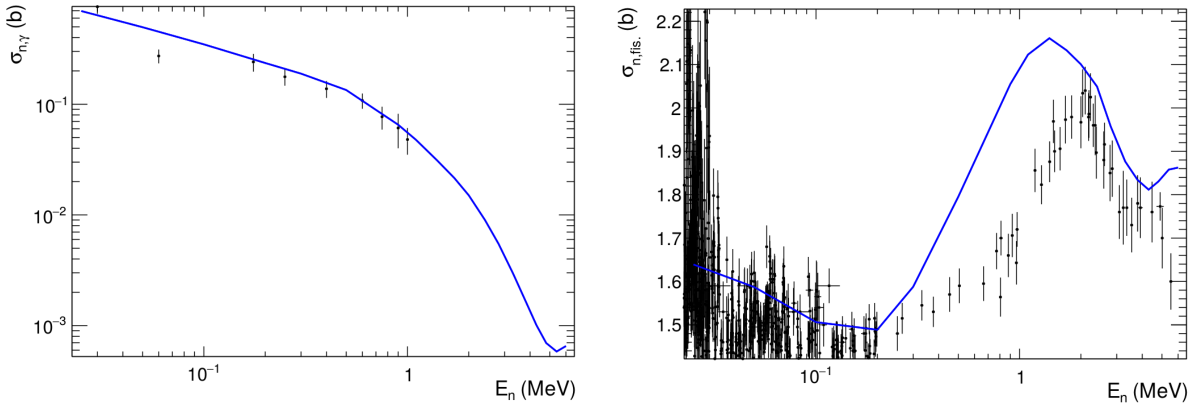

(a) Radiative capture cross section.

(b) Fission cross section.

Figure 6.22: The level densities come from a HFB+Gogny calculation ("ldmodel 6") and Goriely's hybrid model was used for the γSF ("strength 5"), see Talys manual [26].

Summary of the Sensitivity Analysis

The sensitivity analysis performed proves that small variations on the parameters can have a strong impact on the calculations. The fluctuations of each parameter make the calculation vary in a different way and in a different energy region. Furthermore, some changes have a strong impact on the decay probabilities under the neutron separation energy, but this does not reflect on the calculated cross sections.

This different influence on the calculations of each parameter depending on the excitation energy means that one could potentially tune simultaneously several parameters. This is envisaged as the continuation of this work. By systematically varying the parameters, one could determine first the range between which each parameter should lie, and then varying all of them within this intervals we would be able to propagate an uncertainty to the calculated cross sections.

Chapter 7

Conclusion and Perspectives

7.1 Conclusion

To summarize, in this work we have simultaneously measured and studied, for the first time, the γ-decay and the fission probabilities of ^{240}Pu via the surrogate reaction method. It has involved preparing the experiment, collecting the data, analyzing and interpreting them.

From an experimental point of view, we were able to measure the P_γ (using Ge detectors and scintillators) of a fissile nucleus, which is a complicated task, and we performed a thorough uncertainty analysis. Even if there were some problems during the experiment, such as the change in gain of different detectors, the unexpected target contaminants, etc., we managed to solve them and obtain fruitful results for the $^{240}Pu(^4He,{}^4He')$ reaction. In contrast, we could not account for the contaminants in the case of the ^3He beam. This made the results of the $^{240}Pu(^3He,{}^3He')$ reaction not exploitable. In addition, the ones of the $^{240}Pu(^3He,{}^4He)$ reaction obtained with telescope number 1 were of poor quality, in chapter 4 we give the results for telescope number 2.

The theoretical interpretation of the experimental results obtained with the ^4He beam was a success. The fission and γ-decay probabilities, obtained for the $^{240}Pu(^4He,{}^4He')$ reaction, were well reproduced with the parameters deduced from the $n + {}^{239}Pu$ evaluation and the spin distributions calculated with the reaction model of Marc Dupuis, see fig. 6.7. This means that the underlying reaction mechanisms have been well understood and that the structure parameters of the decaying nucleus are approximately correct. Having grasped the essence of the inelastic scattering reactions of alpha particles, means that they can be used as a complementary information for the evaluation of neutron induced data, for example deducing the class II states or the barrier widths. This was the aim of this work, to improve our understanding of the surrogate reaction method and to be able to use $(^4He,{}^4He')$ reactions confidently in the future.

Furthermore, the parameter sensitivity analysis, performed in section 6.3.1, reveals that the decay probabilities and the cross sections are sensitive even to small variations in the parameters, and that these variations have an impact on different energy regions. This opens the possibility to deliver neutron induced cross sections using just the surrogate data, as recently done in [23]. In our case, where fission is in competition with radiative capture, doing this is very ambitious, due to the large number of parameters involved in fission. Nevertheless, we are confident that we will succeed in doing this in the near future.

7.2 Perspectives

During this thesis we could not prove whether it is possible or not to calculate (n, f) and (n, γ) cross sections using solely the surrogate data, it will be done as a continuation of this work. The first step will be to depart from a set of standard parameters and try to find a set of them that reproduces the surrogate data. If this is possible, then we would perform thorough sensitivity analysis of the parameters, to determine the margins with which each parameter can be varied. Next, we would randomly vary all the parameters within those limits and calculate the cross sections for each set of parameters. Finally, the fission and radiative capture cross sections could then be obtained by averaging all of the calculations, and their dispersion would give a confidence interval.

With all the feedback gained from this work, the CENBG collaboration aims to apply the same method and set-up as in this work, to the inelastic scattering reaction $^{242}Pu(^{4}He, ^{4}He')^{242}Pu$ which is the surrogate of $n + {}^{241}Pu$. This nucleus, ^{241}Pu, is of great interest for reactor physics but it is really difficult to perform direct measurements due to its short half-life $\sim 14y$, which makes it a really interesting candidate to apply the surrogate reaction method. It would be possible to calculate the spin-parity distribution of the $^{242}Pu(^{4}He, ^{4}He')^{242}Pu$ reaction with the same kind of microscopic calculation as in this thesis. In contrast, the reaction model parameters should be fixed departing from some standard parameters, for instance RIPL [53], not with neutron data. Then, using the procedure described in the paragraph above, one could deduce the (n, f) and (n, γ) cross sections. Achieving this would be a great leap forward in the field, and would confirm that the surrogate method can provide neutron induced cross sections of short lived actinides.

From an experimental point of view, the future of surrogate reactions however is to perform the experiments in inverse kinematics. This will allow to overcome several of the problems associated to the experiments in direct kinematics, i.e. target contaminants or low γ-detection efficiencies. When this technique is fully developed it will provide a wealth of data to the community. This technique will allow to have access to very short-lived nuclei for which there are no targets. In addition the heavy residue can be detected after n or γ emission which increases the detection efficiency impressively and allows one to measure the neutron emission probability, which is extremely complicated to measure in direct kinematics. Performing the experiments in storage rings enables one to have a very precise determination of the angle and to neglect straggling and energy losses in the target, thus a precise measurement of E^*, all with similar counting rates to those of direct kinematics.

A storage ring is an ensemble of beam pipes and electro-magnetic devices arranged in such a way to permit heavy ions to revolve with frequencies of around 1 MHz at 10 MeV/u. To correctly maintain the ions revolving in the ring, the amount of atomic reactions that take place within the ring have to be minimized, thus the ring is operated in ultra-high vacuum conditions $\sim 10^{-12} mbar$. This puts severe conditions to performing reactions in this kind of rings, which have just started to be possible at the Experimental Storage Ring of the GSI in Germany.

Probably the most important quality of storage rings is beam cooling. It allows to reduce the energy and the position spread of the stored radioactive ions. Beam cooling takes place within a few seconds, which sets the lower limit on the half-live of the radioactive ions that can be stored. The combination of the electron cooler and the dipole magnets ensures the good quality of the stored beam in terms of emittance and purity. The electron cooler can compensate the angular and energy straggling, and energy loss of the beam in the gas target. In addition, the frequent ($\sim$ 1 MHz) passing of the reaction zone allows ultra-thin gas targets ($10^{13} atoms/cm^2$) to be used with no windows. All these factors provide a good energy resolution and thus allow to accurately measure the excitation energy of the decaying nucleus.

To make use of all the impressive properties of the storage rings, the CENBG is developing a new experimental set-up to simultaneously measure γ-decay, neutron emission and fission probabilities. Figure 7.1 represents schematically the set-up under development. Particle-like telescopes will be installed near to the target to identify the reaction channel and determine the excitation energy of the heavy nuclei produced in the surrogate reaction. Downstream the target, a fission detector made out of solar cells will detect fission fragments in coincidence with a scattered target-like particle. Unreacted beam-like ions and the ones that did not fission continue their path and go through two dipoles where they are separated. The heavy ions that undergo a reaction are detected in beam-like detectors, which are position sensitive and permit to distinguish between γ-decay and neutron emission. Thanks to the focusing of the nuclei in the beam direction, in inverse kinematics the detection efficiencies are nearly 100%, which is much larger than in direct kinematics experiments.

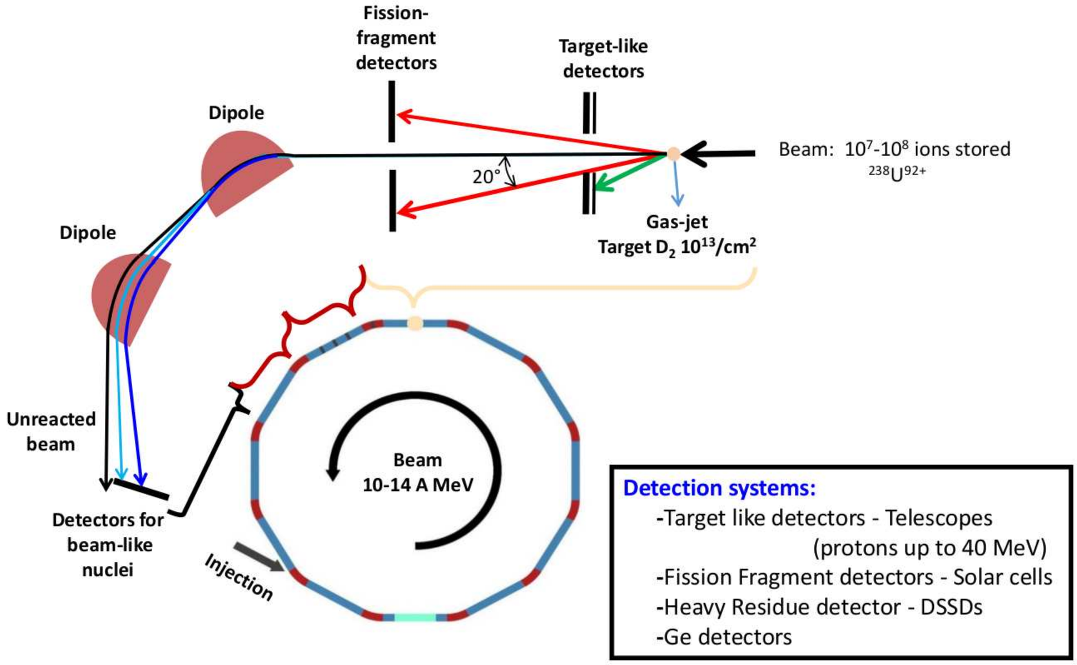

Figure 7.1: Schematic representation of the measurement of the surrogate reaction $^{238}U+d$ at a storage ring [112].

Figure 7.1 represents in addition to the set-up the concrete example of $^{238}U^{92+}$ impinging on a deuterium target. This reaction has already been studied in direct kinematics [10], which will allow to compare the results obtained with both methods. If these results are in good agreement it would mean that the surrogate reaction method in inverse kinematics is an excellent alternative to deduce neutron induced cross sections of highly radioactive isotopes. It would permit to measure with a good energy resolution, and no contaminants, the decay probabilities of this kind of isotopes.

All in all, an impressive progress is currently being made in the surrogate reaction field. As mentioned in chapter 2, in a study recently published [23], they succeeded to produce neutron capture cross sections from surrogate data. In the case of nuclei that can undergo fission, this remains to be proven, hopefully in the near future. Anyhow, we believe that this PhD thesis will help to make the state of the art advance in this direction.

Appendix A

Angles of the Scattered Particle Detectors

A Monte-Carlo simulation in C++ of the geometry of the telescope detectors gave the following angles in degrees:

Strip	θ	$\Delta\theta$	ϕ_{max}	ϕ_{min}
15	119.4	0.9	247.0	293.0
14	121.9	1.1	246.0	294.1
13	124.8	1.1	244.9	295.1
12	127.8	1.2	243.5	296.4
11	130.8	1.3	242.2	297.8
10	133.9	1.4	240.8	299.2
9	137.0	1.5	239.3	302.7
8	140.1	1.6	237.4	302.7
7	143.2	1.8	235.4	304.7
6	146.2	1.9	233.2	306.9
5	149.2	2.0	230.7	309.3
4	152.0	2.2	227.9	312.1
3	154.8	2.4	224.9	315.1
2	157.1	2.5	222.1	317.7

(a) Angles for each strip of telescope number one.

Strip	θ	$\Delta\theta$	ϕ_{max}	ϕ_{min}
15	119.4	0.9	67.0	113.0
14	121.9	1.1	66.0	114.1
13	124.8	1.1	64.8	115.1
12	127.8	1.2	63.6	116.4
11	130.8	1.3	62.3	117.7
10	133.9	1.4	60.6	119.3
9	137.0	1.5	59.2	120.9
8	140.1	1.6	57.4	122.6
7	143.2	1.8	55.4	124.5
6	146.2	1.9	53.3	126.8
5	149.1	2.0	50.7	129.3
4	152.0	2.2	48.0	132.1
3	154.8	2.4	44.8	135.1
2	157.1	2.5	42.4	137.6

(b) Angles for each strip of telescope number two.

Appendix B

Detectors Calibration Coefficients

B.1 Calibration Coefficients of Telescopes

The calibration coefficients are the ones of straight line defined as $E_i = a_i E_{ch,i} + b_i$ where the subindex i stands for the Si-Li or ΔE, E is the energy in MeV, E_{ch} is the energy in channels, and a and b are the calibration coefficients, in MeV/channel and MeV respectively. The numerical values are given in tables B.1 and B.2.

Strip	$a_{SiLi,1}$	$b_{SiLi,1}$	$a_{\Delta E,1}$	$b_{\Delta E,1}$	$a_{SiLi,2}$	$b_{SiLi,2}$	$a_{\Delta E,2}$	$b_{\Delta E,2}$
2	0.005915	0.1671	0.002542	-0.0227	0.006098	-0.5875	0.002710	-0.1350
3	0.005875	0.3059	0.002480	-0.0305	0.006071	-0.4951	0.002668	-0.2451
4	0.005890	0.2077	0.002563	-0.0572	0.006026	-0.3529	0.002644	-0.0948
5	0.005893	0.2282	0.002507	-0.0361	0.006058	-0.4677	0.002702	-0.1440
6	0.005934	0.0883	0.002531	-0.0460	0.006034	-0.3766	0.002643	-0.1307
7	0.005894	0.2403	0.002519	-0.0723	0.006043	-0.3893	0.002645	-0.0788
8	0.005853	0.4186	0.002429	0.0952	0.006025	-0.2883	0.002645	-0.1809
9	0.005851	0.4176	0.002450	0.0002	0.006010	-0.2381	0.002628	-0.1321
10	0.005856	0.4030	0.002441	0.1237	0.005979	-0.1092	0.002572	0.0583
11	0.005873	0.3650	0.002419	0.1187	0.006008	-0.1764	0.002542	-0.0281
12	0.005879	0.3633	0.002497	0.0326	0.006005	-0.1347	0.002525	-0.0686
13	0.005859	0.4713	0.002405	0.0512	0.006019	-0.1512	0.002614	-0.0635
14	0.005852	0.5366	0.002409	0.0381	0.006038	-0.1937	0.002582	-0.2102
15	0.005867	0.5274	0.002427	-0.0204	0.006039	-0.2112	0.002607	-0.1614

Table B.1: Calibration coefficients of the telescopes for the ^4He beam.

Strip	$a_{SiLi,1}$	$b_{SiLi,1}$	$a_{\Delta E,1}$	$b_{\Delta E,1}$	$a_{SiLi,2}$	$b_{SiLi,2}$	$a_{\Delta E,2}$	$b_{\Delta E,2}$
2	0.01010	-0.3614	0.002468	0.0272	0.01047	-1.149	0.002623	-0.0407
3	0.01008	-0.3499	0.002429	-0.0210	0.01043	-1.086	0.002627	-0.2200
4	0.01013	-0.4932	0.002503	-0.0153	0.01040	-1.044	0.002590	-0.0706
5	0.01012	-0.4669	0.002499	-0.0835	0.01043	-1.118	0.002669	-0.1312
6	0.01011	-0.4625	0.002571	-0.1473	0.01043	-1.130	0.002778	-0.3933
7	0.01010	-0.4153	0.002515	-0.1306	0.01042	-1.081	0.002598	-0.0531
8	0.01010	-0.3718	0.002462	-0.0283	0.01042	-1.051	0.002623	-0.1883
9	0.01009	-0.3646	0.002477	-0.1054	0.01040	-0.987	0.002649	-0.2102
10	0.01009	-0.3895	0.002495	-0.0223	0.01041	-1.096	0.002661	-0.1506
11	0.01008	-0.3671	0.002445	-0.0212	0.01040	-0.982	0.002569	-0.1372
12	0.01010	-0.3633	0.002485	-0.0211	0.01042	-0.988	0.002578	-0.2211
13	0.01010	-0.3383	0.002434	-0.0753	0.01040	-0.920	0.002603	-0.0886
14	0.01011	-0.3356	0.002462	-0.1152	0.01040	-0.906	0.002542	-0.1715
15	0.01010	-0.2388	0.002368	0.0054	0.01040	-0.930	0.002737	-0.3767

Table B.2: Calibration coefficients of the telescopes for the ^3He beam.

B.2 Calibration Coefficients of Liquid Scintillators

In table B.3 a and b are the calibration coefficients of the C_6D_6 detectors, in keV/channel and keV respectively.

C_6D_6 number	a	b
1	3.05603	-427.914
2	3.49443	-493.874
3	3.39847	-588.304
4	3.29234	-481.256

Table B.3: Calibration coefficients of liquid scintillators.

B.3 Calibration Coefficients of the Germanium Detectors

In table B.4 a and b are the calibration coefficients of the Ge detectors, in keV/channel and keV respectively.

Ge number	a_{HG}	b_{HG}	a_{LG}	b_{LG}
2	0.638122	-39.2803	2.025712	-87.19
3	0.783745	-58.5558	2.365093	-193.17
4	0.625526	-45.6103	1.937492	-102.18
5	0.614443	-41.9416	2.379073	-189.84
6	0.649010	-45.9236	2.451082	-184.22

Table B.4: Calibration coefficients of the Ge.

Appendix C

Alternative Error Estimation

An alternative method to evaluate error is developed here and compared with the approach explained in chapter 4. The formulas derived are just the result of applying equation (4.6):

$$(\Delta f(x_1, ..., x_n))^2 = \sum_{i=1}^{n} \sum_{j=1}^{n} \frac{\partial f}{\partial x_i} \frac{\partial f}{\partial x_j} \sigma_{x_i} \sigma_{x_j} \rho_{ij}$$

with $\rho_{ii} = 1$.

C.1 Fission Probability Uncertainty

In the case of the fission probability if the dependence on all the variables is written explicitly:

$$P_f(N_f, N_{ter}, N_{det}, N_{cont}, \varepsilon_f) = \frac{N_f - N_{ter}}{\varepsilon_f \cdot (N_{det} - N_{cont} - N_{ter}/\varepsilon_f)} \tag{C.1}$$

where N_f is the number of detected fission events in coincidence with the telescopes, N_{ter} is the number of ternary fission events deduced from the low energy part of the fission coincidence spectra, N_{det} is the number of scattered particles detected with the telescopes, N_{cont} is the estimated number of events induced by the contaminants in the carbon backing and ε_f is the fission detection efficiency.

To obtain the error associated to the fission probability expressed in C.1, one needs to calculate the partial derivatives and the typical deviations associated to each variable, but also identify any possible correlations between variables. The partial derivatives explicitly take the form described in equations C.2 to C.6:

$$\frac{\partial P_f}{\partial N_f} = \frac{1}{\varepsilon_f N_{det} - \varepsilon_f N_{cont} - N_{ter}} \tag{C.2}$$

$$\frac{\partial P_f}{\partial N_{ter}} = \frac{N_f - \varepsilon_f (N_{det} - N_{cont})}{(\varepsilon_f N_{det} - \varepsilon_f N_{cont} - N_{ter})^2} \tag{C.3}$$

$$\frac{\partial P_f}{\partial N_{det}} = \frac{-\varepsilon_f (N_f - N_{ter})}{(\varepsilon_f N_{det} - \varepsilon_f N_{cont} - N_{ter})^2} \tag{C.4}$$

$$\frac{\partial P_f}{\partial N_{cont}} = \frac{\varepsilon_f(N_f - N_{ter})}{(\varepsilon_f N_{det} - \varepsilon_f N_{cont} - N_{ter})^2} \tag{C.5}$$

$$\frac{\partial P_f}{\partial N_f} = \frac{-(N_f - N_{ter})(N_{det} - N_{cont})}{(\varepsilon_f N_{det} - \varepsilon_f N_{cont} - N_{ter})^2} \tag{C.6}$$

As the variables, N_f, N_{det}, N_{ter} and N_{cont}, follow a Poisson distribution, their standard deviation is $\sigma_{N_i} = \sqrt{N_i}$, where $i = f,\ det,\ ter,\ cont$. In contrast, the error associated to the fission efficiency is given by the simulation. Thus, the only thing left is to determine the correlation coefficients between different variables. This is really complicated or even impossible, so most of the variables were considered independent from the others except for N_f and N_{det}, whose correlation coefficient $\rho_{fs} = 0.2866$ was estimated from the data as explained in section 4.8. Introducing all these terms in equation (4.6) gives the fission probability uncertainty.

C.2 Gamma Decay Probability Uncertainty

As with fission, writing the gamma decay probability explicitly:

$$P_\gamma(N_\gamma, N_t, N_{ter}, N_{det}, N_{cont}, \varepsilon_f, \varepsilon_\gamma) = \frac{N_\gamma - N_t/\varepsilon_f}{\varepsilon_\gamma(N_{det} - N_{cont} - N_{ter}/\varepsilon_f)} \tag{C.7}$$

where N_γ is the number of detected γ-rays in coincidence with the telescopes, N_t is the number of triple coincidences gamma-fission fragment-ejectile, N_{ter} is the number of ternary fission events deduced from the low energy part of the fission coincidence spectra, N_{det} is the number of scattered particles detected with the telescopes, N_{cont} is the estimated number of events induced by the contaminants in the carbon backing, ε_f is the fission detection efficiency and ε_γ is the γ-ray detection efficiency.

The partial derivatives of equation (C.7) with respect to each variable are written in equations (C.8) to (C.14):

$$\frac{\partial P_\gamma}{\partial N_\gamma} = \frac{\varepsilon_f}{\varepsilon_\gamma(\varepsilon_f N_{det} - \varepsilon_f N_{cont} - N_{ter})} \tag{C.8}$$

$$\frac{\partial P_\gamma}{\partial N_t} = \frac{-1}{\varepsilon_\gamma(\varepsilon_f N_{det} - \varepsilon_f N_{cont} - N_{ter})} \tag{C.9}$$

$$\frac{\partial P_\gamma}{\partial N_{det}} = \frac{N_t\varepsilon_f - N_\gamma\varepsilon_f^2}{\varepsilon_\gamma(\varepsilon_f N_{det} - \varepsilon_f N_{cont} - N_{ter})^2} \tag{C.10}$$

$$\frac{\partial P_\gamma}{\partial N_{cont}} = \frac{-(N_t\varepsilon_f - N_\gamma\varepsilon_f^2)}{\varepsilon_\gamma(\varepsilon_f N_{det} - \varepsilon_f N_{cont} - N_{ter})^2} \tag{C.11}$$

$$\frac{\partial P_\gamma}{\partial N_{ter}} = \frac{N_t - \varepsilon_f N_\gamma}{\varepsilon_\gamma(\varepsilon_f N_{det} - \varepsilon_f N_{cont} - N_{ter})^2} \tag{C.12}$$

$$\frac{\partial P_\gamma}{\partial \varepsilon_f} = \frac{N_t N_{det} - N_\gamma N_{ter} - N_{cont} N_t}{\varepsilon_\gamma(\varepsilon_f N_{det} - \varepsilon_f N_{cont} - N_{ter})^2} \tag{C.13}$$

$$\frac{\partial P_\gamma}{\partial \varepsilon_\gamma} = \frac{N_t - N_\gamma \varepsilon_\gamma}{\varepsilon_\gamma^2 (\varepsilon_f N_{det} - \varepsilon_f N_{cont} - N_{ter})} \tag{C.14}$$

Like in the case of fission, the variables N_γ, N_t, N_{det}, N_{ter} and N_{cont} follow a Poisson distribution, their standard deviation is $\sigma_{N_i} = \sqrt{N_i}$, where $i = \gamma$, t, det, ter, $cont$. Similarly the error associated to the fission efficiency is given by the simulation. The one corresponding to the gamma detection efficiency is obtained from the fitting procedure explained in subsection 4.6.2, the error in the fit parameters is then extrapolated to higher energies. The correlation coefficients retained are the same as those in table 4.6.

Appendix D

Figures of the Decay Probabilities

D.1 Results per Angle of the $^{240}Pu(^{4}He, ^{4}He')$ Reaction

In this section we present the results obtained per angle for the inelastic scattering of alpha particles by ^{240}Pu. We recall that the seven studied angles are related to the strips as follows:

Strips	Angle #	$\theta(^o)$	$\Delta\theta(^o)$
2-3	1	156.0	3.4
4-5	2	150.6	3.0
6-7	3	144.7	2.6
8-9	4	138.6	2.2
10-11	5	132.4	1.9
12-13	6	126.3	1.7
14-15	7	120.7	1.4

Table D.1: Average angles for each group of four strips, two from each telescope.

The decay probabilities of $^{240}Pu^{*}$ as a function of excitation energy are represented in figure D.1. The γ-decay probabilities were obtained with liquid scintillators in combination with the germanium detectors. The same probabilities with a subtraction of the background induced by ^{244}Cm in fission probabilities, subsection 4.5.1, are plotted in figure D.2.

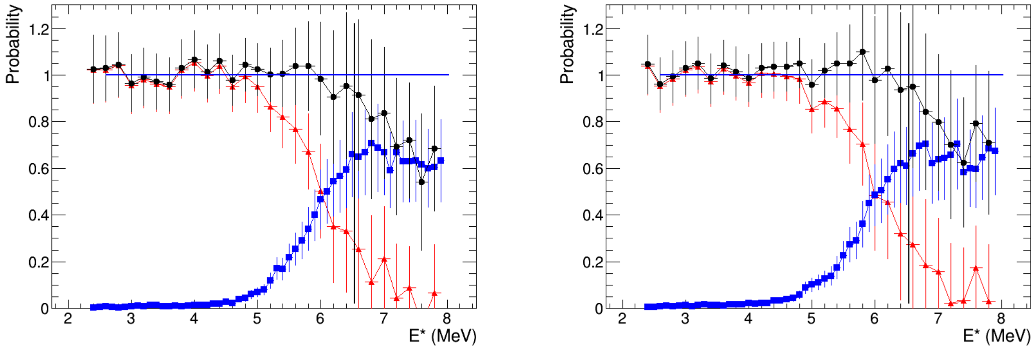

(a) Ejectile angle 120.7^o

(b) Ejectile angle 126.3^o

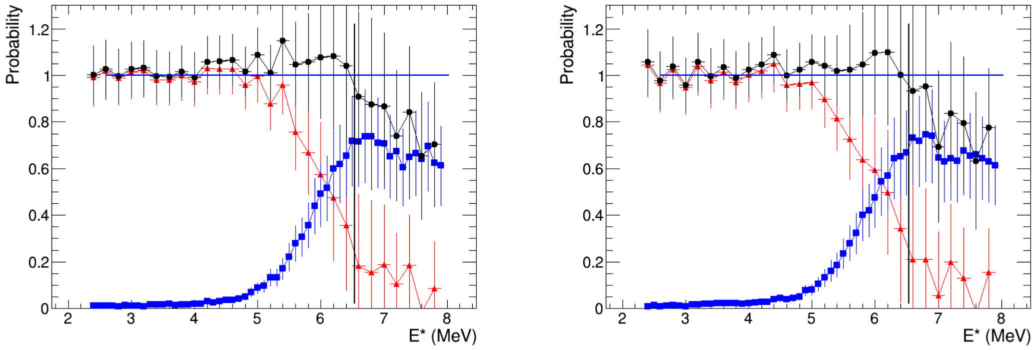

(c) Ejectile angle 132.4^o

(d) Ejectile angle 138.6^o

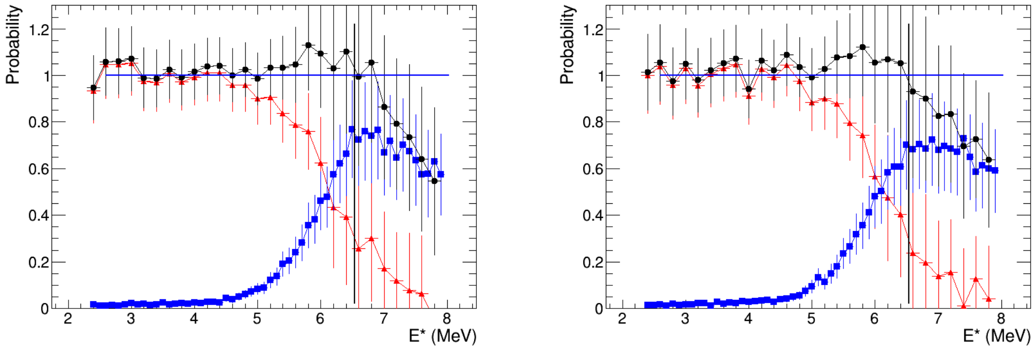

(e) Ejectile angle 144.7^o

(f) Ejectile angle 150.6^o

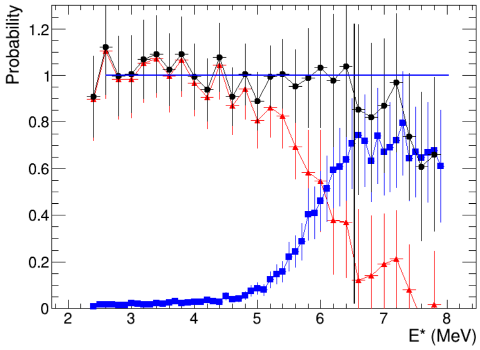

(g) Ejectile angle 156.0^o

Figure D.1: Decay probabilities: fission (blue squares), gamma-decay (red triangles) and sum of both (black circles), as a function of excitation energy for each one of the studied ejectile angles. No ternary fission background subtraction was applied.

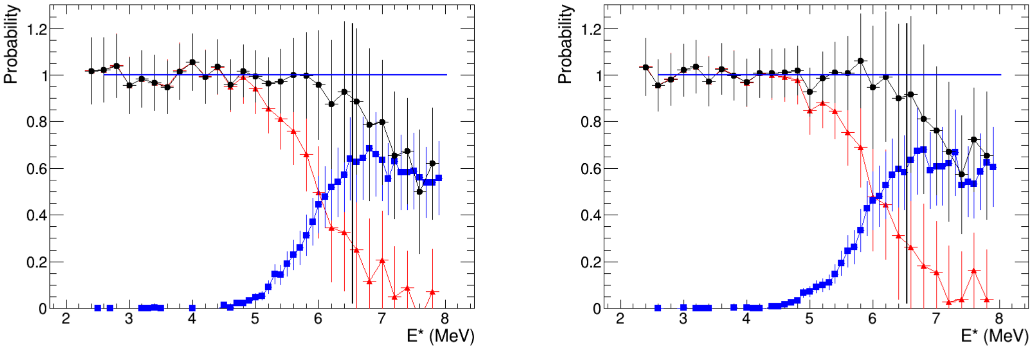

(a) Ejectile angle 120.7^o (b) Ejectile angle 126.3^o

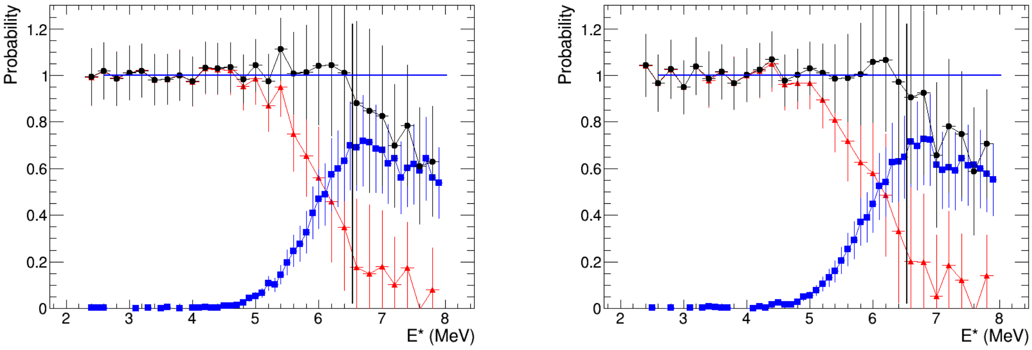

(c) Ejectile angle 132.4^o (d) Ejectile angle 138.6^o

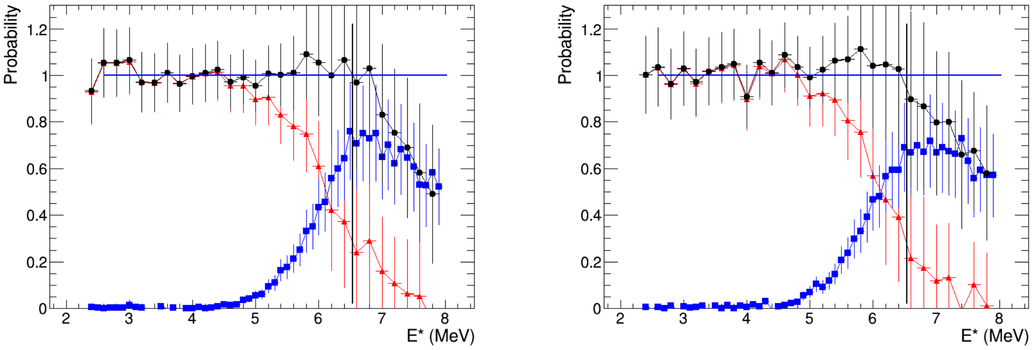

(e) Ejectile angle 144.7^o (f) Ejectile angle 150.6^o

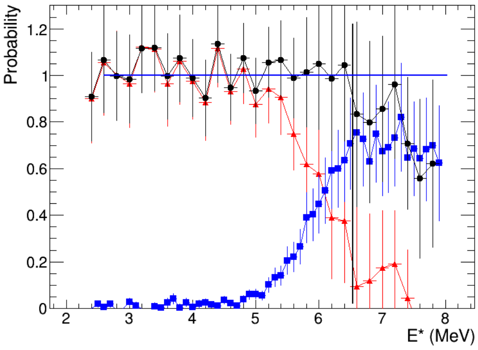

(g) Ejectile angle 156.0^o

Figure D.2: Decay probabilities: fission (blue squares), gamma-decay (red triangles) and sum of both (black circles), as a function of excitation energy for each one of the studied ejectile angles. Ternary fission background was subtracted.

D.2 Results of the $^{240}Pu(^{3}He,^{4}He)$ Reaction

In this section we present the results for the $^{240}Pu(^{3}He,^{4}He)$ reaction. As explained in chapter 4, the telescope number 1 had a lot of noise in the case of the ^{3}He beam. Also, the lack of statistics makes the gamma decay probability useless. Therefore we give the results of the fission probability as a function of excitation energy of $^{239}Pu^{*}$ obtained with telescope two in figure D.3. The results are compared to the ones given by Back *et al.* [14] with a $^{238}Pu(d,p)$ reaction and the neutron induced probability with which they compare in [47].

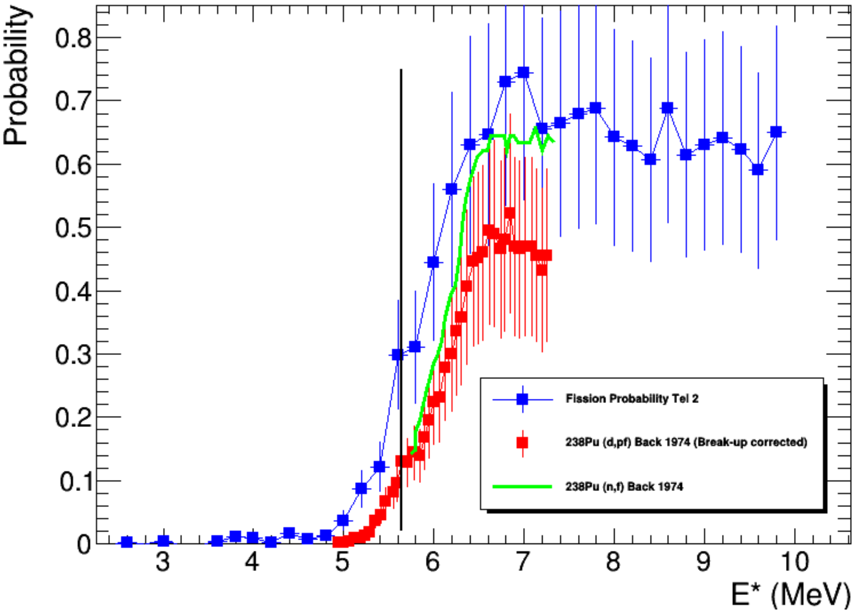

Figure D.3: Fission probability as a function of excitation energy of $^{239}Pu^{*}$ obtained with telescope number 2 (blue squares). The data are compare to the (d,p) and the neutron induced data given by Back *et al.* [14]

Our fission probability is systematically higher than the one obtained with the (d,p) reaction. This could be due to a problem with the calibration, of one or both sets of experimental data, a shift of 200 keV would bake the data agree better up to 6.5 MeV. The difference could also be due to the background peaks in the proton spectra of the (d,p) reaction, which adds to the deuteron background for $E^{*} > S_{n}$. Even though the authors of [14] corrected for the break-up, this can be very difficult and still have an effect on the surrogate probabilities. However, between 6.4 and 7.2 MeV our data are in good agreement with the neutron fission probability.

Appendix E

Deduction of the Differential Cross Sections

The total wave function of a nuclear reaction can be built as the superposition of an incoming wave packet $\Psi_{in}(\mathbf{r}, t)$ and a scattered one $\Psi_{scat}(\mathbf{r}, t)$. However, for the sake of simplicity, we will in a first approach assume that these wave functions take the form of plane waves, which is a reasonable approximation when considering a *flux* of particles. Under this hypothesis the incoming wave takes the explicit form:

$$\Psi_{in}(\mathbf{r}, t) = e^{i(\mathbf{p}\cdot\mathbf{r}-Et)/\hbar} \tag{E.1}$$

where $\mathbf{p} = -i\hbar\nabla$, is the linear momentum operator and $E = \mathbf{p}^2/2m$ is the total kinetic energy. Even though $|\Psi_{in}(\mathbf{r}, t)|^2$ is not integrable, this approximation is useful when studying the probability current $\mathbf{J}_{in}$ as defined in equation (E.2). The reason is that it reduces the problem to calculating the transmission coefficients of the wave when interacting with the nucleus.

$$\mathbf{J}_{in} = \frac{\hbar}{2mi}(\Psi_{in}\nabla\Psi^*_{in} - \Psi^*_{in}\nabla\Psi_{in}) \tag{E.2}$$

Moreover, when $|\mathbf{r}| \to \infty$ then $\Psi_{scat}(\mathbf{r}, t)$ takes the form of a spherical wave. The reason is that the region in which $U(\mathbf{r})$ is significant, where $\Psi_{scat}(\mathbf{r}, t)$ is generated, can be assumed to be small in comparison to the distance. Thus, in the limit $|\mathbf{r}| \to \infty$ along a fixed direction $\mathbf{u}_r = \mathbf{r}/|\mathbf{r}|$, the total wave function $\Psi = \Psi_{in} + \Psi_{scat}$ can be approximated by:

$$\Psi(\mathbf{r}, t) \approx \Psi_{in}(\mathbf{r}, t) + f(\mathbf{p}', \mathbf{p})\frac{exp[i/\hbar(|\mathbf{p}||\mathbf{r}| - Et)]}{|\mathbf{r}|} \tag{E.3}$$

where $\mathbf{p}' = \sqrt{\frac{2mE}{\hbar^2}}\mathbf{u}_r$, $E = \mathbf{p}'^2/2m$ and $f(\mathbf{p}', \mathbf{p})$ is the scattering amplitude. This function f represents the magnitude of Ψ_{scat} in each direction if $|\mathbf{r}| \to \infty$.

When substituting eq. (E.1) in eq. (E.2) one obtains the following relation between the probability current and linear momentum:

$$\mathbf{J}_{in} = \frac{\mathbf{p}}{m} \tag{E.4}$$

If we now imagine a flat surface S perpendicular to $\mathbf{p}$ at a distance $|\mathbf{r}| \to \infty$ and time $t \to \infty$, then the flux $\mathbf{J}_{in}$ through that surface in the direction $\mathbf{n} = \mathbf{p}/|\mathbf{p}|$ is:

$$\int_S \mathbf{n} \cdot \mathbf{J}_{in} ds = \mathbf{n} \cdot \mathbf{J}_{in} S = \frac{|\mathbf{p}|}{m} S \tag{E.5}$$

The probability flux due to $\mathbf{J}_{in}$ by unit of time and area is $|\mathbf{p}|/m$. Therefore the next step is to evaluate the probability current $\mathbf{J}_{scat}$, associated to outgoing wave Ψ_{scat} when $|\mathbf{r}| \to \infty$ (second term of the summation in equation (E.3)). To that end, Ψ_{in} is replaced by Ψ_{scat} in equation (E.2), and after several steps, here omitted, one arrives to the following expression:

$$\mathbf{J}_{scat} \approx \frac{|\mathbf{p}|}{m} |f(\mathbf{p}', \mathbf{p})|^2 \frac{\mathbf{u}_r}{|\mathbf{r}|^2} \tag{E.6}$$

Using equation (E.6) and taking into account that $ds = |\mathbf{r}|^2 d\Omega$, and $d\Omega = sen(\theta) d\theta d\phi$, then scattered flux $\mathbf{J}_{scat}$ through differential ds of a sphere of radius $|\mathbf{r}| \to \infty$ per unit of time is:

$$ds \mathbf{J}_{scat} \mathbf{u}_r \sim \frac{|\mathbf{p}|}{m} |f(\mathbf{p}', \mathbf{p})|^2 d\Omega \tag{E.7}$$

We will now define the differential cross section $d\sigma/d\Omega$ over the direction $\mathbf{u}_r$, or equivalently $\mathbf{p}'$, as the probability current associated to $\mathbf{J}_{scat}$ through ds per unit of time and solid angle, divided by the incident flux $|\mathbf{p}|/m$, which simplifies to eq. (5.3):

$$\frac{d\sigma}{d\Omega} = \frac{1}{|\mathbf{p}|/m \cdot d\Omega} \frac{|\mathbf{p}|}{m} |f(\mathbf{p}', \mathbf{p})|^2 d\Omega = |f(\mathbf{p}', \mathbf{p})|^2 \tag{E.8}$$

Equation (E.3) can be justified in the context of the Lippmann-Schwinger formalism, where, making use of Green's functions, a relation between $f(\mathbf{p}', \mathbf{p})$ and the potential that causes the scattering $U(\mathbf{r})$ can be established. The formal procedure will be here omitted but a detailed proof can be found in several quantum mechanics textbooks, for instance [78]. The exact expression of the scattering amplitude obtained is an infinite summation, truncating it to the first order is known as Born's approximation:

$$f(\mathbf{p}', \mathbf{p}) \simeq f_{Born}(\mathbf{p}', \mathbf{p}) = -\frac{m}{2\pi\hbar^2} \int exp\left[i \left(\frac{\mathbf{p} - \mathbf{p}'}{\hbar} \right) \mathbf{r}' \right] U(\mathbf{r}') d^3\mathbf{r}' \tag{E.9}$$

It can be proven that the approximation done in equation (E.9) gets more accurate the higher the difference between the energy of the particle and the magnitude of the potential, and is useful to have a first estimate of a cross section.

Instead of reducing the problem to the scattering of a plane wave by a potential, it is more correct to represent incoming particles as wave packets of the form:

$$\Psi_{in}(\mathbf{r}, t) = \int A(\Omega_{p'}) e^{i(\mathbf{p} \cdot \mathbf{r} - Et)/\hbar} d\Omega_{p'} \tag{E.10}$$

where $A(\Omega_{p'})$ is a weight function of the different plane waves forming the packet and the direction of linear momentum $\mathbf{p}$' is characterized in spherical coordinates by $d\Omega_{p'} = sin(\theta_{p'}) d\theta_{p'} d\phi_{p'}$. A derivation of the formulas obtained in this formalism can be found in [78].

Appendix F

Optical Model Parametrization

F.1 Model of Soukhovitskii *et al.*

Actinides, such as plutonium, are deformed nuclei therefore the optical potential is deformed and thus in spherical coordinates $U(\mathbf{r},E) \equiv U(r,\theta,\phi,E)$. Axial symmetry around ϕ is assumed and only the dependence on θ is kept so that the potential may be written as follows:

$$\begin{aligned} U(\mathbf{r},E) = &- [V_V(E) + iW_V(E)] f(r, a_V, R_V(\theta)) \\ &+ 4a_D [V_D(E) + iW_D(E)] \frac{d}{dr} f(r, a_D, R_D(\theta)) \\ &+ \left(\frac{\hbar}{\mu_\pi c}\right)^2 \frac{[V_{SO}(E) + iW_{SO}(E)]}{r} (\hat{\sigma} \cdot \hat{L}) \frac{d}{dr} f(r, a_{SO}, R_{SO}(\theta)) \\ &+ V_C(r, a_C, R_C(\theta)) \end{aligned} \tag{F.1}$$

where the form factors f are of the Woods-Saxon type:

$$f(r, a_i, R_i(\theta)) = \frac{1}{1 + exp\left(\frac{r - R_i(\theta)}{a_i}\right)} \tag{F.2}$$

and as in this case axial symmetry was assumed, the dependence on the azimuth disappears and the radii in equation 5.17 can be expressed as:

$$R_i(\theta) = r_i A^{\frac{1}{3}} \left[1 + \sum_{\lambda=2,4,\ldots} \beta_\lambda Y_\lambda^0(\theta)\right] \tag{F.3}$$

However, in the parametrization of JENDL 4.0, the development of the radius in equation F.3 is truncated to the third term:

$$R_i(\theta) = r_i A^{\frac{1}{3}} \left[1 + \beta_2 Y_2^0(\theta) + \beta_4 Y_4^0(\theta) + \beta_6 Y_6^0(\theta)\right] \tag{F.4}$$

with $i =$ V, D, SO and C standing for volume, surface, spin-orbit and Coulomb respectively, and A the mass of the target nucleus.

The first term of the right hand side of equation F.1 represents the volume-central term of the interaction between the projectile and the target nucleus. It is split into a real part V_V and an imaginary one W_V that tends to remove flux from the elastic channel. The second term represents the imaginary surface-central term, and it is specially important at low incident energies as the projectile cannot penetrate deep into the target. The third term accounts for the contribution of the spin-orbit coupling to the potential, and the higher the energy is, the stronger the impact it has on the cross sections. The last term is the Coulomb potential and it only plays a role when the projectile is also a charged particle, for neutrons this term is zero and it will be neglected in the following because the evaluation will be done using neutron-induced reaction data.

The potential presented in equation (F.1) is dispersive, which means that it is consistent with the causality principle, which ensures that the scattered wave is not emitted before the incident one arrives. This is guaranteed adding a correction term $\Delta V(\mathbf{r}, E)$ to the real central potential. Under certain circumstances the real part $\Delta V(\mathbf{r}, E)$ can be calculated through the dispersion relation.

$$\Delta V(\mathbf{r}, E) = \frac{\mathcal{P}}{\pi} \int_{-\infty}^{\infty} \frac{W(\mathbf{r}, E')}{E - E'} dE' \tag{F.5}$$

where $\mathcal{P}$ indicates that Cauchy's principal value of the improper integral should be taken. For energy-dependent geometry one should use (F.5) to calculate the correction to the real potential, but to simplify the problem, the parameters are assumed to be independent of energy. The dependence on the geometry is included in the Woods-Saxon functions $f(r)$, and therefore they can be extracted from the integral (F.5), leaving $\Delta V(E)$ and $W(E)$. In this kind of dispersion relation treatment the real volume term V_V is the sum of two terms:

$$V_V(E) = V_{HF}(E) + \Delta V_V(E) \tag{F.6}$$

where V_{HF} is the Hartree-Fock (HF) term, calculated with an expression derived by Lipperheide [113]:

$$V_{HF}(E) = A_{HF} \cdot exp[-\lambda_{HF}(E - E_F)] \tag{F.7}$$

where A_{HF} is a constant to be determined, λ_{HF} is an additional parameter and E_F is the Fermi energy. The dependence on the energy E of equation (F.7) arises when substituting the non-local potential (i.e. with finite range interactions) by a local one (with punctual interactions). The term $\Delta V_V(E)$ is calculated by substituting $W_V(E)$ in (F.5).

$$\Delta V_V(E) = \frac{\mathcal{P}}{\pi} \int_{-\infty}^{\infty} \frac{W_V(E')}{E - E'} dE' \tag{F.8}$$

In the case of the surface real term V_D, the only contribution to it is the dispersive term, so that:

$$V_D(E) = \Delta V_D(E) = \frac{\mathcal{P}}{\pi} \int_{-\infty}^{\infty} \frac{W_D(E')}{E - E'} dE' \tag{F.9}$$

Once the dispersion relations between the imaginary terms and the real ones have been determined, (F.5) to (F.9), the difficulty is to find a suitable functional form for W_V and W_D. For the volume term in [28] an energy dependence in the following the form of Brown and Rho [114] is given:

$$W_V(E) = A_V \frac{(E - E_F)^2}{(E - E_F)^2 + B_V^2} \tag{F.10}$$

where A_V and B_V are undetermined parameters. The E-function of the imaginary surface term W_S proposed by Delaroche *et al.* [115]:

$$W_S(E) = A_S \frac{(E - E_F)^2}{(E - E_F)^2 + B_S^2} exp(-C_S|E - E_F|) \tag{F.11}$$

where as in (F.7) and (F.10), A_S is constant to be calculated, and B_S and C_S are additional parameters of the model.

The dependence on the isospin (the Lane term [116] and [117]) of the potential is taken into account in the real $V_{HF}(E)$ and the imaginary surface $W_S(E)$ as following:

$$A_{HF} = V_0 \left[1 + (-1)^{Z'+1} \frac{C_{viso}}{V_0} \frac{N - Z}{A} \right] \tag{F.12}$$

$$A_S = W_0 \left[1 + (-1)^{Z'+1} \frac{C_{wiso}}{W_0} \frac{N - Z}{A} \right] \tag{F.13}$$

where V_0, C_{viso}, W_0 and C_{wiso} are parameters of the model. And for energies E below the Fermi energy, the symmetry condition is used:

$$W(2E_F - E) = W(E) \tag{F.14}$$

The assumption that the imaginary potential $W_V(E)$ is symmetric about $E' = E_F$, is not valid when $|E' - E_F|$ is large. In some cases, for projectile energies above $50MeV$ there is already an important difference, although this value is arbitrary and it is another parameter of the model E_a. When $E < E_F - E_a$ or $E > E_F + E_a$ an alternative form $\tilde{W}_V(E)$, proposed by Mahaux and Sartor [118], is used instead of $W_V(E)$.

The energy dependence of the spin-orbit potential follows the form suggested by Koning and Delaroche [83] plus a dispersive term first added by Morillon and Romain [119]:

$$V_{SO}(E) = V_{SO} exp[-\lambda_{SO}(E - E_F)] + \frac{\mathcal{P}}{\pi} \int_{-\infty}^{\infty} \frac{W_{SO}(E')}{E - E'} dE' \tag{F.15}$$

$$W_{SO}(E) = W_{SO} \frac{(E - E_F)^2}{(E - E_F)^2 + B_{SO}^2} \tag{F.16}$$

To sum up, there are twenty-three parameters to be adjusted, plus three for the Coulomb interaction.

F.2 Numerical Values from JENDL

The numerical values of the parameters from JENDL 4.0 of the optical model potential [28] for the reaction $^{239}Pu(n, tot)$:

- Eight for the volume terms:
  $V_0 = 50.054\ MeV$
  $\lambda_{HF} = 0.01004\ 1/MeV$
  $C_{viso} = 15.9\ MeV$
  $A_V = 12.04\ MeV$
  $B_V = 81.36\ MeV$
  $E_a = 385\ MeV$
  $r_V = 1.2568\ fm$
  $a_V = 0.633\ fm$
- Six parameters for the surface potential:
  $W_0 = 17.1463\ MeV$
  $B_S = 11.19\ MeV$
  $C_S = 0.01361\ 1/MeV$
  $C_{wiso} = 11.19\ MeV$
  $r_S = 1.1803\ fm$
  $a_S = 0.601\ fm$
- Six for the spin-orbit interaction:
  $V_{SO} = 5.75\ MeV$
  $\lambda_{SO} = 0.005\ 1/MeV$
  $W_{SO} = -3.1\ MeV$
  $B_{SO} = 160\ MeV$
  $r_{S0} = 1.1214\ fm$
  $a_{SO} = 0.59\ fm$
- Three for the electromagnetic interaction:
  $C_C = 1.3$
  $r_C = 1.2452\ fm$
  $a_C = 0.545\ fm$
- Three deformation parameters:
  $\beta_2 = 0.227635$
  $\beta_4 = 0.06501$
  $\beta_6 = -0.01837$

Appendix G

Talys 1.9 Input Parameters

In this appendix we describe the parameters deduced from the evaluation with Talys 1.9 [26], where the input file used was:

Basic Input Parameters :

```
projectile n
element pu
mass 239
energy energies
ejectiles n g
ffevaporation y
maxrot 8
maxlevelstar 30
preequilibrium y
preeqspin y
widthfluc y
dispersion y
soswitch 8
```

Level Densities :

```
ldmodel 1
colldamp n
```

Fission :

```
fission y
fismodel 1
hbtransfile 94 240 hbstates240Pu
class2file 94 240 myclass2states
```

240*Pu Barrier Parameters* :

```
deltaW 94 240 3.2500 1
```

```
T 94 240 0.3250 1
E0 94 240 -0.4725 1
Exmatch 94 240 3.0800 1
s2adjust 94 240 1.0 1

deltaW 94 240 1.1140 2
T 94 240 0.3650 2
E0 94 240 -0.4750 2
Exmatch 94 240 2.9574 2
s2adjust 94 240 1.0 2

fisbar 94 240 5.970 1
fishw 94 240 0.850 1
fisbar 94 240 5.100 2
fishw 94 240 0.650 2
```

239*Pu Barrier Parameters* :

```
deltaW 94 239 1.5000 1
T 94 239 0.3300 1
E0 94 239 -0.5394 1
Exmatch 94 239 3.2056 1
s2adjust 94 239 1.0 1

deltaW 94 239 0.1800 2
T 94 239 0.3600 2
E0 94 239 -0.3914 2
Exmatch 94 239 3.0056 2

fisbar 94 239 6.650 1
fishw 94 239 0.900 1
fisbar 94 239 5.750 2
fishw 94 239 0.600 2
```

Gamma Strength Function :

```
gnorm 1
strength 8
strengthM1 8
upbendc 94 240 1.8e-8 E1
upbende 94 240 1.0e-1 E1
```

OMP JENDL :

```
optmod 94 239 JENDL239Pu n
deformfile 94 JENDLPu.def
```

G.1 Modified Files

Most of the options used in the input are default in Talys, and depend on the keywords used. However some files were modified in the given input. The file "JENDL239Pu" contains the parameters of the optical model, for several neutron energies, used for the coupled channels calculation and its derived from JENDL 4.0, appendix F. The file "JENDLPu.def" contains the deformation parameters of this evaluation also needed for the optical model calculation. The file "hbstates240Pu" contains the head-band states over the fission barriers given by Bouland *et al.* [40] here we detail them. Finally, "myclass2states" contains the class-II states retained after the evaluation and comparison with the surrogate data.

JENDLPu.def:

```
94 239 8 R B 239Pu
0 R 0 0.22764 0.06501 -0.0184
1 R 0
2 R 0
3 R 0
4 R 0
5 R 0
7 R 0
9 R 0
94 240 5 R D 240Pu
0 R 0 1.72265 0.54811
1 R 0
2 R 0
3 R 0
4 R 0
```

hbstates240Pu:

```
1 9 0.990
1 0.000000 0.0 1
2 0.700000 0.0 -1
3 0.800000 1.0 -1
4 0.150000 2.0 1
5 1.150000 1.0 1
6 0.850000 2.0 -1
7 0.450000 0.0 1
8 0.370000 4.0 1
9 1.740000 0.0 -1
2 9 0.650
1 0.000000 0.0 1
2 0.100000 0.0 -1
3 0.550000 1.0 -1
4 0.800000 2.0 1
5 1.000000 1.0 1
6 0.900000 2.0 -1
```

7 1.500000 0.0 1
8 1.700000 4.0 1
9 1.740000 0.0 -1

myclass2states:
1 2.900 0.0 1
2 3.500 0.0 -1
3 3.550 1.0 -1
4 3.700 2.0 1
5 4.950 1.0 -1

Bibliography

[1] G. Boutoux, et al. The extrapolated-efficiency method, a new technique to determine the γ-cascade detection efficiency in experiments based on the surrogate-reaction method. *Nuclear Instruments and Methods in Physics Research A*, (700):59–64, 2013.

[2] Q. Ducasse, et al. Application of the EXtrapolated Efficiency Method (EXEM) to infer the gamma-cascade detection efficiency in the actinide region. *Nuclear Instruments and Methods in Physics Research A*, (826):60–64, 2016.

[3] Q. Ducasse, et al. Investigation of the $^{238}\mathrm{U}(d,p)$ surrogate reaction via the simultaneous measurement of γ-decay and fission probabilities. *Phys. Rev. C*, 94:024614, Aug 2016.

[4] G. Boutoux, et al. Study of the surrogate-reaction method applied to neutron-induced capture cross sections. *Physics Letters B*, 712(4):319 – 325, 2012.

[5] Jurado, B., et al. Investigation of the surrogate-reaction method via the simultaneous measurement of gamma-emission and fission probabilities. *EPJ Web Conf.*, 146:11006, 2017.

[6] Delaune, O., et al. Measurement of the ssion probability of 173Yb using surrogate reactions. *EPJ Web of Conferences*, 93:02010, 2015.

[7] G. Kessedjian. *Mesurres de sections efficaces d'actinides mineurs d'interet pour la transmutation.* PhD thesis, U. Bordeaux, 2008.

[8] G. Boutoux. *Sections efficaces neutroniques via la methode de substitution.* PhD thesis, U. Bordeaux, 2011.

[9] C. Theroine. *Etude de la reaction de capture neutronique radiative pour le noyau instable 173Lu par la methode directe et par reaction de substitution.* PhD thesis, U. Paris XI, 2013.

[10] Q. Ducasse. *Etude de la metode de substitution a partir de la mesure simultanee des probabilites de fission et d'emission gamma des actinides 236U, 238U, 237Np et 238Np.* PhD thesis, U. Bordeaux, 2015.

[11] N. Bohr. Neutron Capture and Nuclear Constitution. *Nature*, (137):344, 1936.

[12] V. Weisskopf. Nuclear Physics. *Rev. Mod. Phys.*, 29:174–181, 1957.

[13] J. D. Cramer and H. C. Britt. Neutron Fission Cross Sections for ^{231}Th, ^{233}Th, ^{235}U, ^{237}U, ^{239}U, ^{241}Pu, and ^{243}Pu from 0.5 to 2.25 MeV Using (t, pf) Reactions. *Nuclear Science and Engineering*, 41(2):177–187, 1970.

[14] B.B. Back, et al. Fission of U, Np, Pu and Am isotopes excited in the (d, p) reaction. *Nuclear Physics A*, 165(3):449 – 474, 1971.

[15] M. Petit, et al. Determination of the ^{233}Pa(n,f) reaction cross section from 0.5 to 10 MeV neutron energy using the transfer reaction ^{232}Th(^{3}He,p)^{234}Pa. *Nuclear Physics A*, 735(3):345 – 371, 2004.

[16] G. Kessedjian, et al. Neutron-induced fission cross sections of short-lived actinides with the surrogate reaction method. *Physics Letters B*, 692(5):297 – 301, 2010.

[17] J. J. Ressler, et al. Surrogate measurement of the ^{238}Pu(n, f) cross section. *Phys. Rev. C*, 83:054610, May 2011.

[18] R. O. Hughes, et al. ^{236}Pu(n, f), ^{237}Pu(n, f), and ^{238}Pu(n, f) cross sections deduced from (p, t), (p, d), and $(p, p^{'})$ surrogate reactions. *Phys. Rev. C*, 90:014304, Jul 2014.

[19] S. Boyer, et al. Determination of the ^{233}Pa(n, γ) capture cross section up to neutron energies of 1MeV using the transfer reaction ^{232}Th$(^{3}\mathrm{He}, p)$. *Nuclear Physics A*, 775(3):175 – 187, 2006.

[20] L. A. Bernstein, et al. Deducing the 237U destruction cross-sections using the Surrogate Ratio Method. In *UCRL-PROC-220800*. Lawrence Livermore National Laboratory, 2006.

[21] N. D. Scielzo, et al. Measurement of γ-emission branching ratios for ^{154,156,158}Gd compound nuclei: Tests of surrogate nuclear reaction approximations for (n, γ) cross sections. *Phys. Rev. C*, 81:034608, Mar 2010.

[22] J. E. Escher, et al. Constraining Neutron Capture Cross Sections for Unstable Nuclei with Surrogate Reaction Data and Theory. *Phys. Rev. Lett.*, 121:052501, Jul 2018.

[23] A. Ratkiewicz, et al. Towards Neutron Capture on Exotic Nuclei: Demonstrating $(d, p\gamma)$ as a Surrogate Reaction for (n, γ). *Phys. Rev. Lett.*, 122:052502, Feb 2019.

[24] R. Pérez Sánchez, et al. Experimental set-up for the simultaneous measurement of fission and γ-emission probabilities induced by transfer or inelastic-scattering reactions. *Nuclear Instruments and Methods in Physics Research Section A: Accelerators, Spectrometers, Detectors and Associated Equipment*, 933:63 – 70, 2019.

[25] *Kaliveda user's manual*, 2018. indra.in2p3.fr/kaliveda/usersguide.html.

[26] *Talys 1.9 user's manual*, 2017. www.talys.eu/documentation.

[27] Keiichi Shibata, et al. JENDL-4.0: A New Library for Nuclear Science and Engineering. *Journal of Nuclear Science and Technology*, 48(1):1–30, 2011.

[28] E. Sh. Soukhovitskii, et al. Dispersive coupled-channel analysis of nucleon scattering from ^{232}Th up to 200 MeV. *Phys. Rev. C*, 72:024604, Aug 2005.

[29] Hilaire, S., et al. Potential sources of uncertainties in nuclear reaction modeling. *EPJ Nuclear Sci. Technol.*, 4:16, 2018.

[30] Dupuis, M., et al. Potential sources of uncertainties in nuclear reaction modeling. *Eur. Phys. J. A*, 54:168, 2015.

[31] J. N. Wilson, et al. Indirect (n, γ) cross sections of thorium cycle nuclei using the surrogate method. *Phys. Rev. C*, 85:034607, Mar 2012.

[32] V. V. Desai, et al. Determining ^{234}Pa(n,f) cross sections using the surrogate method. *Phys. Rev. C*, 89:024606, Feb 2014.

[33] A. Pal, et al. Determination of ^{238}Pu(n, f) and ^{236}Np(n, f) cross sections using surrogate reactions. *Phys. Rev. C*, 91:054618, May 2015.

[34] B. L. Goldblum, et al. Surrogate ratio methodology for the indirect determination of neutron capture cross sections. *Phys. Rev. C*, 81:054606, May 2010.

[35] S. Q. Yan, et al. Examination of the surrogate ratio method for the determination of the ^{93}Zr$(n, \gamma)\,^{94}$Zr cross section with ^{90,92}Zr(^{18}O,^{16} O) ^{92,94}Zr reactions. *Phys. Rev. C*, 94:015804, Jul 2016.

[36] M. Guttormsen, et al. Constant-temperature level densities in the quasicontinuum of Th and U isotopes. *Phys. Rev. C*, 88:024307, Aug 2013.

[37] T. A. Laplace, et al. Statistical properties of ^{243}Pu, and ^{242}Pu(n, γ) cross section calculation. *Phys. Rev. C*, 93:014323, Jan 2016.

[38] F. Zeiser and et. al. Restricted spin-range correction in the Oslo Method: The example of nuclear level density and γ-ray strength function from (d,p)240Pu. In *eprint arXiv:1904.02932*, April 2019.

[39] F. Farget. Experimental Description of Fission Fragment Yields. In *Fission experiments and theoretical advances (FIESTA)*, 2017.

[40] J. E. Lynn, P. Talou, and O. Bouland. Reexamining the role of the $(n, \gamma f)$ process in the low-energy fission of ^{235}U and ^{239}Pu. *Phys. Rev. C*, 97:064601, Jun 2018.

[41] J.D. Cramer and H.C. Britt. Fission Studies of Thorium, Uranium, and Plutonium Isotopes with (t, pf) Reactions*. *Physical Review C*, 2(6), 1970.

[42] W. Younes and H. C. Britt. Simulated neutron-induced fission cross sections for various Pu, U, and Th isotopes. *Phys. Rev. C*, 68:034610, Sep 2003.

[43] G. Kessedjian, et al. Fission probabilities of 242Am, 243Cm, and 244Cm induced by transfer reactions. *Physical Review C*, 91(044607), 2015.

[44] S. N. Ghoshal. An Experimental Verification of the Theory of Compound Nucleus. *Phys. Rev.*, 80:939–942, Dec 1950.

[45] V.F. Weisskopf. The formation of the compound nucleus. *Physica*, 22(6):952 – 958, 1956.

[46] O. Bouland, J. E. Lynn, and P. Talou. R-matrix analysis and prediction of low-energy neutron-induced fission cross sections for a range of Pu isotopes. *Phys. Rev. C*, 88:054612, Nov 2013.

[47] B. B. Back, et al. Fission of odd-A and doubly odd actinide nuclei induced by direct reactions. *Phys. Rev. C*, 10:1948–1965, Nov 1974.

[48] H. C. Britt and J. B. Wilhelmy. Simulated (n,f) Cross Sections for Exotic Actinide Nuclei. *Nuclear Science and Engineering*, 72(2):222–229, 1979.

[49] W. Younes and H. C. Britt. Neutron-induced fission cross sections simulated from (t, pf) results. *Phys. Rev. C*, 67:024610, Feb 2003.

[50] B. B. Back, et al. Fission of doubly even actinide nuclei induced by direct reactions. *Phys. Rev. C*, 9:1924–1947, May 1974.

[51] B. F. Lyles, et al. Absolute and relative surrogate measurements of the $^{236}\mathrm{U}(n, f)$ cross section as a probe of angular momentum effects. *Phys. Rev. C*, 76:014606, Jul 2007.

[52] Ian J. Thompson. Coupled reaction channels calculations in nuclear physics. *Computer Physics Reports*, 7(4):167 – 212, 1988.

[53] R. Capote, et al. RIPL, Reference Input Parameter Library for Calculation of Nuclear Reactions and Nuclear Data Evaluations. *Nuclear Data Sheets*, 110(12):3107 – 3214, 2009. Special Issue on Nuclear Reaction Data.

[54] Jutta E. Escher, et al. Compound-nuclear reaction cross sections from surrogate measurements. *Rev. Mod. Phys.*, 84:353–397, Mar 2012.

[55] C. Plettner, et al. Estimation of (n, f) cross sections by measuring reaction probability ratios. *Phys. Rev. C*, 71:051602, May 2005.

[56] V. V. Desai, et al. Determination of the $^{239}\mathrm{Np}$ (n, f) and $^{240}\mathrm{Np}(n, f)$ cross sections using the surrogate reaction method. *Phys. Rev. C*, 88:014613, Jul 2013.

[57] N. D. Scielzo, et al. Statistical γ rays in the analysis of surrogate nuclear reactions. *Phys. Rev. C*, 85:054619, May 2012.

[58] M. Guttormsen, T. Ramsøy, and J. Rekstad. The first generation of γ-rays from hot nuclei. *Nuclear Instruments and Methods in Physics Research Section A: Accelerators, Spectrometers, Detectors and Associated Equipment*, 255(3):518 – 523, 1987.

[59] M Guttormsen, et al. The unfolding of continuum γ-ray spectra. *Nuclear Instruments and Methods in Physics Research Section A: Accelerators, Spectrometers, Detectors and Associated Equipment*, 374(3):371 – 376, 1996.

[60] A Schiller, et al. Extraction of level density and γ strength function from primary γ spectra. *Nuclear Instruments and Methods in Physics Research Section A: Accelerators, Spectrometers, Detectors and Associated Equipment*, 447(3):498 – 511, 2000.

[61] A. C. Larsen, et al. Analysis of possible systematic errors in the Oslo method. *Phys. Rev. C*, 83:034315, Mar 2011.

[62] A. Gilbert and A. G. W. Cameron. A composite nuclear-level density formula with shell corrections. *Can. J. Phys.*, 43:1446–1496, 1965.

[63] R. W. Hockenbury, A. J. Sanislo, and N. N. Kaushal. KeV capture cross section ^{242}Pu. In *Conference on Nuclear Cross Sections and Technology*, volume 2 of *Conference on Nuclear Cross Sections and Technology*, pages 584–586, 1975.

[64] K. Wisshak and F. Käppeler. Neutron Capture Cross-Section Ratios of Plutonium-240 and Plutonium-242 Versus Gold-197 in the Energy Range from 50 to 250 keV. *Nuclear Science and Engineering*, 69(1):39–46, 1979.

[65] Kris Heyde, Peter von Neumann-Cosel, and Achim Richter. Magnetic dipole excitations in nuclei: Elementary modes of nucleonic motion. *Rev. Mod. Phys.*, 82:2365–2419, Sep 2010.

[66] R. Bass. *Nuclear Reactions with Heavy Ions*. Springer-Verlag, 1980.

[67] *Micron Semiconductors detector catalogue*, 2018. http://www.micronsemiconductor.co.uk/strip-detectors-double-sided/.

[68] Gunter Siegert. Photovoltaic cells as fission product detectors. *Nuclear Instruments and Methods*, 164(3):437 – 438, 1979.

[69] C. Theisen, et al. SAPhIR: a fission-fragment detector. In *American Institute of Physics Conference Series*, volume 447 of *American Institute of Physics Conference Series*, pages 143–150, October 1998.

[70] M. Petit, et al. Determination of the ^{233}Pa(n, f) reaction cross section from 0.5 to 10 MeV neutron energy using the transfer reaction ^{232}Th(^{3}He, p) ^{234}Pa. *Nuclear Physics A*, 735:345–371, May 2004.

[71] F. B. McLean and T. R. Oldham. Charge Funneling in N- and P-Type Si Substrates. *IEEE Transactions on Nuclear Science*, 29(6):2017–2023, Dec 1982.

[72] C. Hsieh, P. C. Murley, and R. R. O'Brien. Collection of charge from alpha-particle tracks in silicon devices. *IEEE Transactions on Electron Devices*, 30(6):686–693, June 1983.

[73] N.N. Ajitanand, et al. The photovoltaic cell an eminent fission fragment detector. *Nuclear Instruments and Methods in Physics Research Section A: Accelerators, Spectrometers, Detectors and Associated Equipment*, 300(2):354 – 356, 1991.

[74] S. Vermote, et al. Ternary alpha and triton emission in the spontaneous fission of 244Cm, 246Cm and 248Cm and in the neutron induced fission of 243Cm, 245Cm and 247Cm. *Nuclear Physics A*, (806):1–14, 2008.

[75] G. Vladuca and Anabella Tudora. Improved Los Alamos model applied to the neutron induced fission of 239Pu and 240Pu and to the spontaneous fission of Pu isotopes. *Annals of Nuclear Energy*, 28(7):689 – 700, 2001.

[76] K.-H. Schmidt, et al. General Description of Fission Observables: GEF Model Code. *Nuclear Data Sheets*, 131:107–221, January 2016.

[77] H. C. Britt and F. Plasil. Fission of U^{238} and Pu^{240} Nuclei Excited by Inelastic Alpha-Particle Scattering. *Phys. Rev.*, 144:1046–1059, Apr 1966.

[78] C. Sanchez del Rio. *Fisica cuantica.* Piramide, 2015.

[79] J. J. Griffin. Statistical Model of Intermediate Structure. *Phys. Rev. Lett.*, 17:478–481, Aug 1966.

[80] J. Raynal. ECIS-06, 2007.

[81] Robert E. Le Levier and David S. Saxon. An Optical Model for Nucleon-Nuclei Scattering. *Phys. Rev.*, 87:40–41, Jul 1952.

[82] H. Feshbach, C. E. Porter, and V. F. Weisskopf. Model for Nuclear Reactions with Neutrons. *Phys. Rev.*, 96:448–464, Oct 1954.

[83] A. J. Koning and J. P. Delaroche. Local and global nucleon optical models from 1 keV to 200 MeV. *Nucl. Phys.*, A713:231–310, 2003.

[84] Efrem Sh Soukhovitskii, et al. Global coupled-channel optical potential for nucleon–actinide interaction from 1 keV to 200 MeV. *Journal of Physics G: Nuclear and Particle Physics*, 30(7):905–920, may 2004.

[85] P. Romain, B. Morillon, and H. Duarte. Bruyeres-le-Chatel Neutron Evaluations of Actinides with the TALYS Code: The Fission Channel. *Nuclear Data Sheets*, 131:222 – 258, 2016. Special Issue on Nuclear Reaction Data.

[86] J. A. Harvey, et al. High-resolution neutron transmission measurements on 235U, 239Pu and 238U. In *Nuclear Data for Science and Technology (Mito, JAPAN)*, pages 115–118, 1988.

[87] W. P. Poenitz, J. F. Whalen, and A. B. Smith. Total Neutron Cross Sections of Heavy Nuclei. *Nuclear Science and Engineering*, 78(4):333–341, 1981.

[88] W. P. Poenitz and J. F. Whalen. Neutron Total Cross Section Measurements in the Energy range from 47 keV to 20 MeV. Technical report, Argonne National Laboratory, 1983. ANL/NDM-80.

[89] Gang Yue, et al. Neutron Scattering Angular Distributions in 239Pu at 570 and 700 keV. *Nuclear Science and Engineering*, 122(3):366–373, 1996.

[90] H. H. Knitter and M. Coppola. Elastic neutron scattering measurements on239Pu in the energy range between 0.19 and 0.38 MeV. *Zeitschrift für Physik A Hadrons and nuclei*, 228(3):286–294, Jun 1969.

[91] P E Hodgson. Compound nucleus reactions. *Reports on Progress in Physics*, 50(9):1171–1228, sep 1987.

[92] A.J. Koning, S. Hilaire, and S. Goriely. Global and local level density models. *Nuclear Physics A*, 810(1):13 – 76, 2008.

[93] H. A. Bethe. Nuclear Physics B. Nuclear Dynamics, Theoretical. *Rev. Mod. Phys.*, 9:69–244, Apr 1937.

[94] A. V. Ignatyuk, K. K. Istekov, and G. N. Smirenkin. *Soviet Journal of Nuclear Physics*, 29:450, 1979.

[95] Torleif Ericson. The statistical model and nuclear level densities. *Advances in Physics*, 9(36):425–511, 1960.

[96] Various. Handbook for calculations of nuclear reaction data. Technical report, International Atomic Energy Agency, 1998.

[97] A. V. Voinov, et al. Level densities of ^{74,76}Ge from compound nuclear reactions. *Phys. Rev. C*, 99:054609, May 2019.

[98] S. Hilaire, et al. Temperature-dependent combinatorial level densities with the D1M Gogny force. *Phys. Rev. C*, 86:064317, Dec 2012.

[99] Said Mughabghab. *Atlas of neutron resonances: resonance parameters and thermal cross sections Z= 1-100.* 2006.

[100] Niels Bohr and John Archibald Wheeler. The Mechanism of Nuclear Fission. *Phys. Rev.*, 56:426–450, Sep 1939.

[101] D. M. Brink. PhD thesis, Oxford University, 1955.

[102] Peter Axel. Electric Dipole Ground-State Transition Width Strength Function and 7-Mev Photon Interactions. *Phys. Rev.*, 126:671–683, Apr 1962.

[103] J. Kopecky and M. Uhl. Test of gamma-ray strength functions in nuclear reaction model calculations. *Phys. Rev. C*, 41:1941–1955, May 1990.

[104] G. M. Tveten, et al. The gamma-ray strength function of ^{89}Y and ^{90}Y, 2018.

[105] M. Bolsterli, et al. New Calculation of Fission Barriers for Heavy and Superheavy Nuclei. *Phys. Rev. C*, 5:1050–1077, Mar 1972.

[106] M. Brack, et al. Funny Hills: The Shell-Correction Approach to Nuclear Shell Effects and Its Applications to the Fission Process. *Rev. Mod. Phys.*, 44:320–405, Apr 1972.

[107] J. C. Hopkins and B. C. Diven. Neutron Capture to Fission Ratios in U233, U235, Pu233. *Nuclear Science and Engineering*, 12(2):169–177, 1962.

[108] V. N. Kononov. *Atomnaya Energiya*, 38(2):82, 1975.

[109] R. Batchelor and K. Wyld. Neutron scattering by U-235 and Pu-239 for incident neutrons of 2, 3 and 4 MeV. Technical report, Atomic Weapons Establishment (AWE), 1969.

[110] V. N. Andreev. Inelastic scattering of neutrons of the fission spectrum and neutrons with an energy OF 0.9 MeV in U-235 and Pu-239. Technical report, Neitronnaya Fizika, Moskva 1961, p.287, 1961.

[111] A.J. Koning and M.C. Duijvestijn. A global pre-equilibrium analysis from 7 to 200 MeV based on the optical model potential. *Nuclear Physics A*, 744:15 – 76, 2004.

[112] A. Henriques. Present and future investigations using the surrogate reaction method. In *Sakura-2019 Workshop*, 2019.

[113] R. Lipperheide. A semi-phenomenological nuclear optical-model potential. *Zeitschrift fur Physik*, 202:58–69, December 1967.

[114] G.E. Brown and Mannque Rho. The giant Gamow-Teller resonance. *Nuclear Physics A*, 372(3):397 – 417, 1981.

[115] J. P. Delaroche, Y. Wang, and J. Rapaport. Neutron$-^{90}$Zr mean field from a dispersive optical model analysis. *Phys. Rev. C*, 39:391–404, Feb 1989.

[116] A.M. Lane. Isobaric spin dependence of the optical potential and quasi-elastic (p, n) reactions. *Nuclear Physics*, 35:676 – 685, 1962.

[117] A.M. Lane. New Term in the Nuclear Optical Potential: Implications for (p, n) Mirror State Reactions. *Phys. Rev. Lett.*, 8:171–172, Feb 1962.

[118] C. Mahaux and R. Sartor. Dispersion relation approach to the mean field and spectral functions of nucleons in 40Ca. *Nuclear Physics A*, 528(2):253 – 297, 1991.

[119] B. Morillon and P. Romain. Dispersive and global spherical optical model with a local energy approximation for the scattering of neutrons by nuclei from 1 keV to 200 MeV. *Phys. Rev. C*, 70:014601, Jul 2004.

Resumé

Cette thèse porte sur l'étude des probabilités d'émission gamma (P_γ) et de fission (P_f) du noyau composé (NC) $^{240}Pu^*$ obtenues en utilisant la méthode de substitution. Cette méthode expérimentale vise, par le choix approprié de réactions nucléaires, à former un NC identique à celui formé dans une réaction de capture neutronique. Le but est de combler le manque de données nucléaires pour les noyaux de courte durée de vie pour la physique des réacteurs, la gestion des déchets radioactifs et l'astrophysique. Cependant, on a constaté avec les mesures précédentes qu'il y a une difference entre la population de spin J^π des réactions neutroniques et celles de substitution. La conséquence est que la P_γ de substitution est systématiquement plus haute que celle induite par des neutrons, alors que pour la P_f on trouve un bon accord. Pour mieux comprendre ce fait, on a mesuré simultanément la P_γ et P_f du $^{240}Pu^*$ formé lors de la réaction $^{240}Pu(^4He, ^4He')$, ce qui est très compliqué. Nous expliquons dans ce travail de thèse les détails du dispositif expérimental, l'analyse de données et ses incertitudes. Les résultats expérimentaux sont interprêtés à l'aide du code Talys 1.9 avec des paramètres fixés par les données neutroniques. D'autre part, le J^π du noyau composé est calculé avec un model de réaction directe par M. Dupuis (CEA/DAM/DIF). Cette distribution combinée avec les paramètres de réaction donne les probabilités théoriques, lesquelles réproduissent très bien nos données experimentales. Ce bon accord indique une bonne compréhension du mécanisme de réaction mis en jeu dans la réaction $^{240}Pu(^4He, ^4He')$. Ceci ouvre la voie pour utiliser les probabilités de désexcitation de substitution pour fixer les paramètres clefs du modèle statistique et ainsi obtenir des prédictions de sections efficaces des noyaux de courte durée de vie.

Abstract

This thesis is a study of the gamma decay (P_γ) and fission (P_f) probabilities of the compound nucleus (CN) $^{240}Pu^*$ obtained with the surrogate reaction method. This experimental method aims, by the appropriate choice of nuclear reactions, to form a CN identical to that formed in a n-capture reaction. The goal is to fill the deficit of nuclear data for short-lived nuclei relevant for reactor physics, nuclear waste management and astrophysics. However, it has been found in previous measurements that there is a difference between the population of spin and parity (J^π) in n-induced reactions and that of surrogate ones. This causes the surrogate P_γ to be consistently higher than the n-induced one, but in the case of fission the agreement is good in general. To better understand this, an experiment was made to simultaneously measure the P_γ and P_f as a function of the excitation energy of $^{240}Pu^*$, formed through the reaction $^{240}Pu(^4He, ^4He')$. We explain in this thesis work the details of the experimental device, the analysis of the data and their uncertainties. The experimental results are interpreted using the Talys 1.9 code with parameters set with the n-data. On the other hand, the J^π of the compound nucleus is calculated with a direct reaction model, by a collaborator. This distribution in combination with the reaction parameters gives the theoretical probabilities, which reproduce very well our experimental data. This excellent agreement indicates a good understanding of the studied surrogate reaction and opens the door to use surrogate data to deduce the n-induced fission and capture cross sections of short-lived nuclei.